Multi-microscopy Characterisation of III-nitride Devices and Materials

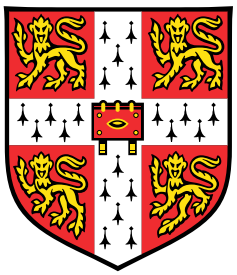

Christopher Xiang Ren

Department of Materials Science and Metallurgy
University of Cambridge

This dissertation is submitted for the degree of
Doctor of Philosophy

Wolfson College

March 2017

To my parents, Min He and Jianrong Ren. We did it!

Declaration

I hereby declare that except where specific reference is made to the work of others, the contents of this dissertation are original and have not been submitted in whole or in part for consideration for any other degree or qualification in this, or any other university. This dissertation is my own work and contains nothing which is the outcome of work done in collaboration with others, except as specified in the text and Acknowledgements. This dissertation contains fewer than 65,000 words including appendices, bibliography, footnotes, tables and equations and has fewer than 150 figures.

Christopher Xiang Ren
March 2017

Acknowledgements

First and foremost I would like to thank my supervisor Dr. Rachel Oliver for welcoming me into the GaN group with open arms. Without Rachel's guidance and support I would almost certainly not have managed to produce any of the work presented in this thesis.
I am also indebted to my colleagues at the Cambridge Centre for GaN (James, Tim, An, THomas, Tom , Helen, Lok-Yi and Fabien) for providing a jovial and friendly work environment. I have been very fortunate to work closely with Dr. Tongtong Zhu, whose rare combination of determination, efficiency and cynicism has helped fill many of the chapters in this thesis. Tongtong has consistently provided me with interesting samples to study throughout my PhD and for that I will remain forever grateful.
I'd like to thank Graham Sharp and Dr. Lata-Sahonta for TEM training, and Ted Thrush and Dick Plumb for probe station training. Without their help, I might still be attempting to turn on my LEDs to study them.
I'm of course extremely grateful for the emotional and financial support my parents and brother have provided me over the years, and for encouraging me to apply to the University of Cambridge in the first place. I'd also like to thank my friends in Manchester (Annie, Danny, Holly, Harriet, Joe, Tom, Victoria and Henry) for providing much needed trips away from the Cambridge, and remaining my friends when all I could talk about was how difficult the world of research can be to deal with. I'd like to thank Wolfson College Brazilian Jiu-Jitsu and Axis Jiu-Jitsu for providing an outlet for my frustration during my PhD, and reminding me that all of life's problems don't seem so bad when being painfully strangled.
Finally, I'd like to thank Alice Durieux for her support throughout my thesis and providing a pet cat to entertain me. Especially the cat.

Abstract

III-nitride optoelectronic devices have become ubiquitous due to their ability to emit light efficiently in the blue and green spectral ranges. Specifically, III-nitride light emitting diodes (LEDs) have become widespread due to their high brightness and efficiency. However, III-nitride devices such as single photon sources are also the subject of research and are promising for various applications. In order to improve design efficient devices and improve current ones, the relationship between the structure of the constituent materials and their optical properties must be studied. The optical properties of materials are often examined by photoluminescence or cathodoluminescence, whilst traditional microscopy techniques such a transmission electron microscopy and scanning electron microscopy are used to elucidate their structure and composition. This thesis describes the use of a dual-beam focussed ion beam/scanning electron microscope (FIB/SEM) in bridging the gap between these two types of techniques and providing a platform on which to perform correlative studies between the optical and structural properties of III-nitride materials.

The heteroepitaxial growth of III-nitrides has been known to produce high defect densities, which can harm device performance. We used this correlative approach to identify hexagonal defects as the source of inhomogeneous electroluminescence (EL) in LEDs. Hyperspectral EL mapping was used to show the local changes in the emission induced by the defects. Following this the FIB/SEM was used to prepare TEM samples from the apex of the defects, revealing the presence of *p*-doped material in the active region caused by the defect. APSYS simulations confirmed that the presence of *p*-doped material can enhance local EL.

The deleterious effects of defects on the photoelectrochemical etching of cavities were also studied. We performed TEM analysis of an edge-defect contained in unetched material on the underside of a microdisk using FIB/SEM sample preparation methods. The roughness and morphology of microdisk and nanobeam cavities was studied using FIB-tomography (FIBT), demonstrating how the dual-beam instrument may be used to access the 3D morphology of cavities down to the resolution of the SEM and the slicing thickness of the FIB.

This tomography approach was further extended with electron tomography studies of the nanobeam cavities, a tecchnique which provided fewer issues in terms of image series

alignment but also the presence of reconstruction artefacts which must be taken into account when quantitatively analysing the data.

The use of correlative techniques was also used to establish the link between high Si content in an interlayer running along the length of microrods with changes in the optical emission of these rods.

The combination of CL, FIB/SEM and TEM-based techniques has made it possible to gain a thorough understanding of the link between the structural and optical properties in a wide variety of III-nitride materials and devices.

Table of contents

List of figures

List of tables

Nomenclature

Acronyms / Abbreviations

1-D	One-Dimensional
AFM	Atomic Force Microscopy
AlN	Aluminium Nitride
BSE	Back Scattered Electron
BSF	Basal-plane Stacking Fault
C-AFM	Conductive Atomic Force Microscopy
EBL	Electron Blocking Layer
EL	Electroluminescence
ET	Electron Tomography
FIBT	Focussed Ion Beam Tomography
FSR	Free Spectral Range
GaAs	Gallium Arsenide
GaN	Gallium Nitride
InN	Indium Nitride
LED	Light-Emitting Diode
PD	Partial Dislocation
PSF	Prismatic Stacking Fault

SEM	Scanning Electron Microscope
SE	Secondary Electron
SPS	Single Photon Source
WGM	Whispering Gallery Mode

Chapter 1

Introduction

Gallium nitride (GaN) has been described as 'the most important semiconductor material since silicon' [1], and indeed the influence of this incredible material and its associated alloys (termed III-nitrides) is pervasive in modern society. The impact of III-nitride materials is perhaps best evidenced by the recent global transition from traditional lighting sources to semiconductor lighting solutions based on III-nitride materials. Since the first demonstration of a high-brightness blue light emitting diode (LED) in 1991 by Shuji Nakamura [2], the widespread use of III-nitride LEDs for general lighting purposes has blossomed into a multi-billion pound industry.

The extraordinary optical properties of III-nitride materials have also enabled their application beyond general lighting: the development of III-nitride based lasers has found applications in telecommunications [3], medicine [4] and data storage, whilst III-nitride optical emitters have been used as single photon sources (SPSs) which have applications in cryptography for secure communications [5].

The optoelectronic properties of III-nitride materials are somewhat astonishing: GaN suffers from a defect density several orders of magnitude higher than other optically active semiconductor materials such as gallium arsenide (GaAs) [6] yet is still optically active. Nonetheless, the effects of defects originating from the heteropitaxial growth of GaN are considered deleterious in terms of III-nitride device operation, highlighting the fickle relationship between the compositional and structural properties of III-nitride and their optical properties. This work aims to explore the manner in which the microstructural properties of photonic III-nitride devices affect their performance by combining multiple microscopy techniques to examine the same feature at the micro- and nano-scale, thus allowing us to link specific structural features with emissive properties at the device level. The experimental research in this thesis is separated into four main sections.

The first section details the investigation of inhomogeneous electroluminescence (EL) of in-

dium gallium nitride (InGaN) quantum well (QW) LEDs. By employing the use of scanning probe techniques, electron microscopy and spatially resolved luminescence spectroscopy the underpinning cause of inhomogeneous LED emission behaviour was elucidated.
The second section involves microscopy-based investigation into the mechanisms behind incomplete etching in the fabrication of III-nitride based microdisk cavities and the effect of this issue on the overall optical performance of these cavities. Using focussed ion beam techniques developed over the course of this work, the first direct observation of a dislocation which had induced a whisker on the underside of a microdisk cavity was reported.
The third section describes the microscopy of one dimensional (1-D) photonic crystal cavity (PCC) 'nanobeam' cavities. This section concerns the use of tomographic techniques such as electron tomography (ET) and focussed ion beam tomography (FIB-T) to investigate the manner in which fabrication issues can affect the 3-D morphology and thus the quality of III-nitride nanobeam cavities.
The final section describes a correlative study of III-nitride nano and micro-rods grown at the Cambridge Centre for Gallium Nitride. By examining both the optical properties of these rods using luminescence spectroscopy methods and examining the microstructure using electron microscopy, the growth conditions of these rods were optimised.
This introductory section will introduce the material properties of III-nitrides, common material issues and challenges encountered and III-nitride devices such as microcavities, LEDs and nanowire devices.

1.1 III-Nitride Material Properties

1.1.1 Crystal Structure

GaN can crystallise into distinct crystal structures: hexagonal (wurtzite) and cubic (zinc blende and rock salt). Under ambient conditions, wurtzite GaN is the most commonly studied form as it is the most structurally stable. Thus, the work discussed in this thesis concerns wurtzite III-nitrides. A schematic of a wurtzite III-nitride crystal structure is shown in Fig.1.1 and consists of stacked hexagonal close-packed planes following an ABABAB stacking sequence. Atoms of the respective elements (gallium and nitrogen) are tetrahedrally bonded to one another. However, in the case of III-nitrides this structure deviates from ideal tetrahedral bonding and results in a non-zero dipole moment for each unit cell which will be discussed in the following sections. Fig.1.1 shows the wurtzite crystal structure, with polar (0001) and non-polar facets (11-20) and(1-100) highlighted.

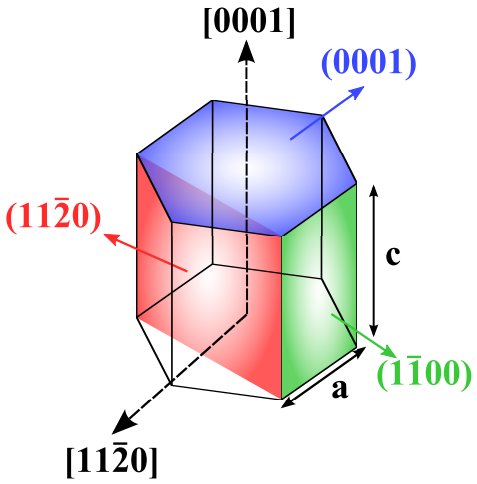

Fig. 1.1 Wurtzite crystal structure and lattice parameters **a** and **c**, the (0001),(11-20) and (1-100) planes are shown. Courtesy of J. Griffiths.

A 4-index Miller-Bravais notation (hkil) is used to denote the crystal planes where the index i is defined by the relation:

$$i = -(h+k) \tag{1.1}$$

The crystallographic planes (0001), (1-100) and (11-20) shown in Fig.1.1 are often termed the c, m and a-planes in the literature. The fundamental unit cell of the wurtzite GaN crystal structure with its associated lattice parameters **a** and **c** is shown in Fig.1.2

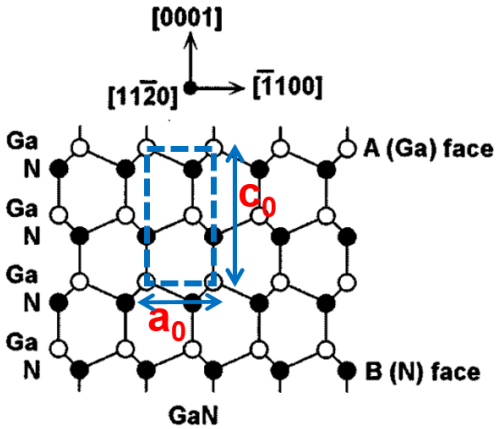

Fig. 1.2 Unit cell (dashed line) for GaN crystal structure and lattice parameters $\mathbf{a_0}, \mathbf{c_0}$. Adapted from [7]

Other members of the III-nitride materials such as indium nitride (InN) or aluminium nitride (AlN) have different lattice parameters due to the differing atomic radii of aluminium and indium relative to gallium.

Alloy	**a** (Å) at T = 300K	**c** (Å) at T = 300K
GaN	3.189	5.185
InN	3.545	5.703
AlN	3.112	4.982

Table 1.1 Room temperature lattice parameters for GaN, InN and AlN [8].

III-nitride photonic devices often involve heterostructures between ternary alloys of the materials shown in Table 1.1. Lattice parameters of a relaxed ternary alloy $A_xB_{1-x}N$ can be estimated using Vegard's law [9]:

$$\mathbf{a} = x\mathbf{a}_{AN} + (1-x)\mathbf{a}_{BN} \tag{1.2}$$

$$\mathbf{c} = x\mathbf{c}_{AN} + (1-x)\mathbf{c}_{BN} \tag{1.3}$$

Typical indium compositions for blue LEDs range between 15-20 %, which leads to a lattice mismatch of approximately 2 %, resulting in considerable amounts of strain in these GaN/InGaN heterostructures.

1.1.2 Band Structure

One of the principal driving factors behind the interest in III-nitrides for photonic devices is their direct bandgap which collectively spans the visible spectrum and beyond. The bandgap of III-nitride binary alloys is given below in Table.1.2.

Alloy	Bandgap (eV)
GaN	3.51
InN	0.78
AlN	6.25

Table 1.2 Direct bandgaps of GaN, InN and AlN [8].

Ternary alloying modifies the bandgap as shown in Fig.1.3. In theory the entire range of 0.78-6.25 eV is accessible through alloying, though material limitations reduce the full effective range for III-nitride devices [10]. It is important to note the value of the bandgap

energy for InN is widely debated, having been revised down to less than half of it's originally agreed value in 2003 [8].

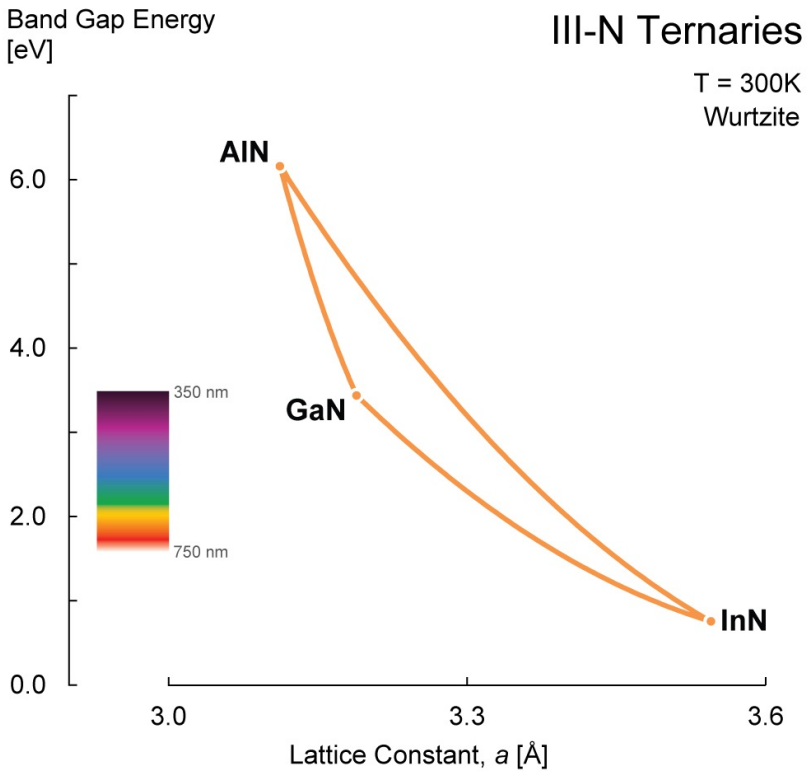

Fig. 1.3 Bandgap at room temperature for III-nitride materials with the visible spectrum shown on the left. Courtesy of K. Montgomery.

The bandgap of a ternary alloy $A_xB_{1-x}N$ is given by a modified Vegard's Law:

$$E_g = xE_g^{AN} + (1-x)E_g^{BN} - x(1-x)C \tag{1.4}$$

Where C is a bowing parameter which accounts for deviation from a linear relation between ternary alloy composition and bandgap energy. The value of the InGaN bowing parameter has been widely debated in the literature due to the lack of a reliable value for the bandgap energy for InN [8]. Although the current value of 1.4 eV is reported, there are also suggestions the bowing parameter may be composition dependent [11–13].

In considering the optical properties of III-nitride materials it is also important to consider the effects of impurities and defects. Crystal disorder introduces further energy states which would be 'forbidden' in an ideal crystal lattice leading to an effective smearing of the bandgap. Sub-bandgap absorption can occur due to the introduction of these defective states. The smearing out of the absorption edge of the material is known as the 'Urbach tail', and can be a highly deleterious source of loss in III-nitride cavity structures [14].

1.1.2.1 Quantum Confinement Effects

The first prototype high-brightness blue III-nitride LED consisted of a GaN *p-n* junction, or a 'homojunction' [2]. However modern LED structures consist of heterostructures known as quantum wells. QWs consist of a thin layer of low bandgap material between two quantum barriers with a higher bandgap. Carriers in the low bandgap material are effectively confined in one direction, hence the term 'quantum well'. This confinement leads to the discretisation of the carrier wavefunctions within the well, as shown schematically in Fig.1.4.

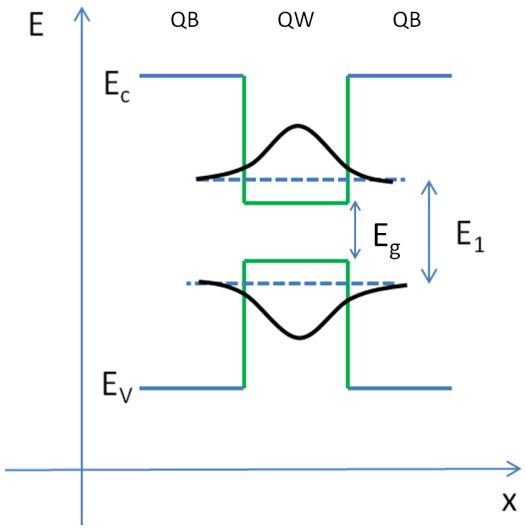

Fig. 1.4 Band diagram of a quantum well. The bandgap of the well material is denoted E_g, the energy of the ground state transition is denoted E_1 and the conduction and valence bands are denoted E_c, E_v respectively [15].

Thus the energy of the transition in the QW is given by the following relation:

$$h\nu = E_1 - E_{ex} \tag{1.5}$$

where E_1 is the energy of the ground state transition and E_{ex} is the exciton binding energy. For an infinite potential well of thickness L, the ground state E_1 is given by:

$$E_1 = \frac{\hbar^2 \pi_2}{2m^* L^2} \tag{1.6}$$

where $\hbar$ is the reduced Plank constant, m^* is the carrier effective mass. As such, the energy of the optical transition is related to the thickness of the well.

1.1.3 Built-in Fields

III-nitride materials in wurtzite structure are termed 'polar' materials, due to the fact they exhibit a spontaneous polarisation field [16]. This occurs due to the III-nitride bonding structure's deviation from an ideal tetrahedral structure along the (0001) axis of the crystal, combined with the ionicity of the bond [15]. This deviation causes each unit cell to possess a non-zero dipole moment along the principal axis of the tetrahedral bonding structure, resulting in an overall spontaneous polarization in the crystal. As the III-nitride wurtzite structure is non-centrosymmetric, the direction of the polarization depends on whether the crystal exhibits (+ *c*) or (-*c*) polarity, as shown in Fig.1.5

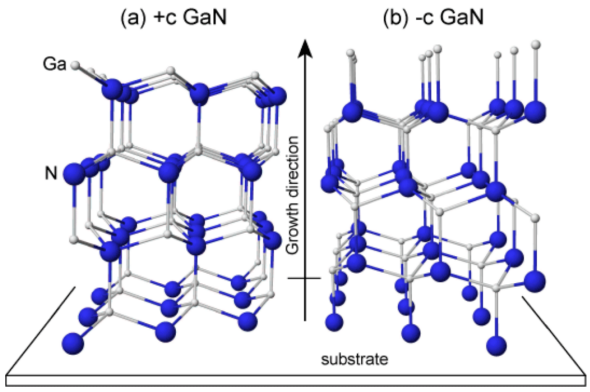

Fig. 1.5 Illustration of Ga-face (+ *c*) and N-face (-*c*) GaN wrutzite crystal exhibiting polarity along the *c*-axis. Reproduced from [17].

This non-zero dipole moment is particularly strong for III-nitrides relative to other III-V semiconductors due to the strong electronegativity and small size of nitrogen compared to other group V elements, resulting in a metal-nitrogen bond with greater ionicity than other III-V bonds [18]. However it is worth noting most III-V have a cubic crystal structure and thus can not be polar. Fig.1.6 shows a GaN unit cell with lattice parameters *c* and *a* denoted.

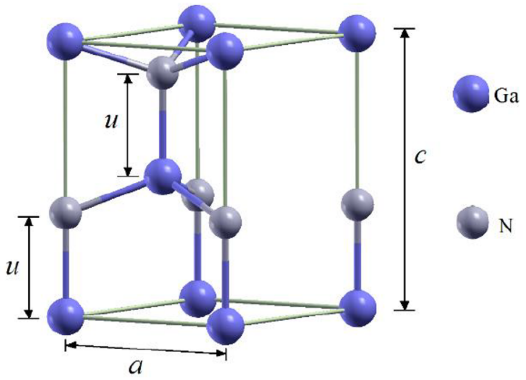

Figure 1. Unit cell 1x1-MN/GaN (M = V, Cr and Mn) multilayers.

Fig. 1.6 GaN unit cell with lattice parameters c and a [19]

If all nearest neighbour bond lengths are equal, an ideal hexagonal closed packed crystal exhibiting zero spontaneous polarisation would have a ratio of lattice parameters denoted by:

$$\frac{c}{a} = (\frac{8}{3})^{0.5} = 1.63299 \tag{1.7}$$

The degree of spontaneous polarisation observed in III-nitride materials is thus determined by the amount their lattice parameter ratio deviates from this ideal value. The values for bulk III-nitride materials are given in Table.1.3.

Alloy	$\frac{\mathbf{c}}{\mathbf{a}}$
GaN	1.6259
InN	1.6116
AlN	1.6010

Table 1.3 Bulk $\frac{c}{a}$ ratios for GaN, InN and AlN [15].

A lower $\frac{\mathbf{c}}{\mathbf{a}}$ ratio indicates a higher angle between the three bonds at the base of the tetrahedral bonding structure, resulting in a lower compensation polarisation along the (0001) axis and a higher spontaneous polarisation. Thus, according to Table.1.3 the strongest spontaneous polarisation is observed in AlN and the weakest in GaN.
It is important to note that materials which exhibit spontaneous polarisation also exhibit piezoelectric polarisation [16]. Strain experienced by the material results in the distortion in of the crystal lattice, which can either alleviate or exacerbate the deviation from the ideal tetrahedral structure resulting in additional polarisation fields. This piezoelectric polarization is a crucial consideration in III-nitride devices which often consist of QW heterostructures as

lattice mismatches with underlying layers result in the expansion or contraction of III-nitride films. Interestingly two different polarisation configurations are obtained for AlGaN and InGaN coherently strained to GaN. In the case of InGaN the piezoelectric field acts against the spontaneous field, whilst the opposite is true for AlGaN strained to GaN. Within the context of visible light LEDs, InGaN containing QWs are dominated by the piezoelectric contribution to the polarization fields [20] due to the sizeable lattice mismatch between GaN and InN (11%) [21].

1.1.3.1 The Quantum Confined Stark Effect

III-nitride photonic devices often consist of QWs, which have been discussed in section 1.1.2.1. Given the presence of built-in fields in III-nitride materials, it is important to consider the effect polarisation fields will have on the band structure and thus optical properties of quantum wells as shown in Fig.1.7

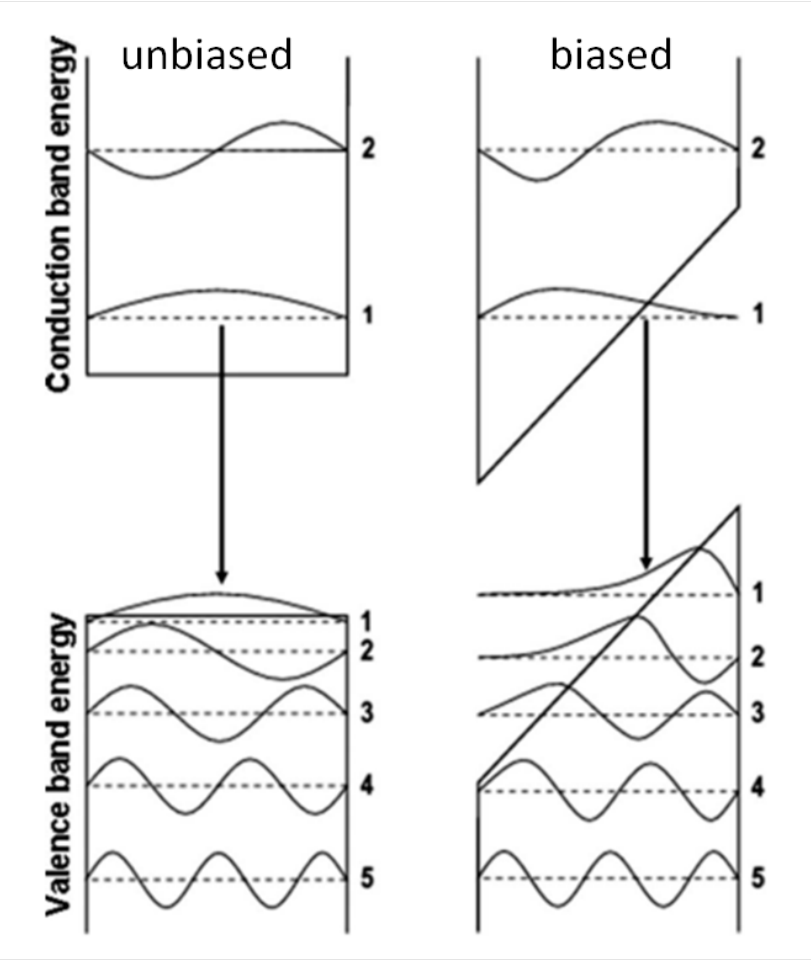

Fig. 1.7 Unbiased and biased quantum well energy levels with associated carrier wavefunctions. Under an applied field in the x-direction labelled in the figure, the overlap between the electron and hole carrier wavefunctions is reduced. Reproduced from [22].

The field-induced transition from a rectangular to a 'sawtooth'-shaped potential well results in the reduction in energy of the optical transition, meaning the photons emitted from the QW are red-shifted. However, as the carrier density within the QW is increased, by either optical or electrical injection, the polarization fields are effectively screened resulting in a carrier density-dependent optical transition energy.
A further effect of the polarization fields is to spatially separate the carrier wave functions, thus reducing their overlap as shown in Fig.1.7. This results in a reduced probability for the radiative recombination carriers thus reducing the efficiency of III-nitride QW emitters.

1.1.4 Defects in III-nitrides

Many issues with III-nitride based optoelectronic devices arise from the high defect densities inherent to the heteroepitaxially grown material. Dislocation densities tend to be several orders of magnitude higher in nitride devices relative to other III-V materials due to the lack of a low cost, widely-available lattice matched substrate [6]. Lattice mismatch and alloy specific growth temperatures results in the presence of imperfections in the crystal structure of the epitaxial film known as defects. These defects can result in perturbations to the electrical and optical properties of an 'ideal' crystal, and are often classified based on their spatial dimensions. 0-D defects are often referred to as point defects, 1-D defects are commonly termed linear defects or dislocations, 2-D defects are known as planar defects or stacking faults, and there are a variety of 3-D defects known as volume defects.

1.1.4.1 0-D Defects

Point defects exist in four fundamental main forms, shown in Fig.1.8. Vacancies, where an atom is missing from the lattice, and self-interstitial point defects are termed 'native defects': there is no inclusion of foreign atoms. These two types of intrinsic point defects are shown in Fig.1.8 a) and b) respectively. Although other forms of point defects do exist, they are combinations of these four forms [23].
In the case of GaN, three types of vacancies can exist: gallium vacancies, nitrogen vacancies and divacancies. The gallium vacancy (V_{Ga}) has a low formation energy in *n*-type GaN, is acceptor-like and has a low migration barrier. Due to this low migration energy, it is expected that gallium vacancies form complexes with more stable defects. Gallium vacancies and associated complexes are thought to be the cause of yellow luminescence observed in *n*-type GaN [6].
Nitrogen vacancies initially attracted a large amount of interest due to the common belief that their energy levels were close to or within the conduction band. Due to this, the *n*-type conductivity of undoped GaN was attributed to nitrogen vacancies [24]. However, calculations have shown the thermal equilibrium concentration of nitrogen vacancies to be too low to account for the observed conductivity. Nitrogen vacancies are also expected to have relatively low migration barriers, indicating complexes involving more stable defects may occur during high-temperature growth or annealing, especially in *p*-type GaN [23].
The inclusion of foreign atoms can result in a foreign interstitial point defect, or a substitional impurity, both are shown in Fig.1.8 c) and d) respectively. The formation of self-interstitial or antisite (swapping of Ga and N lattice positions in the lattice) have a low occurence due to the small lattice constant of GaN and large size mismatch between Ga and N atoms [23].

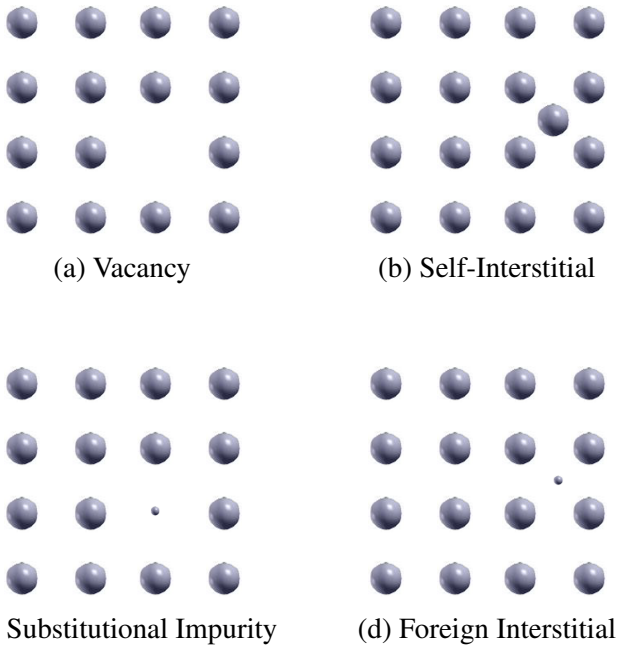

(a) Vacancy (b) Self-Interstitial

(c) Substitutional Impurity (d) Foreign Interstitial

Fig. 1.8 Point Defects:vacancy, self-interdtitial, substitutional impurity and foreign interstitial.

Point defects are responsible for a plethora of deleterious effects at the device level in III-nitrides: they can reduce radiative efficiency, produce undesired luminescence and a collection of point defects may act as parasitic current paths [23].

1.1.4.2 1-D Defects

Dislocations in GaN epilayers are categorised in two main forms: misfit dislocations (MDs) and threading dislocations (TDs). The origins of misfit dislocations are quite well understood: they occur through the release of misfit strain at interfaces between two crystals of differing lattice constants. The process is shown in Fig.1.10: a film with a lattice parameter greater than the substrate is grown as is typical for III-nitride epilayers (GaN on sapphire or InGaN on GaN) and as a result the grown layer experiences compressive stress and forms a pseudomorphic layer. The top layer is strained and matched to the lower layer due to its smaller lattice parameter. Strain relaxation occurs as the pseudomorphic relationship is broken when the top film reaches a critical thickness (the thickness at which the homoegeneous strain energy within the layer becomes large enough to favour the formation of dislocations) and results in the formation of misfit dislocations [25].

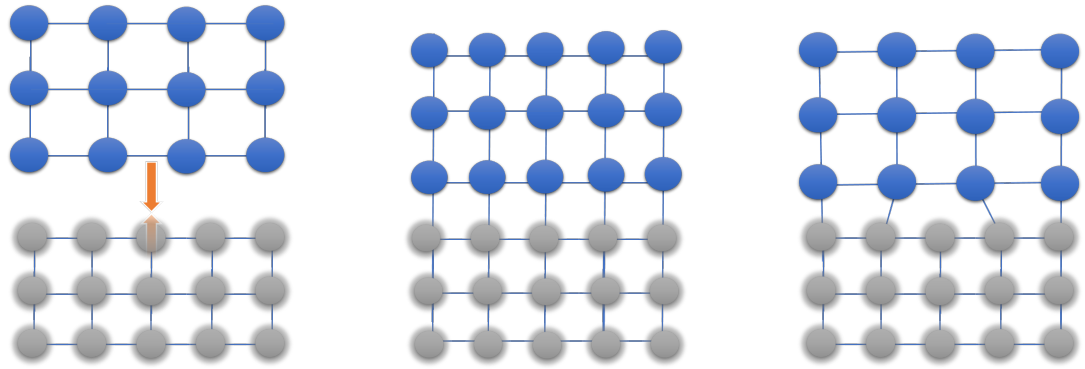

(a) (b) (c)

Fig. 1.9 Misfit dislocation formation through strain relaxation for heteroepitaxial growth: a) the film is grown on a substrate of smaller lattice size b) the film maintains a pseudomorphic relationship with the substrate c) the film relaxes through the formation of a dislocation.

The origins of TDs are however still widely debated. TDs are not believed to relieve mismatch stress, and typically propagate perpendicular to the planar surface. TDs are classified into three categories based on their Burgers vector, as shown in Table.1.4.

Dislocation type	**Burgers vector**
a type	$\frac{1}{3} < 11\bar{2}0 >$
c type	$< 0001 >$
a + **c** type	$\frac{1}{3} < 11\bar{2}3 >$

Table 1.4 Burgers vectors for pure edge (**a**), pure screw (**c**) and mixed (**a** + **c**) TDs

It was initially reported that GaN islands on sapphire during the initial stages of growth may be misorientated with respect to one another and that TDs were generated during the coalescence of these misorientated islands [26]. This was seemingly disproven by a transmission electron microscopy data from a study on partially coalesced GaN on sapphire layers at various growth stages, which indicated the large majority of TDs seemed to initiate from within the nucleation layers at the GaN/sapphire interface rather than at coalescence boundaries [27]. Oliver *et al.* used silane treatment to enlarge dislocation pits and observe them using atomic force microscopy, finding no significant relationship between boundary regions and the locations of dislocations [28]. It was however suggested that dislocations may arise from the overgrowth of smaller islands by larger ones. Thus, while there is convincing evidence that TDs do not originate due to island coalescence, the actual mechanism behind their generation remains an area of active research.

1.1.4.3 2-D Defects

Stacking faults are defects which disrupt the regular stacking sequence of the crystal structure, as shown in Fig.1.11. In non-polar heterostructures they can intersect the QW layers. As a result of this, stacking faults are a more pressing concern than dislocations in epitaxial films grown along alternative directions to the c -plane, as in polar materials stacking faults tend to remain in the nucleation layers [10]. Fig.1.10 shows different forms of stacking faults in $(11\bar{2}0)$ GaN (a-plane) on r-plane sapphire. Basal-plane stacking faults (BSFs) are atomic layers with a modified stacking sequence in the wurtzite crystal matrix. These BSFs can transfer to another stacking plane through prismatic stacking faults (PSFs). BSFs can also be bound by partial dislocations (PDs).

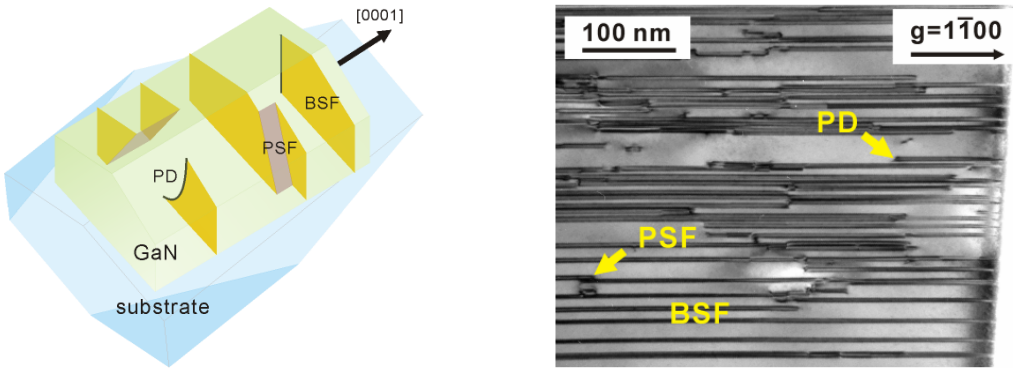

(a) (b)

Fig. 1.10 a) a-plane GaN showing basal plane stacking faults (BSFs), prismatic stacking faults (PSFs) and stacking faults bounded partial dislocations (PDs) shown schematically b) and in TEM. Adapted from [29].

Three types of BSFs exist in wurtzite crystals, they are classified based on their displacement vector $\vec{R}$ as shown in Table.1.5 and in Fig.1.11.

BSF type	**Displacement vector $\vec{R}$**
I_1	$\frac{1}{6} < 20\bar{2}3 >$
I_2	$\frac{1}{3} < 10\bar{1}0 >$
E	$\frac{1}{2} < 0001 >$

Table 1.5 BSF types in wurtzite materials.

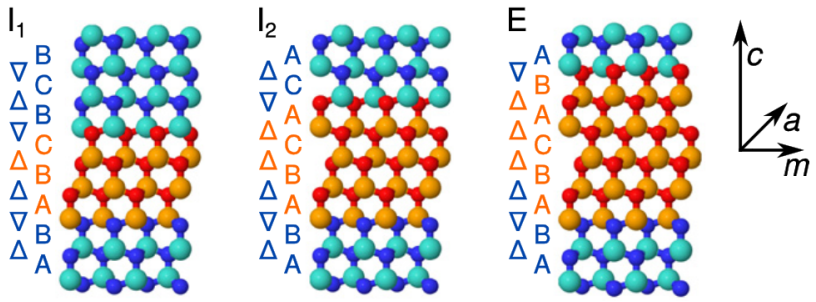

Fig. 1.11 Stacking sequences for stacking fault types. The change in stacking sequence is highlighted in the figures [30].

Whilst TDs are considered completely undesirable due to the adverse effects they may have on radiative processes and carrier transport, it has been suggested the presence of BSFs on the optical properties may be beneficial in some cases. As first indicated by Rieger *et al.* [31] and Rebane *et al.* [32], BSFs may be considered as zinc-blende QWs in a wurtzite matrix, thus enabling radiative recombination through confinement. The characteristic BSF luminescence has been used to determine the spontaneous polarization of wurtzite GaN [33] as well as the diffusion length in GaN nanowires[34].

1.1.4.4 3-D Defects

There are many forms of 3-D defects in III-nitrides such as voids, nanopipes and cracks. In this particlar section we will focus on those relevant to the work featured in later chapters of this work.

Inverted hexagonal pyramid defects, also known as V-pits, are defects commonly found at the surface of InGaN/GaN QW structures. They form as a result of a TD intersecting the QW layers in heterostructures. It is believed that the low temperatures required for the growth of the InGaN layers allow even minute perturbations of the surface to persist into inclined facets with low growth rates, such as the $(1\bar{1}01)$ facets. The apex of TDs thus provide optimal conditions for the formation of V-pits during the growth of InGaN layers [35]. Interestingly, TEM studies have shown that the QW layers disrupted by the defect grow along the semi-polar facets at a lower thickness [35–37]. Fig.1.12 shows a TEM image of a V-pit in an InGaN/GaN multiple QW structure with a schematic describing this defect and the manner it affects the growth of the QWs.

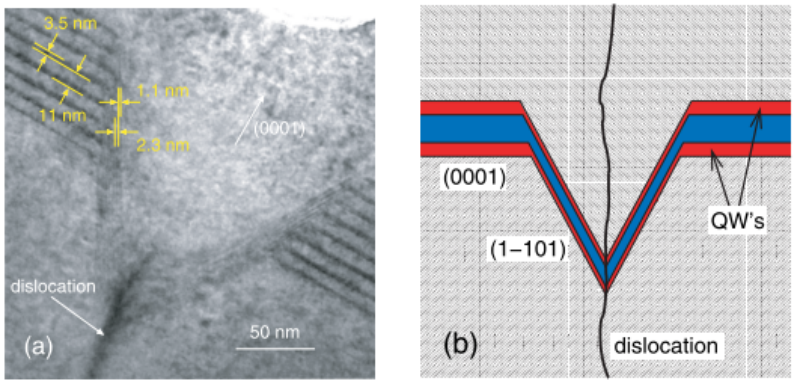

Fig. 1.12 a) TEM image of a hexagonal inverted pyramid defect b) Schematic of a V-pit with its associated TD [35].

The existence of TDs as non-radiative recombination centres has been well documented [6], however it has been suggested that V-pits suppress this non-radiative recombination and provide an increase in light emission efficiency in III-nitride devices by providing an energy barrier surround TDs [35]. Hangleiter *et al.* suggested the thinner wells grown along the semi-polar facets of the V-pit provided an energy barrier of several hundred meV relative to the normal *c*-plane QWs [35], thus providing a potential landscape shielding carriers from TDs, as shown in Fig.1.13.

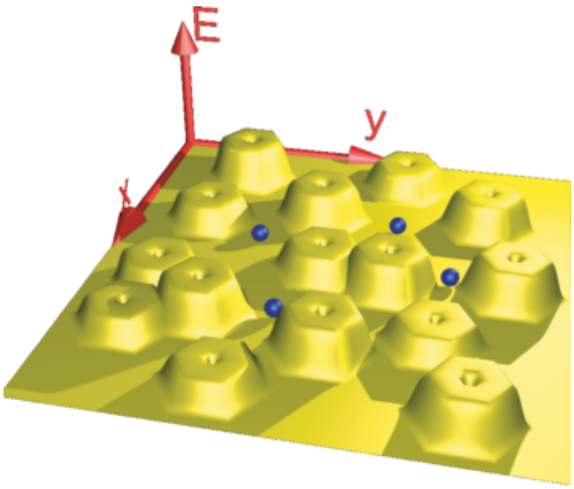

Fig. 1.13 Potential landscape due to V-pits decorating the apex of TDs: carriers (blue) need to overcome the energy barriers to recombine non-radiatively at the TDs [35].

1.2 III-nitride Devices

1.2.1 Light Emitting Diodes

Light emitting diodes (LEDs) are the most widespread commercial application of III-nitride materials. These devices typically consist of a p-n junction. This consists of material containing excess acceptor (p-doped) and another containing excess donor impurities (n-doped) which are brought into contact. This allows holes from the p-type material and electrons from the n-type material to diffuse across the junction until an equilibrium state is reached. A region where the electric field from the charged dopants on either side prevents diffusion is formed known as the depletion region. The application of forward bias reduces the built-in potential across the depletion region and allows for the flow of electrons and holes across the junction, as shown schematically in Fig.1.14.

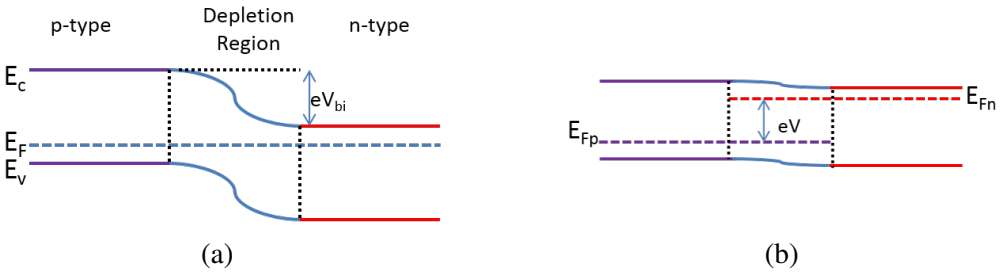

Fig. 1.14 a) p-n junction at equilibrium, with the conduction band, Fermi level and valence band denoted E_c, E_F and E_v respectively, the built in potential across the junction is denoted as V_{bi} b) under forward bias of V.

A schematic of a general LED structure is shown in Fig.1.15. Visible light III-nitride LED structures typically contain a magnesium doped p-region and a silicon doped n-region. An electron blocking layer (EBL) consisting of a material with a higher bandgap than GaN (in this case AlGaN) is often used to prevent the leakage of electrons into the p-doped region and confine them in the InGaN QW active region.

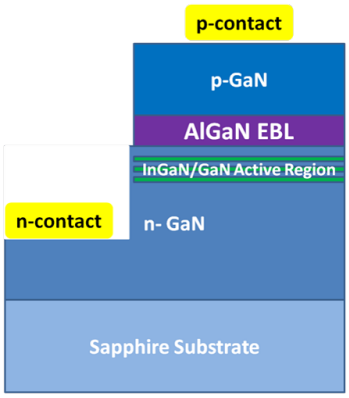

Fig. 1.15 Typical visible light LED structure grown on a sapphire substrate [15].

1.2.2 Microcavities

Microcavity emitters possess rather singular optical properties due to their dimensions. By matching one or more dimensions of the cavity to the order of the wavelength of confined light a plethora of effects can be produced such as low-threshold lasing, directional luminescence and enhanced nonlinear conversion [38]. Confining a dipole within a microcavity can modify its emissive properties by altering the photon density of states. The interaction rate between the confined dipole and a cavity photon relative to the average rate of dissipation of a cavity determines whether the microcavity operates in the weak-coupling or strong-coupling regime.

Weak coupling occurs when dissipation overwhelms the dipole-cavity photon interaction: the effect of the microcavity in this case is to alter the vacuum description of the dipole lifetime, resulting in an increase in spontaneous emission rate for on-resonance cavity modes, known as the Purcell effect [39]. Weakly-coupled microcavity systems have applications across a wide range of optoelectronic devices due to this effect: from enhancing the recombination rate and extraction efficiency of embedded single photon emitters [40] to the development of high efficiency, low threshold lasers [41].

An interaction occurring on shorter timescales than the average dissipation rate of the cavity photon is defined as being in the strong coupling regime and results in the formation of admixed eigenstates populated by quasiparticles known as polaritons, which are hybrid particles combining a photon and an electric dipole. The bosonic nature of these quasiparticles has led to the observation of spontaneously emitted coherent light from condensates of exciton-polaritons, a phenomenon also known as polariton lasing [42]. The expected threshold energy for coherent emission from a polariton laser is expected to be much smaller than that of a conventional laser due to the lack of the requirement of population inversion , thus rendering polariton lasers extremely attractive in low-threshold lasing applications [38].

Beyond polariton lasing, strong coupling in microcavities is also required for key quantum information processing tasks such as the entanglement of distinguishable quantum systems and controlled coherent coupling [43, 44].

1.2.2.1 Cavity Parameters and Design

The ability of a microcavity to confine light is a crucial parameter in producing the required effects and is known as the cavity 'quality factor', Q, which is described by Eq. 1.8.

$$Q = \frac{\nu_0}{\delta\nu_0} \tag{1.8}$$

Where ν_0 is the resonant frequency of the cavity mode and $\delta\nu_0$ is the mode bandwidth. Cavity quality factor can be understood as a parameter describing the rate of energy decay the resonant mode undergoes within the cavity and thus may be alternatively described using an exponential characteristic decay constant τ_{cav} as shown in Eq.1.9, where Q^{-1} is the proportion of energy lost during a single cavity round-trip.

$$Q = \pi\tau_{cav}\nu_0 \tag{1.9}$$

The manner in which the resonant mode fields interact with the cavity geometry is determined by the effective modal volume of the cavity, which is described by Eq.1.10.

$$V_{eff} = \int_V \frac{\varepsilon_0(\mathbf{r})|\mathbf{E}(\mathbf{r})|^2}{max[\varepsilon_0(\mathbf{r})|\mathbf{E}(\mathbf{r})|^2]}dV \tag{1.10}$$

where $|\mathbf{E}(\mathbf{r})|^2$ is the normalised electric field amplitude, ε_0 is the dielectric constant and V is the quantization volume. V_{eff} describes the manner in which the cavity supports the distribution of the resonant mode, thus in some cases a large evanescent field component must be included in the calculation of the modal volume.
Cavities often support more than one optical mode, which gives rise to another parameter, known as the free spectral range (FSR), which is defined as the frequency spacing between successive resonant modes. This parameter is crucial to lasing cavities as the probability of a photon feeding into a lasing mode is affected by the number of modes supported by the cavity. The FSR as well as parameters needed to define cavity quality factor are shown schematically in Fig.1.16, where successive resonant modes are shaded in the same colour.

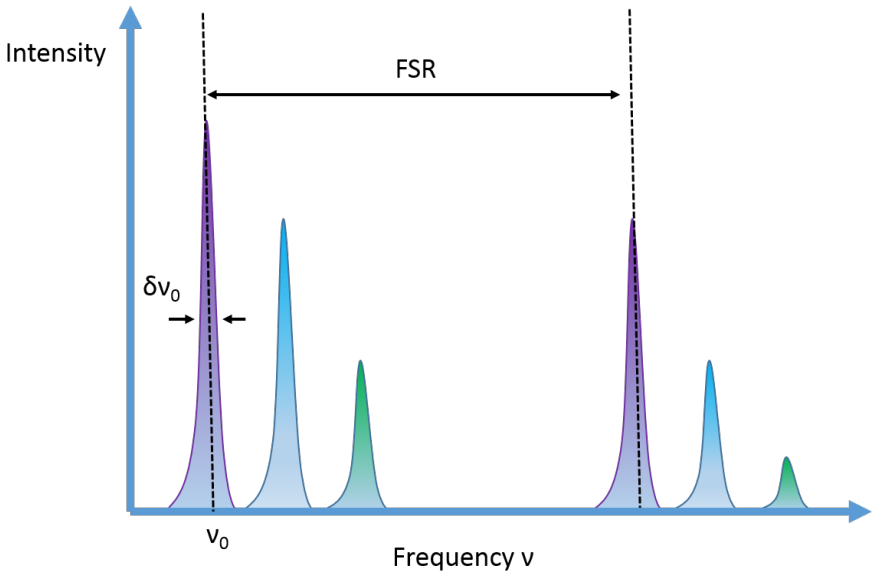

Fig. 1.16 Illustration of the some key parameters such as FSR and resonant cavity mode FWHM.

Cavities modify the optical density of states of an emitter through the generation of standing electromagnetic waves. There are several manners through which to achieve this: at the most basic level an optical cavity is a set of single reflective interfaces, spaced at a specific distance designed to enhance a particular optical mode. However, many cavity designs which employ the use of refractive index mismatches for total internal reflection or an array of boundaries leading to interference enhanced optical modes also exist, as shown in Fig.1.17.

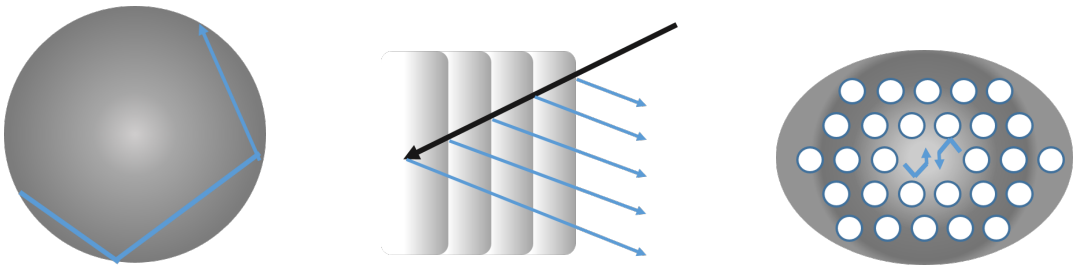

(a) Total internal reflection (b) 1-D interference (c) 2-D interference

Fig. 1.17 Optical resonators.

1.2.2.2 Microdisk Cavities

Total internal reflection can be exploited in circular geometries such as microdisk/ring/sphere devices, in which whispering gallery modes (WGMs) propagate around the periphery of the disk.
Microdisks can be described as a cylinder of with a low height:radius ratio supported by a pillar of a small radius (less than half of the cylinder). The position of the WGMs is described by Snell's law: only light satisfying the condition described by Eq.1.11 is contained within the microdisk due to internal reflection.

$$\theta_c = sin^{-1}(\frac{n_2}{n_1}) \tag{1.11}$$

Assuming the microdisk thickness is small enough to act as a waveguide in the vertical direction, we can consider the propagation of a ray of light in 2-D as in Fig.1.18. The forbidden position of the WGMs as defined by Eq.1.11 is given by R_{min}.

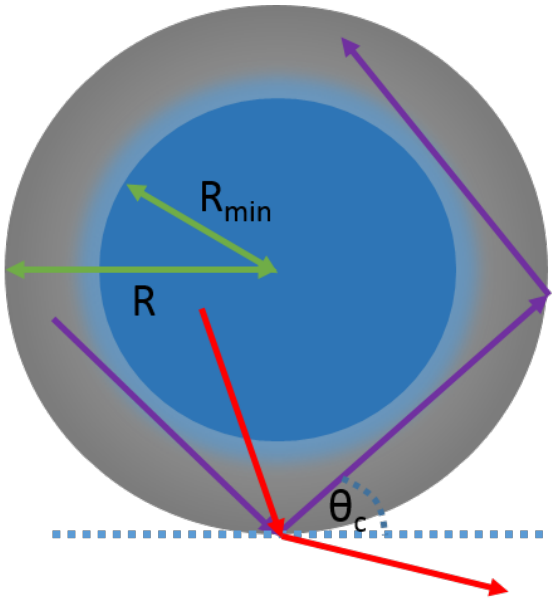

Fig. 1.18 Illustration of the minimum radius R_{min} for WGM propagation. Rays traversing the region $r < R_{min}$ (denoted in red) exceed the critical angle θ_c and thus escape the cavity. Rays travelling outside this region $r > R_{min}$ (denoted in violet) are confined.

Thus the fabrication of microdisks relies heavily on the ability to 'undercut' the microdisk material whilst still leaving a pedestal, as shown in Fig.1.19. This is a particularly challenging problem issue in terms of III-nitride materials due to the excellent thermal and chemical stability of GaN. Early efforts in microdisk nitride fabrication involved dry-etching processes, utilising the refractive index mismatch between the light emitting GaN layers and the

sapphire substrate to confine light [45]. Although stimulated emission and lasing was observed by Chang *et al.* in dry-etched GaN microdisk cavities [46], Haberer *et al.* [47] reduced the required excitation power densities for lasing by an order of magnitude by employing photoelectrochemical (PEC) etching to undercut a sacrificial layer and produce GaN microdisks, thus providing superior optical confinement due to the index contrast of the GaN/air interface relative to the GaN/sapphire interface used by Chang *et al.* [46]. Further improvements in fabrication were achieved by Tamboli et al. with room temperature lasing achieved in GaN/InGaN microdisks through enhancements in microdisk circularity and sidewall smoothness [45].

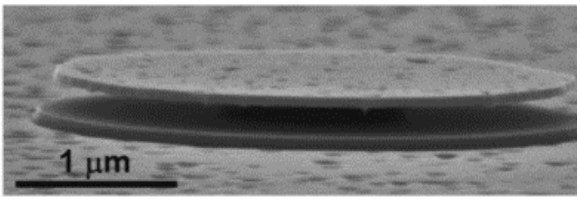

Fig. 1.19 Scanning electron microscope image of a GaN microdisk produced by selective etching of sacrificial AlInN layers [48].

1.2.2.3 Nanobeam Cavities

Photonic crystals are periodic structures which affect photons in an manner analogous to the way atomic lattices affect electrons in solids. They can be considered as artificial materials exhibiting a dielectric function which varies periodicially in either one, two or three dimensions. The principal mechanism of light confinement in this case is known as distributed bragg reflection as is shown in Fig.1.17b).
Whilst micro-toroid and microdisk cavities have the potential to achieve extremely high Q-factors many applications which involve strong coupling, non-linear optical processes and spontaneous emission and other similar processes require a high ratio between the Q-factor and the effective modal volume (V_{eff}). This figure of merit can be achieved in travelling-wave cavity geometries due to the potential for extremely small modal volumes. Yablonovitch [49] and John [50] first proposed the design of 3-D photonic crystal cavities which in theory would possess ultra-high Q-factors, minute modal volumes and perfect reflectivity in all directions. Despite the extremely promising theoretical properties of 3-D photonic crystal cavities, their fabrication has proven to be particularly challenging with few demonstrations of high-Q 3-D PCCs reported in literature [51], [52]. PCCs of lower dimensionality are thus prime candidates for practical applications due to fewer (though not vanishing!) fabrication issues. In particular 1-D PCCs such as suspended structures known as nanobeams are extremely

promising due their ability to realise of high-Q, low V_{eff} cavities even in low index materials such as SiO_2 [53]. For these reasons we will specifically be considering 1-D photonic crystal cavities in the nanobeam geometry in this work.
Electromagnetic field confinement is achieved in nanobeam structures by Bragg scattering from the photonic crystal in one direction, and index guiding in the other two directions. A nanobeam can essentially be considered as a wavelength-scale Fabry-Perot cavity with photonic crystal mirrors [54]: as the nanobeam waveguide mode is trapped and reflected by these mirrors, it also penetrates some distance into them. The mirrors in the case of the nanobeam are the holes in the structure, as denoted by the blue arrow in Fig. 1.20. If the fields terminate at the mirror boundaries, this would lead to large scattering losses due to the large impedance mismatch [55]. In order to avoid this impedance mismatch between the waveguide mode and the Bloch mode of the mirror, the photonic crystal mirrors are tapered in order to match the evanescent mirror Bloch mode [56] as shown in Fig.1.20 by the green arrow.

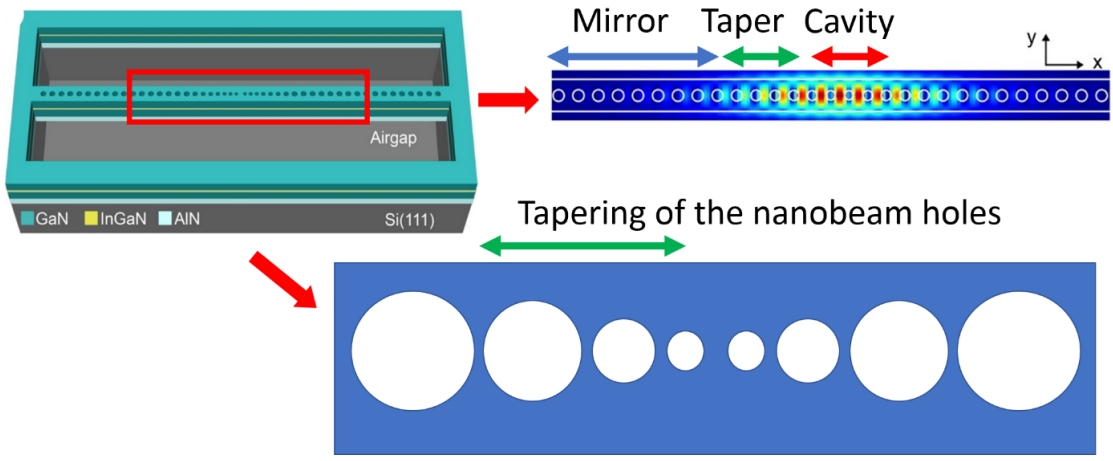

Fig. 1.20 Nanobeam schematic and 3-D FDTD simulation of the electric field intensity profile of the cavity mode adapted from [57]. The tapering of the nanobeam holes is crucial in avoiding large scattering losses.

In the case of III-nitride cavities, the light contained within the nanobeam is often generated by a QW or QD layer incorporated in the nanobeam structure [57, 58]. The fabrication of nanobeam in III-nitride cavities involves issues similar to those encountered in the fabrication of microdisks, discussed in section 1.2.2.2. Due to the requirement of a suspended structure, the undercutting process for the nanobeams is crucial [57].
Despite the promise of large $\frac{Q}{V_{eff}}$ ratios and potential applications ranging from bio-photonics to optical communications, processing issues have hindered the development of III-nitride based photonic crystal cavities, similarly to the development of microdisk cavities discussed

earlier. Indeed, the first high-Q (2400) III-nitride photonic crystal cavity was demonstrated in 2007 by Arita *et al.* [59]. In terms of 1-D nanobeam cavities, Pernice *et al.* reported AlN nanobeam cavities with measured Q-factors of approximately 146000 close to standard telecommunication wavelengths of 1.55 μm [60]. Sergent *et al.* demonstrated a high Q (6.3×10^3) optically active nanobeam cavity with embedded GaN/AlN quantum dots using a layer transfer method rather than the traditional PEC undercut. More recently, continuous wave blue lasing was demonstrated at 460 nm in GaN nanobeams with an InGaN QW active region grown on silicon, where the reported Q-factor was 10^4. Ultra-low threshold (9.1 $\mu J/cm^2$) lasing was also reported by Niu *et al.* in GaN nanobeam cavity structures with a fragmented InGaN QW active layer which provided additional confinement for photo-generated carriers relative to continuous QW active layers [58].

1.2.3 Nanowires for Nanophotonic Devices

The lack of readily available, low-cost substrates for the epitaxial growth of GaN and its associated alloys has motivated research into the growth of III-nitrides in nanowire geometries. Studies have shown that epitaxial GaN nanowires can be grown with far lower dislocation densities relative to bulk GaN due to a large surface-to-volume ratio [61]. Furthermore, QWs grown radially along the non-polar facets of nanowires allow for the reduction of the polarization fields which can deleteriously affect the optical properties of polar III-nitride emitters without the need for expensive non-polar substrates [61].

Beyond the material benefits of the nanowire growth geometries in the III-nitrides, the reduced dimensionality of nanowires will potentially allow for the realisation of highly efficient, low-threshold compact light sources for applcations such as information processing and optical communications [62]. As such, nanowires may provide a solution to one of the most challenging areas of modern optoelectronics: the miniaturisation of active optoelectronic components [62]. In terms of their employment as active optoelectronic components, nanowires have the additional benefit of having to intrinsic mirrors in the form of their crystalline end-facets thus naturally forming cavities. Due to the increasingly demanding nature of modern optoelectronic device development, research into nanowire devices is currently an extremly active area of research.

The first demonstration of GaN nanowire based lasing was reported by Johnson *et al.*, who demontrasted lasing at wavelengths of 370-380 nm at a threshold of approximartely 700 nJ/cm^2 [63]. Progress in the epitaxial growth of heterostructure nanowires lead to the demonstration of InGaN/GaN MQW nanowire lasing in 2008 by Qian *et al.*, by varying the indium composition of the MQW structures lasing at wavelengths ranging from 380 to 478 nm was achieved [64]. Whilst both these demonstrations of nanowire lasing were achieved

by using the simplest cavity geometry (Fabry-Perot), polariton lasing in GaN nanowries was demonstrated by Das *et al.* by strongly coupling a single GaN nanowrie to a large-area dielectric microcavity [65]. Alternative cavity coupling designs have since been expanded to include plasmonic coupling, first demonstrated in InGaN/GaN nanowires by Wu *et al.* by coupling a bundle of GaN/InGaN nanowires to a gold plate through a dielectric nanogap layer [66]. These nanowire laser applications are shown schematically in Fig.1.21

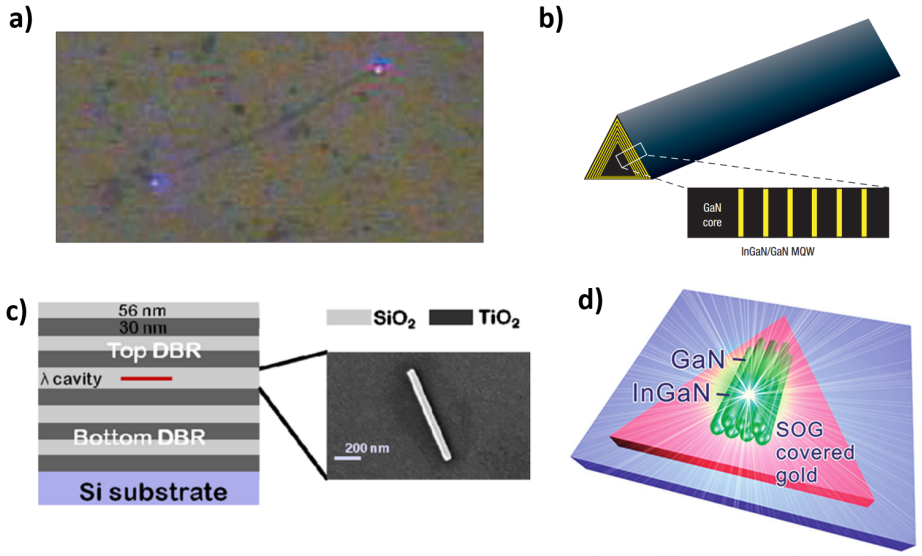

Fig. 1.21 a) Lasing from the end-facets of a GaN nanowire b) schematic of the triangular InGaN/GaN MQW nanowire grown by Qian *et al.* c) GaN nanowire coupling to a dielectric cavity d) GaN/InGaN nanowire bundle coupling to a gold plate through a nanogap layer. Adapted from [63–66] respectively.

Nanowire single photon sources have also been achieved, due to the benefit of site-controlled quantum dots. Electrically injected blue single photon sources based on III-nitride nanowires have been reported by Deshpande *et al.* operating at 10 K. In this particular case, an InGaN QD was incorporated into a *p-n* GaN nanowire as shown in Fig. 1.22.

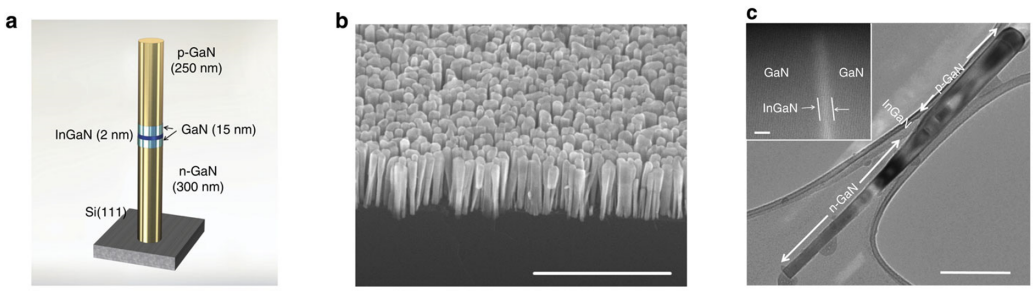

Fig. 1.22 a) Schematic of the InGaN QD in GaN nanowire structure b) SEM micrograph of the nanowire sample grown by MBE c)TEM micrograph of a single nanowire. Adapted from [67].

Holmes *et al.* have also demonstrated room temperature triggered single photon emission from a GaN QD grown in a GaN/AlGaN core-shell nanowire as shown in Fig.1.23.

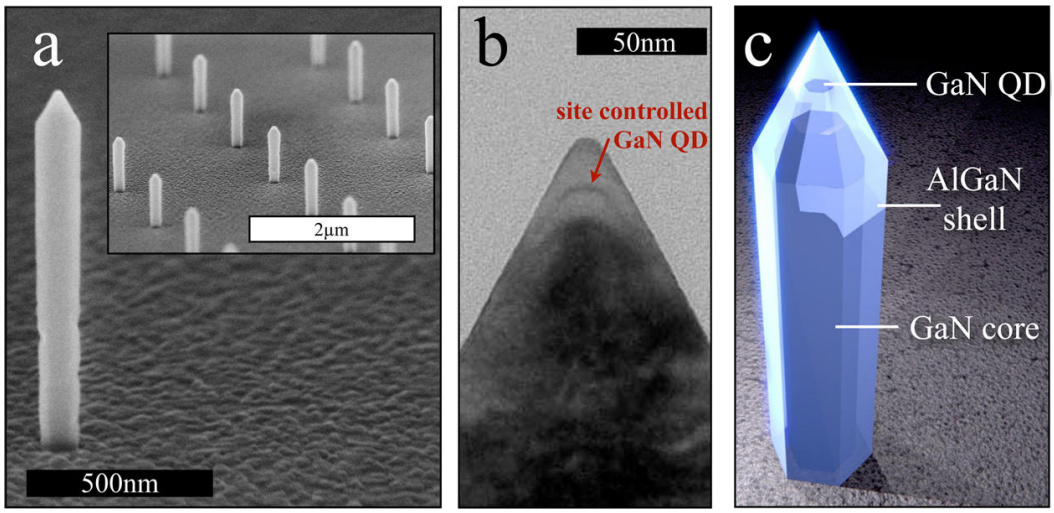

Fig. 1.23 a) SEM micrograph showing the a single nanowire on a patterned SiO_2 substrate grown by MOCVD. The inset shows the array of nanowires grown on the substrate b)showing the site-controlled GaN QD at the tip of the nanowire c)schematic of the nanowire structure [68].

Chapter 2

Experimental Methods

2.1 Transmission Electron Microscopy

A typical transmission electron microscope (TEM) consists of a high voltage (typically 100-400kV) electron gun under extremely high vacuum conditions within a column. The beam of electrons generated by this gun passes through a set of lenses which focus or deflect the beam before it is incident on the sample under examination. If this sample is thin enough to be electron transparent, the electrons passing through it and scattering elastically or inelastically can be collected using a subsequent set of lenses, apertures and a detector. A simplified schematic of a TEM illumination system is shown in Fig.2.1:

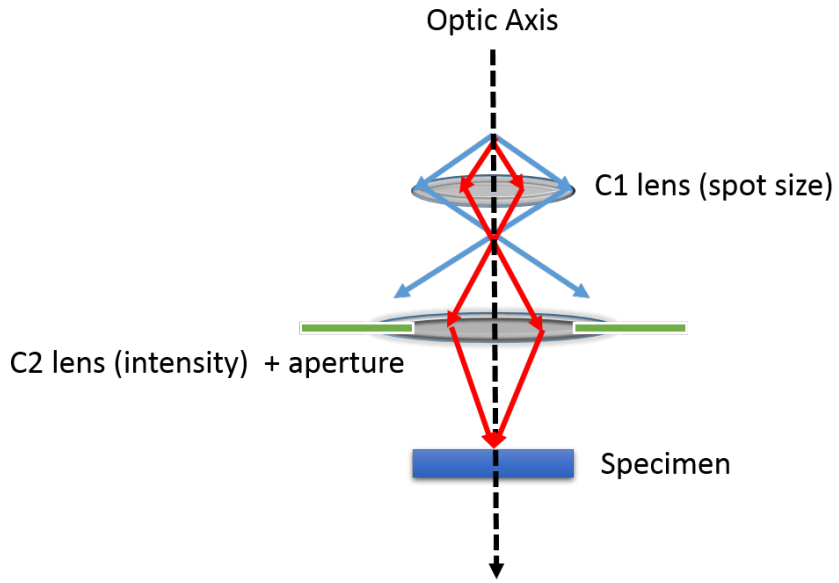

Fig. 2.1 Simplified TEM illumination system.

It important to consider the range of electron-specimen interactions which occur as the high energy electron beam impacts the sample. These interactions can be divided into two main categories according to whether the electron kinetic energy is either conserved or not during the interaction, known as elastic or inelastic respectively. Different elastic and inelastic signals produced by the electron-specimen interaction are illustrated in Fig.2.2.

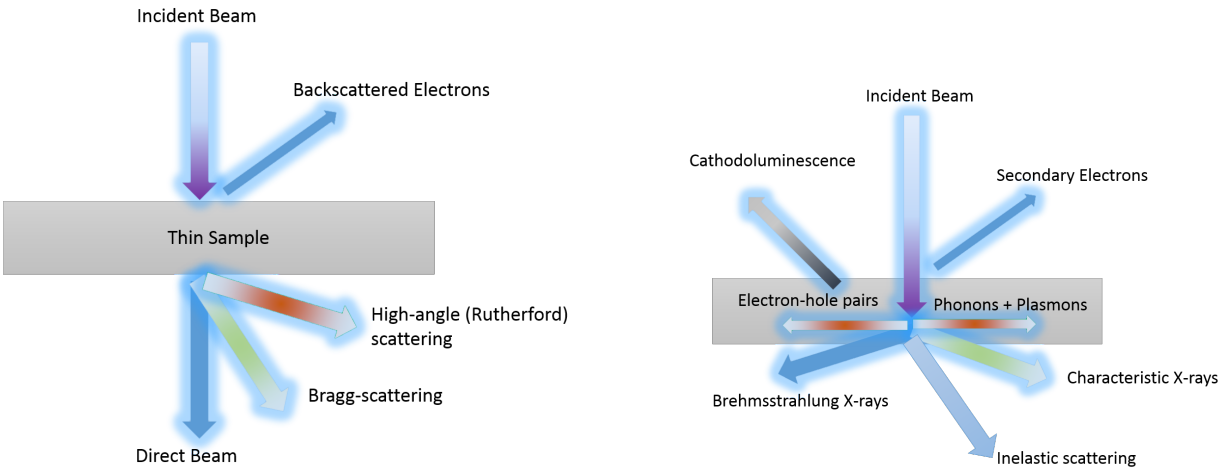

Fig. 2.2 a) Elastic and b) inelastic interactions for a high energy electron beam incident on a thin sample.

Fig.2.2 a) illustrates the importance of sample thickness in TEM. Without a thin specimen, the forward scattered signals such as high-angle and bragg-scattered electrons as well as the direct beam are unavailable. Given the diversity of scattering interactions which can occur throughout the sample and contribute to the final signal, different apertures and detectors must be used to extract useful information. The following sections will introduce the different TEM techniques used in this report and their underlying principles.

2.1.1 Conventional Transmission Electron Microscopy

2.1.1.1 Electron Diffraction

Electron diffraction is the basis for many TEM techniques as it provides local crystallographic specimen information. The process of diffraction occurs for electrons due to their dual nature as both particles and waves.A beam of electrons can thus be interpreted as a plane wave: the incidence of this plane wave on the specimen results in the scattering of the electrons by atoms through the Coloumb interaction, diffracting the wave in a manner described by Bragg's law. This is given by Eq. 2.1.

$$n\lambda = 2d_{hkl}sin\theta_B \tag{2.1}$$

where n is an integer, λ is the wavelength of the plane wave, d_{hkl} is the crystal plane spacing described by the Miller indices h,k and l and θ_B is the angle between the plane normal and the scattered wave, also known as the Bragg angle.
Understanding of the diffraction patterns observed in TEM requires consideration of the reciprocal lattice of the crystal. The reciprocal lattice is defined as the Fourier transform of the crystal lattice, as such the relation of the real-space unit-cell lattice points **a**, **b** and **c** to their reciprocal lattice counterparts $\mathbf{a}^*$, $\mathbf{b}^*$ and $\mathbf{c}^*$ can be described as:

$$\mathbf{a}^* = \frac{\mathbf{b}\times\mathbf{c}}{V_c}, \mathbf{b}^* = \frac{\mathbf{c}\times\mathbf{a}}{V_c}, \mathbf{c}^* = \frac{\mathbf{a}\times\mathbf{b}}{V_c} \tag{2.2}$$

where V_c is the volume of the unit cell and is given by the relation"

$$V_c = \mathbf{a}\cdot\mathbf{b}\times\mathbf{c} \tag{2.3}$$

As such one can define lattice points in reciprocal space which are normal to the plane (*hkil*) in the real lattice as:

$$r^* = h\mathbf{a}_1^* + k\mathbf{a}_2^* + i\mathbf{a}_3^* + l\mathbf{c}^* \tag{2.4}$$

where $\mathbf{a_1}$, $\mathbf{a_2}$, $\mathbf{a_3}$ and **c** are the four hexagonal unit-cell vectors as shown in Fig.2.3.

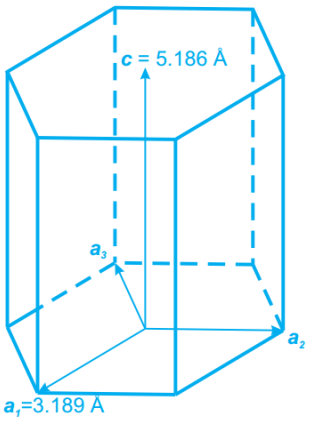

Fig. 2.3 Hexagonal GaN lattice in real space with unit-cell vectors defined. Adapted from [69].

Considering a beam of electrons of wavelength λ incident on a crystal lattice, one can define a sphere in reciprocal space with radius $\frac{1}{\lambda}$ which describes the scattering of the

electron beam known as the Ewald sphere. The intersection of the Ewald sphere with lattice points in reciprocal space represent the diffraction spots which can be observed. Typically, the geometry of the TEM specimen results in elongated reciprocal lattice points known as rel-rods. This elongation allows the Ewald sphere to intersect a greater number of 'points', even with slight deviations to the Bragg condition. The scattering vector **K** can thus be described as:

$$\mathbf{K} = \mathbf{k_D} - \mathbf{k_I} = \mathbf{g} + \mathbf{s} \tag{2.5}$$

where $\mathbf{k_D}$ and $\mathbf{k_I}$ are the diffracted and incident beam wavevectors respectively, **g** is a reciprocal lattice point intersecting the Ewald sphere and **s** is the excitation error, which describes how far the scattering deviates from the exact Bragg diffraction condition. These concepts are shown schematically in Fig.2.4.

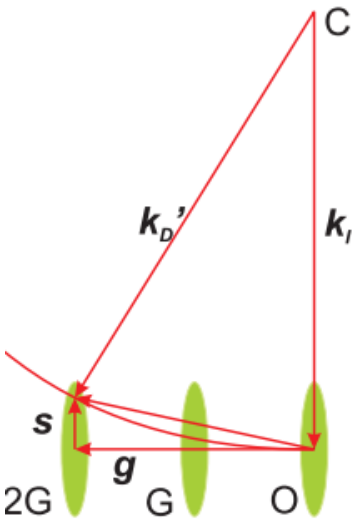

Fig. 2.4 Intersection of the Ewald sphere centered at C with reciprocal lattice rel-rods. Adapted from [69].

Due to the small value of λ (typically picometres), the radius of the Ewald sphere tends to be large relative to the reciprocal lattice spacing, meaning the surface of the sphere is approximately planar relative to the reciprocal lattice rods thus resulting in several spots being observed even in cases where the incident beam is parallel to the zone axis.

2.1.1.2 Diffraction Contrast Imaging

Diffraction contrast imaging is a conventional TEM technique which exploits differing Bragg diffraction conditions in different regions of the sample to create contrast in an image. Image

contrast can be obtained either through bright field (BF) or dark field (DF) imaging, these are shown schematically in Fig 2.5 below:

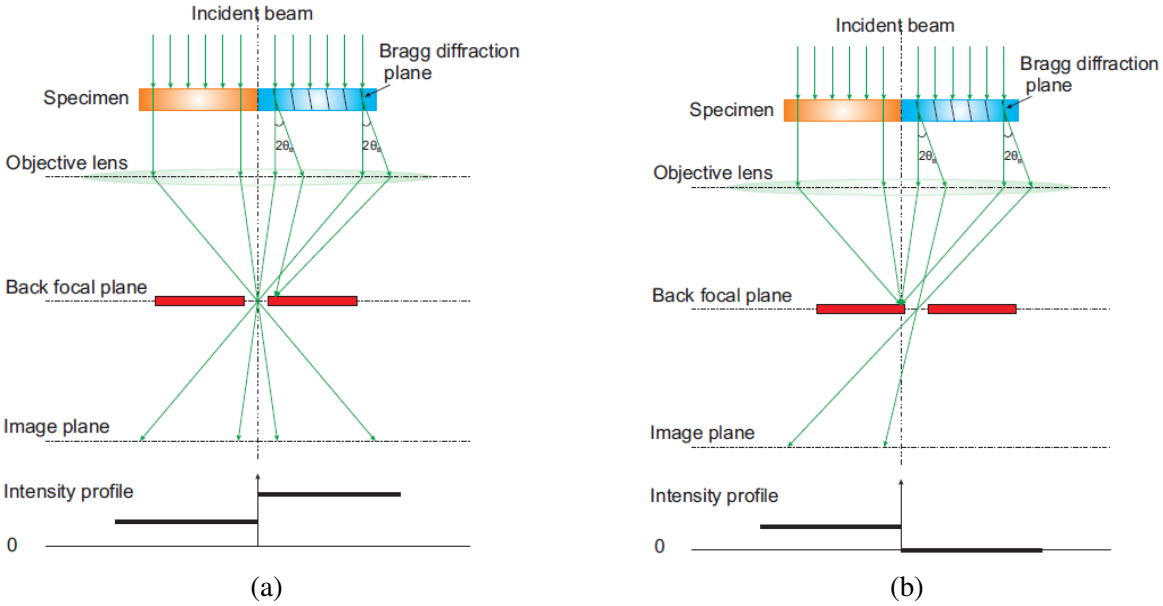

Fig. 2.5 a) Bright-field and b) dark-field imaging [69].

The blue region is shown to satisfy the Bragg diffraction condition for the incident beam whereas the orange region does not. In the case of BF imaging the direct beam is used to generate the image, and as a result the intensity from the orange region is higher than that of the blue region. On the other hand, in DF imaging the diffracted beam is used and the direct beam blocked, resulting in an inverted intensity profile. Barring other electron-specimen interactions such as absorption, the contrast between the BF and DF images is complementary [70].

Figures 2.5 a) and b) demonstrate that the insertion of an aperture at the back-focal plane (BFP) of the objective lens allows for the selection between BF and DF imaging. Without the objective aperture the image consists of a superposition of BF and DF images with a single DF image for every diffracted beam. In order to ensure the diffracted beam is at the optic axis where spherical aberration of the objective lens is less pronounced the incident beam is often tilted, a practice known as centred dark field (CDF) imaging. As dislocations in a crystal structure can be found near strained crystal planes, these will result in diffraction contrast in BF or DF images. However it is important to consider that many diffraction spots can be observed in the electron diffraction pattern, which is undesirable for BF or DF contrast imaging. As such the optimal conditions for are defined as the two-beam condition, in which only one set of planes satisfies the Bragg condition [70], resulting in two beams: the

direct beam and the sole diffracted beam. Under the two-beam condition, image contrast is optimized and the intensity of the two beams can be analytically calculated using the Howie-Whelan equations [70] to deliver detailed information concerning the specimen through the interpretation of contrast in the image.

2.1.1.3 Weak-Beam Dark-Field Microscopy

An alternative technique known as weak-beam dark-field (WBDF) imaging is often used to image dislocations. As indicated by its name, the technique uses a weakly excited beam to form a DF contrast image. A particular diffraction vector **g** associated with a specific set of planes *hkl* is chosen as in regular on-axis DF imaging. The specimen is then tilted to introduce a large excitation error $\mathbf{s_g}$ and bring the first diffraction order G onto the optic axis, in doing so the 3G reflection satisfies the Bragg diffraction and appears brighter, whilst the zero-order beam is very weak as shown schematically below:

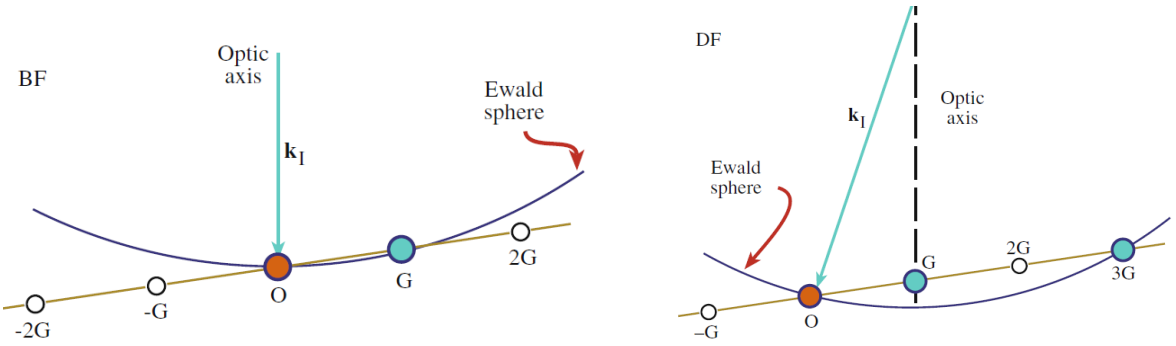

Fig. 2.6 Specimen is tilted from a) to b) for the g-3g condition [70].

As such, most of the lattice planes within the specimen are rotated away from the Bragg condition but near the cores of dislocations these are bent back and appear as high intensity features. The high contrast enables highly detailed imaging of dislocations [70], as shown in Fig.2.7.

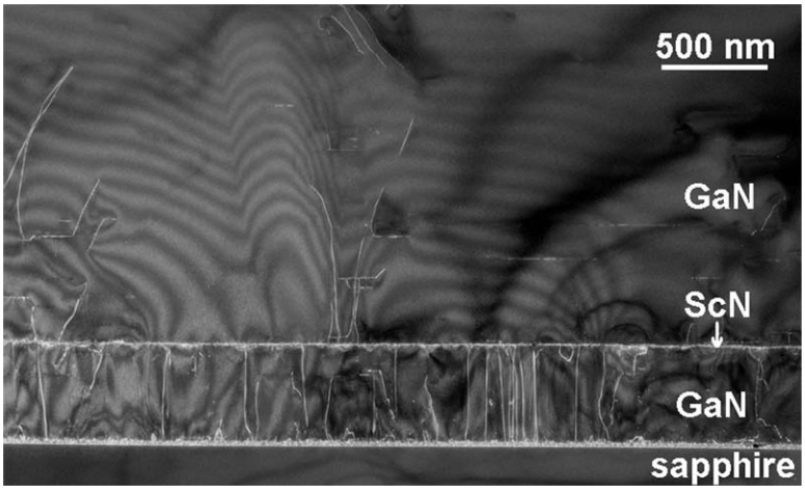

Fig. 2.7 WBDF imaging of dislocations [71].

2.1.2 Scanning Transmission Electron Microscopy

Scanning transmission electron microscopy (STEM) differs from conventional TEM in that a converged electron beam is utilised to generate an image, as opposed to a parallel incident beam as described in section 2.1.1. The convergence of the electron beam generates a probe which can be as small as several angstroms, which is focused and scanned across the sample. Each pixel in the image generated by this technique is acquired from the probe in a separate position by collecting radiation emitted from the sample.

A critical parameter in STEM is the brightness of the source which determines the current in the electron probe. Consequently, field emission guns (FEG) are favoured over thermionic guns such as tungsten or LaB_6 for use in STEM. Another factor which contributes to the preference for FEGs in STEM is the increased spatial localisation of the electron emission compared to thermionic sources, which allows for a smaller probe.

The probe in STEM is a demagnified image of the crossover from the electron gun. The figure below illustrates how a strong gun lens results in a cross over close to the gun such that fewer electrons travel through the collector aperture, leading to a smaller probe with a lower current on the sample.

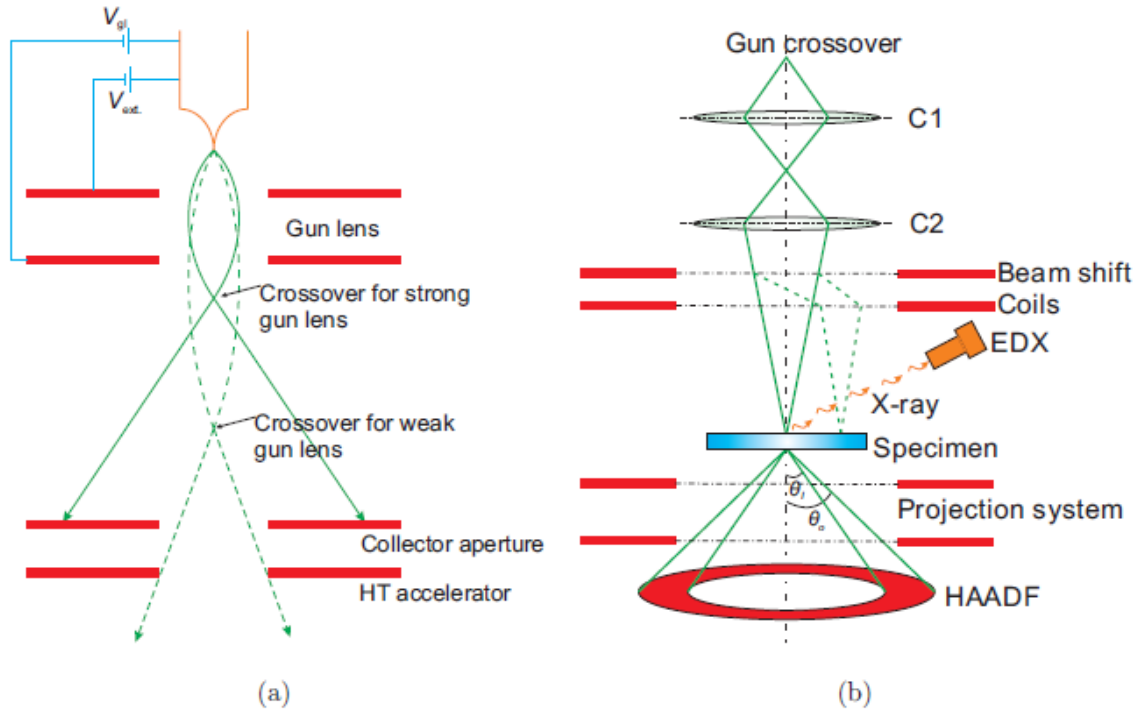

Fig. 2.8 Illustration of a) the FEG source and gun lens b) the column of a STEM with a HAADF for z-contrast imaging and EDX detector [69].

As different STEM techniques such as high-angle annular dark-field (STEM-HAADF) imaging, energy dispersive X-ray spectroscopy (STEM-EDX) or convergent beam electron diffraction (STEM-CBED) imaging will require different probes for optimal results, the strength of the gun lens allows for the adjustment of the required parameters [70].
STEM-HAADF is a STEM technique which allows for what is commonly known as Z-contrast imaging, or imaging by atomic number. The basic principle of operation relies on the fact that electrons scattered by atoms at relatively large angles are mostly incoherent and can be considered as particles rather than waves. At high angles, the intensity of the scattered electrons is proportional to the square of the atomic number Z [72] thus allowing the determination of atomic number of the material at the location of the probe from the brightness of the collected signal. Thus, the use of a high-angle annular dark-field detector allows for the collection of electrons scattered at high angles as shown in Fig 2.8 b). The magnification in STEM-HAADF imaging is controlled by varying the size of the area scanned by the probe, rather than through the use of lenses as in conventional TEM. Strong contrast is typically obtained in HAADF images of III-nitride heterostructures due to the large difference in atomic numbers between the group III elements.

2.1.3 Energy-Dispersive X-ray spectroscopy

Electron-induced X-ray emission allows for the characterisation of sample composition. The high-energy electron beam incident on the sample in TEM can excite an electron from an inner orbital, generating a hole. As electrons from higher energy orbitals relax into this vacancy a characteristic X-ray is released, with an energy equal to the difference between the two states involved in the relaxation transition.
Siegbahn notation is used to describe characteristic X-ray lines: the first component is the elemental atom emitting the X-ray, second is the electron shell which was ionized to emit the X-ray (K, L or M) and the final component describes the relative intensity of the line for each shell (in order of decreasing intensity: α, β, γ) [73]. These are shown schematically in Fig.2.9

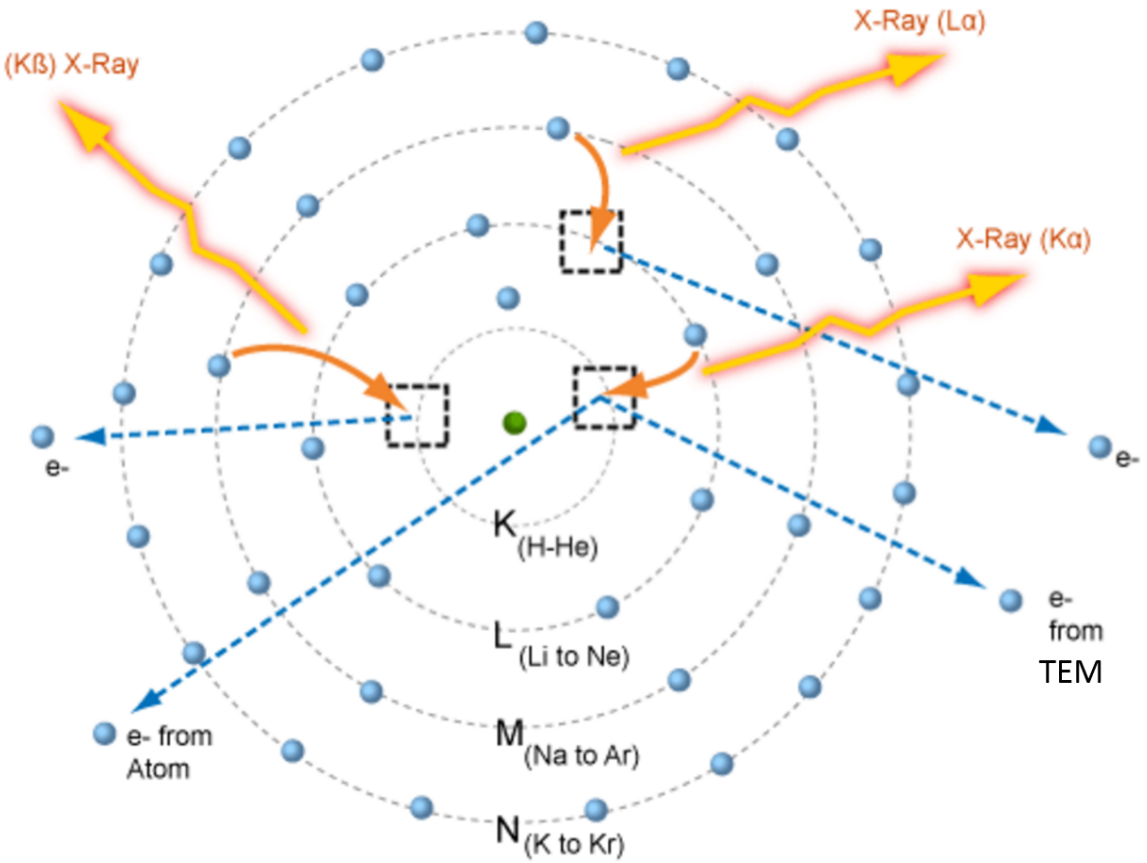

Fig. 2.9 $K_\alpha, K_\beta, and L_\alpha$ X-rays and their associated electronic transitions. Adapted from [73]

These characteristic X-rays can be collected using an energy dispersive detector, where the X-rays generate electron-hole pairs in a silicon *p*-i-n junction.
Energy-Dispersive X-ray spectroscopy (EDX) is typically used in STEM mode, where the

electron beam is condensed into a small probe, which leads to the majority of the X-rays being emitted from a small volume in the sample. This enables the acquisition of spatially resolved elemental maps.

2.2 Electron Tomography

TEM provides a plethora of techniques with which to characterise nano-scale structures, however it is often insufficient to ascertain the 3D morphology of complex structures as it deals with projections of the specimen. A typical exmaple of this is network of super-imposed particles in which particles overlapping in the projection may not in fact be in contact in real space [74].
Tomographic reconstruction is a technique that has been widely used to infer 3D volumes from series of 2D projections. A prime example of this is computed axial tomography scanning (CAT-scanning), a technique that has become prevalent in healthcare. The first demonstration of tomography applied to electron microscopy was reported at the MRC laboratory in Cambridge by De Rosier and Klug [75]. Since then, electron tomography (ET) has progressed in leaps and bounds due to advances in technology pertaining to both microscopy and tomographic reconstruction.
The fundamental tenet of tomography lies in the projection theorem developed by Radon at the dawn of the 20th century. The implication of the theorem is that the acquisition of a set of projected images of an object at varying angles can allow for the reconstruction of the full 3D Fourier transform of said object, and consequently the morphology of the object in real space [74] as shown in Fig.2.10.a)

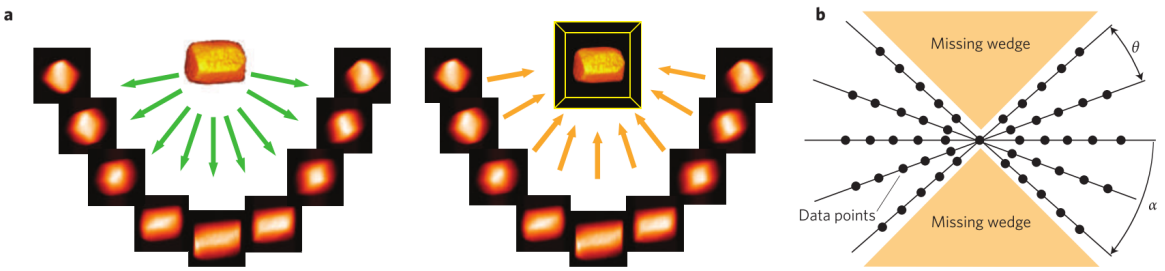

Fig. 2.10 Two-stage tomography process: a tilt series of an object is acquired, then the back projection of these images is used to reconstruct a 3D model of the object [76].

In practical terms, the angular range of the tilt series is an important consideration. A full tilt series acquired between the range $\pm 90^{\circ}$ allows for minimal anisotropy artifacts. However, typical TEM stage and holder combinations will only allow for a range of $\pm 78^{\circ}$ due to the

pole-piece gap, leading to a missing wedge of data which results in distortion in the 3D reconstruction [77]. Despite these issues, it has been shown that for tilt ranges larger than $\pm 75^{\circ}$, the elongation of features due to the missing wedge is below 10% and the volume fraction estimate is within experimental error as other factors such as the interval between images in the series and post-processing can also influence the accuracy of the reconstruction [78].

A common method for tomographic reconstruction is Weighted Backprojection (WBP): this method spreads the specimen mass present in the projection images in equal values amongst computed backprojected rays. This allows for the projection of the specimen back into a reconstructed volume. As the process is repeated for the projection images in the tilt series, the backprojection rays from different images reinforce each other as they intersect at points where the specimen is present [79]. This process typically induces blurring in the reconstructed volume due to an enhancement of low frequencies resulting from the unevenly sampled spatial frequencies in the series [80]. As such, a weighting filter is used to remove the blurring observed in the reconstruction by improving the frequency distribution in Fourier space [80]. An alternative approach to the reconstruction of the specimen volume is to formulate the problem as a system of linear equations, which are solved through the use of iterative methods [81]. This approach is known as the Simultaneous Iterative Reconstruction Technique (SIRT). SIRT performs reconstruction by minimizing the error between projections calculated from the current volume and the experimental projections iteratively [79]. Relative to WBP, SIRT has been shown to yield superior performance under varied experimental conditions and produce the fewest disturbing artifacts in the presence of the 'missing wedge' in the tilt series [82], but is more computationally expensive [79]. The two approaches are shown schematically in Fig.2.11.

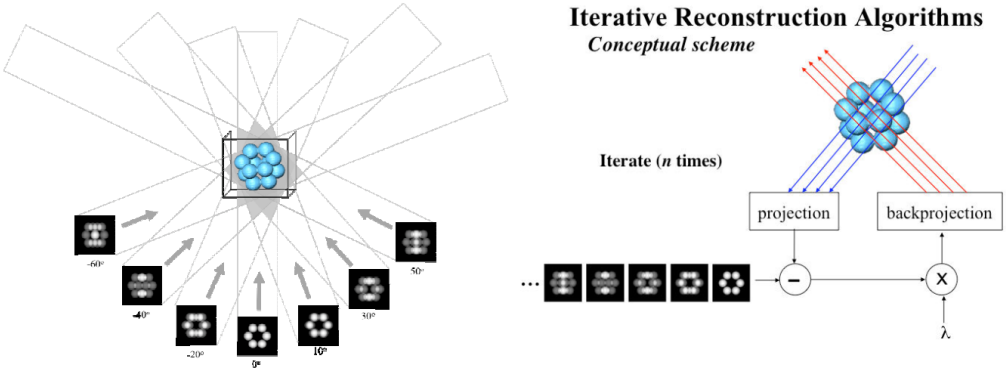

Fig. 2.11 WBP and SIRT reconstruction. Adapted from [79].

In order for the reconstruction to be successful, the signal used in the tilt-series must depend monotically on the thickness of the sample (or some other physical property) [83]. In the case of HAADF-STEM imaging, this is true as the signal intensity depends both on specimen thickness and atomic number.

2.3 Atomic Force Microscopy

Atomic force microscopy is a non-destructive characterisation technique which employs a sharp tip mounted on a cantilever which is rastered across a sample surface. Tip-surface interactions result in changes cantilever position which are measured using the reflection of laser light reflecting off the cantilever and a four-quadrant photodetector as shown in Fig.2.12 [84].

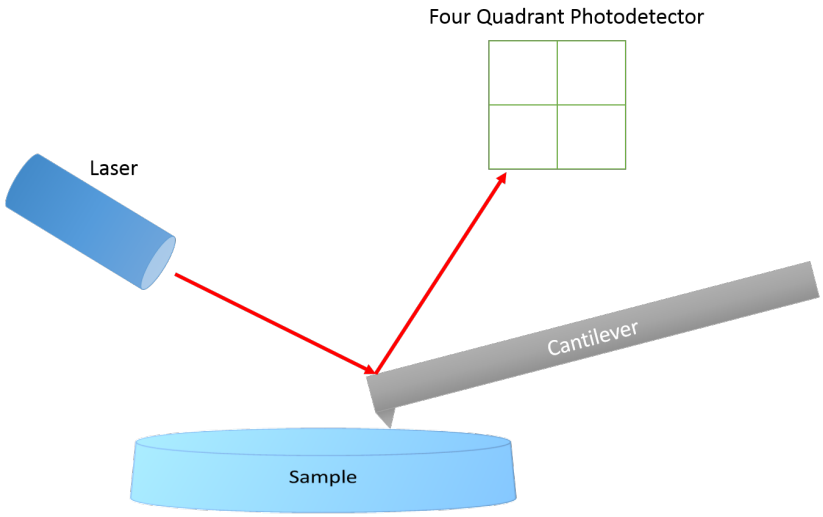

Fig. 2.12 Schematic of an atomic force microscope.

The positioning and movement of the tip is achieved through the use of piezo-electric actuators. In contact mode, a feedback circuit is used to apply a voltage to the piezoelectric crystal in order to maintain a constant tip-sample separation should the tip encounter any features, thus avoiding damage to either the tip or sample. The voltage required to maintain this distance (also known as the setpoint) is registered at each pixel of the scan and is used in conjunction with calibration data to determine a vertical displacement value, thus generating a topographic image [84].
An alternative mode of operation known as tapping mode is often preferred to contact mode. In this mode of operation the tip is made to oscillate close to its resonant frequency by the piezocrystal. Contact between the tip and the sample is achieved at the lowest point of each

oscillation, which damps the oscillation of the tip. The oscillation frequency is maintained by the piezoelectric crystal, thus allowing for the generation of a topographic map. Tapping mode is often preferred to contact mode due to the exclusion of lateral friction which can cause tip wear and sample damage.
The forces experienced by the tip vary depending on the tip-sample separation, as shown in Fig.2.13. Van der Walls forces dominate at large separations attractive the tip to the surface [84]. As the distance is reduced repulsive forces such as hard-sphere repulsion, electron-electron Coulomb interaction and the Pauli-exclusion interaction begin to dominate. The sum of these forces result in cantilever deflection, changing the tip-sample interaction [84].

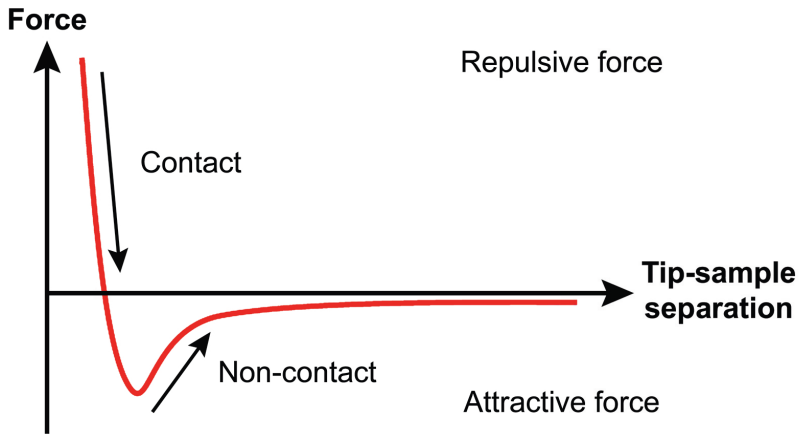

Fig. 2.13 The effect of separation on the tip-sample interaction force [85].

AFM offers excellent vertical resolution limited only by the probes vertical movement and external noise. However, the lateral resolution of this technique is heavily dependent on the shape and size of the tip employed. This is highlighted by Fig.2.14 which depicts a hemispherical tip scanning across a flat-topped island. The apex of the tip is in contact with the surface, but the side of the island also experiences some contact: in this case there is a distinction between the two cases shown in Fig.2.13a) and b) as the error in the measured width of the island varies based on the relative size of the measured object to the tip [84].

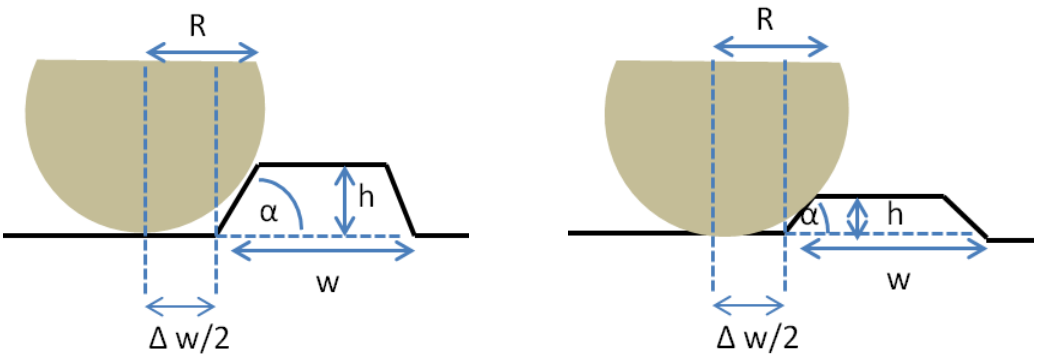

(a) (b)

Fig. 2.14 Interaction of a hemisphere with a flat-topped island for the cases a) $h > R(1 - cos(\alpha))$ and b) $h < R(1 - cos(\alpha))$ adapted from [84].

Similarly, when measuring depth rather than height the ability of the tip to penetrate into the spaces being measured is also a crucial consideration, as shown in Fig.2.16. Thus, increasing the slope of the tip and minimizing the tip apex are desirable to reduce tip-related measurement artefacts when performing atomic force microscopy [84].

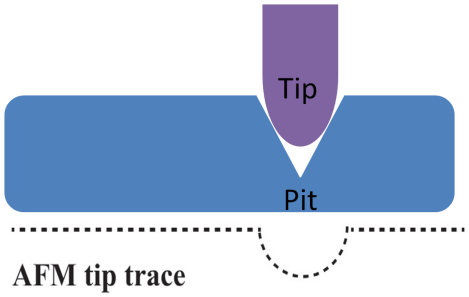

Fig. 2.15 Measurement error in the depth of a pit caused by the finite width of the AFM tip.

2.4 Scanning Electron Microscopy Techniques

A scanning electron microscope (SEM) employs the use of electrons to characterise material morphology and composition. A schematic of a typical SEM design is shown in Fig.2.16.

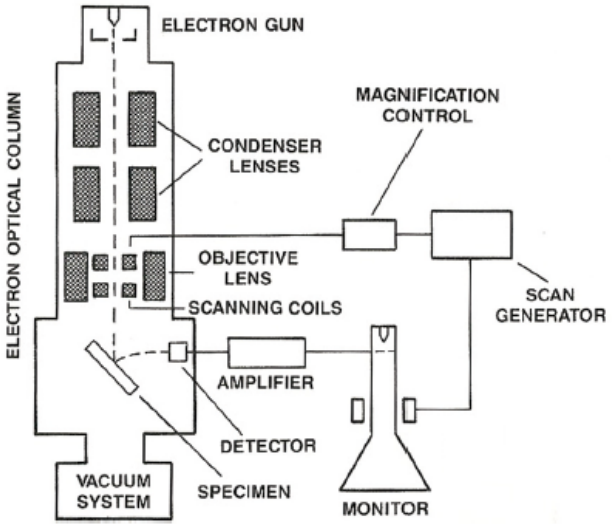

Fig. 2.16 SEM design [86].

The electron gun generates a beam of electrons, typically of energy up to 30 keV. The condenser lenses situated below the gun serve to determine the probe size by adjusting the demagnification of the beam. The objective lens serves to further adjust this demagnification, and is situated directly above the specimen. The scanning coils raster the electron probe across the sample, and the detector thus builds an image of the specimen by collecting various signals which occur due to the electron-specimen interactions [**?**].

As the beam of electrons interacts with the specimen, various processes occur which generate characteristic signals, as shown in Fig.2.17 and previously discussed in Section 2.1. The volume within the sample which contains the energy deposited by the electron beam is known as the interaction volume, the shape and size of which is determined by both the beam energy and sample composition. Inelastic scattering of the electrons results in the production of signals such as secondary electrons (SEs), Auger electrons and characteristic X-rays [70]. Typically, it is the SEs which are used for imaging in SEMs. Elastic scattering can generate back scattered electrons (BSEs), which are collected through the surface on which the beam is incident. Due to the nature of elastic scattering, BSEs have a strong dependence on atomic, and are can thus be used to produce composition-dependent image contrast [**?**].

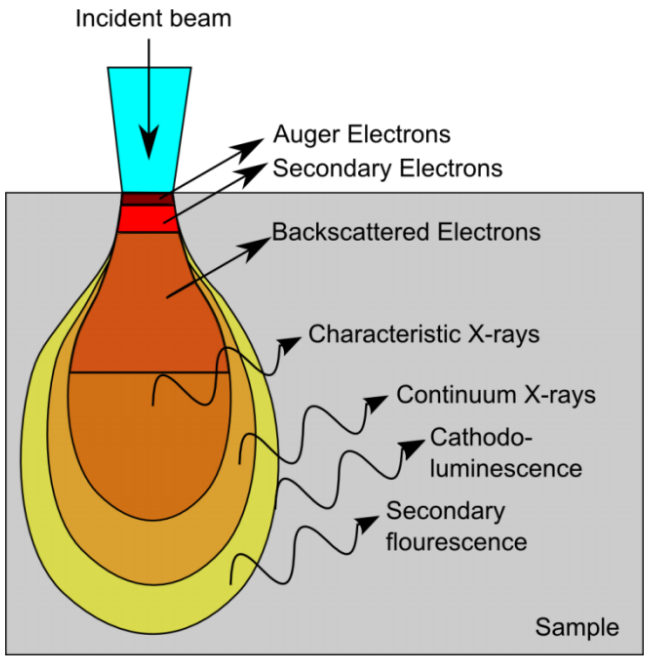

Fig. 2.17 Interaction volumes for different interactions of an electron beam [87].

2.4.0.1 Cathodoluminescence

The absorption of primary electrons in a semiconductor can generate electronic excitations, or electron-hole pairs, with light emission occurring as a consequence of their recombination. This process is known as cathodoluminescence (CL). The electronic transitions which are associated with CL emission require lower energies than those needed to excite X-rays [70].

One of the principal advantages of CL in comparison with photo-excitation spectroscopy techniques used on semiconductors is the limitation of the spatial resolution of the technique by the interaction volume of the electron beam in the material rather than diffraction, which can be considered an intrinsic limitation of most optical far-field techniques [88]. As a result, nanometre-scale characterization of materials can be achieved.

Due to the large number of electron-hole pairs generated within the interaction volume of the impinging electron beam on a bulk semiconductor material,all possible transitions within the material tend to be excited, resulting in the crucial limitation of being unable to selectively excite transitions below a certain energy [88]. Nonetheless, the versatility of CL as a technique has been amply demonstrated in its ability to shed light on the composition of compound materials such as InGaN/GaN structures [89], carrier diffusion length and surface recombination rates [90] and even minority carrier lifetimes [86].

A schematic view of a set-up for CL imaging is show in Fig.2.18:

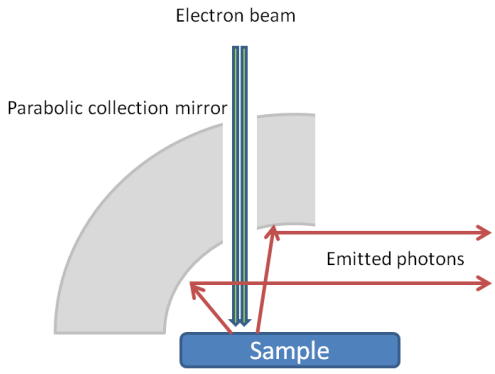

Fig. 2.18 Schematic layout of a CL imaging system.

The electron beam is incident on the sample in the SEM chamber and results in the generation of photons which are collected by a parabolic mirror through a high vacuum feedthrough and coupled into a monochromator. Photomultiplier tubes (PMTs) are the most commonly used detector for this set-up.
The most basic form of CL imaging is known as panchromatic imaging. In this case, the collected light in its entirety is directed to a single detector and the resulting greyscale image intensity is the product of the spectral response of the system and the emission spectrum [88].
An extension of this is the monochromatic imaging mode, in which case only a single band of wavelengths is imaged using a band-pass filter or spectrometer [88].
CL hyperspectral imaging, or CL wavelength imaging is an extension of the aforementioned technique whereby a full luminescence spectrum is recorded at each point during a beam scan, enabling the construction of a spatially and spectrally resolved data set.
In the set-up shown in Fig 2.18, a semi-paraboloidal mirror allows emitted photons to be collected over close to the entire hemisphere. In this case, the beam is scanned across the sample in order to achieve CL hyperspectral imaging, however a number of drawbacks are inherent to this collection geometry:

- The position of the mirror requires a large working distance and can obscure the optical element thus compromising the imaging capabilities of the microscope.

- The small distance between the sample and mirror imposes a restriction on the extent to which the sample can be tilted, which can be an issue in the examination of three-dimensional structures.

- The *étendue* of the system imposes a strict compromise between the field of view of the microscope and the collection efficiency at the spectrometer [88].

In an effort to overcome these limitations, CL hyperspectral imaging systems have been developed, whereby light collection is achieved using an objective placed perpendicular to the electron beam as shown below in Fig 2.19. By allowing the optics to be placed further away from the sample, a far shorter working distance can be used, allowing the electron spot to remain small at low accelerating voltages [88].

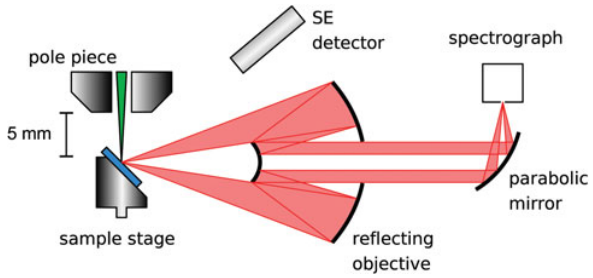

Fig. 2.19 Schematic layout of a CL hyperspectral imaging system [91].

The CL data in this thesis was collected on two separate systems, one employing the collection geometry described in Fig.2.18 and the other shown in Fig.2.19

2.4.0.2 Electron-Beam Induced Current

Electron beam induced current (EBIC) imaging is a technique complementary to scanning electron microscopy. The premise of the measurement is that minority carriers which arise from the incident electron beam of an SEM on a semiconductor junction can diffuse to the junction where they are separated by the built-in field and collected as current by an external circuit (the EBIC amplifier) [92].
Due to the small interaction volumes achievable, EBIC can provide detailed spatial information on minority carrier dynamics. Regions of high signal indicate high collection efficiency and low recombination, for example: the depletion region of a p-n junction appears bright in EBIC imaging. As such EBIC imaging has proven extremely useful in characterising the recombination properties of individual defects across a wide range of semiconductors [93].

2.5 Hyperspectral Electroluminescence Mapping

Hyperspectral electroluminescence (EL) mapping can be used to characterise local variations in EL in optoelectronic devices. The EL mapping data in this thesis was acquired on a modified electron probe micro-analyser (EPMA). The EPMA is fundamentally similar to an SEM with the added functionality of chemical analysis. The primary function of an EPMA

is to acquire elemental analyses at by wavelength-dispersive spectroscopy [94]. In order to perform EL mapping, the electron beam is switched off and a pinhole inserted. A forward bias is then applied to the device being characterised and the stage is moved in order to build up a map of EL emission of the device which is collected by a CCD camera to build up a hyperspectral data set consisting of a full spectrum for each pixel. The spatial resolution of the hyperspectral EL mapping is limited by the magnification of the optical microscope in the EPMA and the pinhole size, in the system used for this work the spatial resolution of the EL measurements was 3μm [95].

2.6 Dual Beam FIB-SEM

In this work a dual beam focused ion beam/scanning electron microscope was used to perform sample preparation as well as 'slice and view' tomography experiments. As we have introduced the basic principles behind SEM we will focus on the FIB in this section.
The FIB is an extremely versatile combination of a scanning ion microscope (similar in principle to the SEM but utilising ions rather than electrons) and a precision machining tool[96]. The ions utilised by the FIB are typically Ga^+, though helium sources also exist . A liquid-metal ion source is used to produce the gallium ions which are focused into a beam and onto the surface of a sample in a similar manner to the SEM using electrostatic lenses and apertures [97]. Due to the complementary nature of FIB and SEM instruments, dual beam FIB/SEM machines have been produced in which the techniques are used synergistically to overcome limitations on individual systems [97]. Aside from a standard electron beam, the FIB-SEM contains an additional gallium ion beam at an angle of 52^o to the axis of the electron beam as shown in Fig.2.20

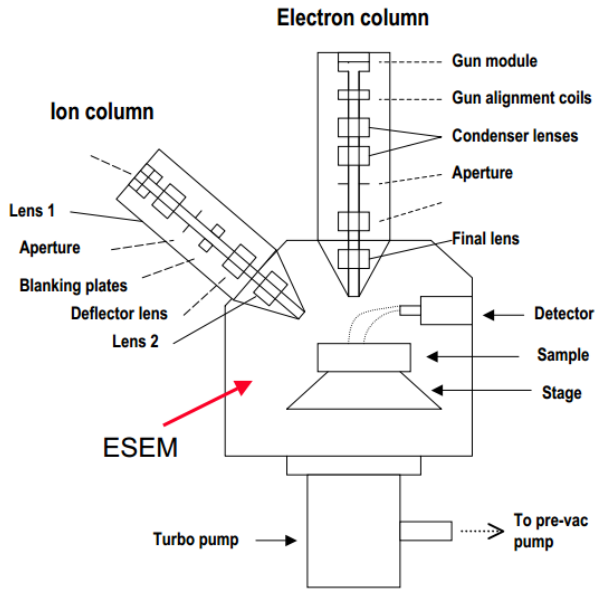

Fig. 2.20 Diagram of a dualbeam FIB-SEM

Due to the large mass of the Ga^+ ions relative to electrons the interaction of the focused ion beam with a sample can cause sputtering of the material, thus allowing for the precise removal of material. Often the SEM is used to monitor the milling process of the FIB as electrons cause negligible damage to the sample relative to the ion beam. Beyond the removal of material, the ion beam can also often be used to deposit material. A gas injection system is typically used to achieve this: a gas containing a metal-organic compound is injected into the chamber where it interacts with the targeted ion-beam at the surface of the sample leading to the heavier metal atoms remaining at the sample surface whilst the organic material is evacuated by the chamber vacuum system. Typically, platinum or carbon can be deposited using this method, though the platinum often contains carbon and other impurities rendering effectively semi-insulting [74].

2.6.1 Sample Preparation

Transmission electron microscopy requires electron transparent samples, typically of a thickness on the order of 100-150 nm. As such the dual beam FIB/SEM allows for site-specific TEM specimen preparation. Unless otherwise stated, all the TEM samples prepared in this work were produced using the FIB/SEM.

The specimen preparation method is shown in Fig.2.21 is as follows:

- A region of interest on the sample surface is identified.
- A protective layer of metal is deposited using the GIS system, first with the electron

beam then with the ion beam.

- Ion milling is used to form trenches on either side of the deposited protective layer

- A probe is then attached to the lamella by connecting the two with ion-beam deposited metal and used to lift the lamella out.

- The lamella is then transferred to a TEM grid, where it is thinned to a suitable thickness.

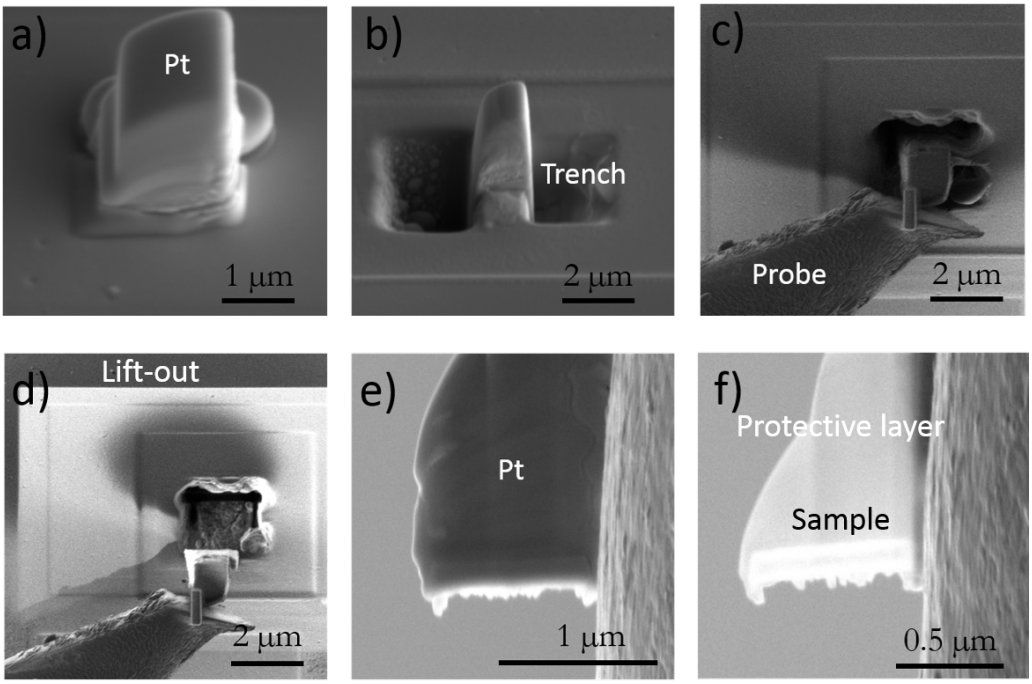

Fig. 2.21 FIB/SEM lamella lift-out and polishing process: a) Protective Pt layer deposition, b) trench milling, c) probe attachment, d) sample lift out e) sample attached onto a TEM grid f) final sample after thinning.

2.6.2 Tomography

FIB/SEM tomography, often referred to as 'slice and view', is a technique which has become relatively widespread in materials and life sciences due to the variety of detection modes available in commercial systems as well as the resolution and volume of material which can be analysed. Typical resolutions that can be achieved (voxel sizes) are in the range 5-10 nm. In FIB/SEM tomography, a small volume of the sample is selected for analysis. This volume is then typically coated with a layer of protective metal in order to prevent ion beam damage. In the experiments described in this thesis, a carbon coating is preferred to the platinum as it provide better contrast in the secondary electron image with GaN. Serial sectioning is then used to analyse the sample: alternating turns of milling and imaging allow for the sequential

erosion of thin layers of material and subsequent imaging as shown in Fig.2.22. In this work we employ only the use of the SE detector for imaging.

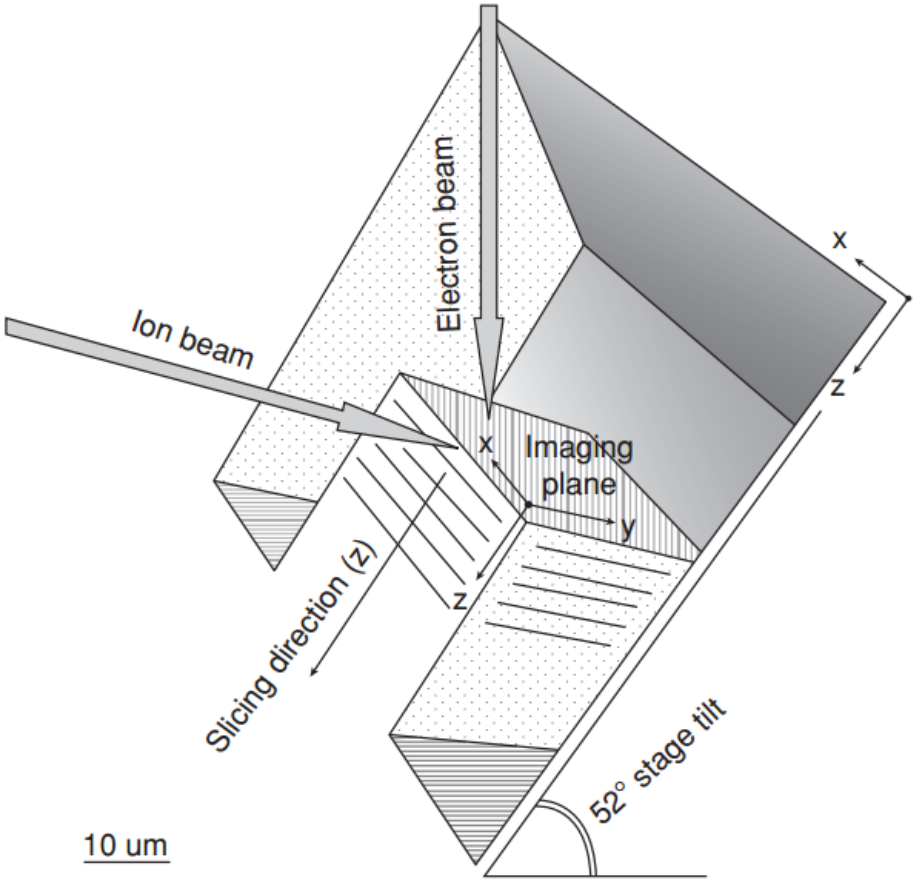

Fig. 2.22 Schematic of sample geometry for serial sectioning in a FIB/SEM instrument [98].

The purpose of serial sectioning is to produce a stack of images which can be transformed into a voxel-based volume data set. As such the thickness of the milled layers should match approximately with the resolution in the imaging plane.
Perhaps the most challenging task in FIB/SEM tomography lies in the extraction of information from the reconstructed 3-D image volume. This procedure, known as 'stack-processing', is very similar to reconstruction protocol used for electron tomography. In this work, the image stack is produced and aligned using the ImageJ [99] plugin StackReg using the 'rigid body' method [100]. Due to the oblique SEM imaging angle of 52^{o}, as discussed in section 2.6, distances measured along the y-axis shown in Fig.2.22 require correction for projection effects. The slice thickness for each layer are derived using the total measured volume divided by the total number of slices [98]. Following this step, thresholding is utilised to binarize the data into the subvolume under examination, and the 'background', this process

is known as segmentation. Accurate evaluation of the subvolume requires high image quality: high contrast and low signal-to-noise ratio are of particular importance [98]. The binary voxel data can be visualized using a wire frame structure calculated from the voxel mask by applying the 'marching cubes' algorithm. Details of the algorithm can be found in [101].

Chapter 3

Inhomogeneous Electroluminescence in InGaN QW LEDs

3.1 Background

$In_xGa_{1-x}N$/GaN QW structures are key structures in present day light emitting diodes in the visible wavelengths. Despite the growth of III-nitride LEDs into a gigantic market with a projected overall worth of 64 billion EUR by 2020, III-nitride alloys suffer from a plethora of material issues arising from heteroepitaxial growth on foreign substrates with large lattice mismatches [6] such as the formation of defects, as mentioned in section 1.1.4. As discussed in section 1.1.4, whilst III-nitride optoelectronic devices appear relatively robust to dislocations relative to other III-V devices, threading dislocations can nonetheless be source of highly undesirable effects in diode structures.

Threading dislocations have been shown to result in inverted pyramidal defects at the surface of nitride epilayers, known as 'V defects'. The effect of these defects on LED performance is hotly debated in literature as they are expected by many to hinder LED performance, as previously discussed in section 1.1.4.4. However, it has been shown that narrower QWs along the sidewalls of V-defects serve to screen carriers from the non-radiative centres at TDs [35].

In this study, a 'multi-microscopy' approach, whereby several microscopy techniques are utilised on the same features, is used to elucidate the origin of inhomogeneous EL in $In_xGa_{1-x}N$/GaN QW structures. The correlation of emissive and structural properties at the surface of the LED structures using several microscopy techniques has allowed for the detection of hexagonal defects at the centre of the inhomogeneities. Following this, structural and compositional information obtained using a combination of techniques is used to simulate

and reproduce the inhomogeneous EL, thus elucidating the mechanism whereby hexagonal defects can cause inhomogeneous EL in LEDs.

3.2 Sample Structure

For this study, a QW InGaN LED structure with a nominal QW thicknesses of 4.5 nm was studied.The sample was grown at the Cambridge Centre for Gallium Nitride, with LED processing carried out at the University of Bath. The structure was grown on a low dislocation density ($5 \times 10^8 cm^{-2}$) GaN template on sapphire, and consists of a 2 μm layer of unintentionally doped GaN followed by a 3 μm silicon doped GaN layer. The active layer consists of a 5 period InGaN/GaN MQW region, with unintentionally doped GaN barriers (7.6 nm). An AlGaN electron blocking layer (20 nm) and a magnesium-doped GaN cap (117 nm) were grown following the active region. The sample code is C5608A. This is shown schematically in Fig. 3.1:

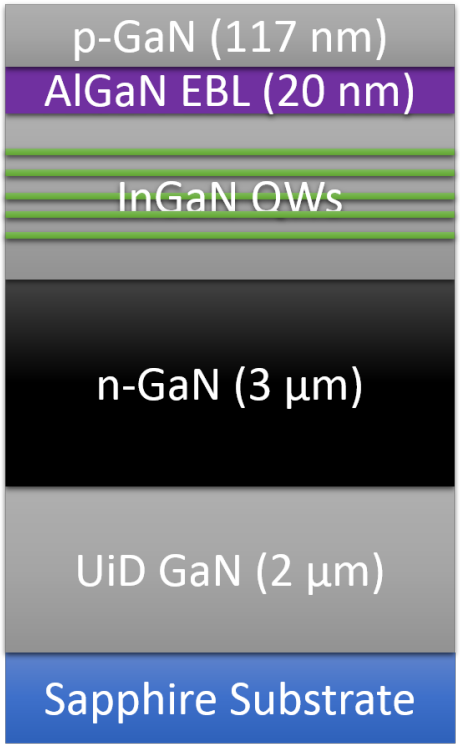

Fig. 3.1 LED structure schematic.

The wafer was processed into $1 \times 1 mm^2$ side contacted LEDs with thin oxidized Ni/Au current spreading *p*-layer Ohmic contact. Ti/Al Ohmic contact stripes were deposited on the *n*-layer and the Ni/Au current spreading layer in an interdigitated geometry.

QW thickness for the sample was determined from X-ray diffraction (XRD) using the method described by Vickers *et al.* [9]. The QWs were grown using the '2T' method, whereby the growth temperature is ramped up immediately following the InGaN growth under ammonia but without metalorganic fluxes. The barrier growth begins towards the end of the temperature ramp, this typically leads to loss of indium during the temperature ramp which can cause gross well-width fluctuations [102] but a higher barrier growth temperature is preferable[103]. '2T' growth is shown schematically in Fig.3.2.

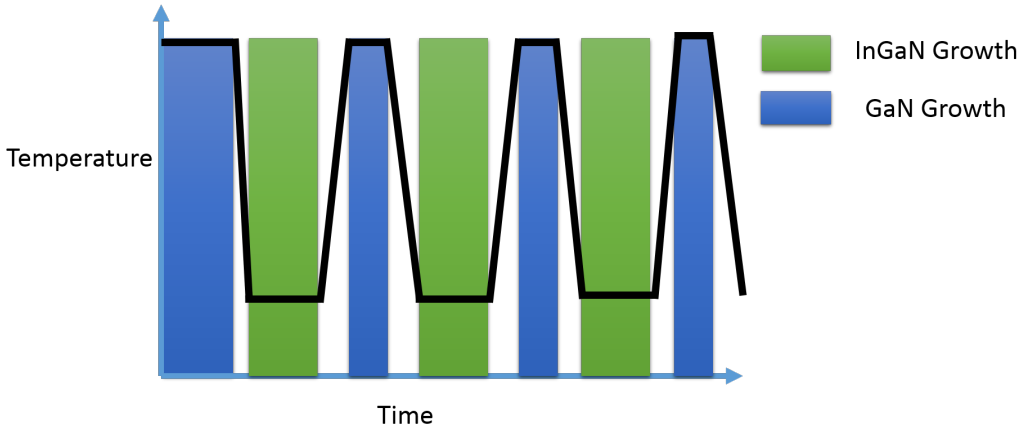

Fig. 3.2 '2T' growth of InGaN/GaN QWs. GaN QB growth is halted during the temperature ramp. The black trace indicates growth temperature over time.

3.3 Experimental

Initial evaluation of the inhomogeneous EL was performed in a Signatone S-1160 probe station under forward bias, as shown in Fig.3.3.

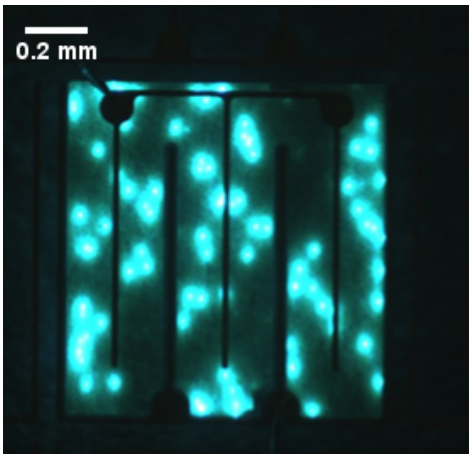

Fig. 3.3 LED EL under a forward bias of 3V. The bright inhomogeneities are visible in the emission of the LEDs.

Following this, hyperspectral EL mapping with CL and EBIC were performed using a modified Cameca SX100 electron probe micro-analyser with a custom built cathodoluminescence set-up. Hyperspectral EL measurements were performed under forward bias, enabling the acquisition spatially resolved EL maps of the inhomogeneities. Following the detection of hexagonal defects at the centre of inhomogeneities using SEM-CL, the defects were analyzed using AFM and C-AFM. Finally, FIB/SEM lamella preparation techniques were used to perform HAADF-STEM and STEM-EDX on the defects, allowing for access nanoscale compositional and structural information required to reproduce the EL in simulations.

3.3.1 Hyperspectral EL Imaging

Hyperspectral EL imaging was performed at Strathclyde University with the assistance of Dr Michael Wallace. In order to study the device under forward current, the LED wafers were mounted on TO-5 headers and bonded with 5 µm Al wire. A Keithley Instrument 2401 source meter was used to apply varying forward currents to the devices and thus allow for the collection of EL.
Full EL spectra were collected with a spatial resolution of approximately 3 µm and analysed using custom software developed by Dr. Paul Edwards, allowing for 2-D maps of EL peak intensity, position and FWHM. At each pixel in the map, a full EL spectrum was collected by an Andor CCD spectrograph. A full set of data extracted from the hyperspectral EL mapping (taken from the background emission of the LED, and not the bright inhomogeneities) is shown in Fig.3.4

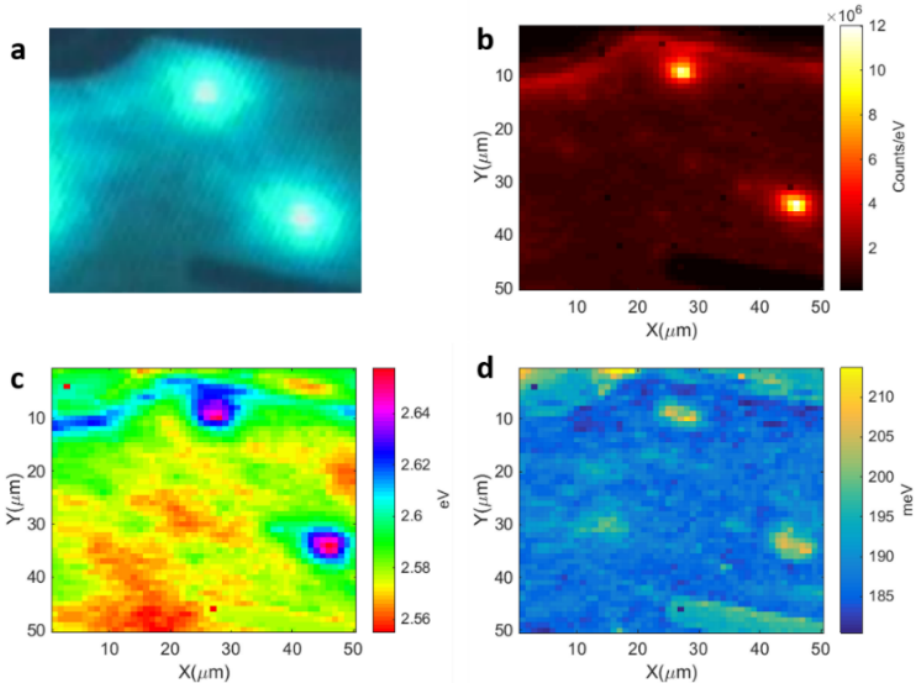

Fig. 3.4 a) Probe station image b) EL peak intensity, c) EL peak energy and d) EL FWHM extracted by fitting the hyperspectral EL data under a forward current of 10 mA

It is interesting to note that from this representative data set, the inhomogeneities observed are brighter by a factor of ~ 6, blue-shifted in terms of peak energy by ~ 0.08 eV and have a larger FWHM. Although these values were observed to shift based on injection current, the overall trend observed in the EL data collected for this LED is represented by Fig.3.4.
All intensity measurements performed on the system at Strathclyde University (for both CL and EL) are reported with units of 'Counts/eV' due to non-uniformity between neighbouring CCD channels in the spectrograph.

3.3.1.1 Current Dependent EL Measurements

Current dependent hyperspectral EL maps of the same area were performed, in order to examine the behaviour of the inhomogeneities with increasing current relative to the 'uniform' background. The peak intensities and peak energies for injection currents for device C5608A ranging from 1-250 mA are shown in Figures 3.5 and 3.6 respectively.

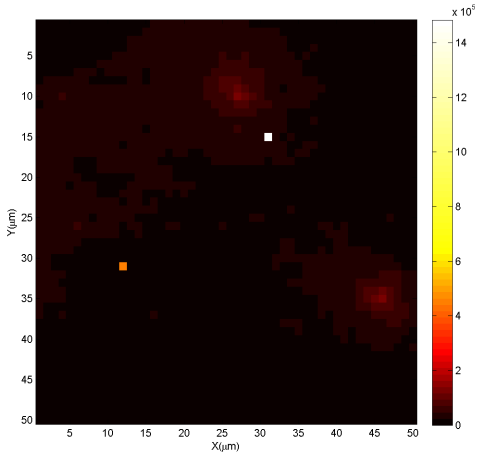

(a) 1 mA

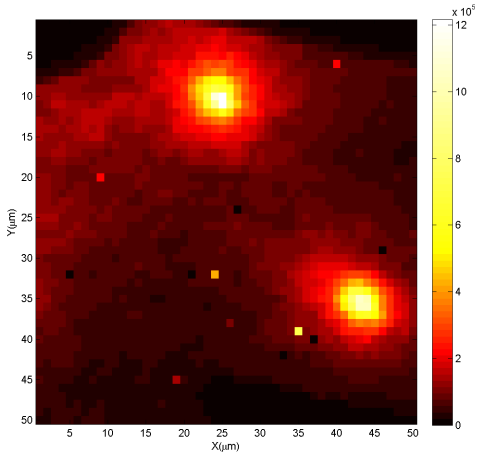

(b) 5 mA

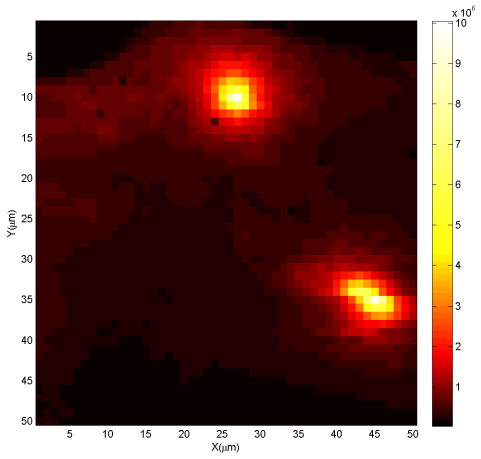

(c) 10 mA

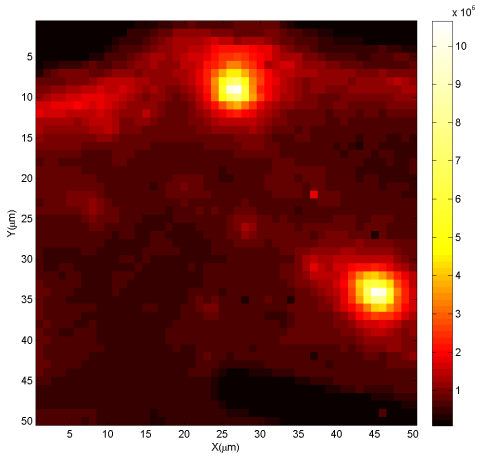

(d) 50 mA

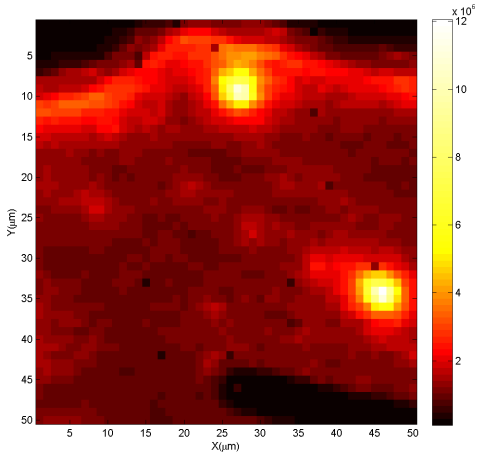

(e) 100 mA

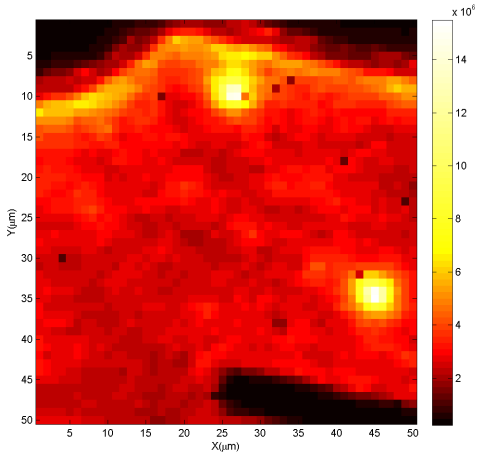

(f) 250 mA

Fig. 3.5 Peak intensity for varying injection current for C5608.

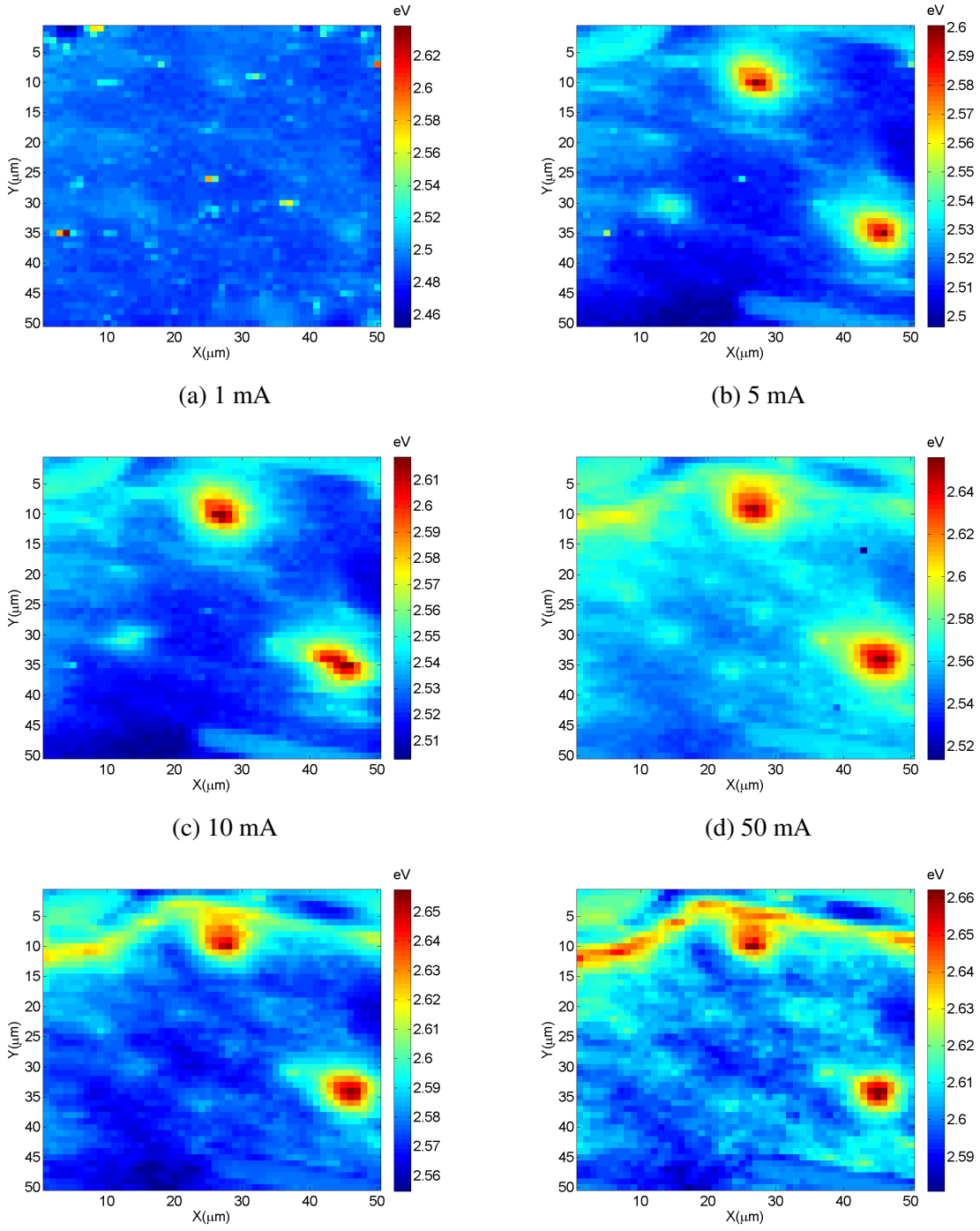

(a) 1 mA

(b) 5 mA

(c) 10 mA

(d) 50 mA

(e) 100 mA

(f) 250 mA

Fig. 3.6 Peak energy for varying injection current for C5608.

The spatially resolved EL data shown in Figures 3.5 and 3.6 allow for the comparison between areas containing the inhomogeneities and the 'background' EL. This is demonstrated in Fig. 3.7 which shows the behaviour of both the inhomogeneities (labelled 'spots') and the averaged background peak intensity with increasing injection current.

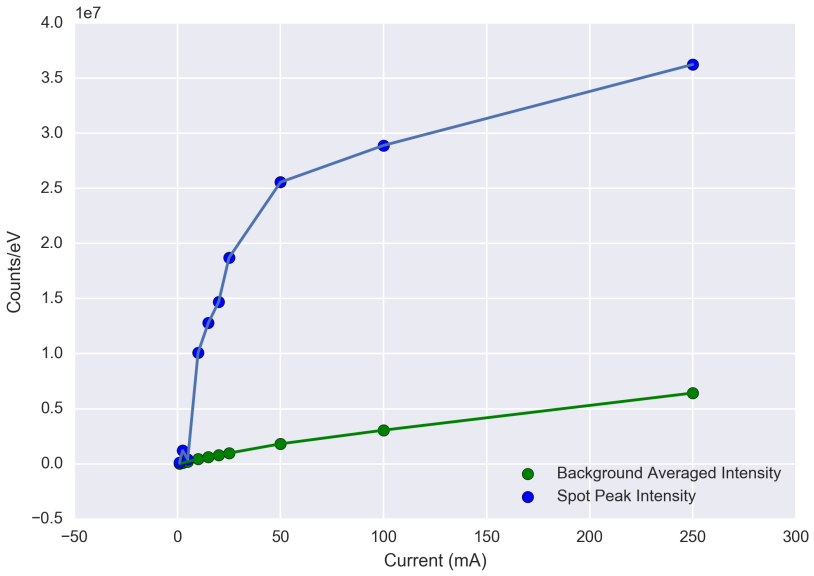

Fig. 3.7 Spot and background average peak intensity against injection current

It is interesting to note that Fig.3.7 shows the inhomogeneities experience a far sharper initial increase in peak intensity relative to the background based on the hyperspectral EL data fitting in the current range 0-50 mA, perhaps indicating enhanced current injection in the areas exhibiting the inhomogeneities.

Fig. 3.8 shows the same current dependent comparison for background and inhomogeneity peak energy. Here we see the same trend, in that the inhomogeneity exhibits a larger current-induced blueshift in the 0-50 mA range relative to the background. The origin of the current-dependent blueshift in InGaN QW structures is attributed to the screening of the QCSE by the additional carriers injected into the wells [22], and as such indicates the inhomogeneities are regions experiencing higher current injection relative to the background.

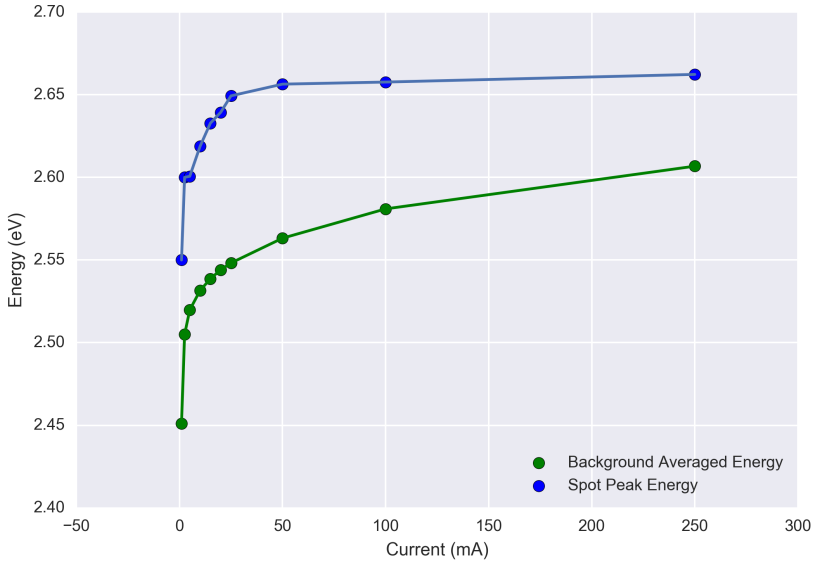

Fig. 3.8 Spot and background average peak energy against injection current

3.3.2 Cathodoluminescence and Electron Beam Induced Current

Having noted the behaviour of the inhomogeneities inferred from the hyperspectral EL data, CL and EBIC data were taken over areas containing the inhomogeneities in order to examine their properties in more detail as electron-beam based techniques allow for a far higher resolution than EL mapping.

In order to achieve simultaneous CL and EBIC measurements, a Keithley Instrument 2401 source/measure unit was utilised in order to main the LED devices at a fixed bias of 0V thus allowing for the measurement of the short circuit current. During the CL image scanning, the Andor CCD camera was set-up to trigger the unit to record the current at each point in the CL spectral acquisition. The CL acquisition was performed with an electron beam at 10 kV and 1 nA. Unfortunately the secondary electron detector was inoperable during the acquisition of this data, as such there is no accompanying SEM micrograph for the CL and EBIC data. The CL and EBIC data for C5608A are shown in Fig.3.9.

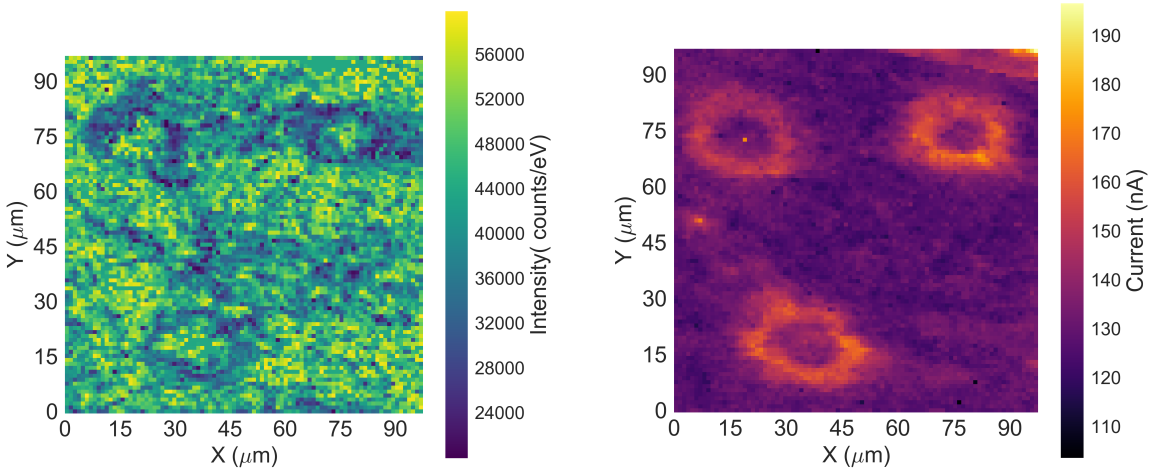

Fig. 3.9 a) CL and b) EBIC maps acquired simultaneously of the area shown in Fig.**??**b.

Fig.3.9a. shows the inhomogeneities exhibit a lower CL intensity relative to the background, in contrast to the EL. Interestingly, the EBIC signal, shown in Fig.3.9 for both inhomogeneities examined seem rather different. The feature closest to the contact region can be seen as a region of high EBIC surrounding a region of lower extracted current.
The low CL intensity detected can be interpreted in several ways: a high density of TDs or point defects could result in non-radiative recombination in these areas [104, 6] or enhanced stress in these regions could result in an enhancement of the QCSE which in turn would redshift and reduce the intensity of the CL emission [15, 22]. The enhanced EBIC in these regions tends to suggest the latter is more likely: the strain enhanced piezoelectric field across the QW stack would likely separate generated carrier-pairs [105] and result in a higher EBIC relative to the less-strained background. We note the size disparity between the features seen here in both the CL and EBIC, which are in the range of 12-15 μm and the inhomogeneities in the EL shown in section 3.3.1.1, which are closer to 10 μm in size. This may suggest that the bright features seen in the EL are in fact contained within the rings shown here, indicating that the features seen here (reduced CL intensity, enhanced EBIC) may be the outer-boundaries of the features. Further analysis in terms of the CL peak energy as well as structural and compositional information are required to explain the change in CL and EBIC seen here. Unfortunately, the CL spectra were corrupted during data transfer, meaning the information regarding the peak CL energy was lost.

3.3.2.1 Scanning Electron Microscopy with Cathodoluminescence

Following the CL and EBIC scans shown in Fig.3.9 performed at Strathclyde University, more detailed SEM-CL experiments were performed at the University of Cambridge using a Philips XL30s field emission SEM at 5 kV equipped with a Gatan MonoCL4 system to record the CL signal. This set-up provides the additional benefit of panchromatic CL imaging, which allows for the detection of the features without the need for detailed EL correlation. Fig. 3.10 shows the morphology of the features in the panchromatic CL and the associated SEM micrograph. The inhomogeneity appears as a region of lower CL intensity, though it is important to note the signal in panchromatic CL mode is the sum of the complete spectrum of photons collected. Nonetheless, this can be considered in relatively good agreement with the CL intensity recorded in Fig.3.9.a. Fig.3.10 reveals the presence of a hexagonal defect (outlined in red) which can be spatially correlated with the centre of the feature in the panchromatic CL image in Fig.3.9.b. We note that in this case the diameter of the feature shown in the pan-CL image (Fig.3.10) is approximately 4-5 μm, far smaller than what is observed in the EL. We expect this to be due to the different excitation methods for both SEM-CL and EL.

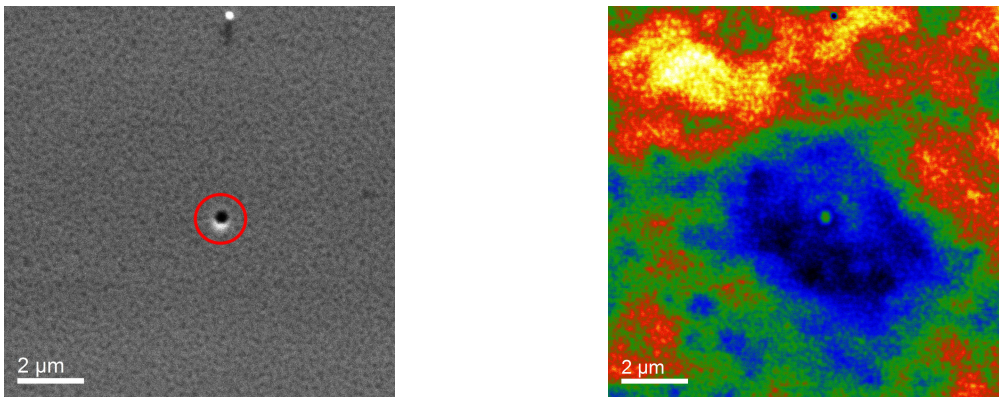

(a) (b)

Fig. 3.10 a) SEM micrograph and b) pan-CL image of an inhomogeneity in C5608A. The pan-CL image utilises a temperature scale (blue = low, red = high).

A hyperspectral CL map of 2×2 μm^2 was taken to examine the emissive properties of the defect in more detail. Fig.3.11.a. shows that as expected, the region close to the hexagonal defect exhibits low CL intensity. Interestingly, the defect also shows extremely low-energy emission relative to the background, most likely due to defect-related yellow band emission [106].

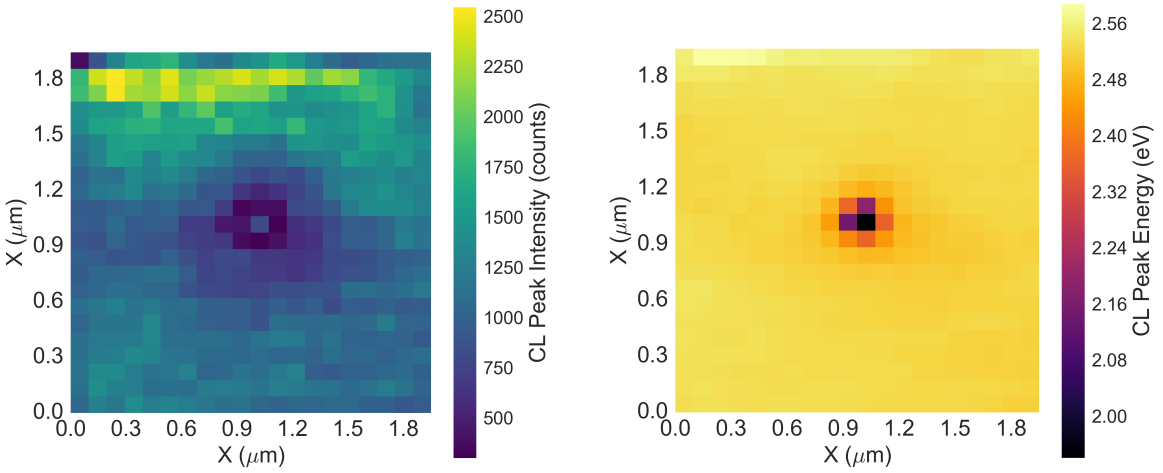

(a) (b)

Fig. 3.11 a) CL maximum peak intensity and b) CL peak energy for the feature shown in Fig.3.10

3.3.3 Hexagonal Defect Structure

The structure of the hexagonal defects found at the centre of the inhomogeneities was examined following their detection using SEM-CL.

3.3.3.1 Scanning Electron Microscopy

In order to achieve a higher resolution in examining the defects via SEM, an FEI Helios Nanolab 650 SEM/FIB with a schottky FEG at 5 kV and through lens detector (TLD) was used to perform high resolution SEM imaging. This is shown in Fig. 3.12.

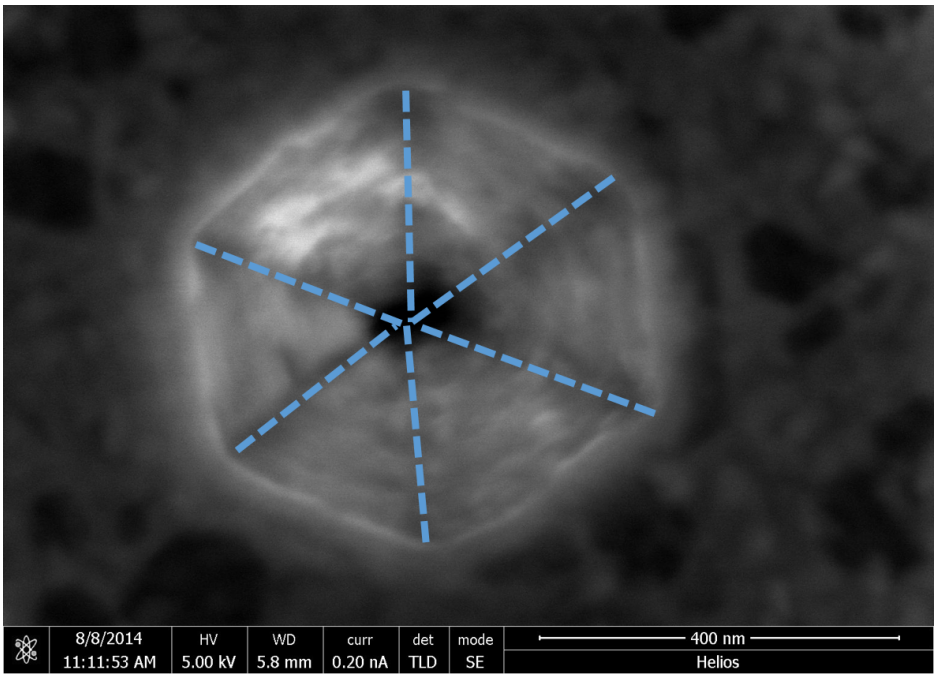

Fig. 3.12 High-resolution SEM image of a hexagonal defect located at the centre of an inhomogeneity in the EL. The vertices of the facets are delineated by dashed lines.

Most hexagonal defects located at the centre of the inhomogeneities fell within the 200-600 nm range, with some exceedingly large defects reaching up to 1 μm in size. This is rather uncommon for hexagonal defects in III-nitrides, as the lateral size of hexagonal defects is typically sub-100 nm [107, 37].

3.3.3.2 Atomic Force Microscopy

The topography of the hexagonal defect was studied by AFM performed on a Veeco Dimension 3100 with RTESP tips with a nominal radius of 8 nm in intermittent contact mode. The defect shown in the SEM micrograph in Fig.3.12 is shown below in the AFM image.

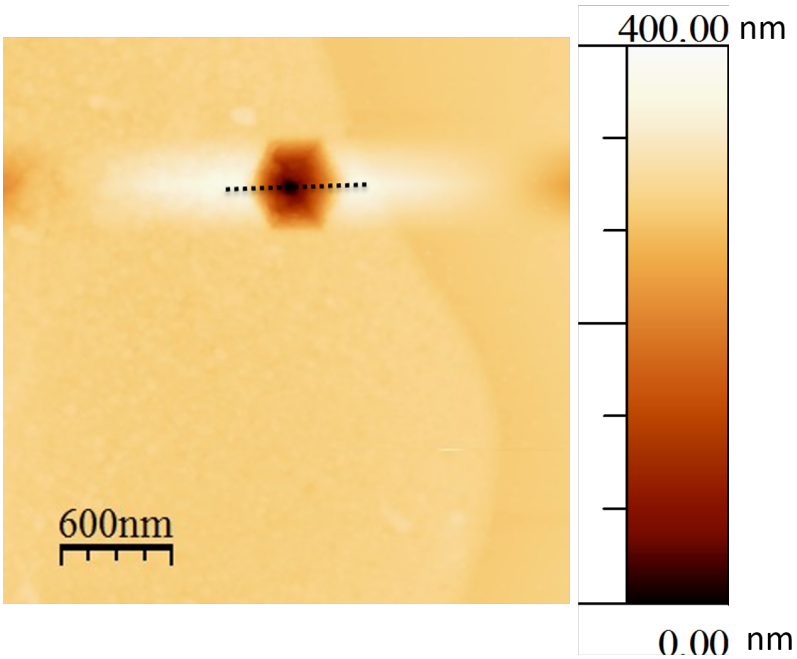

Fig. 3.13 AFM image of the hexagonal defect.

By taking a topography profile across the hexagonal defect, we can resolve the depth of the defect as well as the slope of the facets. From the profile taken in Fig.3.13 we can calculate the angle at the apex of the facets, which yields a value of approximately 60 degrees. The deviation from the ideal value of 60 degrees is expected to be due to drift during the AFM scan, causing the second facet to appear elongated and at a smore shallow angle. The raised area surrounding the pit is an artifact resulting from the large changes in depth encountered by the AFM tip during the scan, and can be reduced by reducing the scanning speed.

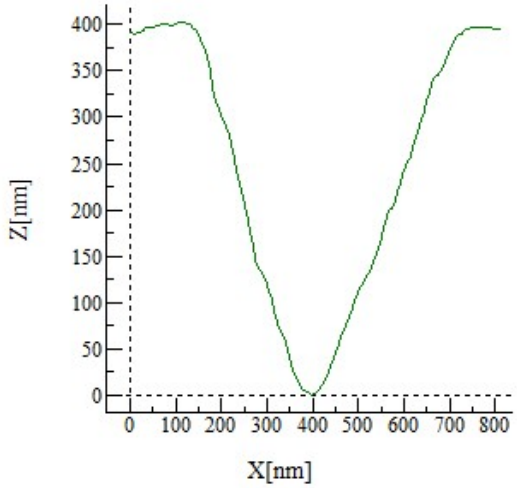

Fig. 3.14 Profile taken across the defect shown in Fig.3.13

3.3.3.3 TEM Lamella preparation

Preparation of TEM lamellae for the analysis of the defects requires some additional steps due to site-specific nature of the experiment. Standard FIB/SEM sample preparation methods simply require a 2 μm thick wedge of the sample to be extracted and thinned down to a thickness of 100-200 nm for TEM experiments. However, analysis of the defect and any associated dislocations which may be present at the apex of the inverted pyramidal shape [108, 109] requires thinning to be performed in an extremely controlled manner. A method devised by Thomas O'Hanlon at the Cambridge Centre for Gallium Nitride was utilised to perform high-precision site specific TEM sample preparation shown in Fig.3.15. A 'marker layer' consisting of a cross intersecting the apex of the defect is deposited using the electron beam, thus allowing for little damage to the unprotected sample and a higher deposition resolution than the ion beam. Following this a protective layer is then deposited using the ion beam, and a standard dual-beam lift-out method is used to extract the wedge of sample containing the defect.

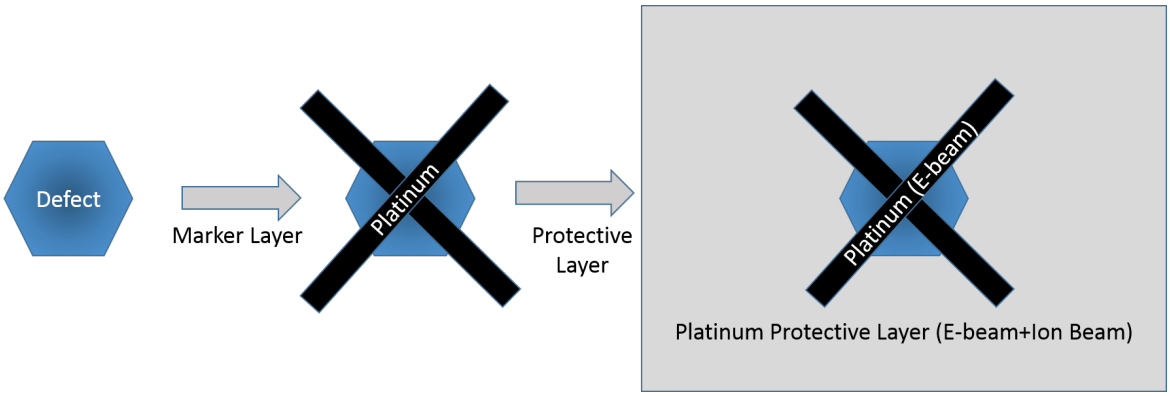

Fig. 3.15 Marker layer deposition for high precision TEM sample preparation.

The purpose of the marker layer is guide the sample thinning process. The electron beam deposited platinum provides contrast against both the sample and the ion-beam platinum in the SEM image. As the sample is imaged in cross-section during the thinning process, the distance between the marker layer 'ends' is an indicator of the proximity to the defect apex. As the defect apex is reached during the thinning process, the two marker stripes should merge into one at the intersection of the cross, as shown in Fig.3.16.

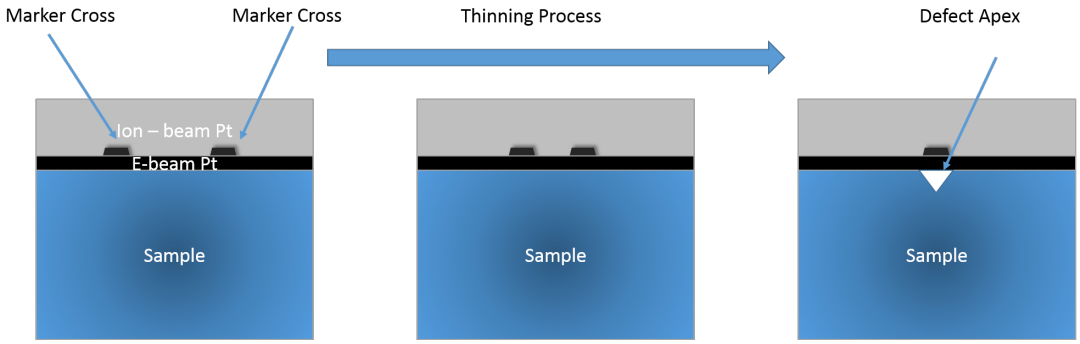

Fig. 3.16 Marker layer deposition for high precision TEM sample preparation.

A successfully thinned sample is shown in Fig.3.17.

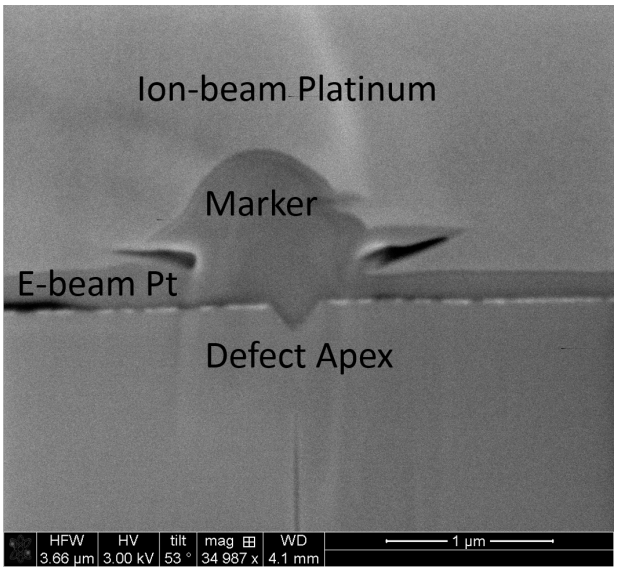

Fig. 3.17 SEM image of a prepared TEM lamella showing the marker position and defect apex.

3.3.3.4 Transmission Electron Microscopy

The site-specific TEM lamella prepared using the dual-beam methods, shown in Fig.3.17, was studied by HAADF-STEM performed on an FEI Osiris microscope with an extreme-FEG (X-FEG) at 200 kV. HAADF-STEM imaging of the defect reveals it originates below the MQW stack, a possible explanation for the large size of the hexagonal defects relative to those reported in literature [35, 37, 107]. We note the dark contrast in HAADF-STEM provided by the protective e-beam deposited Pt layer, which is certainly counter intuitive as Pt is a heavier element than those contained in the LED structure (Ga,In,Al and N). We believe this is due to the high concentration of C in Pt deposited by the dual-beam FIB/SEM, which is also a product of the decomposition of the organometallic precursor used for Pt deposition [110]. In contrast, we note the bright contrast from the Au-Ni *p*-contact at the surface of the LED structure, labelled in Fig.3.18, we believe that the bright feature which can be observed near the apex of the defect and running along on of the facets to the deposition of Au-Ni contact within the defect.

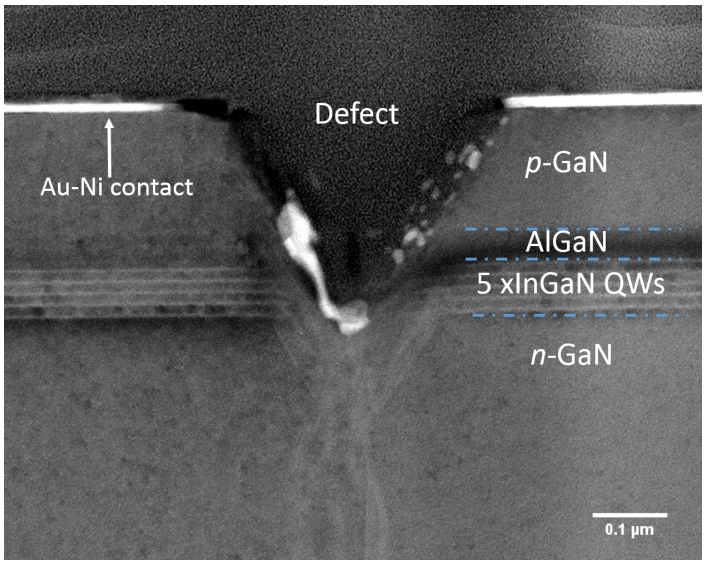

Fig. 3.18 HAADF-STEM image of a prepared TEM lamella showing defect interrupting the QW stack.

The composition of the MQW stack adjacent to the region occupied by the defect was studied using EDX-STEM, where the characteristic X-rays emitted by the sample were recorded by four silicon drift detectors which form a solid angle greater than 0.9 sr. Cliff-Lorimer analysis of the aluminium, gallium and indium was performed using HyperSpy [111] in order to quantify the ternary alloy compositions as shown in Fig.3.19. Details concerning the Cliff-Lorimer approach towards quantitative EDX-analysis can be found in [112]. K-factors for the Cliff-Lorimer analysis were provided by the detector manufacturer. Quantification consistency was tested by performing the quantification process using both Hyperspy and a custom Matlab EDX quantification script authored by Dr. James Griffiths and Dr. Spark Zhang.

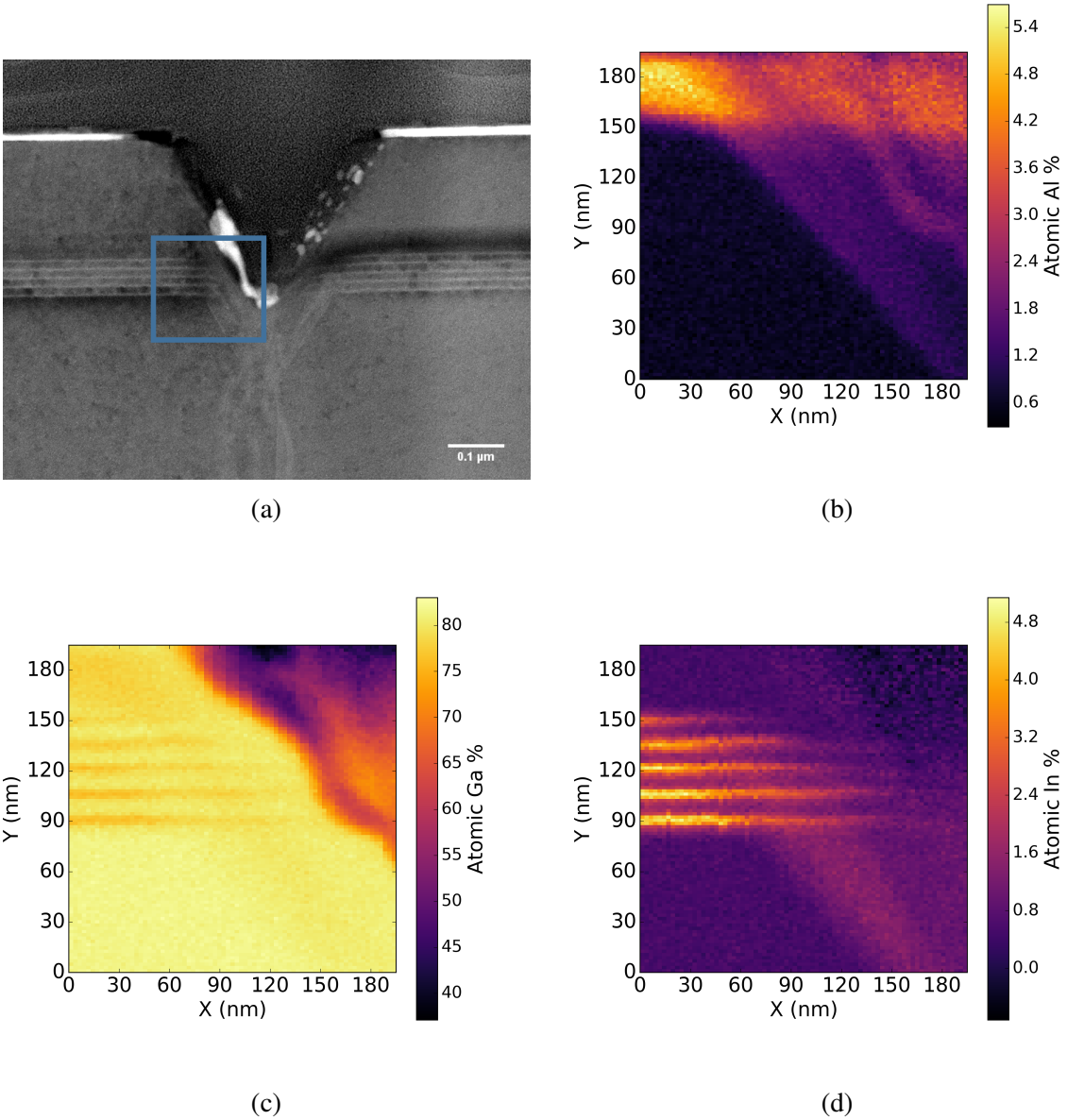

(a) (b)

(c) (d)

Fig. 3.19 Quantification of the ternary alloy compositions: a) HAADF-STEM image showing the region examined by EDX (blue box) b) aluminium atomic percentage, c) gallium atomic percentage and d) indium atomic percentage.

The EDS analysis shows the disruption of the QW stack by the defect, as evidenced by the apparent termination of the QW In signal in Fig.3.19.d. Additionally, the Al signal can be seen to overlap with the QW In signal, suggesting the presence of aluminium in the region disrupted by the defect. Furthermore, there is an observable indium signal originating from below the QWs. Although both the aluminium and indium atomic percentages observed in the region disrupted by the defect appear lower than expected (approximately 3 % and 2 % respectively) it is also important to consider the effect of the sample geometry in the collection of the EDX signal: due to the inverted pyramidal morphology of the defect the collected signal is expected to be reduced, and thus the atomic percentages obtained via quantification are expected to be under-estimates. This is shown schematically in Fig.3.20.

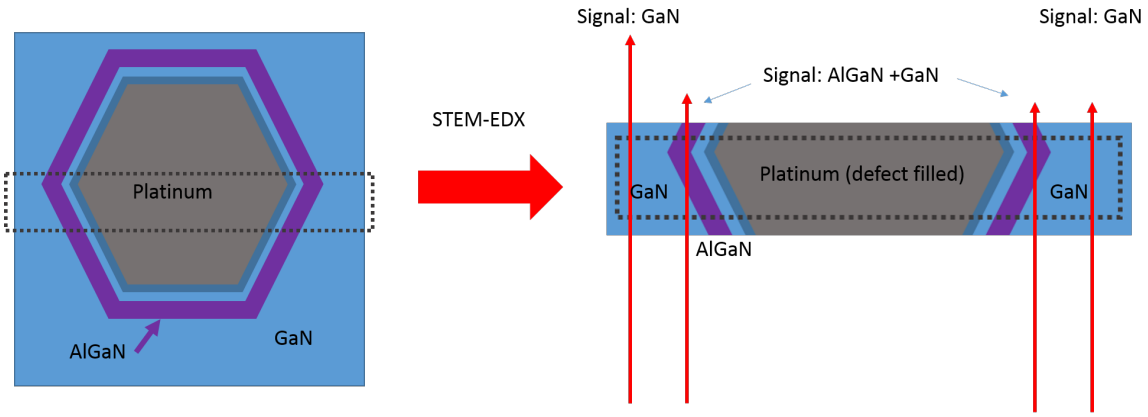

Fig. 3.20 Projection effects in the TEM lamella resulting from the morphology of the defect. The dashed line represents the portion of the sample extracted and made into a lamella. The red arrows represent a simplified trajectory for the electron beam during the STEM-EDX experiment.

In order to confirm the composition of the bright feature captured within our EDX scan, we examined the compositions for the *p*-contact material Au and Ni. Figures 3.21a. and b. show the Au and Ni atomic composition respectively, indicating that the material is likely to be a combination of both. The high Pt content over this area is likely due to projection effects as the material behind the bright feature is likely to be the protective Pt layer. We also note the presence of Cu over the sample, most likely due to deposition from the Cu TEM grid. We note that the presence of Pt and Cu over the majority of the sample may lead to errors in the accuracy of the elemental quantification, however the relative compositions should remain valid.

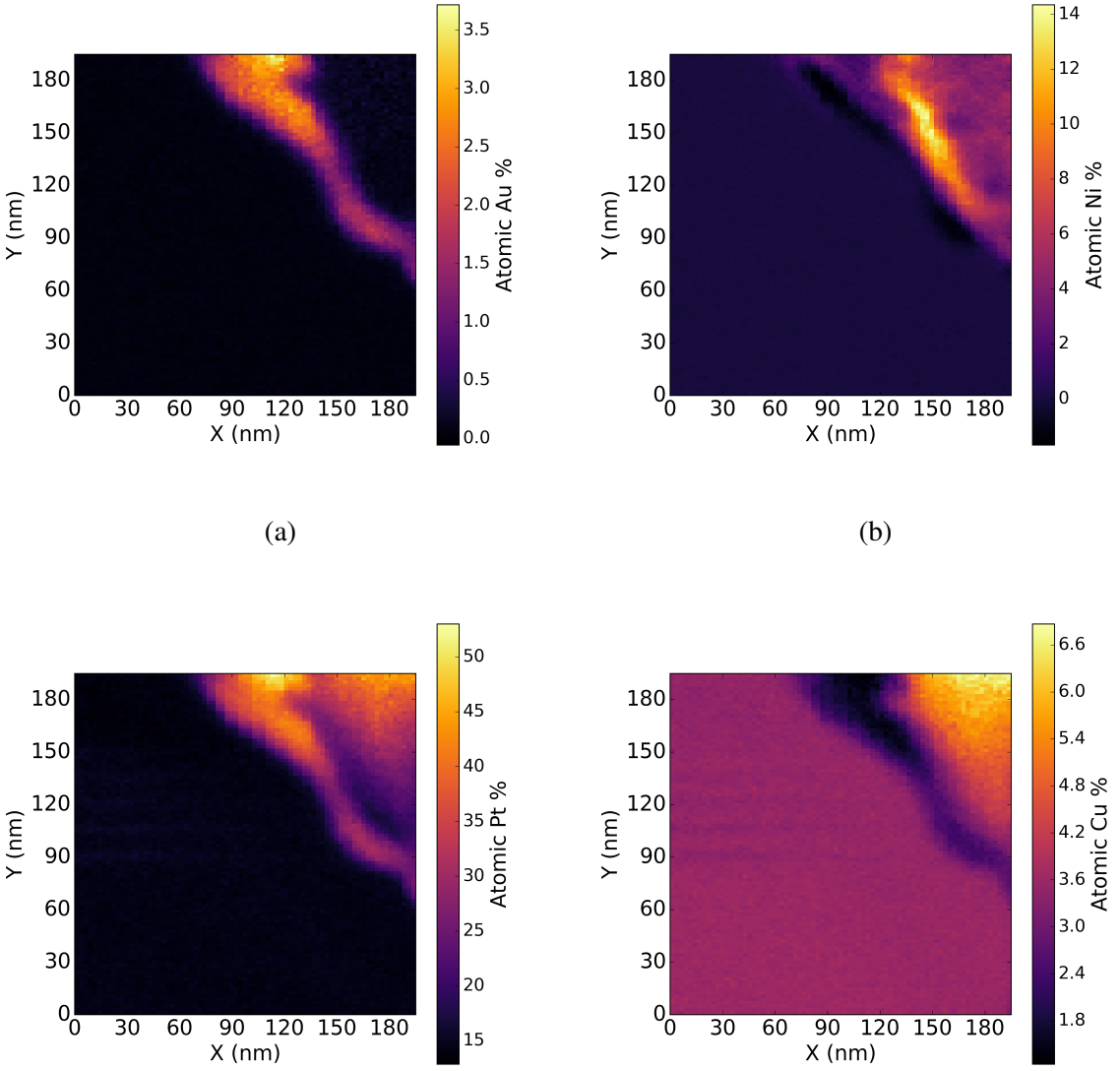

Fig. 3.21 Quantification of the metallic element compositions: a) Gold atomic percentage b) Nickel atomic percentage, c) Platinum atomic percentage and d) Copper atomic percentage.

3.3.4 LED Simulations

In order to investigate the manner in which changes induced by the defect could affect the EL of the LED simulations were performed by Bertand Rouet-Leduc using the APSYS simulation package, with parameters taken from J.Piprek [113]. APSYS couples a quantum-mechanical model for photon emission from the InGaN QWs in LEDs with self-consistently computed semiconductor carrier transport equations. Built-in polarization at nitride material interfaces is calculated using a second-order model described in [114]. Poisson and Schrodinger equations are solved iteratively to account for the QCSE as well as the quantum well deformation which is dependent on device bias. The carrier transport model considers a combination of band-to-band tunneling, thermionic emission at hetero-interfaces, Fermi statistics and the drift and diffusion of carriers [115]. For futher discussion of the mechanics behind the simulations of APSYS, please refer to [115].

3.3.4.1 Deep Inclusion

Fig.3.22 shows the simulated LED structure with a hexagonal defect incorporated. In this case we assume the QW stack simply continues along the edge of the hexagonal defect as described in [35], as the EDX quantification reveals a detected atomic percentage of indium of approximately 4 % below the QW stack. We assume a similar geometry for the AlGaN EBL, which is expected to follow the angled facet of the defect. Thus, this set of simulations deals with what we term a 'deep' AlGaN inclusion, which is expected to penetrate below the QW stack. Although the atomic Al percentage shown in Fig.3.19.b. below the QW stack is reduced relative to the Al percentage in the EBL, this may be due to projection artifacts related to the geometry of the hexagonal defect and the thickness of the TEM lamella.
In this set of simulations, we have set the *p*-GaN doping concentration to $3 \times 10^{19} cm^{-3}$, the *p*-AlGaN EBL doping to $4 \times 10^{19} cm^{-3}$ except on the semi-polar facets of the defect where it is set to $1 \times 10^{19} cm^{-3}$.

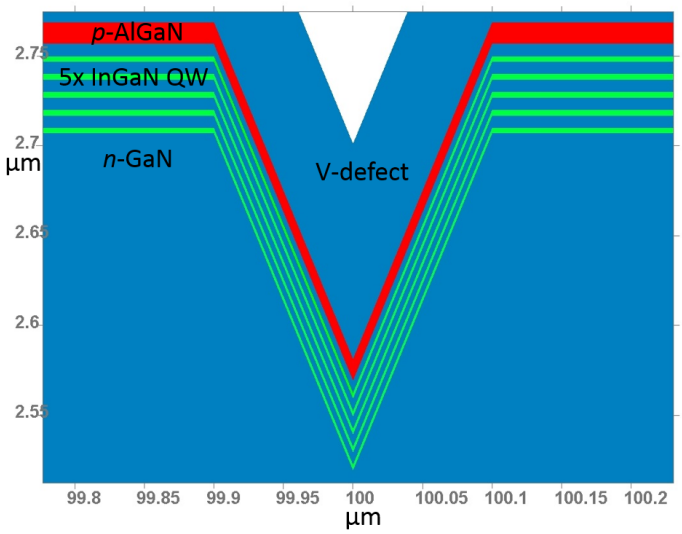

Fig. 3.22 Simulated LED structure.

The simulation results are shown in Fig.3.23.. Fig.3.23. shows a two-dimensional map of the overall radiative recombination rate in units of $10^{28} cm^{-3} s^{-1}$. It is important to note the x-axis of Fig.3.23 is enlarged relative to the y-axis for visualisation purposes. The region closest to the defect at the lowest QW (QW5) shows an increased radiative recombination rate, in agreement with the experimental observation of inhomogeneous EL, which was brighter at the location of the defects within the resolution of the hyperspectral EL data shown in Section 3.3.1.1. Fig.3.24.shows two profiles taken from Fig.3.23.a. intersecting the five QWs and indicates that the rate of radiative recombination is almost doubled in the lowest QW close to the defect when compared with a profile taken further away from the defect.

Under closer examination, Fig.3.24. demonstrates that the 'bottom' QW dominates the overall emission, particularly close to the AlGaN inclusion. We note that the distance label of the x-axis in Fig.3.24,3.25 and 3.26 is the distance from the centre of the hexagonal defect in the simulation. At QW5, which here is the label used to describe the QW closest to the substrate and furthest from the *p*-contact, we can see that the radiative recombination close to the simulated defect (at approximately 150 nm from the apex of the defect and labelled in red) is enhanced by a factor of 2 relative to the profile taken at 400 nm from the defect (in black). Interestingly QW1 and QW2 exhibit slightly lower radiative recombination close to the defect relative to the profile taken at a distance of 400 nm from the defect. The carrier concentrations shown in Figures.3.25 and 3.26 show that this is primarily due to the enhanced hole concentration in the region adjacent to the AlGaN, as the electron concentration is relatively unchanged. Thus we can ascribe the enhanced local carrier concentration to the

presence of the *p*-AlGaN, which injects holes directly into the active region. The effects of hexagonal defect-assisted carrier injection into MQW stacks have been reported by Li *et al.*, who reported that the disruption of the MQW stack by the hexagonal defect combined with thinner QBs allowed for the injection of holes up to 8 pairs of QWs away from the *p*-GaN [116]. Quan *et al.* have also suggested that hole injection via the semi-polar facets of the hexagonal defect occurs at a higher rate resulting in high radiative recombination near the defect, but larger defects may result in localised emission [117].

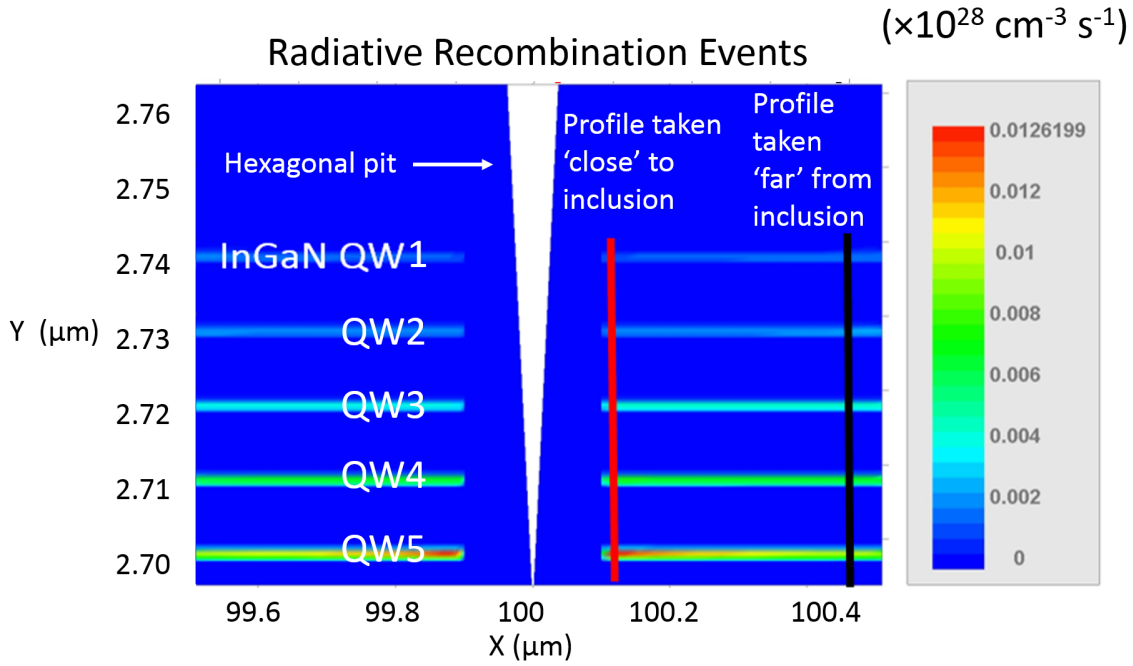

Fig. 3.23 APSYS simulation results: Radiative recombination events. The simulation parameters were as follows: *p*-GaN doping concentration: $3 \times 10^{19} cm^{-3}$, *p*-AlGaN EBL doping: $4 \times 10^{19} cm^{-3}$ except on the semi-polar facets of the defect where it is set to $1 \times 10^{19} cm^{-3}$, AlGaN Al atomic percentage: 4 %, defect depth: 600 nm.

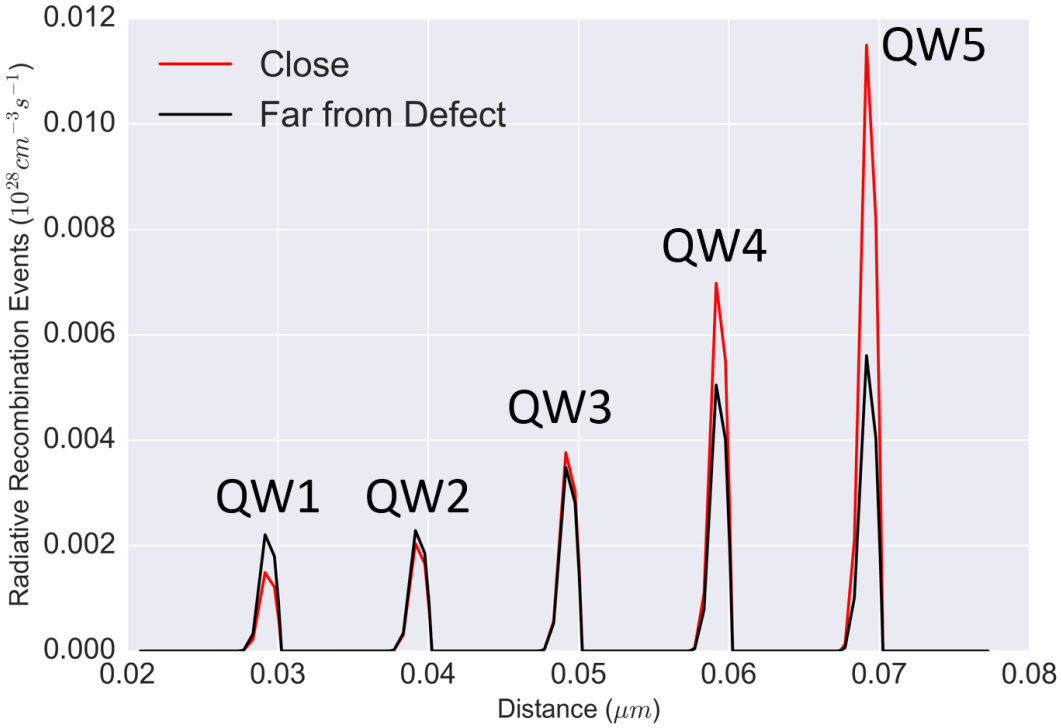

Fig. 3.24 APSYS simulation results: radiative recombination profiles. The simulation parameters were as follows: *p*-GaN doping concentration: $3 \times 10^{19} cm^{-3}$, *p*-AlGaN EBL doping: $4 \times 10^{19} cm^{-3}$ except on the semi-polar facets of the defect where it is set to $1 \times 10^{19} cm^{-3}$, AlGaN Al atomic percentage: 4 %, defect depth: 600 nm.

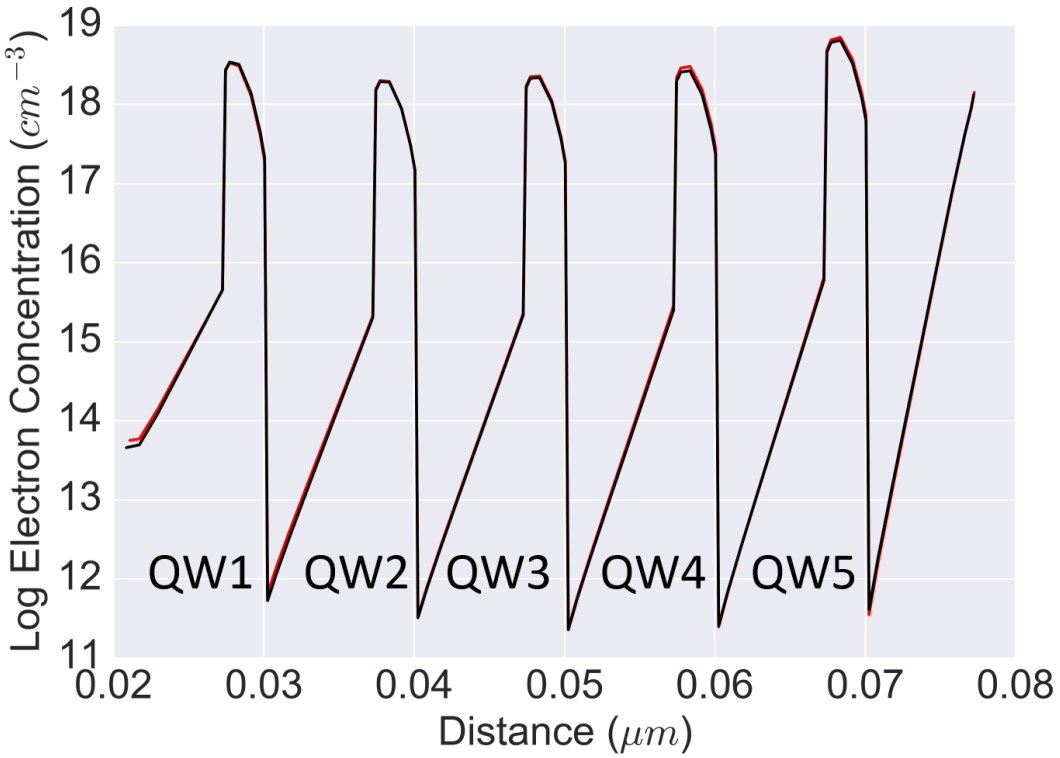

Fig. 3.25 APSYS simulation results: log electron concentration profiles. The simulation parameters were as follows: *p*-GaN doping concentration: $3 \times 10^{19} cm^{-3}$, *p*-AlGaN EBL doping: $4 \times 10^{19} cm^{-3}$ except on the semi-polar facets of the defect where it is set to $1 \times 10^{19} cm^{-3}$, AlGaN Al atomic percentage: 4 %, defect depth: 600 nm.

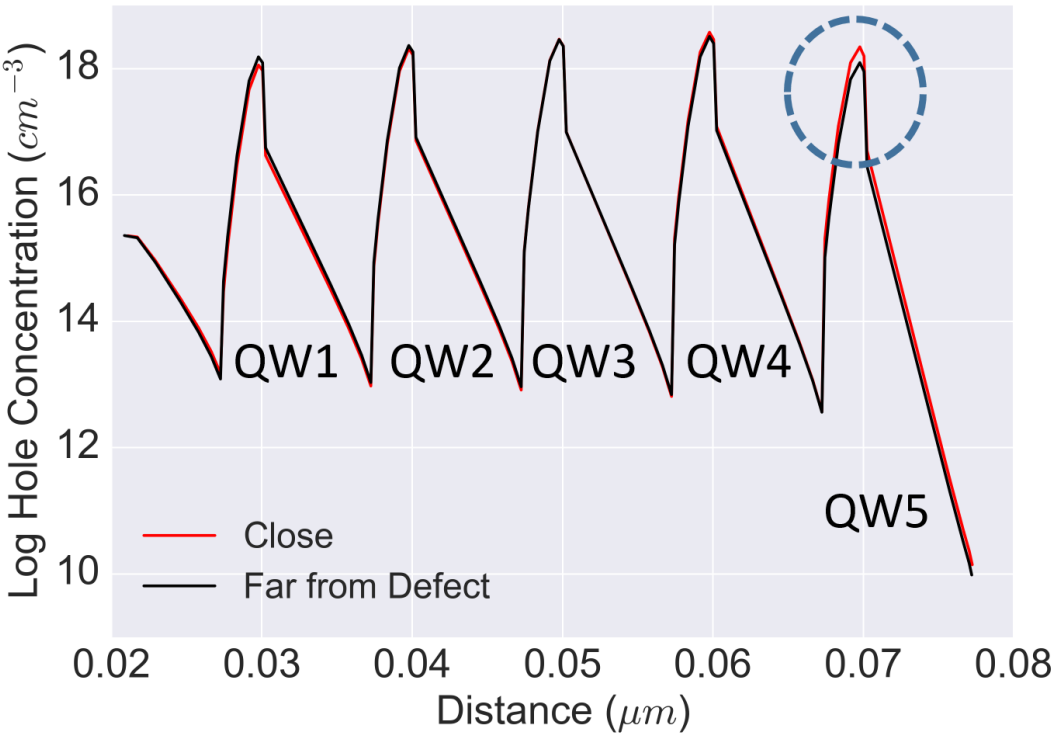

Fig. 3.26 APSYS simulation results: log hole concentration profile. The simulation parameters were as follows: *p*-GaN doping concentration: $3 \times 10^{19} cm^{-3}$, *p*-AlGaN EBL doping: $4 \times 10^{19} cm^{-3}$ except on the semi-polar facets of the defect where it is set to $1 \times 10^{19} cm^{-3}$, AlGaN Al atomic percentage: 4 %, defect depth: 600 nm.

3.3.4.2 Shallow Inclusion

In this simulation we have simulated a structure similar to the composition maps shown in Fig.3.19. We have assumed that the AlGaN EBL may penetrate only slightly in into the QW stack due to the defect, but otherwise the rest of the disrupted region is filled with undoped GaN. The AlGaN EBL doping is set to $5 \times 10^{18} cm^{-3}$ with an Al content of 10%. Thus, in this case we assume no projection artifacts, as opposed to the deep Al inclusion simulated previously. The geometry used for this simulation is shown in Fig.3.27.

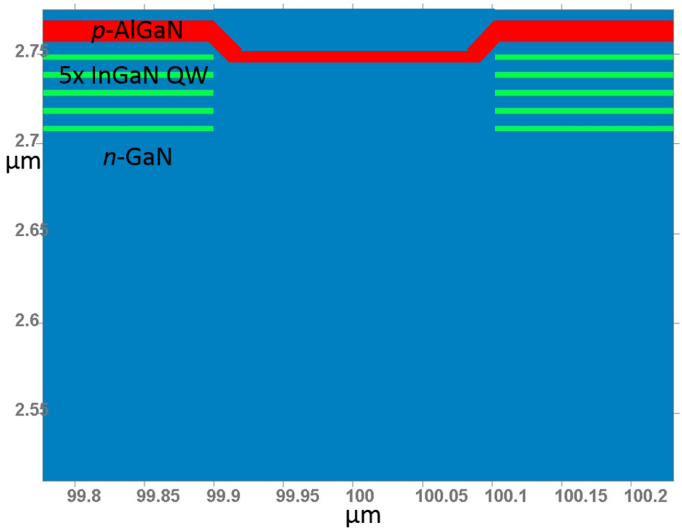

Fig. 3.27 Simulated LED structure for the shallow inclusion.

Fig.**??** shows the simulation results. Fig.3.28. shows that radiative recombination is enhanced in the vicinity of the shallow inclusion, particularly in the second QW (QW2) from the EBL due to carrier injection from the semi-polar facets of the defect. Fig.3.30.c. and Fig.3.31.d. show that the hole concentration is responsible for the local enhancement in radiative recombination near the shallow inclusion as the electron concentration is mostly unchanged. Fig.3.31 show that the enhanced injection of holes results in an order of magnitude increase in radiative recombination in QW2. As such, even in the case of a 'shallow' *p*-AlGaN inclusion induced by a hexagonal defect, the injection of holes into the active region still results in enhanced emission adjacent to the defect.

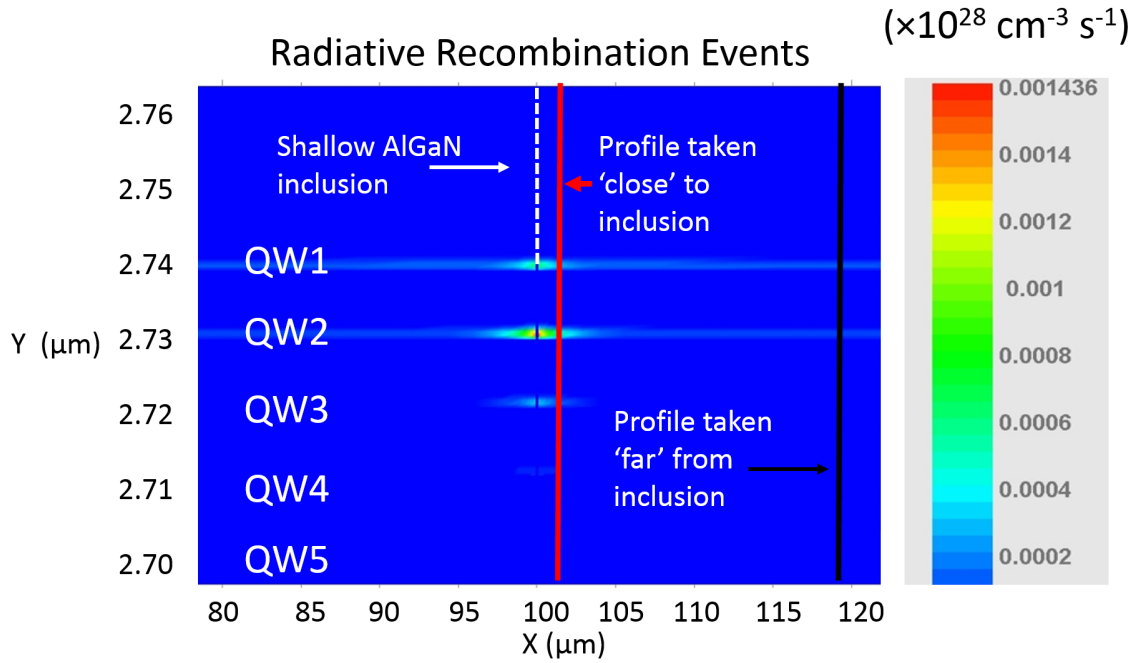

Fig. 3.28 APSYS simulation results: a) Radiative recombination events. The simulation parameters were as follows: p-GaN doping concentration: $3 \times 10^{19} cm^{-3}$, p-AlGaN EBL doping: $5 \times 10^{18} cm^{-3}$, AlGaN Al atomic percentage: 10 %, defect depth: 100 nm.

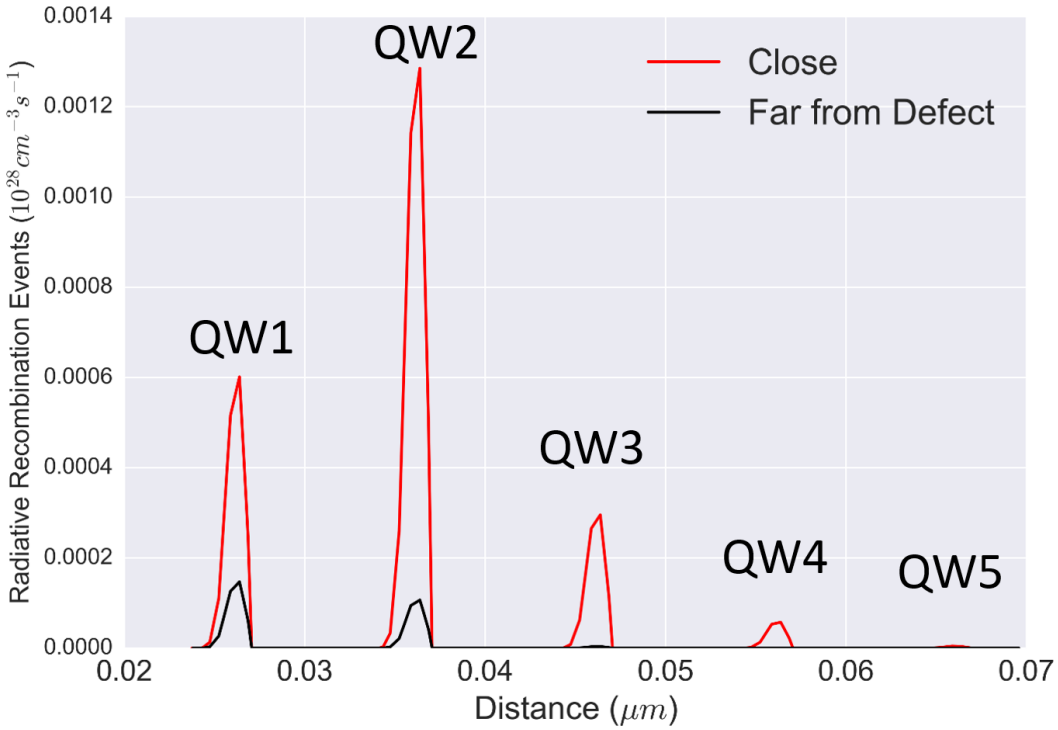

Fig. 3.29 APSYS simulation results: a) Radiative recombination events. The simulation parameters were as follows: *p*-GaN doping concentration: $3 \times 10^{19} cm^{-3}$, *p*-AlGaN EBL doping: $5 \times 10^{18} cm^{-3}$, AlGaN Al atomic percentage: 10 %, defect depth: 100 nm.

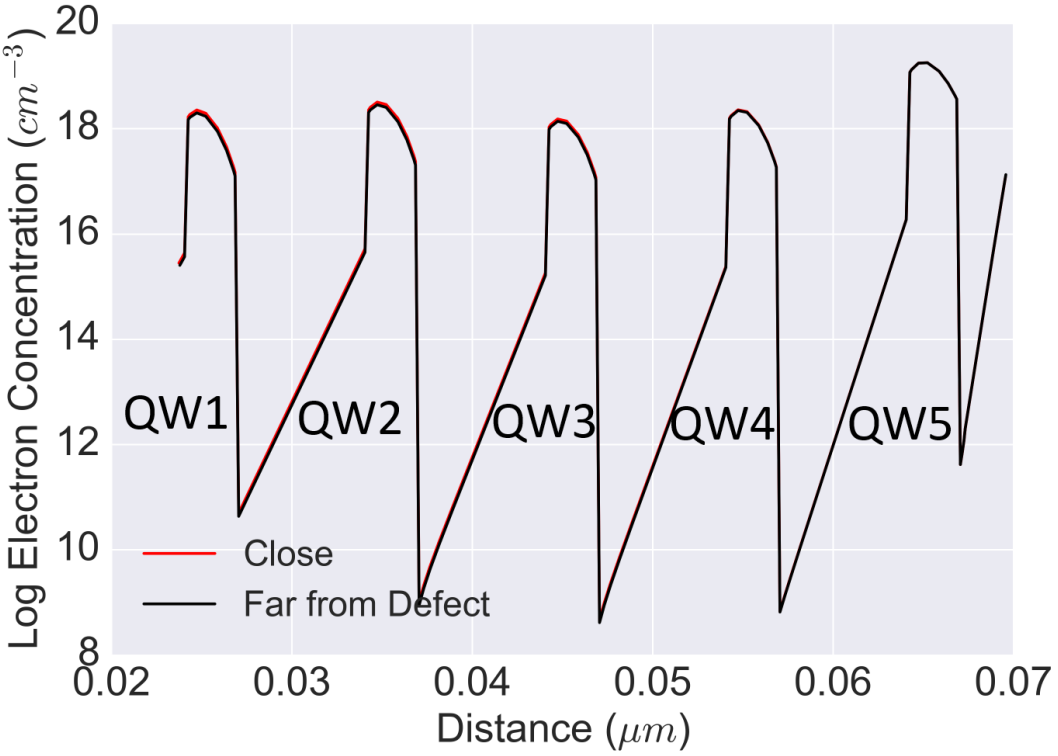

Fig. 3.30 APSYS simulation results: electron concentration. The simulation parameters were as follows: *p*-GaN doping concentration: 3 $\times 10^{19} cm^{-3}$, *p*-AlGaN EBL doping: 5 $\times 10^{18} cm^{-3}$, AlGaN Al atomic percentage: 10 %, defect depth: 100 nm.

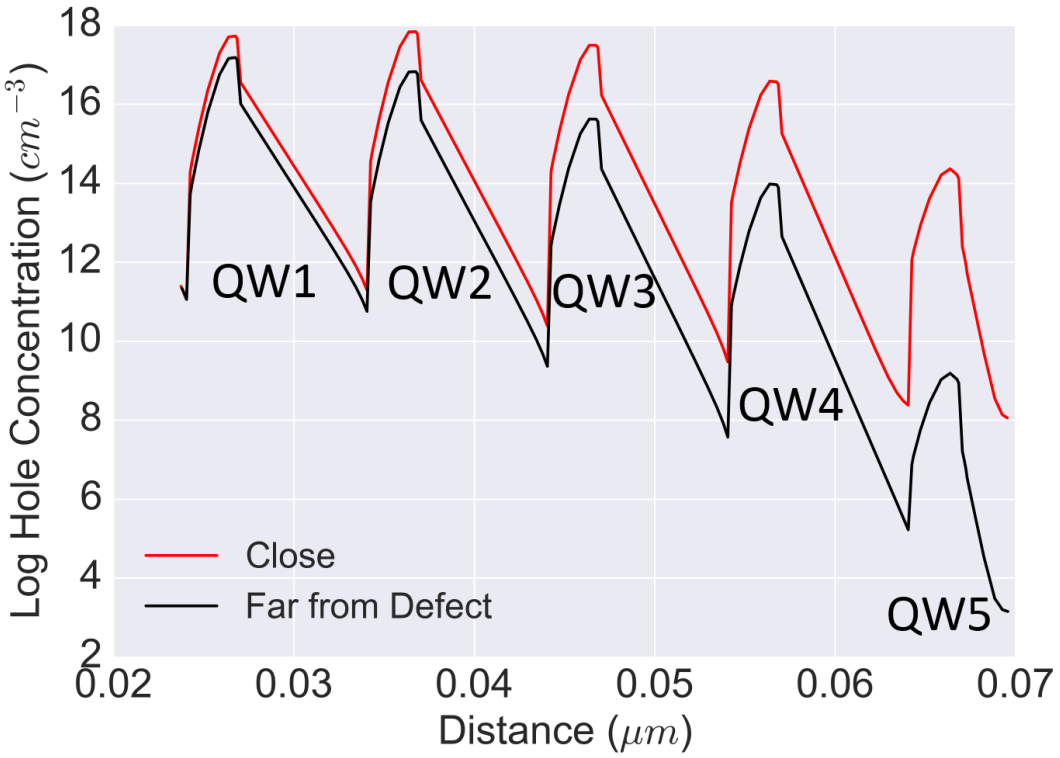

Fig. 3.31 APSYS simulation results: hole concentration. The simulation parameters were as follows: *p*-GaN doping concentration: $3 \times 10^{19} cm^{-3}$, *p*-AlGaN EBL doping: $5 \times 10^{18} cm^{-3}$, AlGaN Al atomic percentage: 10 %, defect depth: 100 nm.

In order to reconcile the results of the simulations with the EL data, we must consider that the EL data is extracted light from the LED, rather than the emitted light.. The simulated emission pattern suggests enhanced radiative recombination within approximately 5 μm of the hexagonal defect, however the hyperspectral EL data suggests a circular area of enhanced emission, as shown in Fig.3.5. Considering the critical angle for the light extraction from the surface of the LED due to Snell's law as shown in Fig.3.32:

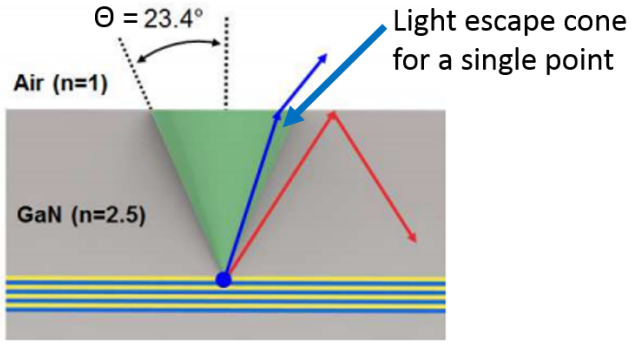

Fig. 3.32 Critical angle for an air/GaN interface [118].

We can see the extracted light is in fact a convolution of multiple light escape cones, as such despite the lack of emission from the hexagonal defect itself, we expect the EL data to appear as a singular bright area rather than a hollow area as depicted by the APSYS simulations. This is shown schematically in Fig.3.33.

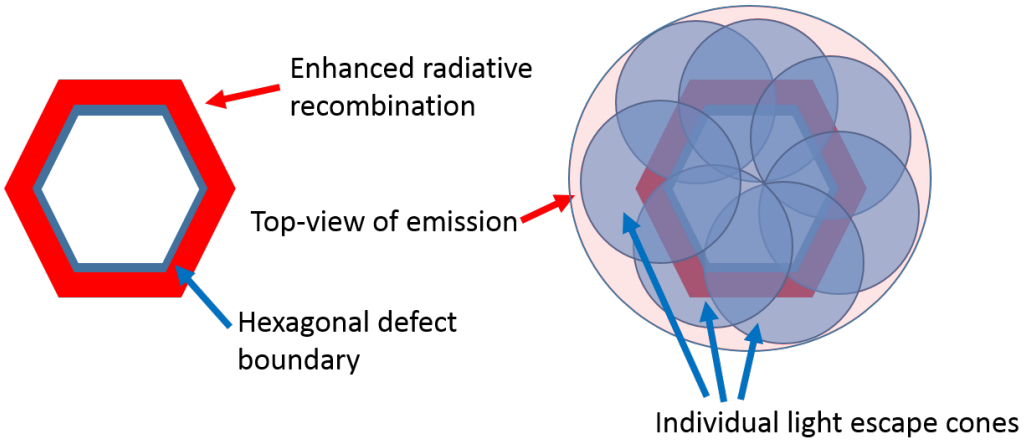

Fig. 3.33 Left: actual emission pattern surrounding the defect due to enhanced carrier injection. Right: Top-view of the emission: the hollow morphology is lost due to the convolution of multiple light escape cones surrounding the defect.

3.3.5 Origin of the Defect

In the previous sections we have established the cause of the inhomogeneous EL to be the presence of large hexagonal defects. However, it is also important to establish the origin of these hexagonal defects, as their elimination is the key to the production of LEDs with uniform emission, unlike those studied here.

3.3.5.1 Threading Dislocation Analysis

Hexagonal defects are typically associated with threading dislocations [119], as such we performed TEM on the FIB prepared lamella in order to observe threading dislocation associated with the hexagonal defects observed at the centre of inhomogeneities in the EL. The TEM image is shown in Fig. 3.34. Interestingly, rather than a single TD, we can observe a 'bundle' of dislocations associated with the defect with several 'loops' also apparent.

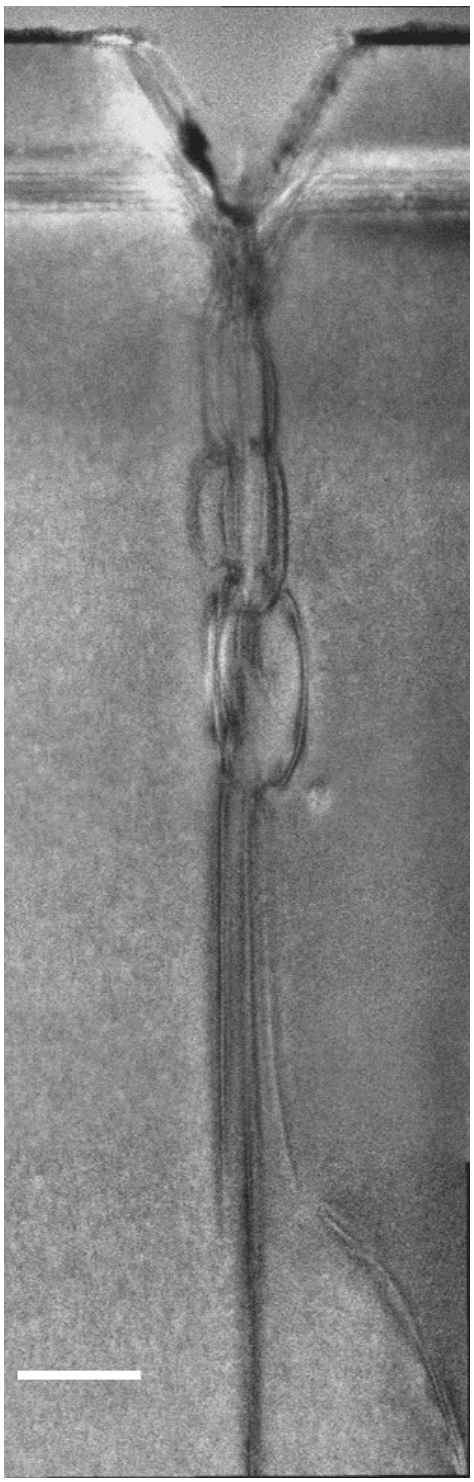

Fig. 3.34 TEM image viewed along the $(10\bar{1}0)$ direction of the dislocations associated with the hexagonal defect shown in Fig.3.18. The scale bar corresponds to a length of 200 nm.

In order to characterise the dislocations shown in Fig.3.34, WBDF-TEM was performed. The results are shown in Fig.3.35.

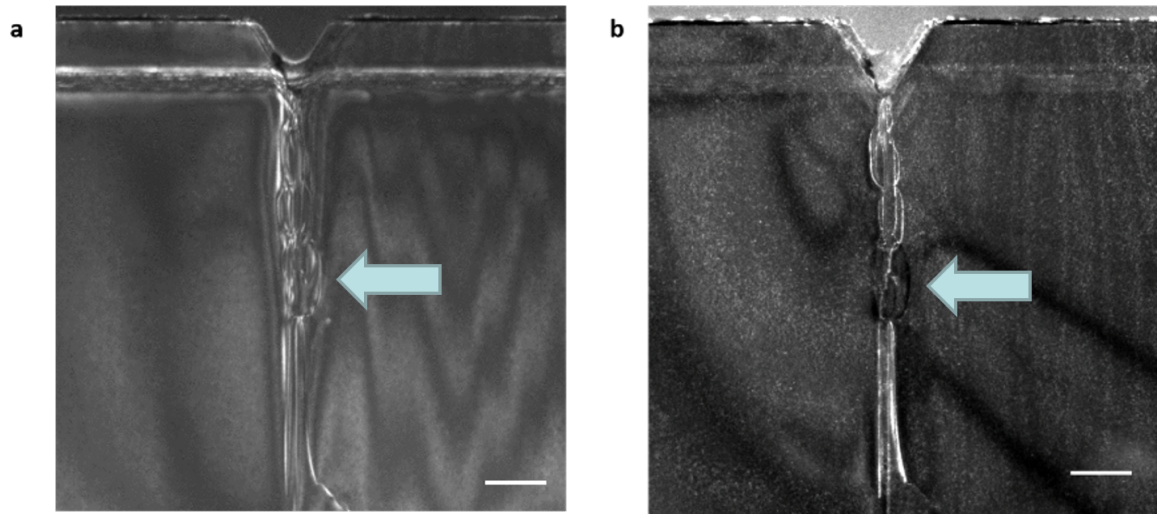

Fig. 3.35 WBDF-TEM of TDs associated with the hexagonal defect under a) **g**=$< 11\bar{2}0 >$ and b) **g**=$< 0001 >$. The scale bar corresponds to a length of 150 nm.

Fig.3.35 shows that the majority of TDs associated with the pit are mixed in nature, with some exceptions such as the 'dislocation loop' which shows no contrast under when viewed under the condition **g**=$< 0001 >$. Nonetheless, the number of TDs associated with a single defect here is astonishing.

The bundle of TDs observed here could potentially be attributed to the vertical side facets in GaN islands during the inital growth of the GaN template on sapphire. Datta *et al.* showed that threading dislocations associated with basal plane stacking faults are located at coalescence boundaries between two GaN grains, and can open up into hexagonal defects at the surface, as shown in Fig.3.36 [120]. In order to avoid GaN grains with vertical side facets, Datta *et al.* suggest initialising epilayer growth at a low V/III ratio or increased pressure as these conditions favour the formation of GaN islands with inclined side facets[121, 122], thus allowing TDs to bend laterally during film coalescence rather than propagate upwards towards the epilayer surface and form hexagonal defects.

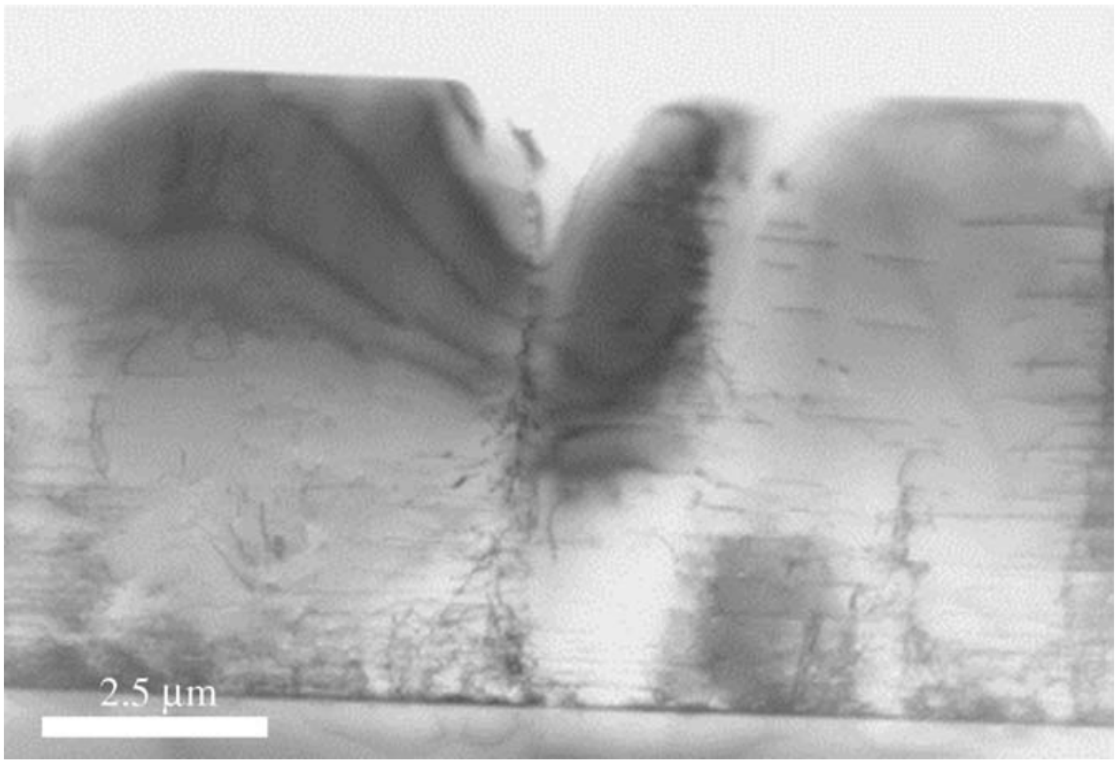

Fig. 3.36 BF-TEMimage of a coalescence boundary between two GaN grains and associated threading dislocations opening up into a hexagonal defect [120].

3.4 Conclusion

First and foremost we have utilised a host of microscopy techniques to identify the cause of inhomogeneous EL in III-nitride LEDs. Hyperspectral EL mapping was performed over a set of inhomogeneities in order to determine their spectral properties. Using this data, the inhomogeneities were established to be blueshifted and have a larger emission FWHM. Further current dependent EL-measurements revealed that the inhomogeneities exhibited emissive properties consistent with higher local carrier concentration.
SEM-based techniques were used to further elucidate the properties of the inhomogeneities. Panchromatic CL was used to reveal dark regions surrounding the inhomogeneities, as well as hexagonal defects at the centre of the inhomogeneities.
A FIB-based technique to deposit marker layers was used in order to produce a TEM lamella through the apex of a hexagonal defect at the centre of an inhomogeneity. This allowed for STEM-EDX mapping of the region surrounding the defect apex, revealing the presence of Al from the AlGaN EBL in the active region.
APSYS simulations were performed in order to examine the effect of AlGaN penetrating

within the active layer for both a 'deep' (penetrating all the way through to the *n*-GaN) and 'shallow' (penetrating down to only the first QW) inclusion. Both sets of simulations demonstrated that the *p*-doped AlGaN can indeed enhance local EL through the injection of holes into the active region, thus establishing the presence of *p*-doped material within the active region due to the hexagonal defect as a likely cause for the inhomogeneities observed. Conventional TEM techniques were used to observe a bundle of TDs associated with the hexagonal defect, establishing that the defects are likely due to sub-optimal template growth conditions. Datta *et al.* suggest the presence of TD bundles at coalescence boundaries can be ascribed to GaN grains with vertical side facets. As such, template growth in a low V/III ratio or increased pressure is necessary to encourage the formation of GaN islands with inclined $\{1\bar{1}01\}$ or $\{11\bar{2}2\}$ is necessary to avoid vertically propagating TD bundles [120].

3.5 Future Work

We have established the root cause of the EL inhomogeneity as the presence of hexagonal defects, however not all inhomogeneities observed in the panchromatic CL were associated with detectable defects in the SEM. This may be due to several reasons: the hexagonal defects may have 'filled' during the growth process, or are of much smaller size (<50 nm [107, 37]) and are thus not easily detectable due to the presence of the Ni/Au *p*-contact. Cross-sectional TEM of an inhomogeneity without a large defect at the centre may provide the answer to this question. The presence of the V-defects as 'leakage' pathways has been well supported in literature [116, 117], however it is possible the bundle of dislocations associated with the defect may provide additional leakage pathways. Conductive-AFM may serve to provide a clearer image of the conductive properties of the defects.

Chapter 4

Characterisation of III-Nitride Microdisk Cavities

4.1 Background

Microcavities possess particular optical properties, as discussed in section 1.2.2. Strongly-coupled cavities are crucial in accomplishing important quantum information processing tasks such as controlled coherent coupling and the entanglement of quantum systems [44]. Weakly-coupled microcavity systems have many applications in optoelectronic devices such as high efficiency, low threshold lasers [39]. Applications for both strong and weak coupling cavities are discussed in more detail in section 1.2.2.

Though various geometries for cavities exist, in this chapter we will specifically address III-nitride microdisk cavities. Microdisk III-nitride cavities have presented several challenges in terms of fabrication due to the chemical and thermal properties of GaN discussed in section 1.2.2.2. Currently, one of the most effective method for the fabrication of III-nitride microdisk cavities is PEC etching of an InGaN sacrificial superlattice (SSL) [14]. This in itself presents issues, as El-Ella *et al.* have shown that the growth of the InGaN SSL with a quantum dot (QD) layer can introduce dislocations into the structure [123]. Furthermore, PEC etching can be a difficult process to control as it is heavily dependent on conductivity and hence can be defect-selective [124–126] and dopant-selective [125], occasionally resulting in protrusions or roughness [14] on the etched underside of microdisk cavities which can heavily influence microdisk Q-factor [14]. The work contained in this chapter is a microscopy-based investigation into the structural properties of GaN/InGaN microdisk cavities.

4.1.1 PEC etching

As discussed in section 1.2.2.2, the ability to perform an effective 'undercut' is a crucial aspect in the fabrication of III-nitride microcavities. PEC etching is a commonly used technique to achieve an undercut microdisk and will be introduced here. PEC etching was first reported in III-nitrides by Minsky *et al.* [127], and is an extremely effective method to perform selective etching as it can be defect-selective and bandgap-selective. To achieve an undercut on a III-nitride microdisk the following set-up is typically used: a GaN filter is used to absorb light emitted by a Xenon lamp, allowing light of wavelength longer than 360nm to interact with the structure thus ensuring the majority of carriers are generated in the sacrificial InGaN layer. Holes generated by the incident light diffuse toward the surface of the InGaN layer which in this case acts as an anode whilst the electrons diffuse toward to the metal cathode due to both the overall potential in the connected cell and the band-bending occurring at the surfaces. This process is shown schematically in Fig.4.1.

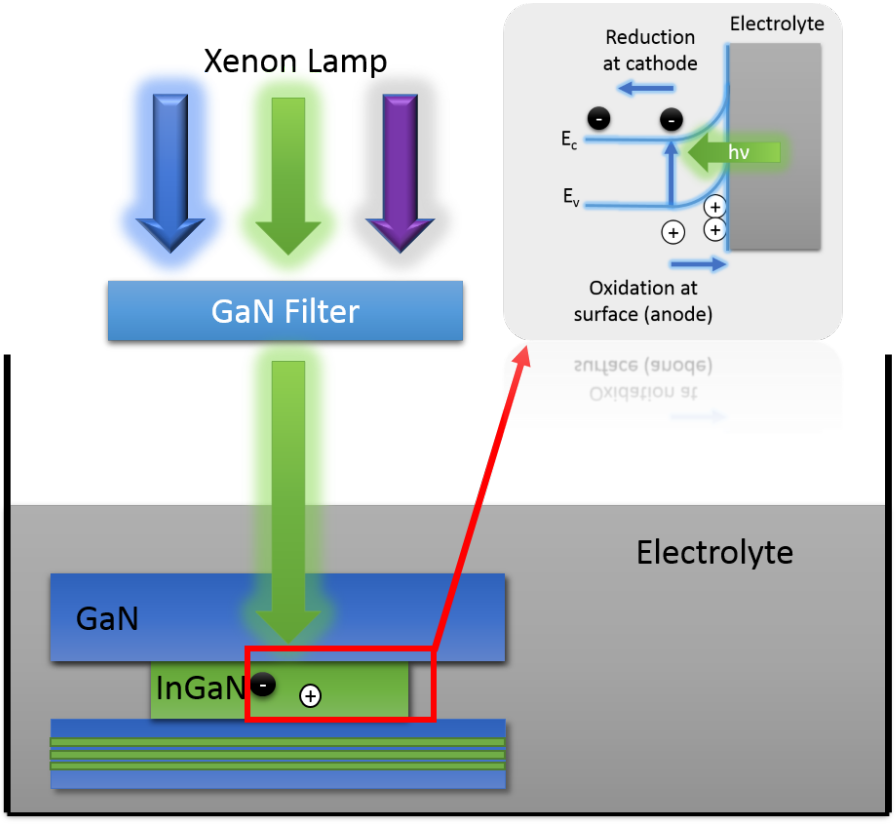

Fig. 4.1 PEC etching set-up, with the charge transfer process shown in the inset.

The excess concentration of holes at the sacrificial layer surface drives the oxidation of InGaN, forming Ga_2O_3, In_2O_3 and N_2, while at the cathode a reduction process is driven by

the excess electrons. The oxide generated by the reduction process is then dissolved in the electrolyte, thus etching the sacrificial layer. It is clear that the etch rate of the sacrificial layer is governed by several factors: the rate of generation of the photo-generated electron hole pairs, their diffusion rates towards the anode or cathode, and the concentration of the electrolyte (HCl in this case). It is due to this photo-generated carrier concentration dependence that the PEC etching process is defect and dopant selective.

4.1.2 Whisker Generation in PEC Etching

Youtsey *et al.* demonstrated the ability of dislocations to hinder the progress of PEC etching and used this to determine the dislocation density of n-type GaN films. Unetched material (or 'whiskers') remained at dislocation sites after the PEC etching process due to the electrically active nature of dislocations in GaN, as shown in Fig. 4.2.

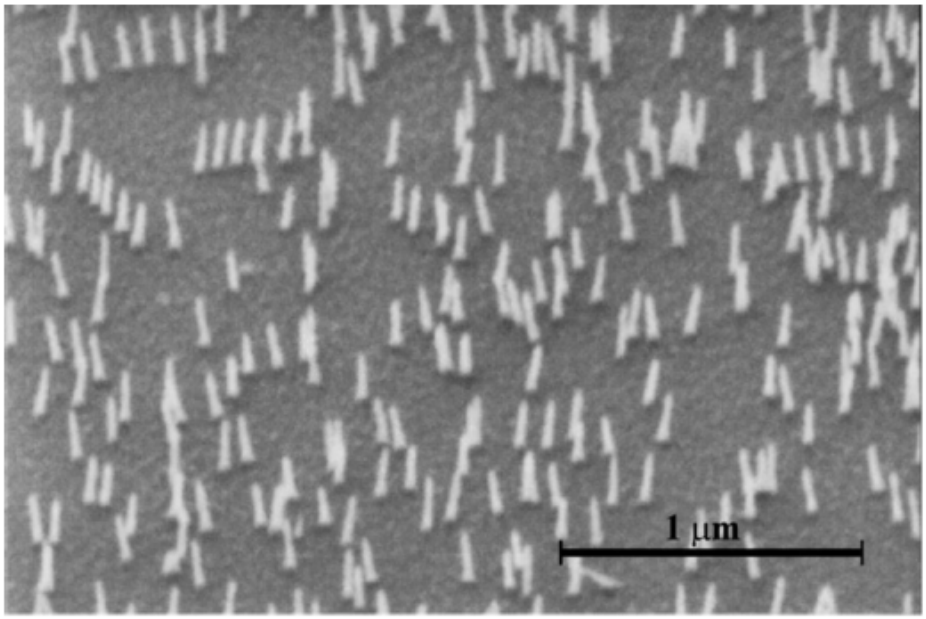

Fig. 4.2 SEM image of whiskers produced by etching of dislocations in an MOCVD GaN film grown on a silicon carbide (SiC) substrate. Reproduced from [125]

It was confirmed through cross-sectional TEM that both mixed and edge dislocations result in the formation of whiskers [126].
The mechanism through which the presence of dislocations impedes the PEC etching process relates to the charge trapping property of TDs: it has been suggested based on cathodoluminescence (CL) studies that TDs act as non-radiative recombination centres, as mentioned in section 1.1.4.2. In this case, photogenerated holes in the vicinity of TDs would be prevented

from diffusing to the epilayer surface thus resulting in unetched material. There is also evidence for negatively charged TDs in n-type GaN [128], which could lead to hole-trapping at TDs presenting an alternative or additional explanation for the reduction in surface hole concentration and thus reduced etch rate in areas adjacent to TDs [126].

4.1.3 Q-factor Reduction in Microdisks

El-Ella *et al.* first demonstrated the effect of dislocations on the Q-factor of GaN microdisks containing an InGaN QD active layer. By carefully controlling the In compostion of the SSL, the authors were able to produce two sets of microdisks, one with a dislocation density of $3 \times 10^9 cm^{-2}$ (sample A) and the other with a lower density of $7 \times 10^8 cm^{-2}$ (sample B). As expected, microdisks fabricated from sample A exhibited a larger density of whiskers on the underside of the disk. SEM was used to establish that 90% of disks fabricated from material A exhibited whiskers, compared to only 20% of disks fabricated from structure B. The difference between the two samples in terms of Q-factor is illustrated in Fig.4.3 which includes data for eight microdisks fabricated from each sample.

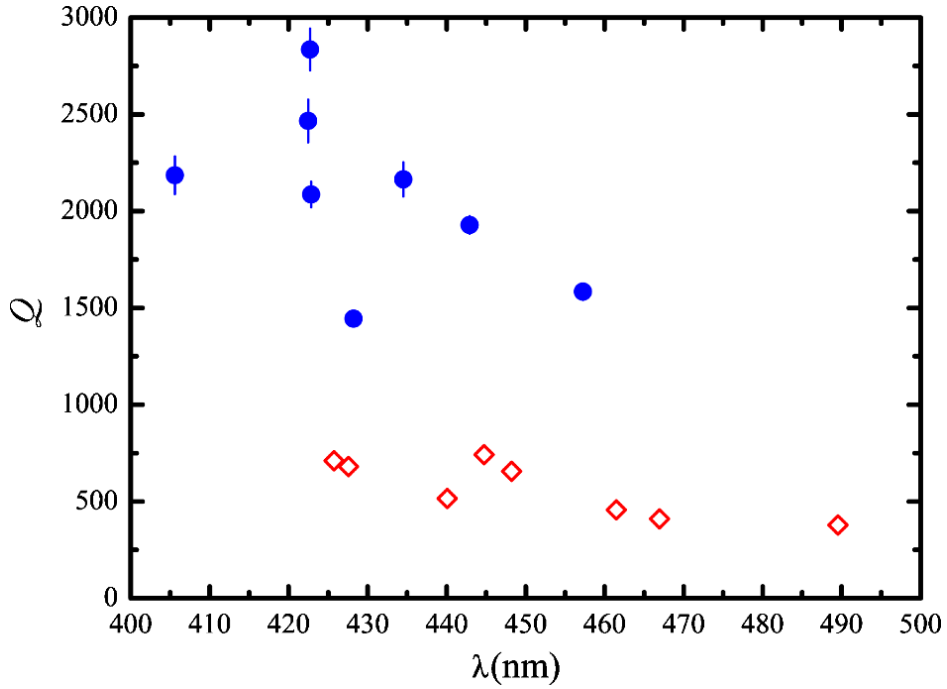

Fig. 4.3 Q values from eight modes of microdisks fabricated from structure A(◊) and B ((•). Reproduced from [129].

All microdisks fabricated from sample B show a larger Q-factor than all microdisks from sample A. The average Q-factors for microdisks fabricated from samples A and B were

600 and 2000 respectively, suggesting a strong correlation between Q-factor and dislocation density [129].

Puchtler *et al.* addressed these issues by identifying not only the number but also the position of TDs in individual microdisk cavities and evaluating the effect of these parameters on microdisk Q-factors[14]. Unlike the study by El-Ella *et al.*, this work correlated the performance of each individual device structure with its specific structure. In this study, dark spots in CL images (arising from non-radiative recombination as discussed in section 1.1.4.2) were used as a signature for the presence of dislocations, and hence whiskers.

The authors established the correspondence of dark spots in the CL to whiskers by comparing plan-view panchromatic CL images with side-view SEM images of the microdisks. The results of these correlative measurements are shown in Fig.4.4.

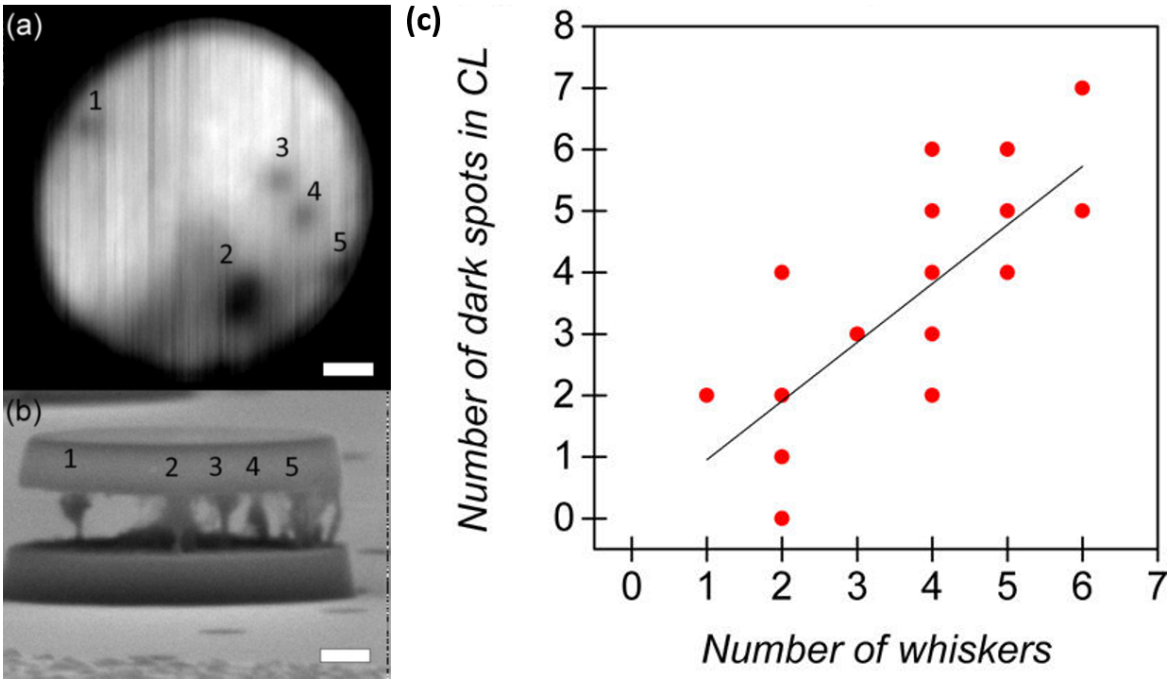

Fig. 4.4 a) Sample plan-view CL b) Corresponding side-view SEM image of an undercut microdisk with whiskers corresponding to the dark spots shown in a). c) Relationship between whiskers on the underside and dark features counted in plan-view CL. Adapted from [14].

Following this, the authors reported the correlation between dislocation number and position and Q-factor extracted from the modal peaks in micro-PL. Whilst dislocation number and microdisk Q-factor were shown to be inversely correlated, this was found to hold true only for dislocations located at a distance > 0.4 μm from the centre, suggesting only dislocations located within the outer-periphery of the microdisks (where the WGMs

are confined as discussed in section 1.2.2.2) have an effect on Q-factor. These results are summarised in Fig.4.5.

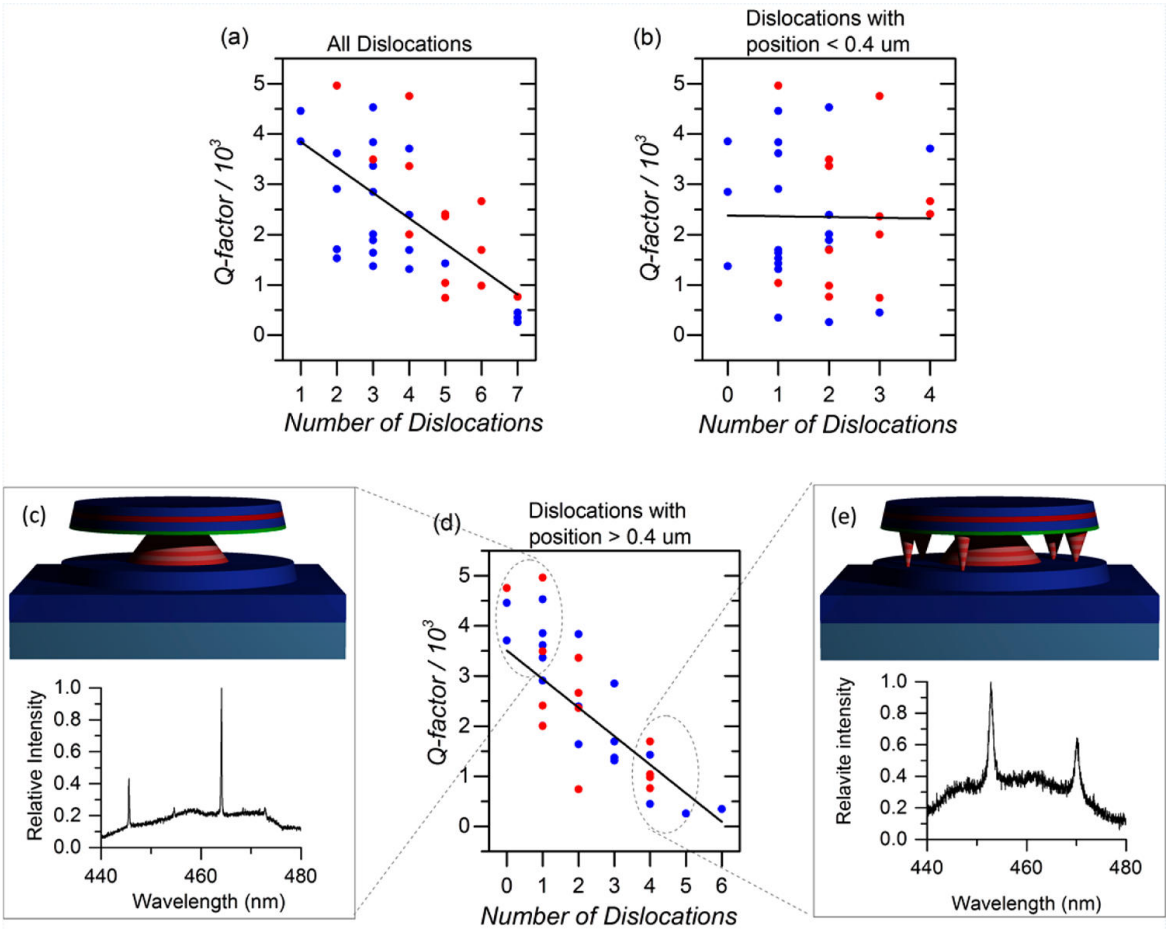

Fig. 4.5 a)Microdisk Q-factor vs. threading dislocation number for radial positions: a) 0- 0.6 μm b) < 0.4 μm d) >0.4 μm for QD (blue) and QW (red) containing microdisks. c) and e) show a schematic of, and representative PL spectrum taken from microdisks of low and high dislocation number in the periphery of the disks. Reproduced from [14].

The mechanism behind the deleterious effect of TDs on Q-factor were investigated by Puchtler *et al.* through the use of finite difference time domain (FDTD) simulations [14]. The presence of a whisker on the underside of a microdisk was simulated as a pyramidal protrusion with a range of dimensions and positions on the underside, producing results which suggest the Q-factor of the first order WGM decreases as the position of the whisker approaches the periphery of the microdisk and provides a radiative pathway for light confined in this region to escape [14]. The results of these simulations are shown in Fig.4.6.

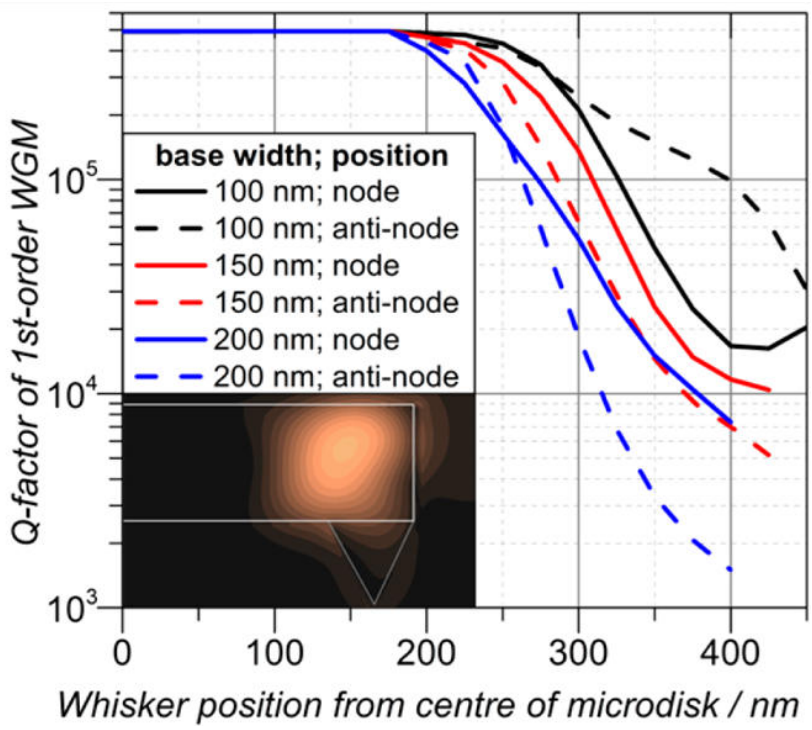

Fig. 4.6 Effect of radial position on the influence of a whisker on microdisk Q-factor. The whisker was simulated as a pyramid with a height of 150 nm and base widths of 100, 150, and 200 nm. The inset shows a side-on view of the field profile for a whisker located at the edge of the microdisk: light leaks into the whisker region and is radiated, thus introducing loss in the cavity. Reproduced from [14].

TDs have been shown to increase impurity levels at dislocation cores and in an extended region affected by their associated strain field during sample growth. TEM studies of dislocations have revealed strain related changes in doping occuring on the scale of several nanometres[130, 131]. Threading dislocations can also have associated vacancy states giving rise to 'yellow-band' optical transitions, though these are far away from the wavelength range of III-nitride cavities [132, 133]. In considering the impact of these factors on absorption in the micodisk, Puchtler *et al.* reported no significant effect on cavity Q-factor for linear attenuation coefficients up to $10^9 cm^{-1}$ (several orders of magnitude greater than the expected value for highly doped GaN [134]) associated with dislocations modelled as a cylinder of radius 4 nm.

4.2 Microdisk Characterisation

In this section we will report on the experimental microscopy work performed on microdisks. A FIB based lamella preparation method was developed in order to prepare TEM samples from the microdisks, allowing for the observation of a dislocation in a whisker from the underside of a microdisk as well as the characterisation of the microdisk active region. Furthermore, FIB tomography experiments were performed on the microdisk, allowing us to further characterise the structural properties of the microdisks.

4.2.1 Samples

Samples for this study were grown on *c*-plane GaN on a sapphire substrate. The active layers of the structure consist of three InGaN layers(QW or QD) in a 200 nm cavity membrane grown above a SSL $In_xGa_{1-x}N/In_yGa_{1-y}N$ where x = 0.005 and y = 0.065. The purpose of the alternating In composition SSL is to confine carriers generated during the PEC process into localised regions. An unmodulated In composition would result in the separation of electron-hole pairs due to the inherent polarization fields present in InGaN, resulting in asymmetric etching [123]. The bottom of the microdisk membrane contains 20 nm $Al_{0.2}Ga_{0.8}N$ layer which restricts the photo-generated carriers from the PEC process within the SSL, acting as an etch stop during undercutting and reducing damage to the microdisk membrane. The SSL is grown on a 500 nm *n*-GaN layer which provides a highly conductive pathway for photo-generated carriers to be removed by propagating to an electrical contact. A schematic of the structure following the PEC undercut is shown in Fig.4.7.

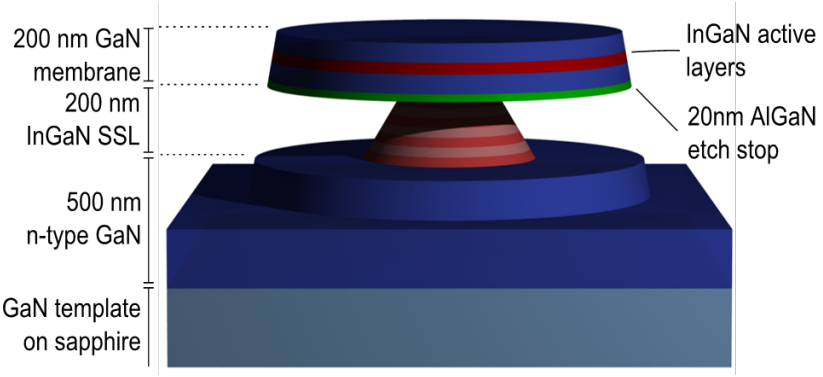

Fig. 4.7 Schematic of the microdisk structure. Courtesy of Dr. T. Puchtler.

4.2.2 Whisker Analysis

In sections 4.1.2 we have discussed the manner in which dislocations hinder the PEC etching process and cause the formation of 'whiskers' on the underside of microdisk. Furthermore we have addressed the deleterious effect of these whiskers on microdisk Q-factor in section 4.1.3. In this section we will present FIB/SEM techniques developed in order to produce TEM lamellae from delicate structures such as microdisks which have allowed for the direct observation of a TD in a whisker from a microdisk using TEM.

4.2.3 FIB/SEM Sample Preparation

The microdisks studied here were found to be extremely sensitive to ion-beam damage during Pt deposition, even with a protective electron beam Pt layer deposited first. As such for the preparation of delicate structures it is key to restrict the usage of the ion-beam as much as possible.
In order to isolate a whisker on the underside of a microdisk for TEM examination, a target whisker is identified, and the sample is rotated in the FIB/SEM chamber to ensure optimal whisker orientation with respect to the TEM lamella, as shown in Fig.4.8.

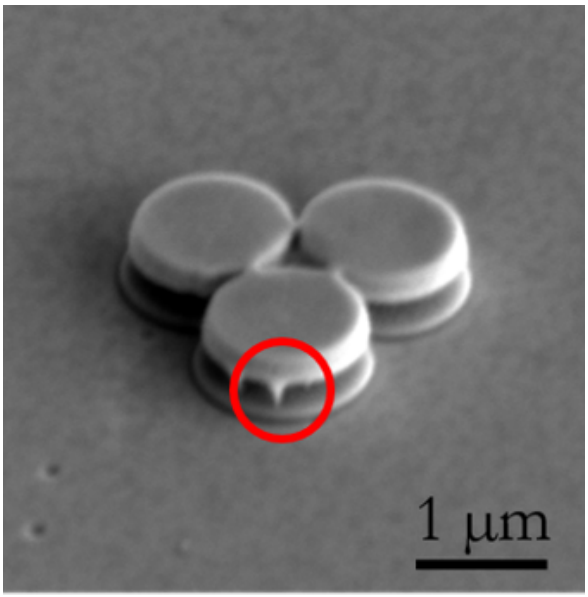

Fig. 4.8 SEM micrograph taken at 3 kV and 0.16 nA of a PEC undercut microdisk with a whisker circled in red.

A thick (approx. 2 μm) protective layer of electron beam Pt is deposited on the surface of the microdisk. It is crucial to avoid using the ion-beam in this step to deposit Pt due to the fragility of the thin microdisk membrane (< 300 nm). An additional benefit in using

electron-beam deposited Pt is the superior contrast provided between the protective layer and the microdisk in the SEM image. A standard FIB-lift out process is then applied to the sample, taking care to ensure the position of the whisker at the end of the lamella where the Omniprobe^{TM} is attached to the sample. The thinning process is then carefully monitored to ensure it is halted before milling the whisker away. As the whisker itself provides a clear marker for the thinning, the process described in section 3.3.3.3 is not required to ensure precise thinning. Typical FIB-prepared TEM lamellae sample thicknesses lie in the 100 nm range [97], as such the initial positioning and monitoring of the whisker are crucial to the successful preparation of the sample. Images of the entire process are shown in Fig.4.9

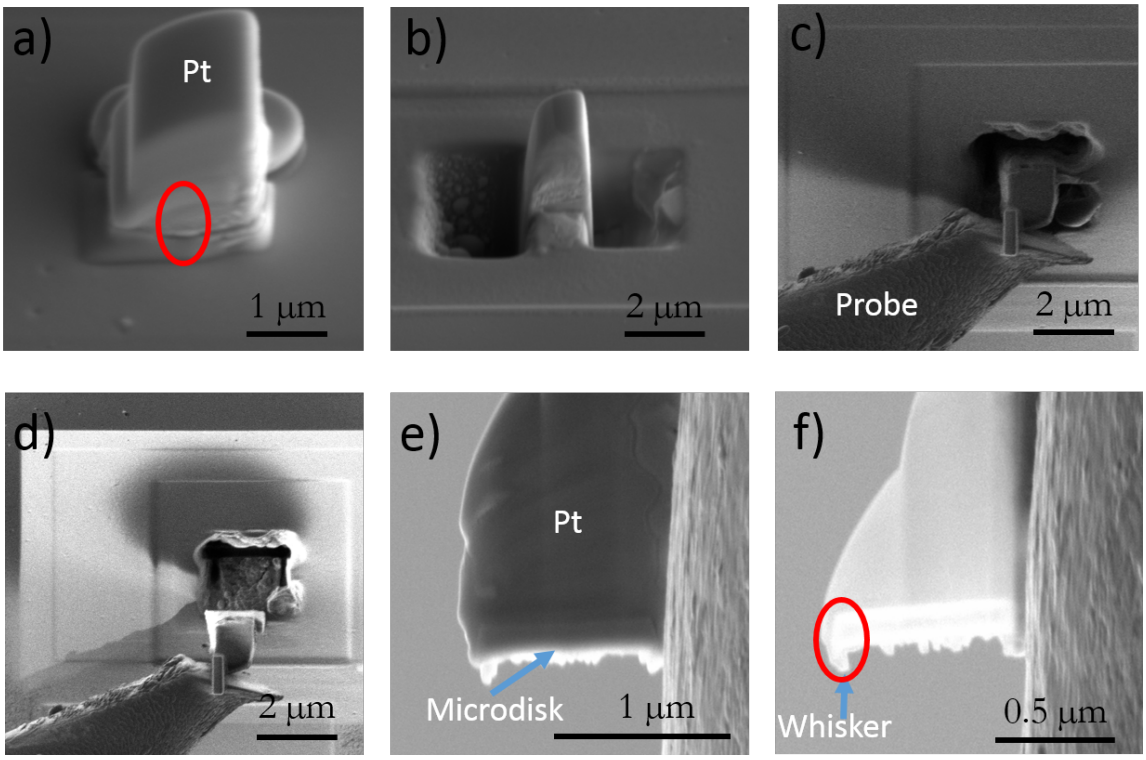

Fig. 4.9 Whisker lift-out process: a) SEM electron beam deposited platinum with the approximate position of the whisker as shown in Fig. 4.8 circled in red b) milling of trenches by ion beam c)ion-beam image taken after attaching the lift-out probe to the sample using ion-beam deposited Pt and of d) sample release and lift-out e) SEM image of the initial stages of thinning and f) the final stages of thinning with the whisker visible (red ellipse).

4.2.4 STEM

Following the successful preparation of a TEM lamella, the sample was characterised using STEM-HAADF and BF-STEM. Fig.4.10. shows the presence of a threading dislocation

running through the whisker, as well as damage induced by the ion-beam thinning process, illustrating the fragility of the microdisk membrane.

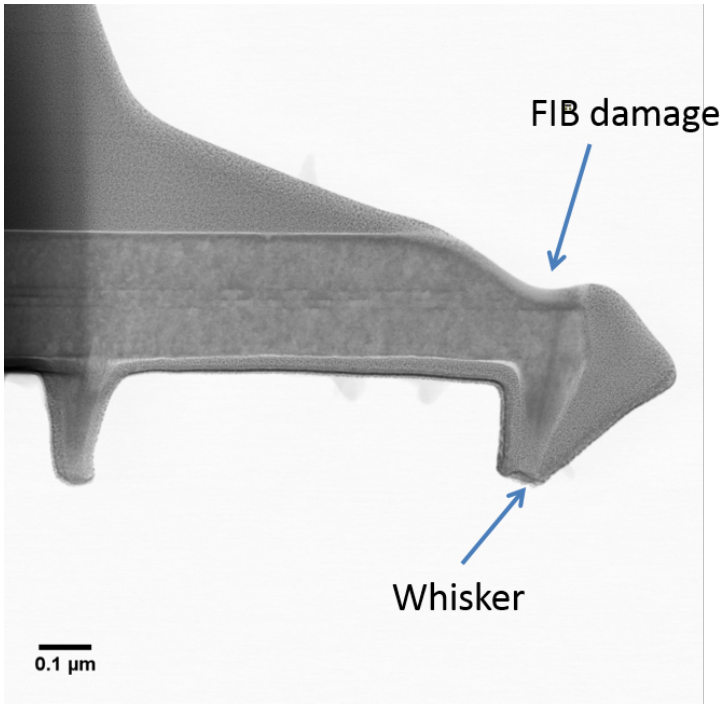

Fig. 4.10 Low magnification BF-STEM of the whisker.

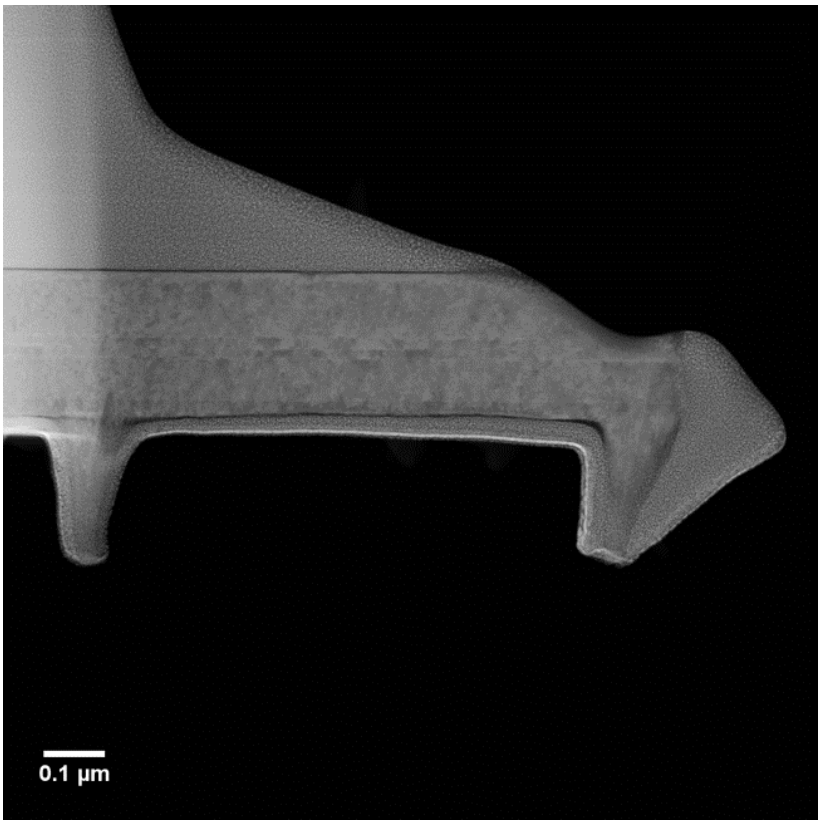

Fig. 4.11 Low magnification DF-STEM of the whisker.

A higher magnification BF-STEM image of the dislocation is shown in Fig.4.12, with the dislocation highlighted with a red arrow.

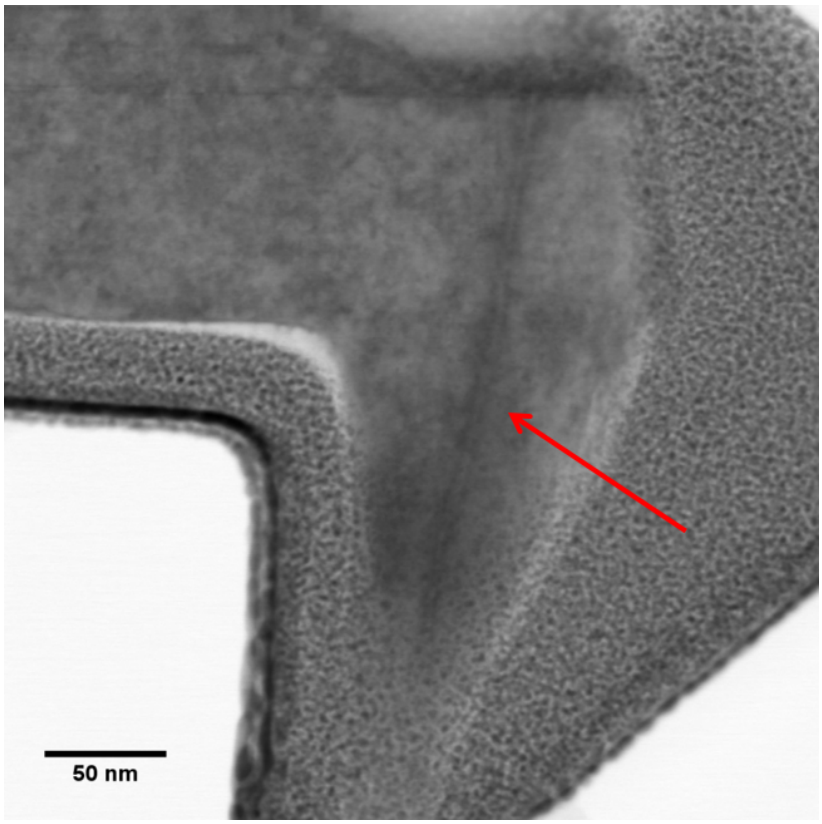

Fig. 4.12 High magnification BF-STEM of the whisker, the red arrow points to the dislocation.

4.2.5 WBDF-TEM

The dislocation was characterised using the WBDF-TEM technique described in section 2.1.1.3. The results are shown in Fig.4.13. The TD observed here is shown to be a pure edge type dislocation, as shown by the bright constrast produced by the TD when activating **g** = $< 11\bar{2}0 >$ (Fig.4.13.a.) which is absent when activating **g** = $< 0002 >$(Fig.4.13.b.).

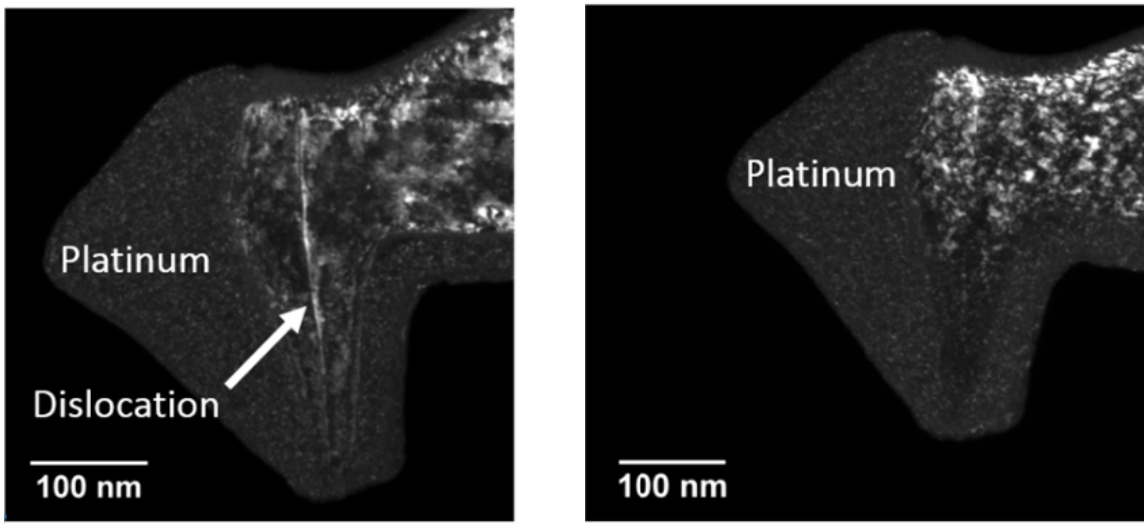

(a) (b)

Fig. 4.13 a)WBDF activating $\mathbf{g} = < 11\bar{2}0 >$ b) WBDF activating $\mathbf{g} = < 0002 >$. The dislocation is only visible along the direction, confirming its nature as a pure edge dislocation.

These results are the first direct observation of a dislocation within a whisker on the underside of a dislocation. It is expected that mixed, edge and pure dislocations all result in the formation of whiskers under PEC etching [126, 135].

4.2.6 Active Region Analysis

The ability to fabricate TEM lamella from microdisks allows unique insight into not only defect-induced whiskers, but also the composition and structure of the active region of the microdisk. In order to demonstrate this we fabricated a TEM lamella from a microdisk with a structure described by Fig.4.7, where the active region consists of 3 x InGaN QD layers.

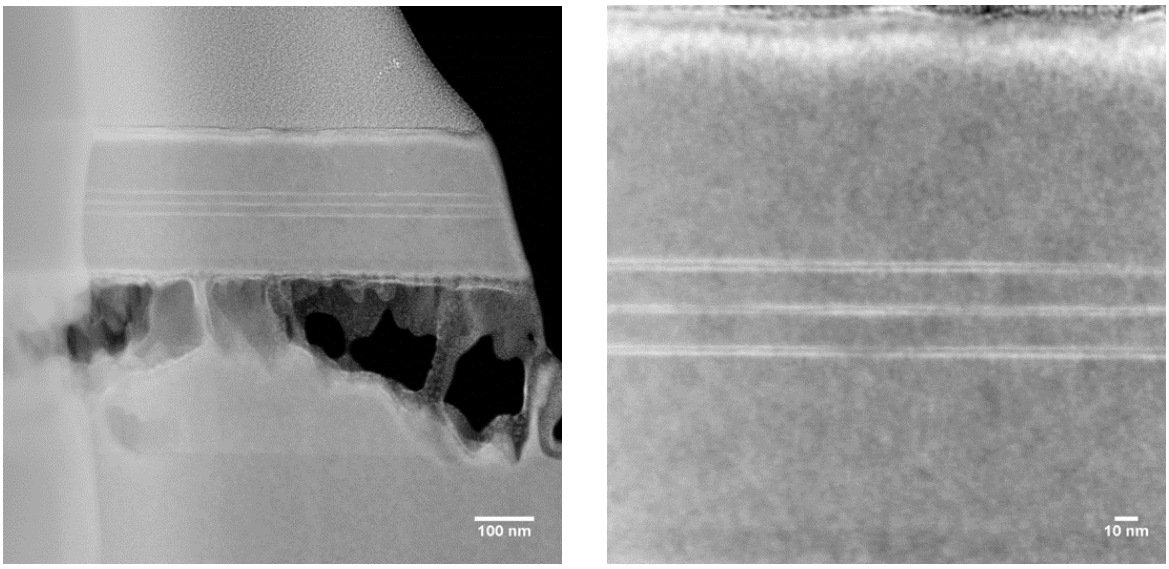

(a) (b)

Fig. 4.14 a)STEM-HAADF image of a microdisk lamella produced with the membrane, SSL pedestal and *n*-GaN layer and b) higher magnification image of the InGaN active region.

Fig.4.14.b. shows the apparent 'splitting' of the InGaN QD layers. Compositional mapping was performed to examine the splitting of the layers using EDX and is shown in Fig.4.16a. and 4.16b.
Fig.4.16.b. shows the In composition reaches close to 0 in between the split lines of the QD containing layer, with a split spacing of approximately 2.5 nm, indicating the layer is close to fully split. As such, the fabrication of TEM lamellae from processed microdisks allows for detailed insight into the structure and composition of the active regions of microdisks providing the potential for correlated measurements between the optical and structural properties of the microdisks. We note this splitting is observed in unprocessed samples and is thus unlikely to occur due to the microdisk fabrication process.The splitting of the InGaN layers may be linked to the modified droplet epitaxy (MDE) method used to grow the InGaN QD layers whereby an InGaN epilayer is made to undergo partial decomposition using an annealing step which leads to the formation of indium droplets and a floating indium layer prior to the growth of the GaN cap [136]. Indeed, Massabuau *et al.* have shown that under certain growth conditions an InGaN QW layer can result in an 'InGaN tail' present in the surrounding QB due to an indium adatom segregation effect [137]. We suspect the incorporation of this floating indium layer may lead to the splitting of the InGaN layers shown here, though this process is still not well understood and beyond the scope of this chapter. Nonetheless, the presence of the QDs in these microdisks was confirmed utilising

micro-PL and the microdisks exhibited well defined modes despite the splitting of the InGaN layer [14].

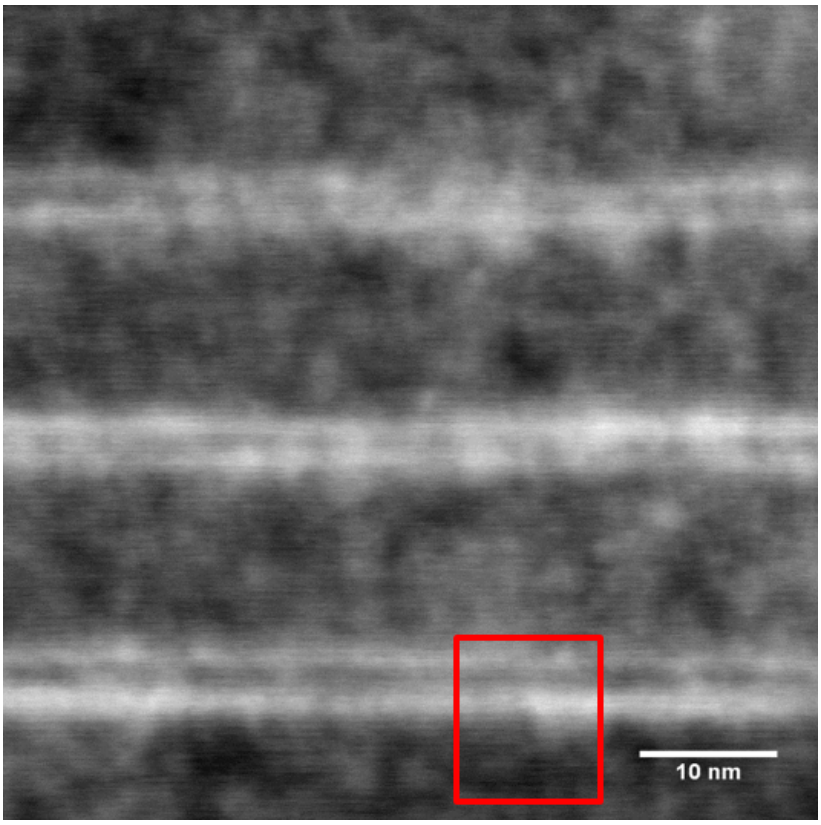

Fig. 4.15 STEM-HAADF of the active region of the microdisk (scale bar = 10 nm).

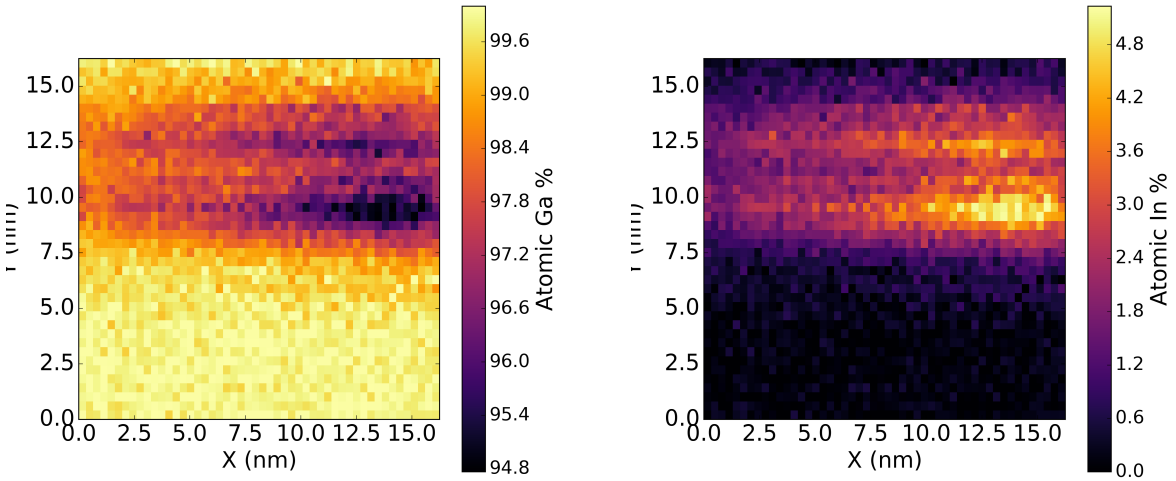

(a) (b)

Fig. 4.16 a) Ga atomic percentage b) In atomic percentage.

4.2.7 FIB Tomography

The mechanism of the PEC etching process causes etching to occur in the presence of photogenerated carriers, as discussed in section 4.1.1. In the case of microdisk membranes containing an InGaN active region the PEC etching process can damage the active region, even with the incorporation of an AlGaN etchstop as discussed in section 5.2. Beyond potential damage from the PEC etching process, microdisk sidewall and underside roughness can be sources of scattering losses and Q-factor reduction in cavities [14]. FIB tomography provides an easy albeit destructive method of mapping the 3-D morphology of microdisks, potentially providing insight into both issues mentioned above.

The microdisks chosen for this tomography study are shown below in Fig.4.17. The damage caused by the PEC etching process to the microdisk membrane is highlighted, as well as the presence of roughness on the underside of the microdisk which is the result of an incomplete PEC etching process.

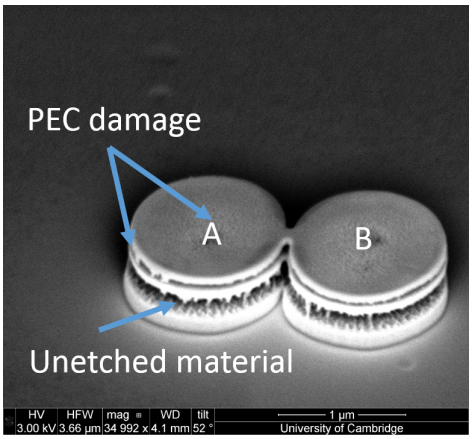

Fig. 4.17 SEM image of two microdisks exhibiting damage due to the PEC etching process.

As discussed in section 2.6.2,a protective layer of electron-beam deposited carbon is deposited first on the microdisks as it provides greater contrast with the GaN microdisk in the secondary electron image. Following this, a Pt layer is deposited to provide further protection. An SEM image taken in cross section during the FIB tomography process of the microdisks shown in Fig.4.17 is shown in Fig.4.18.

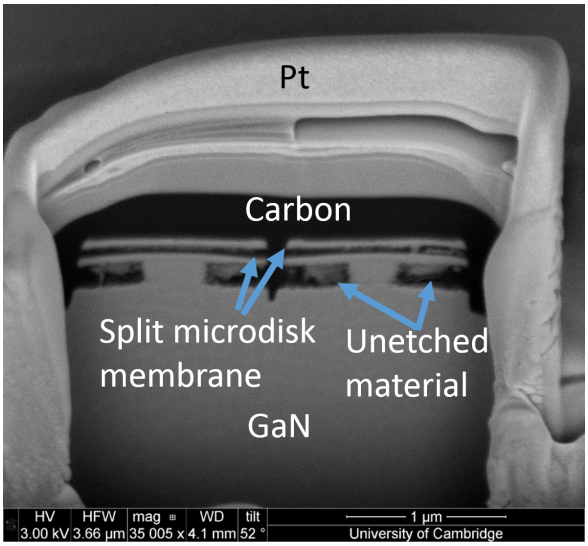

Fig. 4.18 SEM image of a cross-section of the microdisks shown in Fig.4.17.

FIB milling in order to 'slice' the sample was performed at 10 nm step thickness. The reconstruction was performed for the microdisk denoted 'B' in Fig.4.17. Snapshots of the 3D reconstruction are shown in Fig.4.19. The FEI Helios Nanolab showed poor stability throughout the acquisition, as such a complete series containing the microdisk could not be

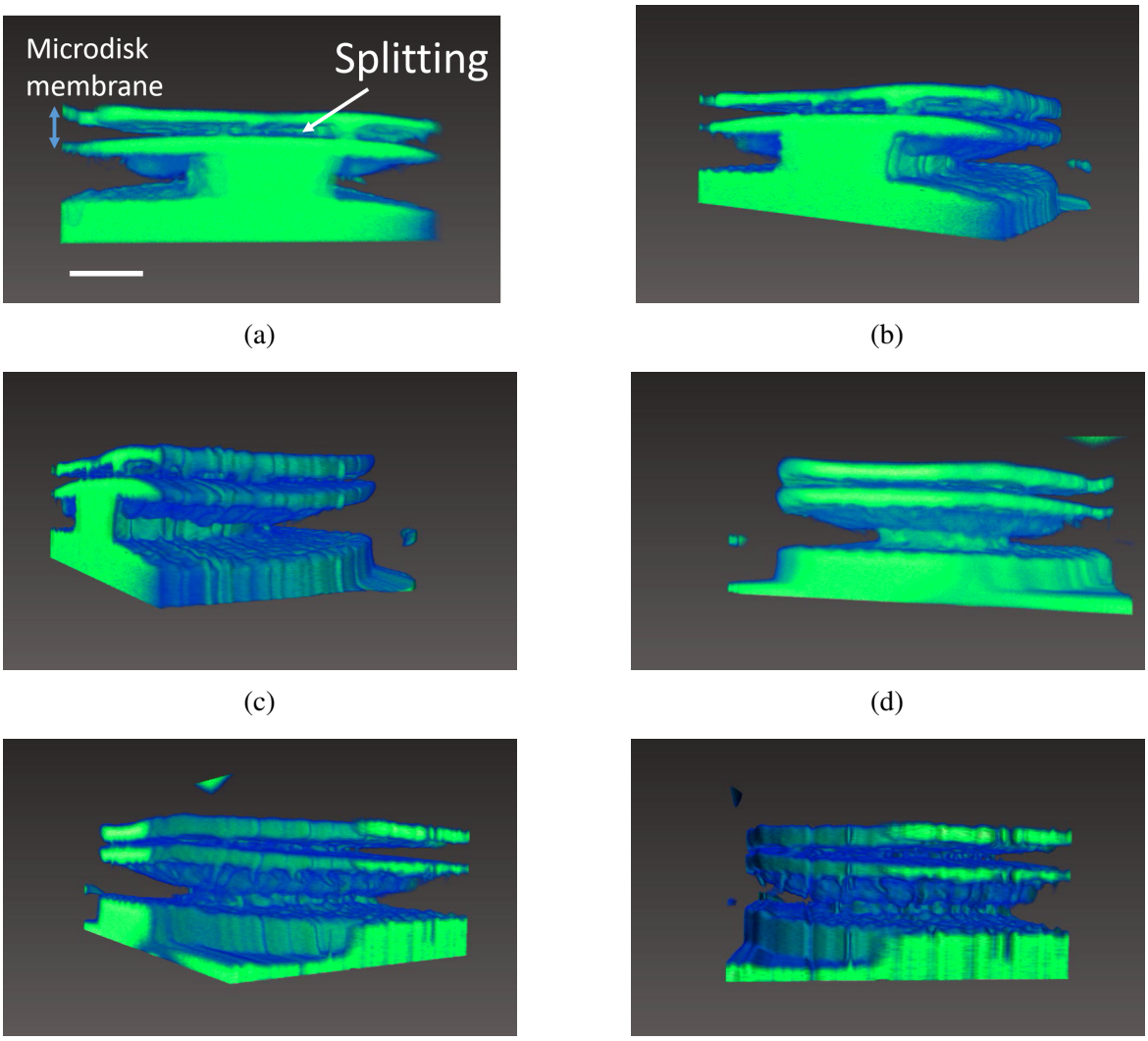

Fig. 4.19 Tomographic reconstruction for microdisk 'B'.

acquired. The datasets were aligned using Avizo 7, which includes stretching in order to compensate for the acquisition angle for the SEM images.

4.2.8 Mesh Roughness Analysis

In order to perform quantitative analysis of the microdisk, the image stack generated through the tomography experiment was reconstructed into an isosurface through the use of a marching cubes algorithm [101] implemented in the scikit-image python package. The algorithm generates a surface from a triangular mesh, thus allowing us to access information concerning the surface of the microdisk down to the resolution of the SEM images in x-y plane, and the

slice thickness in the z-direction. In this set of images the pixel size in each image is 1.2 nm, and the slice thickness is 10 nm.
Reconstruction using scikit-image allows us to access specific parts of the microdisk. In this instance we are interested in the top portion of the 'split' microdisk membrane. Fig.4.20 shows a reconstruction of this region.

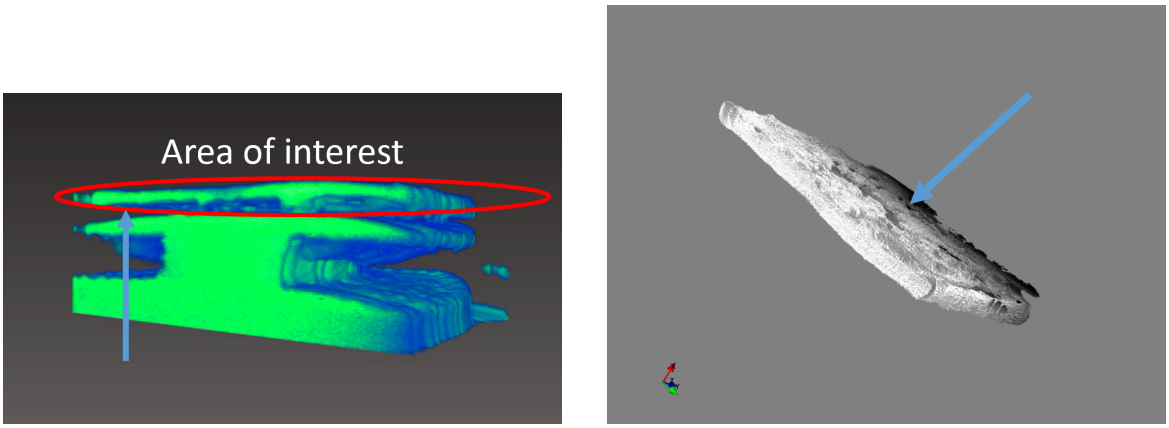

(a) (b)

Fig. 4.20 a)Target volume b) Isosurface reconstruction of the top portion of the microdisk membrane. The blue arrow indicates the same surface and direction in both images.

Fig.4.21 shows a top view of the reconstructed membrane, demonstrating the sub-optimal stacking of the image slices as the perimeter of the microdisk membrane seems distorted from it's expected circular shape. A certain amount of 'roughness' in the microdisk can be seen on the surface.

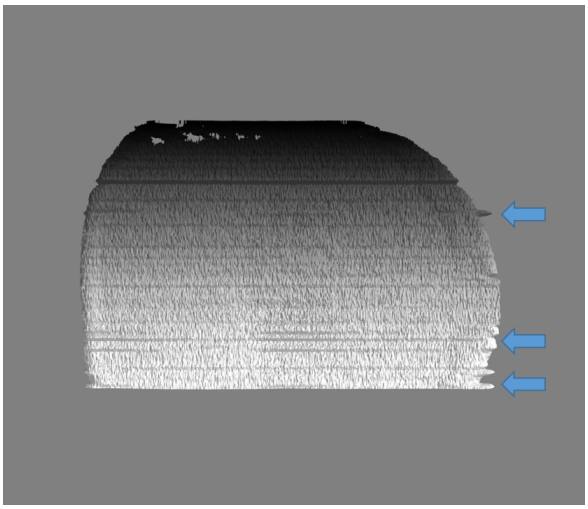

Fig. 4.21 Top view of the reconstructed isosurface. Blatant stacking errors are denoted by blue arrows.

In order to quantify this roughness, we utilise a method described by Vartak *et al.* [138]. The triangular mesh generated by the marching cubes algorithm is composed of triangles represented by vertices. As such, the cross product of any two of vectors between two vertices gives the normal vector of the triangle such that:

$$\mathbf{A} \times \mathbf{B} = |A||B|sin(\theta)\mathbf{N} \tag{4.1}$$

where θ is the angle between the two vectors **A** and **B** This is shown schematically in Fig.4.22.

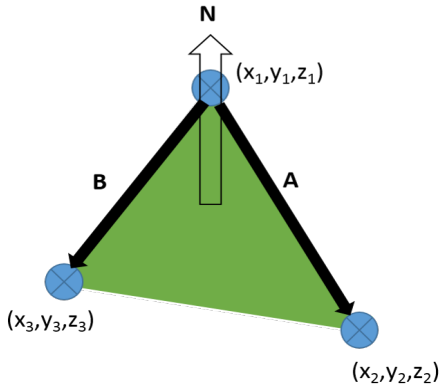

Fig. 4.22 The cross product of any two vectors (**A** and **B**) describing two facets of a triangle in the triangular mesh gives the area normal vector **N**.

The dot product of the normal vectors for each triangle and a vector representing an ideal flat surface gives the angle of orientation of each individual triangle composing the

isosurface. The angle between the ideal surface vector **F** and any triangle with an area vector **N** in the mesh is then given by the relation:

$$\phi = arcos((\mathbf{F}\cdot\mathbf{N})(|\mathbf{F}||\mathbf{N}|)) \tag{4.2}$$

As shown schematically in Fig.4.23. As an extension of this, the magnitude of the dot product gives the distance of elevation over the triangle above the flat surface, thus giving us a measure of vertical translation.

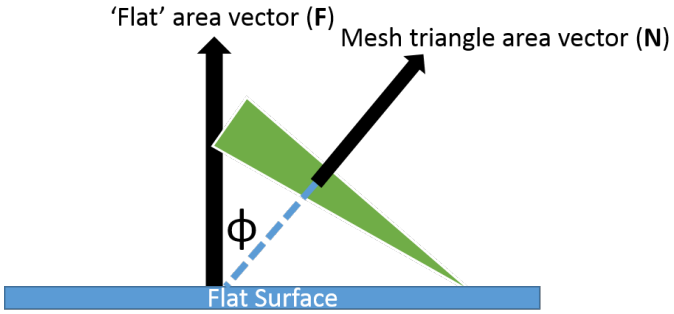

Fig. 4.23 The dot product between the normal vector of a triangle in the mesh and an ideal flat surface gives the angle

As such, the variance of these angles correspond to variations in the orientation of the triangles composing the isosurface and can be interpreted as a measure of corrugation, or roughness. This is highly dependent on the orientation of the surface, the side walls of the isosurface will require a different 'ideal' flat surface relative to the top surface of the microdisk membrane. This method yields an angular variance of 9.4×10^{-4} degrees and a RMS elevation value of 1nm for the surface shown in Fig.4.20.
Performing smoothing and noise removal using a bilateral filter [139] on the individual SEM images comprising the stack should allow for a smoother surface reconstruction as shown in Fig.4.24.

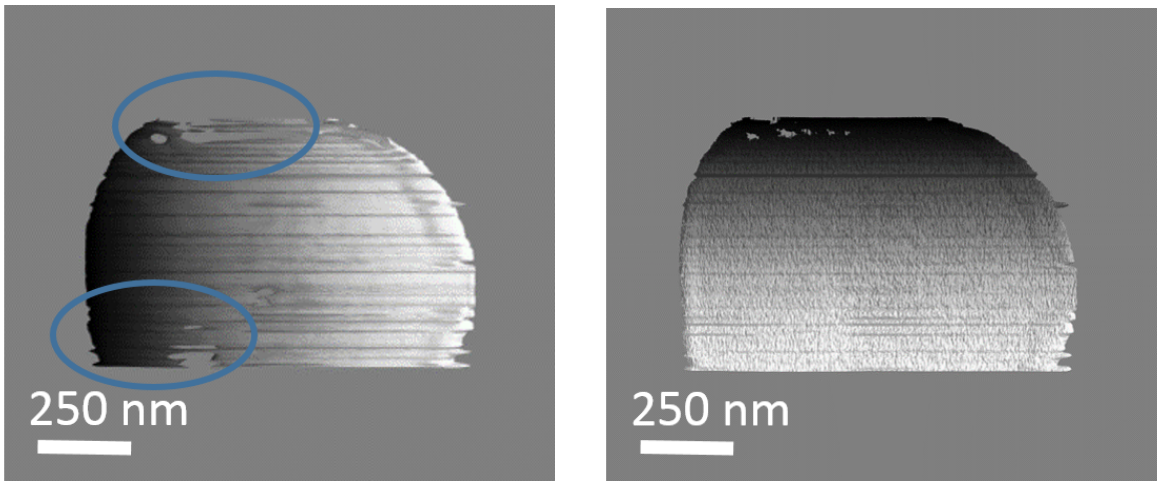

(a) (b)

Fig. 4.24 a) Smoothed isosurface b) unsmoothed.

The smoothed surface yields an angular variance of 4.25×10^{-7} degrees, indicating the angular variance can indeed be used as a measure of roughness in analysing the reconstruction. However, the RMS elevation calculated for the smooth value remained 1 nm. This indicates that the RMS roughness value extracted using this method is dominated by features which are unaffected by the smoothing process, perhaps due to the smoothing function threshold being set too low.

4.2.9 Image Roughness Analysis

An alternative to the computationally expensive method of performing analysis on the 3D mesh is to perform roughness analysis on the individual images taken during the FIB tomography experiment. An individual slice of the image stack used for reconstruction is shown below in Fig.4.25. The images are stored as gray-scale images, with their value describing the intensity at each particular pixel.

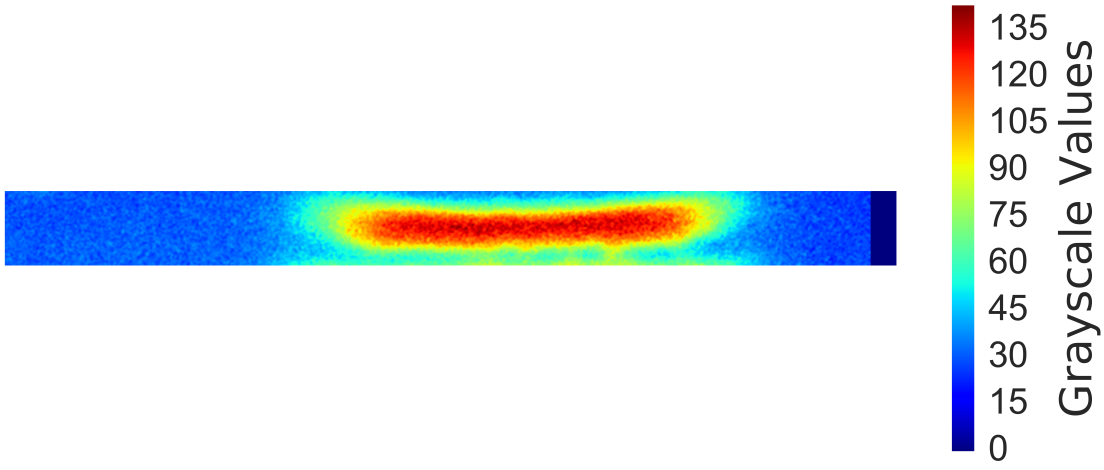

Fig. 4.25 'Slice' of a microdisk taken from the stack of images used for 3D reconstruction

We can use these individual images to extract profiles which describe the surfaces of the microdisk. In this example we have chosen the top surface of the microdisk in order to compare this method with the mesh analysis method presented in section 4.2.8. By choosing a threshold value identical to that used to construct the triangular mesh (60) we can extract the profile of the top surface of the microdisk. Fitting this surface with a polynomial in order to remove any bowing or protrusions from the shape of the microdisk and subtracting this fit gives a 'linear' profile centred with a mean of approximately 0, thus allowing us to extract the root-mean squared (RMS) roughness. The individual plots for the profile, fit and fit subtracted from the profile of the top microdisk surface shown in Fig.4.25 are shown below in Fig.4.26.

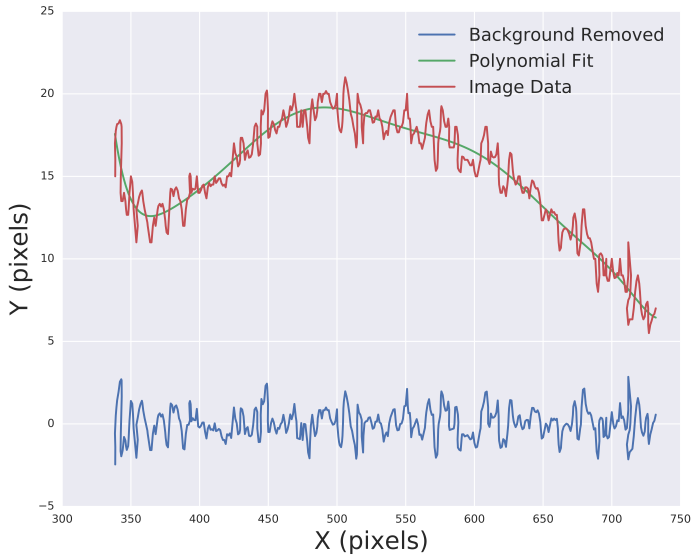

Fig. 4.26 'Slice' of a microdisk taken from the stack of images used for 3D reconstruction

Using the blue plot shown in Fig.4.26 we can thus extract the RMS roughness for each individual image and calculate a mean RMS roughness for all images. A histogram of the extracted RMS roughnesses for all images is shown below in Fig.4.27. The RMS roughness averaged for all images obtained using this method is 1.02 nm, in good agreement with the RMS roughness value obtained via the analysis of the triangular mesh generated by the marching cubes algorithm.

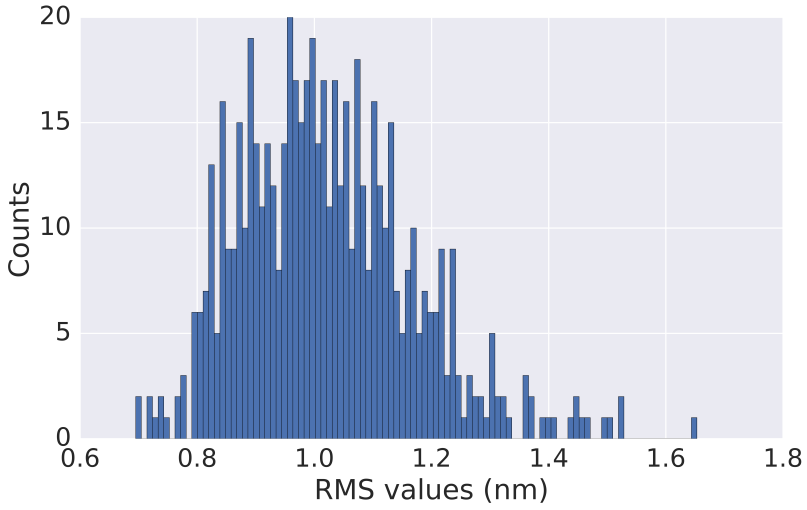

Fig. 4.27 Histogram showing the RMS roughnesses extracted from each individual image.

4.3 Summary

The PEC etching process provides an effective manner in undercutting GaN microdisk membranes. However, due to the mechanism of etching which relies on the presence of photo-generated carriers, dislocations can hinder the etching process resulting in the formation of 'whiskers' of unetched material on the underside of the microdisk, which provide a radiative pathway for WGMs propagating in the microdisk to escape thus reducing cavity Q-factor.
In this chapter, we have presented a manner through which TEM lamellae can be prepared from processed microdisks. Following this we have performed TEM in order to reveal the presence of a dislocation at the centre of a whisker. Using WBDF-TEM we have identified the dislocation type as pure edge, though mixed and pure screw dislocations are expected to result in the formation of whiskers. This preparation method has also allowed us to examine the active region in the microdisk membrane using STEM-HAADF and STEM-EDX, revealing the presence of a 'split' InGaN active region.
Fig.4.19. demonstrates the ability of the FIB tomography process to access detailed information concerning the morphology of the disk. The 'splitting' of the microdisk membrane caused by etching of the active region can be seen in reconstruction, as well as residual material on the underside of the microdisk indicating incomplete etching. We have utilised two different methods of extracting RMS roughness from the FIB tomography data, which both give a result of 1 nm.

4.4 Future Work

A continuation of the work presented in this chapter would likely involve correlated optical and structural measurements. In particular, the TEM lamella preparation allows for insight into the active region of microdisks. As such, an experiment involving the correlation between PL, CL and site-specific STEM-EDX would allow for a comprehensive analysis of the optical and structural properties of the InGaN active region, as well as its interaction with the microdisk cavity. Beyond this, the groundwork for the analysis of the 3D morphology of the microdisks has been presented here, in extending this with AFM measurements of the microdisk membrane surface the accuracy and precision of the tomographic reconstruction may be reassessed. Following this, roughness measurements obtained via FIB tomography coupled with cavity Q-factor measured through micro-PL may provide insight into current fabrication limitations. Ultimately, using the data concerning microdisk membrane morphology obtained by FIB tomography and its optical properties through micro PL, FDTD

simulations may be used to attempt to simulate microdisk Q-factor based on their structural morphology.

Chapter 5

Characterisation of III-Nitride Nanobeam Cavities

5.1 Background

In chapter 4 we have touched upon some challenges in the fabrication of III-nitride cavities due to the properties of III-nitride materials, as well as microscopy-based methods to characterise the structural and compositional properties of these cavities. In this chapter we extend these methods and apply them to 1-D PCCs, or nanobeam cavities. As discussed in section 1.2.2.3, nanobeam cavities provide several advantages over other cavity geometries, namely ease of fabrication relative to 3-D PCC structures and their ability to realise high Q-factor and low effective modal volumes required for applications such as low-threshold lasing. Relative to microdisk cavities, nanobeam cavities require several additional fabrication steps due to their complex geometry and thus are more susceptible to fabrication issues such as non-uniform patterning and incomplete undercutting. This chapter will present the work done on harnessing microscopy techniques in order to characterise the fabrication of III-nitride nanobeam cavities.

5.2 Nanobeam Fabrication

The nanobeam cavities studied in this work were fabricated by Dr. Nan Niu and Danqing Wang in the Hu group at Harvard University. The samples are similar to those described in section , in that they contain InGaN active layers in a GaN membrane, an InGaN SSL for PEC undercutting and an AlGaN layer to prevent the PEC etching from affecting the InGaN active region. The fabrication flow for the devices is shown in Fig.5.1.

The fabrication scheme utilises e-beam lithography to pattern the shape of the nanobeam. XR-1541(XR) e-beam resist is spun on to the surface of the wafer and is patterned to define the nanobeam and circular pads. The resist is then removed, remaining only in the patterned areas and acting as a mask for the inductively coupled plasma (ICP) dry etch. This dry etch allows access to the InGaN SSL which is selectively undercut by the PEC etching method described in section 4.1.1.

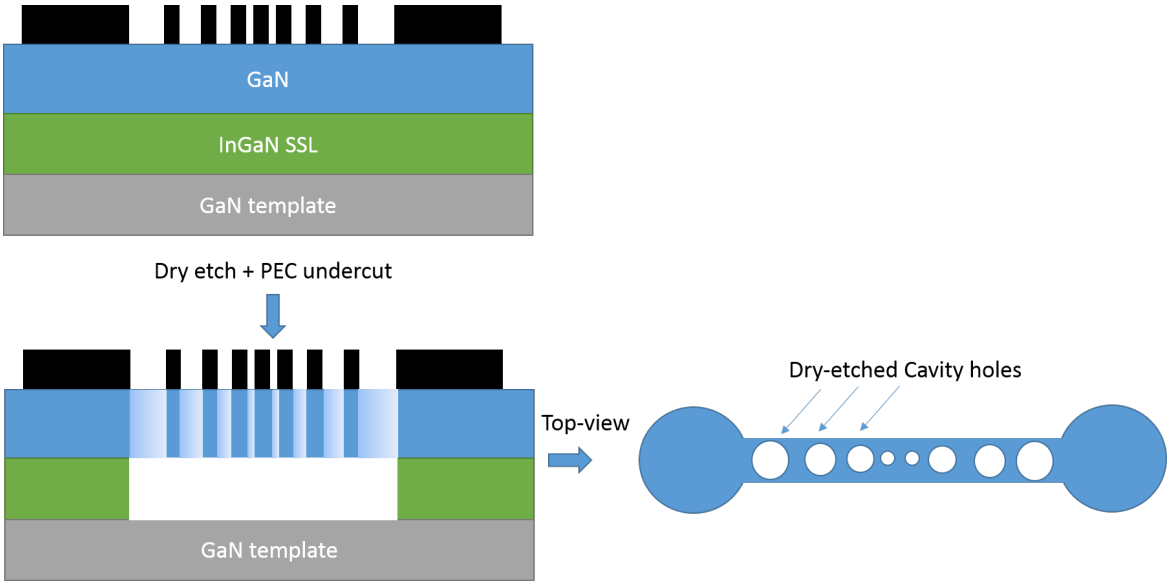

Fig. 5.1 Nanobeam cavity workflow.

Top and side view SEM images of a fabricated nanobeam produced from this process are shown in Fig.5.2.

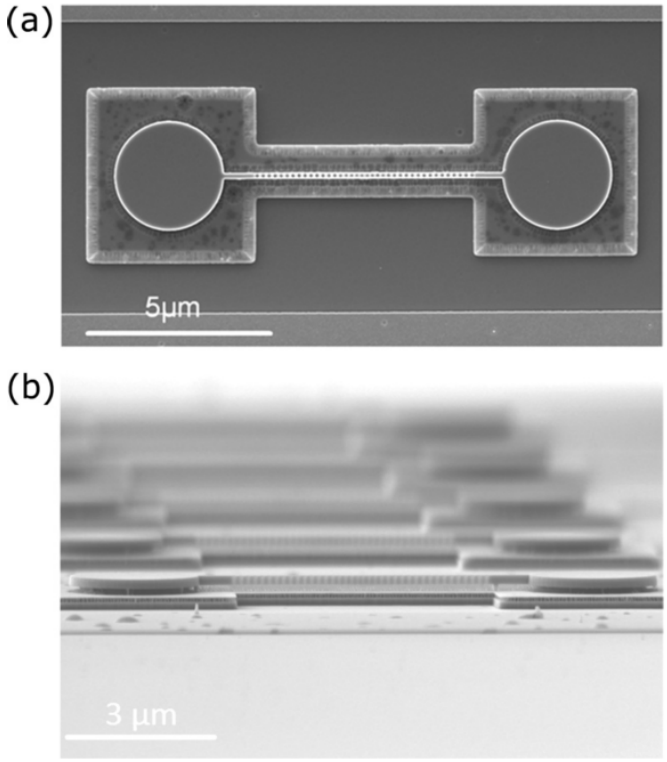

Fig. 5.2 a) Top-view and b) side-view of the suspended nanobeam cavities. Reproduced from [58].

5.3 Experimental

Fig.5.2.a. shows that the nanobeams are extremely narrow in one direction (approximately 125 nm), thus making them electron transparent to a 200 kV electron beam [140]. This introduces an interesting problem in terms of TEM specimen problem: on the one hand the nanobeams are already at the required thickness and thus require no additional thinning once extracted. However, as seen with the microdisks in section 4.2.3 suspended structures are extremely sensitive to ion-beam damage which is required for sample lift-out in FIB/SEM dual beam equipment. Furthemore, the standard method of using protective Pt can not be applied here, as this would cover the entirety of the specimen and hinder TEM/STEM imaging. This section will cover FIB techniques used to extract nanobeams, and the TEM analysis performed on these samples.

5.3.1 Nanobeam Lift-out

In this section we will present the work performed on nanobeam cavities using standard FIB lift-out techniques.
Initial attempts to lift-out nanobeam cavities using standard dual-beam techniques were unsuccessful for several reasons. Firstly, the small width of the nanobeams relative to the Omniprobe provide a difficult target to reach accurately using the probe. Furthermore, even after successfully welding the nanobeam to the Omniprobe using Pt, the fragility of the nanobeams renders the lifting out of a whole nanobeam intact rather difficult, as shown in Fig.5.3.

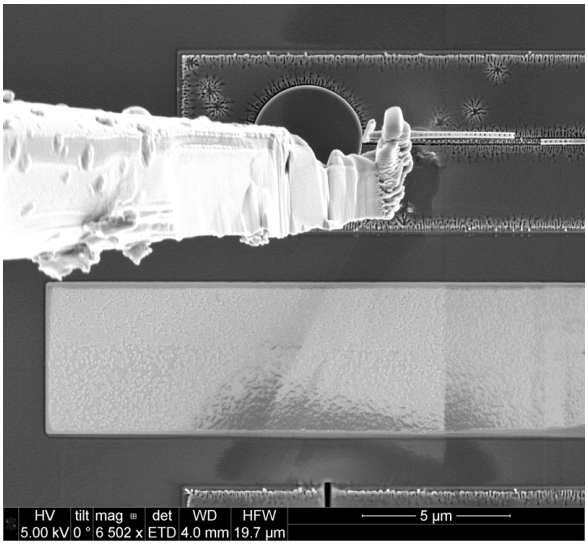

Fig. 5.3 SEM image of the Omniprobe attached to a broken nanobeam cavity.

An additional challenge was encountered when attaching the sample to the TEM grid. In the process of welding the nanobeam, the Pt used would cover the entire sample despite being targeted in a minute region, as shown in Fig.5.4. The image shows that the etched holes are no longer visible, as such this type of sample preparation is unsatisfactory for TEM analysis.

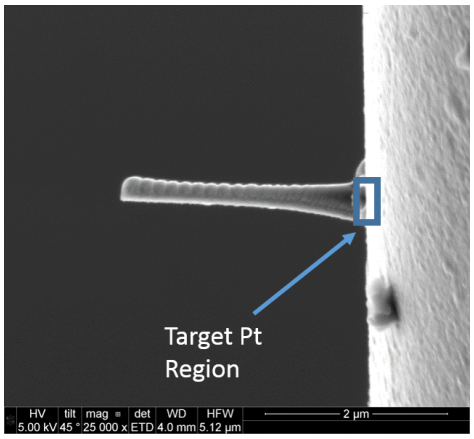

Fig. 5.4 SEM image of a nanobeam attached to a TEM grid covered in platinum.

In order to attempt to mitigate the negative effect of the Pt, carbon was used as a welding material to join the nanobeam to the TEM grid instead, as it was anticipated that the low atomic number of C relative to Pt would result in lower contrast from the carbon layer in STEM-HAADF. Fig.5.5 shows STEM-HAADF images of the carbon covered nanobeam cavity. Despite the presence of carbon which can be seen on the nanobeam, Fig.5.5.b. the contrast from the InGaN active region can be observed.

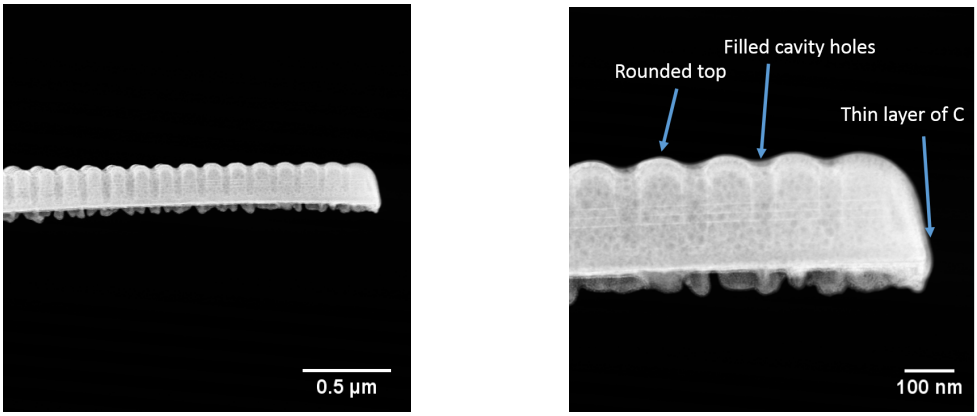

(a) (b)

Fig. 5.5 STEM-HAADF images of a carbon covered nanobeam.

Fig.5.5 shows the holes in the nanobeam cavity are incompletely etched through, indicating the dry etch step described in section 5.2 may have been terminated prematurely.

In order to eliminate the deposition of either Pt or C on the nanobeam lift out, we employed the use of an alternative method of providing adhesion. To this end, we used Kleindeck SEMGlU vacuum compatible glue. By using low imaging currents the glue remains uncured and thus can be manipulated. Utilising a higher beam current (> 1nA)

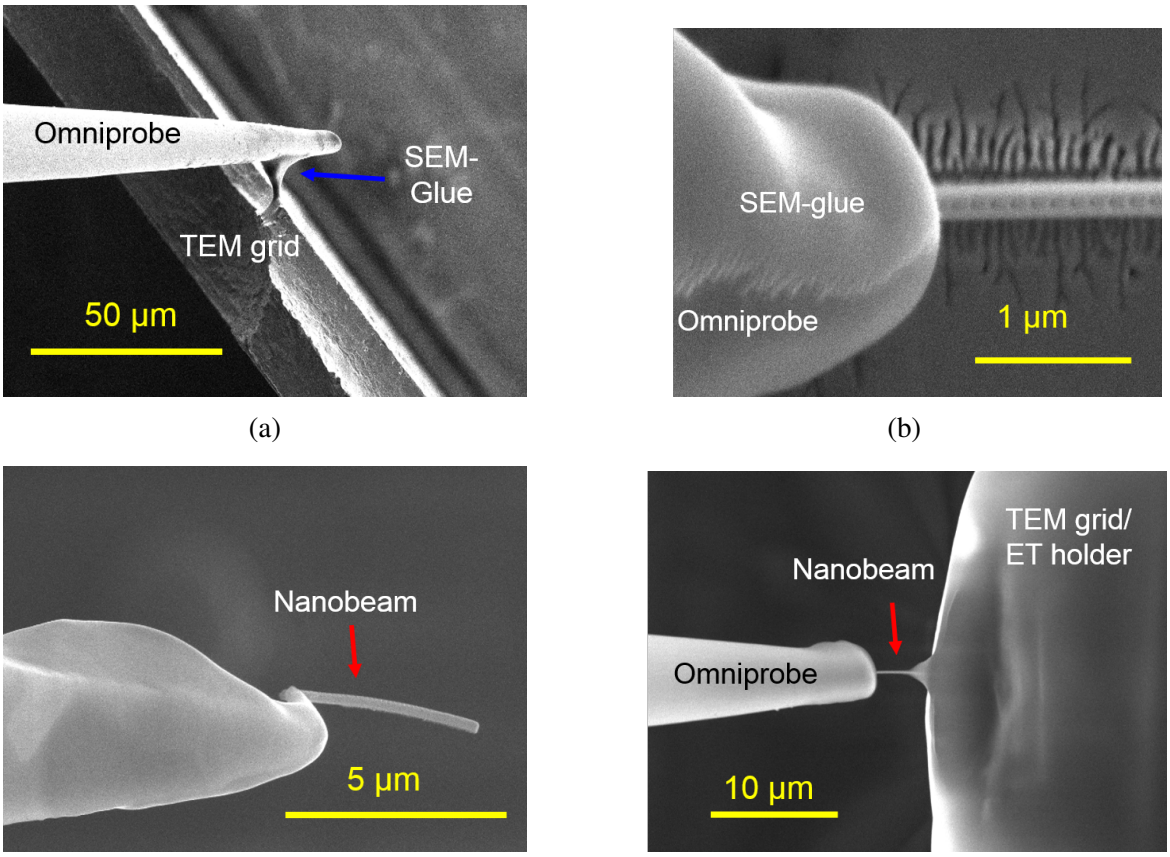

Fig. 5.6 Images of the SEMGLU nanobeam lift-out process: a) glue deposition b) contact on the nanobeam c) lift-out d) mounting on a TEM grid or ET holder. Courtesy of Dr. Fengzai Tang.

and focussing the beam on a small area (corresponding approximately to a magnification of 50 kx) allows for curing of the glue. The lift-out procedure utilising the SEMGLU is as follows: the glue is first attached onto the TEM grid utilising the Omniprobe tip; following this the Omniprobe tip which still contains SEMGLU is brought in contact with a target nanobeam and cured; the regions of the nanobeam which connect it to the circular pads shown in Fig.5.2.a are then milled away in order to release the nanobeam, the nanobeam is then brought in contact with the glue on the holder and the glue is cured to mount the nanobeam onto the holder, finally the omniprobe is released through milling. This process is shown in Fig.5.6.

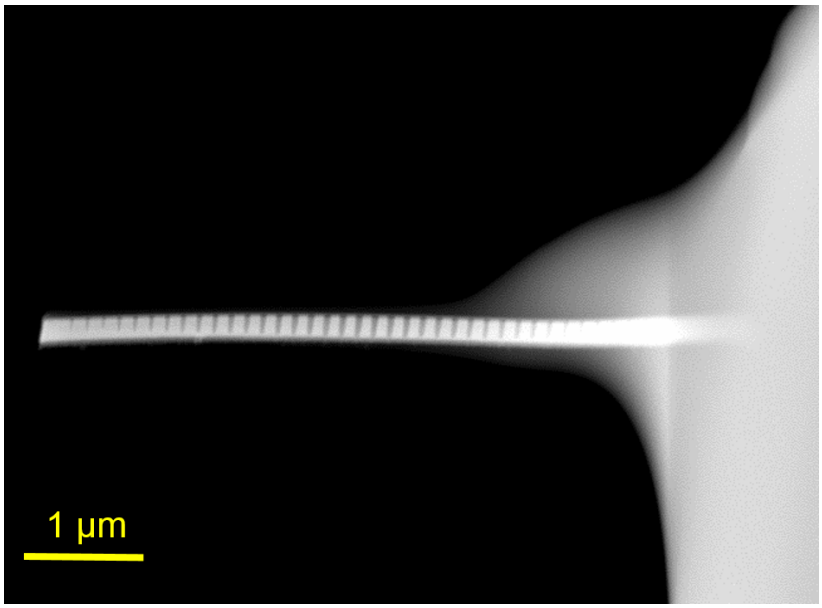

Fig. 5.7 Low magnification STEM-HAADF image of the nanobeam shown in the lift-out process in Fig.5.6. Courtesy of Dr. Fengzai Tang.

STEM-HAADF images taken of the nanobeam shown in Fig.5.6 are shown here. Fig.5.7 demonstrates the effectiveness of the SEMGLU lift-out method in preventing unwanted deposition on the nanobeam. Further inspection at a higher magnfication (Fig.5.8.b.) confirms this as the top surface of the nanobeam between the cavity holes is flat, as opposed to the 'rounded' shapes observed in Fig.5.5 due to carbon deposition. The STEM-HAADF images also show the cavity holes are not etched completely through the thickness of the beam, and also show a slightly tapered profile. The incomplete etching of the cavity holes is likely to be the underlying reason behind the lack of modes and lasing in the nanobeams when examined using micro-PL. There is also no evidence of relaxation of the InGaN active layer or of defects at the nanobeam surface.

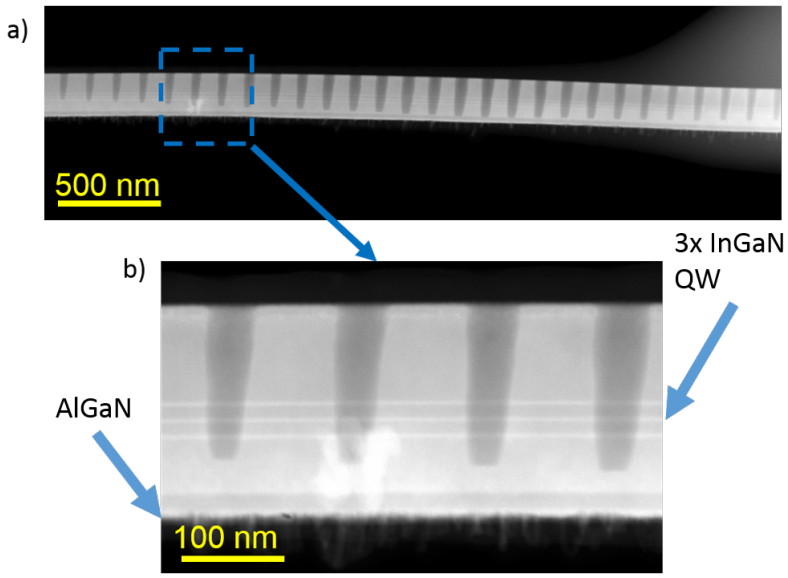

Fig. 5.8 a) STEM-HAADF image of the nanobeam, showing the presence of the dry-etched cavity holes b) higher magnification image of the region shown by the blue box in a), the contrast from the InGaN active region is clear. Courtesy of Dr. Fengzai Tang.

5.3.2 Electron Tomography

Following the successful lift-out of a contamination free nanobeam through the use of SEMGLU, we performed ET experiments on the nanobeam. The experiments described in this section were performed with Dr. Fengzai Tang under the supervision of Dr. Giorgio Divitini.

5.3.2.1 Acquisition

Two tilt series were acquired for this experiment at different magnifications. The first low magnification tilt series was acquired from the nanobeam shown in Fig.5.7 on a range of -76 degrees angle to 76 degrees as described in section 2.2. The tomography holder (Fischione on-axis holder, model 2010) can in principle be fully rotated, however the microscope Compustage will only allow automated rotation up to 76 degrees, beyond which the holder must be rotated manually thus potentially introducing errors of up to 5-6 degrees in terms of the rotation [74]. Instead of adding images with an erroneous tilt angle value to the series we chose to limit the tilt range to that allowed by the stage which is typically considered satisfactory in terms of quantitative ET and limits the missing wedge as discussed in section 2.2. STEM-HAADF images taken at a tilt of 0, 40 and 80 degrees are shown in Fig.5.9. The bending of the nanobeam which can be seen in these images may be due to inhomogeneous curing of the SEMGLU, though the central section of the nanobeam remains straight.

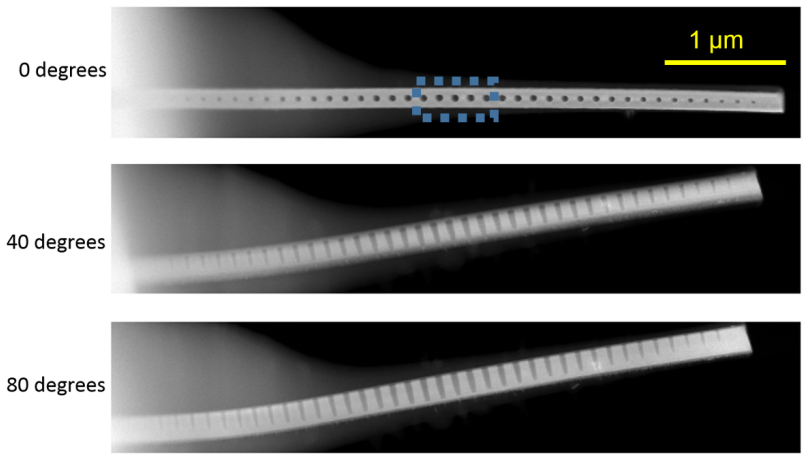

Fig. 5.9 STEM-HAADF images taken at 0, 40 and 80 degrees. The blue box shows the area chosen for the high magnification tilt series.

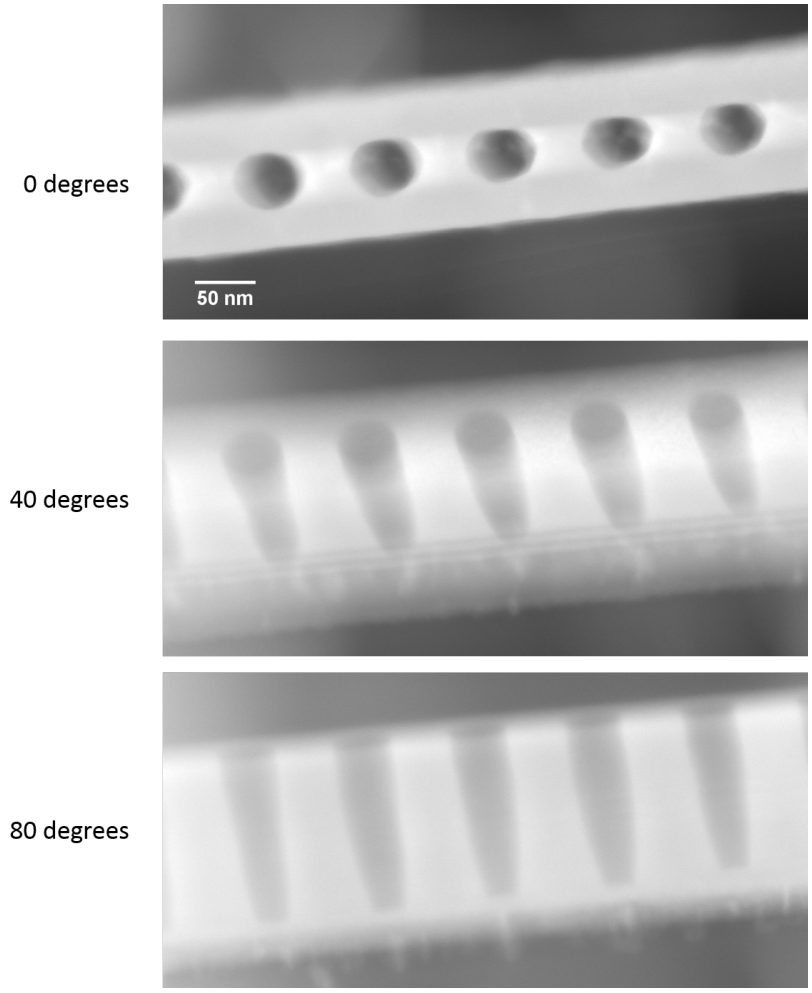

Fig. 5.10 STEM-HAADF images taken at 0, 40 and 80 degrees in the tilt series.

5.3.2.2 Low Magnification Reconstruction

Reconstruction of the dataset was carried out using a weighed back projection algorithm (WBP), which is effective in the case of high contrast datasets providing sharper edges and enhanced contrast relative to the simulatanous iterative reconstruction technique (SIRT) algorithm [74]. Orthogonal slices from the reconstruction at 20 nm, 60 nm, 80 nm and 100 nm depth into the nanobeam are shown in Fig.5.11. The reconstruction produces some artifacts which are observable, such as the bright line through the center of the nanobeam which can be seen at 20 nm, 60 nm and 80 nm and is labelled using the blue arrow.

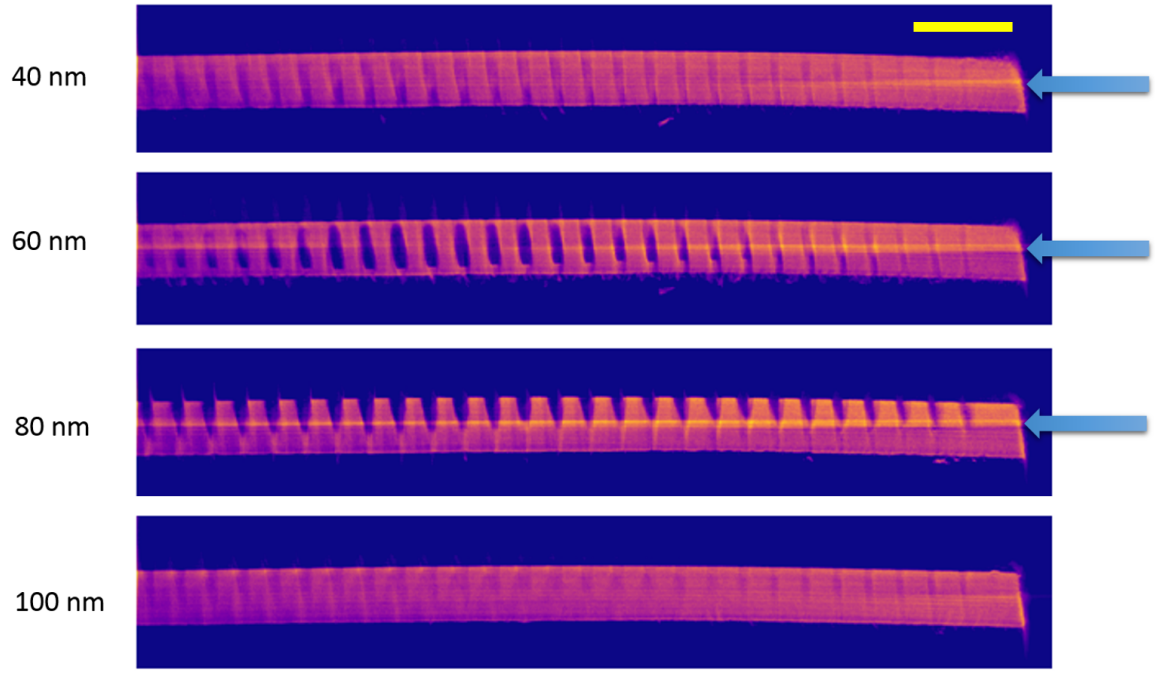

Fig. 5.11 Slices from the tomographic reconstruction at depths of 20 nm, 60 nm, 80 nm and 100 nm for a total nanobeam thickness of approximately 110 nm. The yellow scale bar represents a length of 50 nm. The dry-etched holes of the cavity can be clearly resolved here.

The dataset consisting of slices is then rendered into a 3D model through the use of the same methodology described in section 4.2.8. It is important to note that the data has been chosen in such a way that only the straight portion of the nanobeam is utilised in the reconstruction, as can be seen from Fig.5.11. A top view image of the nanobeam reconstruction is shown below in Fig.5.12.

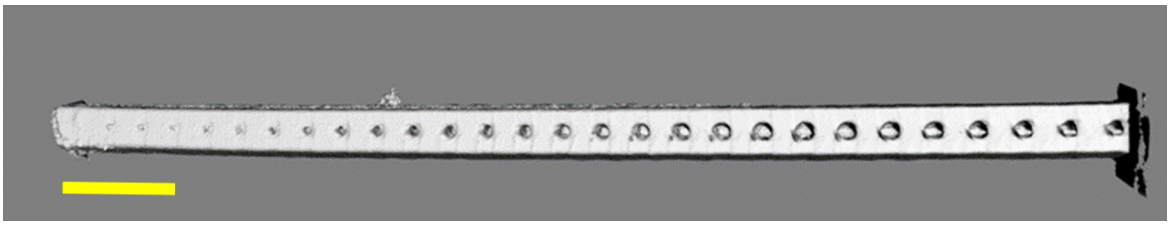

Fig. 5.12 Top-view of the nanobeam ET reconstruction, the scale bar represents a length of 500 nm.

This reconstruction allows for closer examination of the cavity holes, and reveals the level of detail which can be accessed using the ET technique. Reconstruction artifacts may introduce some distortion into the morphology of the cavity (specifically the cavity holes), however a quick comparison between Fig.5.9 at 0 degrees and Fig.5.13 reveals there may by some intrinsic deviation from perfect circularity in the cavity holes due to limitations in the electron-beam lithography and dry-etching step. In order to obtain quantitative information concerning the morphology of the cavity it is thus crucial to separate reconstruction artefacts from true features.

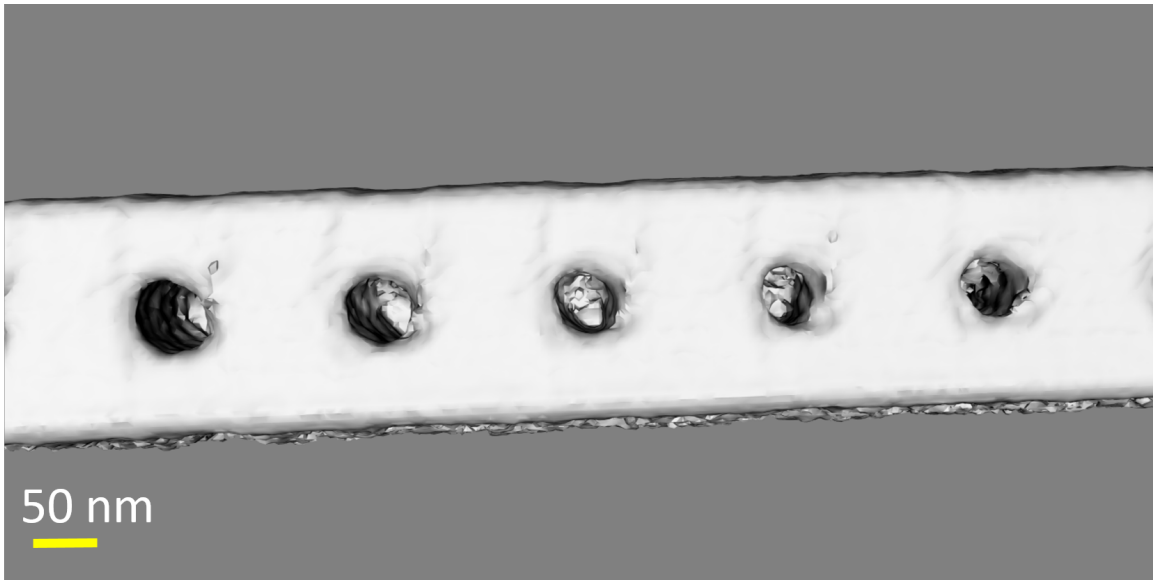

Fig. 5.13 Close-up view of the nanobeam cavity holes.

Fig.5.14 shows a side-on view of the tomographic reconstruction. Interestingly in this case we can observe a slight 'bowing' of the nanobeam along the underside, which may be due to the strain caused by the growth of GaN on the AlGaN etch stop. We can also observe the presence of material on the underside of the nanobeam, which correlates well with the

presence of the of the dry-etched holes. We will discuss potential causes for this unetched material further on in this chapter.

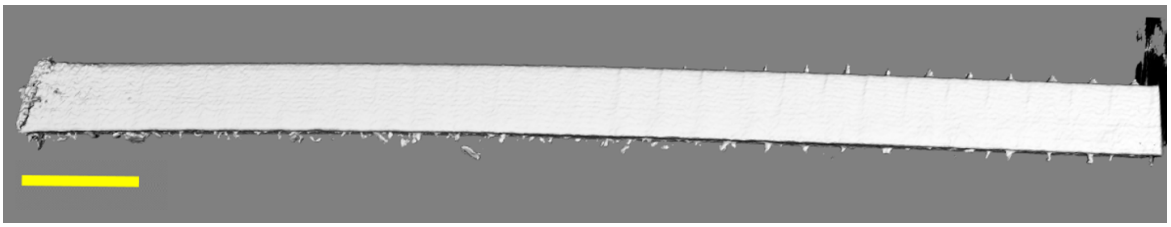

Fig. 5.14 Side-view of the nanobeam ET reconstruction, the scale bar represents a length of 500 nm.

5.3.2.3 High Magnification Reconstruction

Fig.5.15 shows a top-view of a an isosurface reconstructed from the high magnification data-set shown in Fig.5.10. From this data we can see that there seems to be some distortion in the circularity of the etched holes, most likely due to limitations in the e-beam lithography and dry etching process but also potentially due to the effect of the missing wedge in the tilt series. Fig.5.16 shows a view of the reconstructed underside of the nanobeam, where we can observe disruptions and to the surface and unetched material which overlap well with the presence of the cavity holes, as noted for the low magnification reconstruction in Fig.5.14.

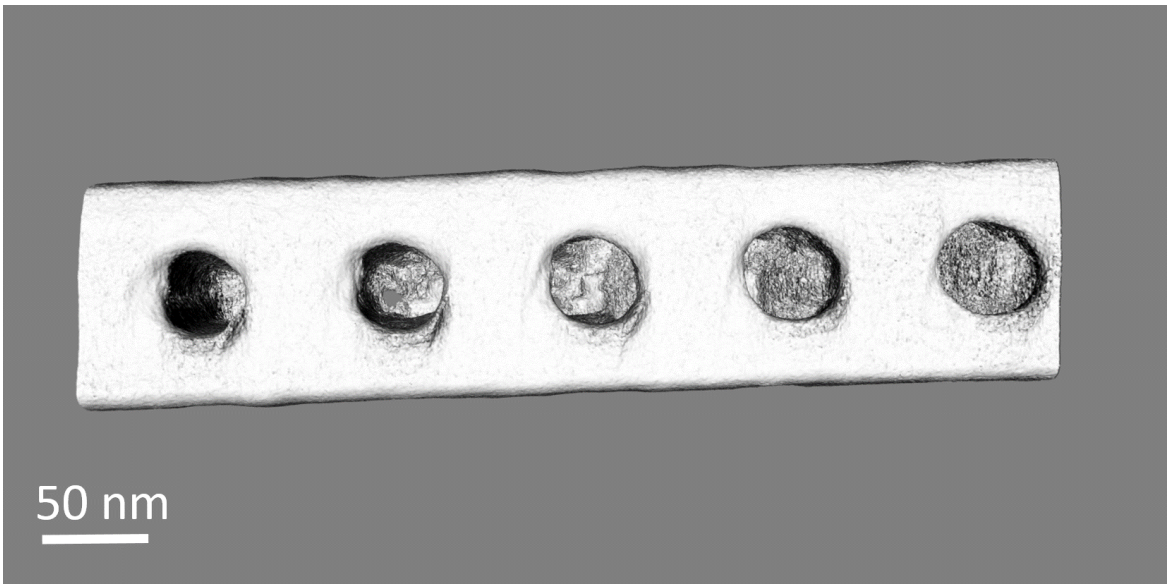

Fig. 5.15 Top-view of the nanobeam ET reconstruction.

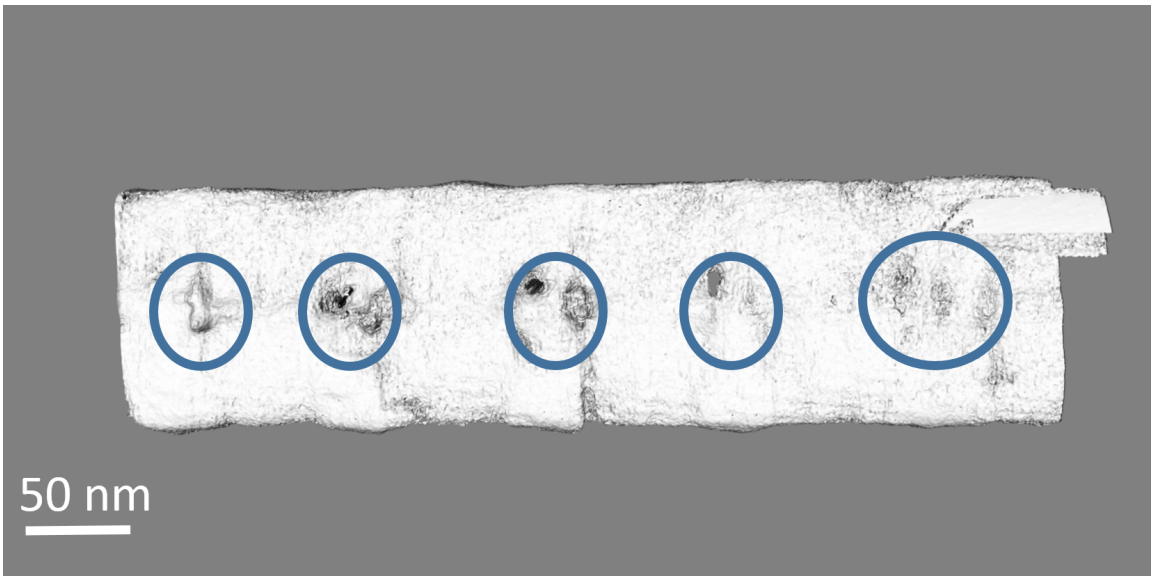

Fig. 5.16 Bottom-view of the nanobeam ET reconstruction.

Fig.5.16 shows a side-view of the reconstructed isosurface, with artifacts arising from the reconstruction highlighted by blue arrows. These are similar to the artefacts observed on the top surface of the isosurface of the low magnification reconstruction shown in Fig.5.14. Similarly, we can observe 'bulging' on the sides of the nanobeam in Fig.5.19, corresponding well with the edges of the cavity holes on the top surface of the nanobeam, which are likely to be artefacts arising from the reconstruction.

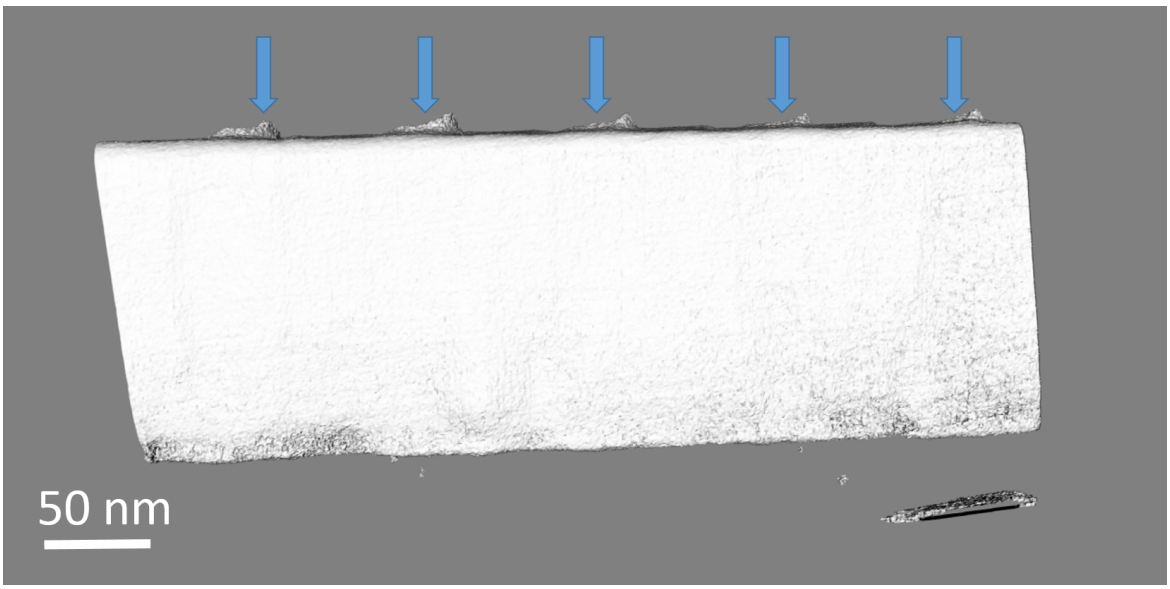

Fig. 5.17 Side-view of the nanobeam ET reconstruction, the scale bar represents a length of 50 nm.

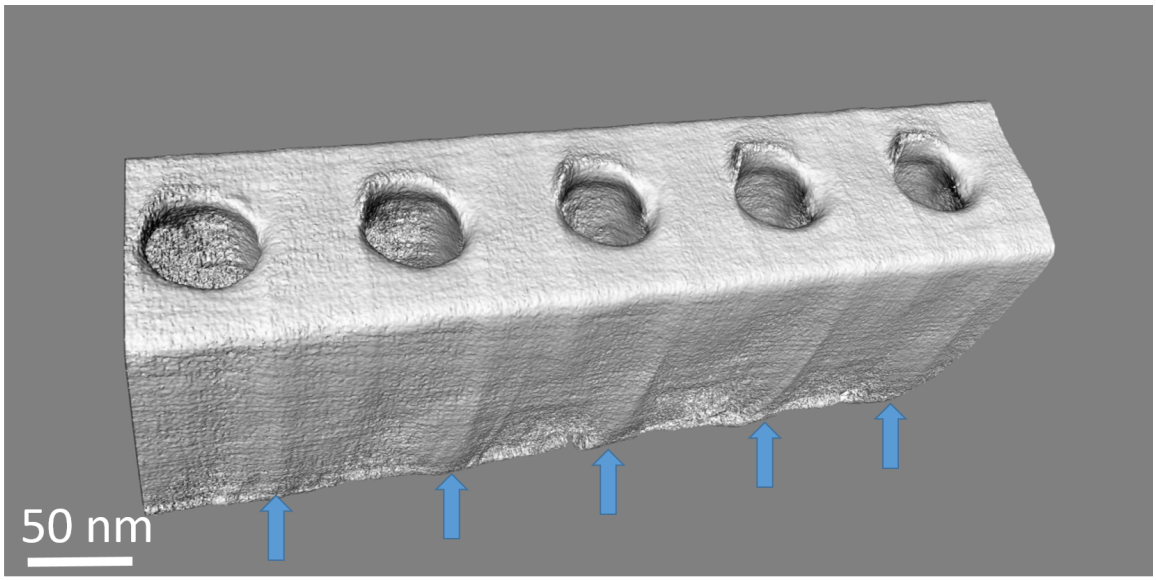

Fig. 5.18 Top-view of the nanobeam ET reconstruction.

We expect the source of the material on the top surface of the nanobeam on the reconstruction to be the tilt of the nanobeam with respect to the incident electron beam. Fig.5.19 shows the effect this has on the perceived contrast in STEM-HAADF: as the the nanobeam is tilted, we do not have a directly vertical view down the etched cavity holes, resulting in some contrast due to the edges of the holes, labelled by the blue arrows. The enhanced contrast at the edges of the cavity holes may result in reconstruction artefacts such as those seen in Fig.5.17.

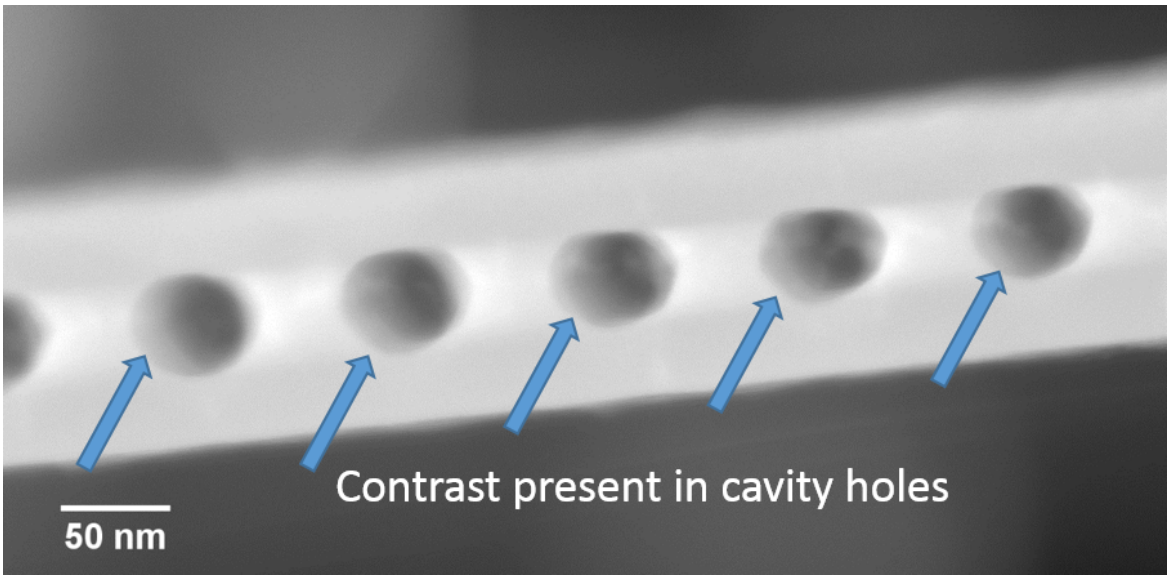

Fig. 5.19 Top-view of the nanobeam taken from the tilt series with the contrast present in the cavity holes labelled using blue arrows.

Similarly, the cause of the ridges shown in Fig.5.19 may also be ascribed to the presence of anomalous contrast in the tilt series. Fig.5.20 shows a STEM-HAADF image taken from the tilt series at 22 degrees, plotted using the matplotlib 'plasma' colour scheme for clarity: upon the application of thresholding we can see that the side walls of the etched cavity holes exhibit higher contrast than the rest of the nanobeam. As such during the reconstruction it is likely these regions are interpreted as thicker regions, resulting in the ridges seen in Fig.5.18.

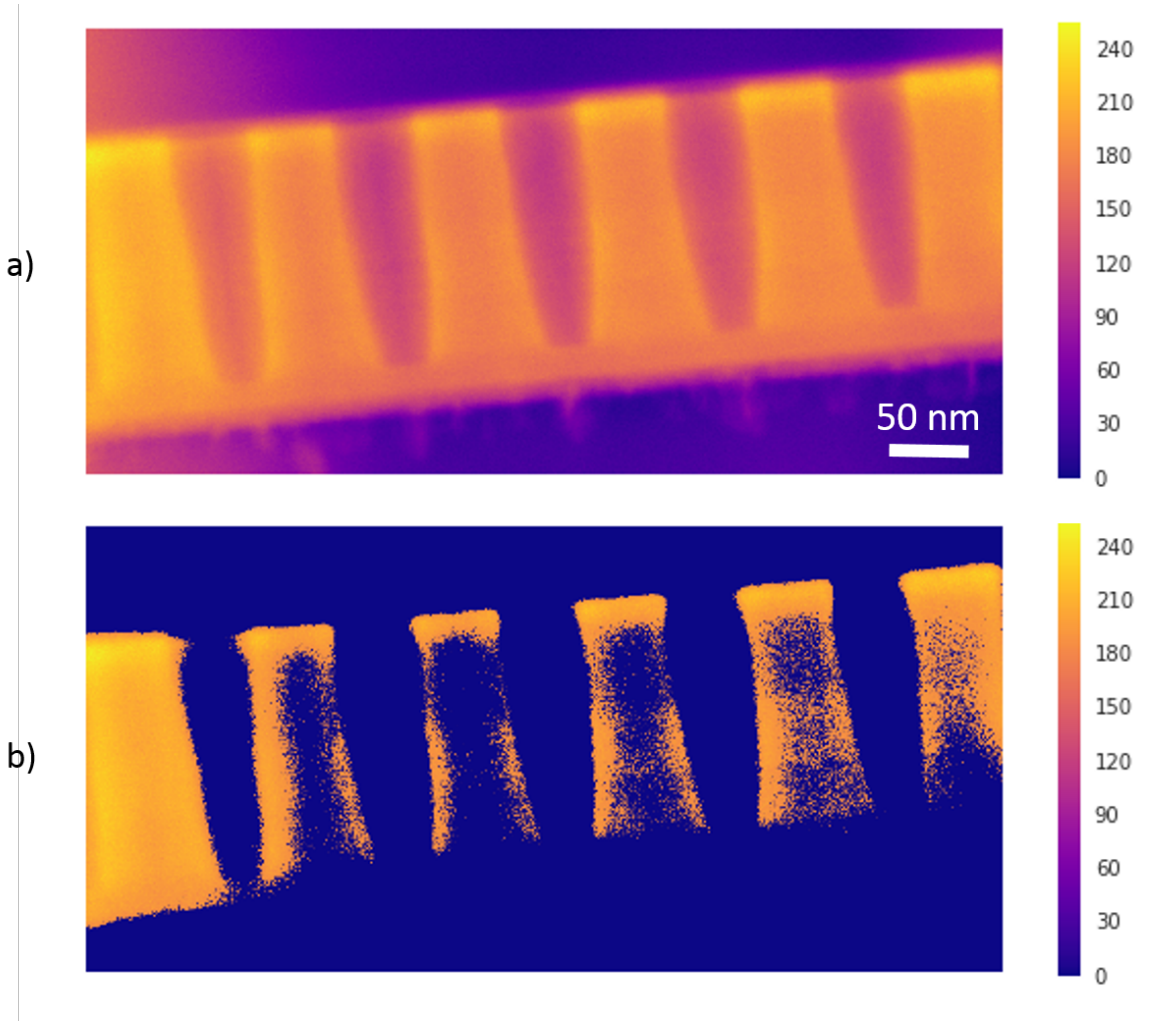

Fig. 5.20 a) STEM-HAADF image taken at 22 degrees in the tilt series b) thresholded image. The colorbar represents the grayscale intensities in the image.

5.3.3 FIB Tomography

In order to investigate alternative routes to obtaining the 3D morphology of the nanobeams, we also performed FIB tomography, a technique we have also used to analyse the morphology of microdisk cavities in Chapter 4. Relative to ET, FIB tomography offers a more convenient method for volume analysis due to the low sample preparation requirements. In fact, FIB tomography requires only the deposition of a protective layer before the experiment can be performed, as opposed to the difficult and time consuming SEMGLU lift-out process discussed in section 5.3.1 required for ET of the nanobeams.

5.3.3.1 Acquisition

The small dimensions of the nanobeam, specifically the cavity holes , require careful tuning of the image acquisition settings in order to optimise resolution, image contrast and brightness. In this particular case we chose to use a C protective layer in order to enhance the contrast with the GaN nanobeam with an additional protective Pt layer deposited on top of the C, and used SEM imaging settings of 2kV and 0.2 nA in immersion mode. Whilst the use of immersion mode does delay the acquisition of data, it also provides superior contrast to regular SEM imaging. An image taken from the slice and view series is shown in Fig.5.5.21 with the Pt, C protective layers and the GaN labelled. Interestingly we can see the effect the PEC etch may have had on the GaN in this case, as it is apparent the GaN has been etched away beneath the nanobeam. Milling of the sample for imaging was performed at an ion beam current of 0.23 nA and a beam energy of 30 kV at 10 nm steps, for a total acquisition time of 3 hours and 10 minutes resulting in 79 slices. The total volume of material analysed was 125 nm x 130 nm x 790 nm with a voxel size of 0.6 nm^3.

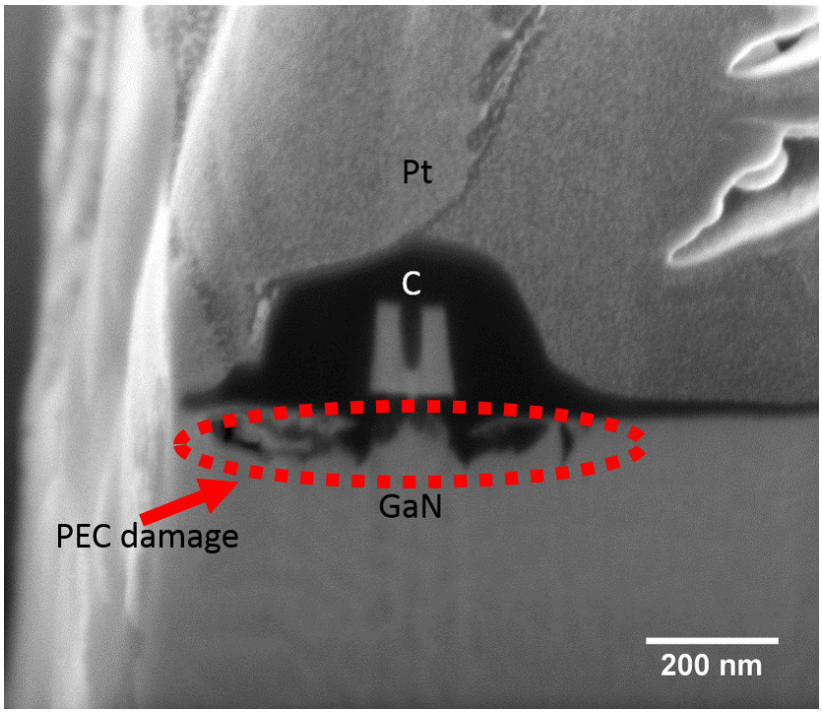

Fig. 5.21 Cross-section SEM image of a nanobeam cavity covered in a protective C layer.

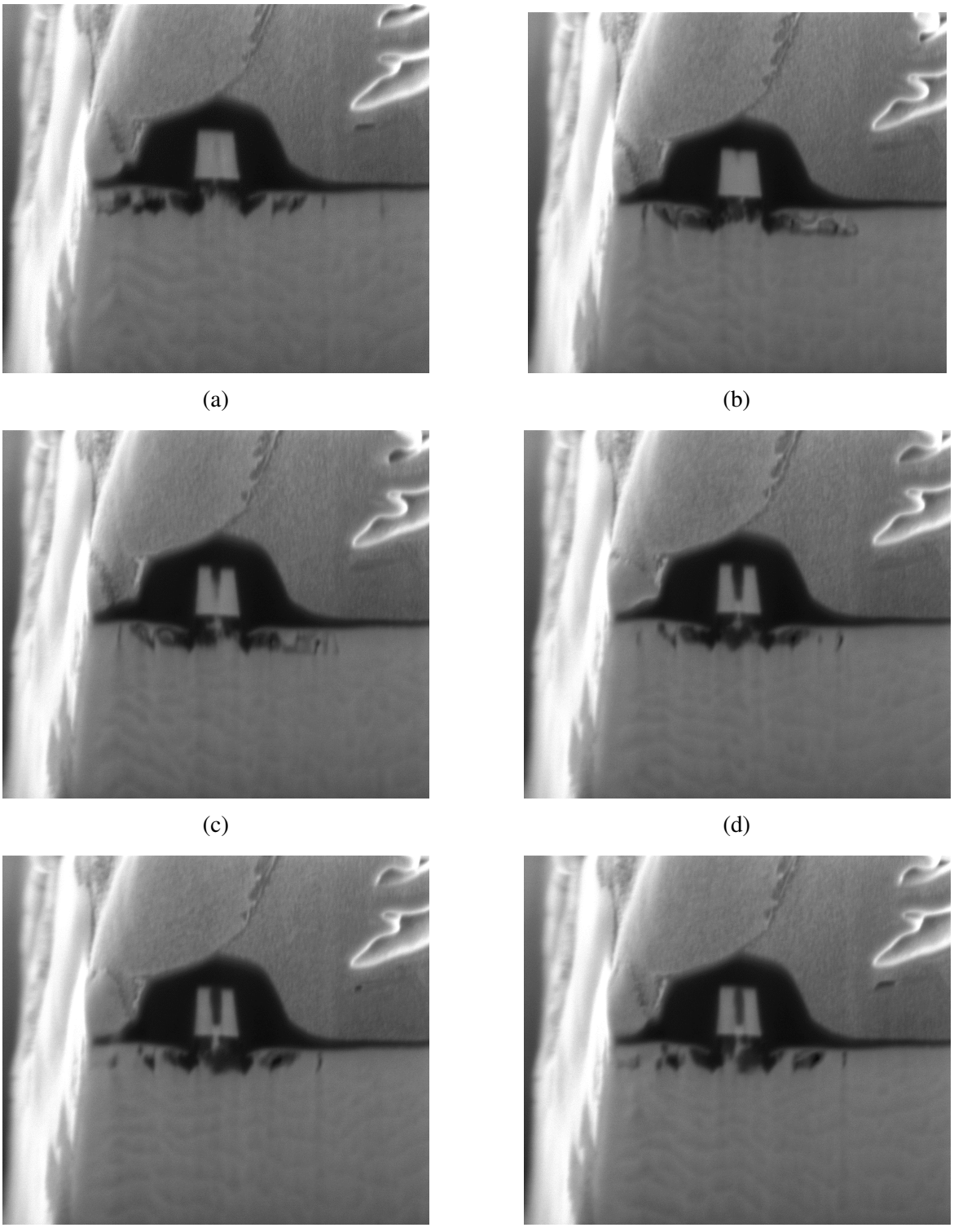

(a) (b)

(c) (d)

(e) (f)

Fig. 5.22 Series of SEM images taken during the FIB tomography experiment taken at slicing depth intervals of 10 nm.

5.3.3.2 Reconstruction

Reconstruction of the slice and view data set was performed in a similar manner to the method described in section 4.2.8, using scikit-image. In order to remove noise inherent to the SEM images without modifying the image edges which are crucial to the reconstruction, we utilised a bilateral filter which is a non-linear, edge-preseving noise-reducing smoothing filter. The application of the bilateral filter allows for each pixel intensity value to be replaced with a weighted average value derived from nearby pixels [141].

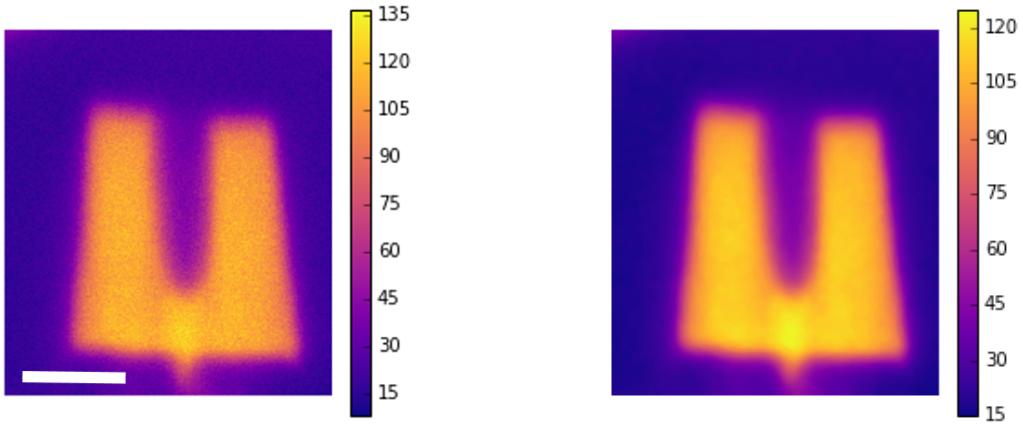

(a) (b)

Fig. 5.23 a) Unfiltered grayscale intensities extracted from the SEM image, the scale bar represents 50 nm b) after the application of a bilateral filter. Note the reduction of the speckle which can be seen in a).

The reconstruction using the filtered dataset is shown below in Fig.5.24. Fig.5.24.a shows a top view of the nanobeam reconstruction, where the cavity holes can clearly be seen. The shape of the holes can be seen in Fig.5.24.b, which is a cross section of the tomographic reconstruction. There are far fewer stack alignment issues relative to the microdisk reconstruction shown in Fig.4.17, as the consistent size of the nanobeam along the direction of the slicing allows for more accurate image alignment in the reconstruction process.

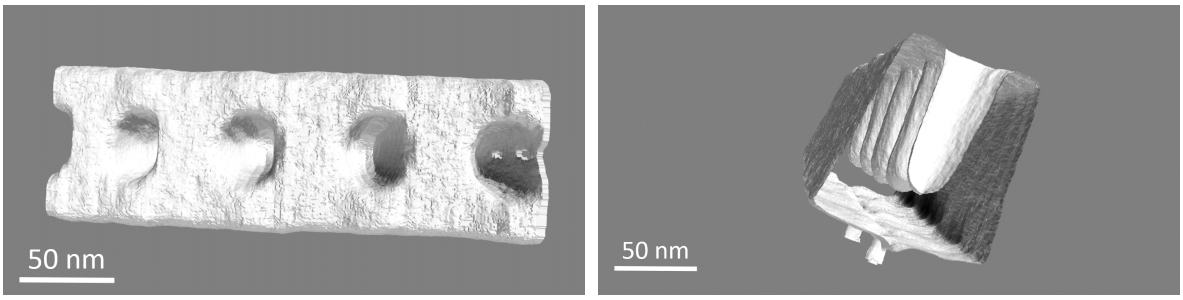

(a) (b)

Fig. 5.24 a) Top side view and b) cross section view of the tomographic reconstruction.

Fig.5.25 shows a sideview for the tomographic reconstruction. This allows us to gain a greater appreciation for errors in the inital 'stacking' of the images from the slice and view experiment. Here the errors are labelled using the blue arrows, and can be detected by comparing the top and bottom surfaces of the reconstruction. For slices containing stacking shifts, the whole slice is displaced in the in-plane vertical direction, resulting in shifts at both the top and bottom surfaces of the reconstruction. Actual corrugation of the nanobeam surface (labelled with the green arrows in this case) is likely to be present only one surface of the reconstruction, as the top and bottom surfaces are etched using different processes as discussed in section 5.2. It is also worth noting that the presence of the stacking shifts seems to correlate well with the presence of the cavity holes, suggesting the cavity holes may induce stacking errors in the initial stack alignment. Unetched material on the underside of the nanobeam due to incomplete PEC etching can be seen in Fig.5.25.

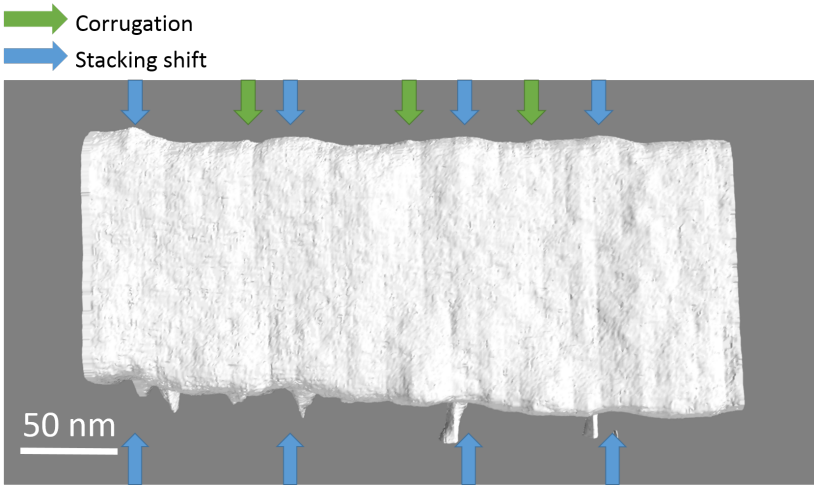

Fig. 5.25 Side-view of the nanobeam tomographic reconstruction. Features which are likely to be corrugation are denoted by the green arrows, and stacking errors denoted by the blue arrows.

5.3.3.3 Analysis

In order to reduce the effect of stacking errors on surface roughness estimations, we perform roughness analysis on the individual SEM images taken in cross section rather than the 3D reconstruction, as detailed in section 4.2.9. The scikit image package provides a convenient manner to extract the contour of the nanobeam structure for each SEM image, as shown below in Fig.5.27. From these images it is clear the main limitation in our roughness estimates is the resolution of the SEM image, as such it is crucial to tune the acquisition parameters to maximise the resolution of the SEM image during slice and view experiments whilst also keeping factors such as drift and acquisition time into account.

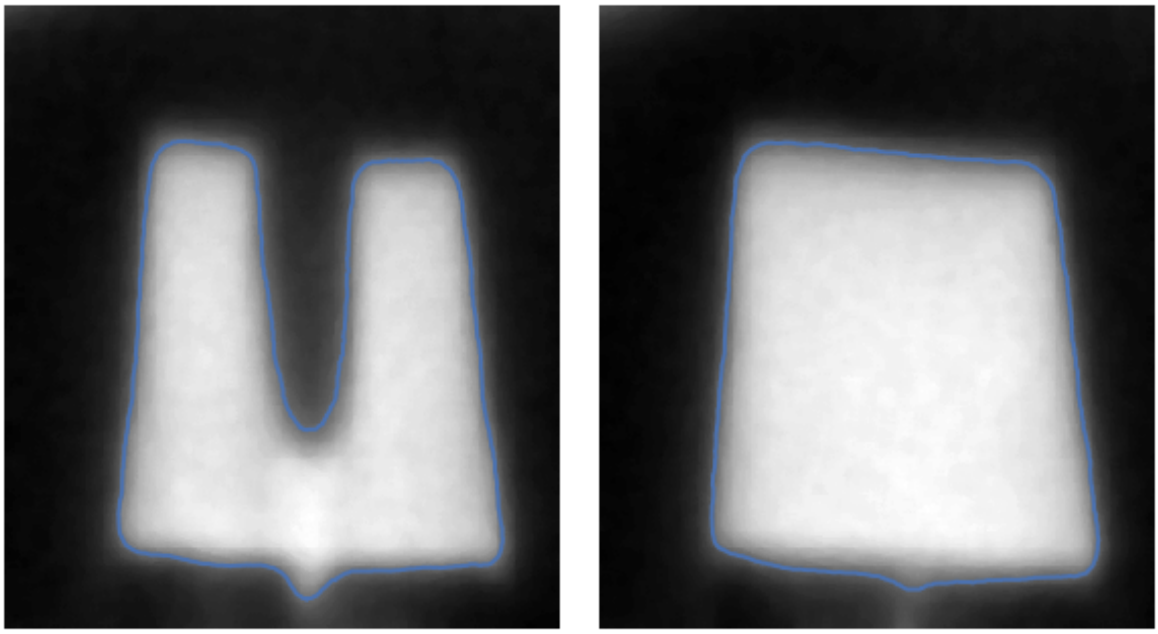

(a) (b)

Fig. 5.26 Two slices from the FIB tomography data set showing the scikit-image marching squares algorithm contour detection outlined blue.

We can see from Fig.5.26 that we can analyse the two side surfaces, a top surface, and bottom surface. Only the bottom surface has been defined by PEC etching, thus we expect this surface to be the roughest due to the presence of unetched material which is clearly visible even in the SEM image shown in Fig.5.22. It is important to note that the marching squares algorithm functions in a manner analogous to the marching cubes algorithm used to reconstruct the 3-D isosurfaces from the tomography data: different threshold values are expected to yield wildly different results in terms of the features incorporated into the contour detection. Fig.5.26.b provides a good example of this: the presence of unetched material

on the underside of the nanobeam has been detected by the algorithm, however the feature appears to continue beyond the detected contour delineated by the blue line. As such, the roughness estimates provided by this method for the underside of the nanobeam are likely to be underestimates due to the reduced contrast of the material in the SEM imaging conditions.

Table 5.1 Nanobeam surface RMS roughness

Surface	Mean RMS roughness (nm)
Top	0.75
Bottom	4.7
Sidewall (image left)	0.9
Sidewall (image right)	1.12

It is important to note the 'top' surface roughness calculation does not include the etched holes. The values shown in the table above are limited fundamentally by the resolution of the SEM as well as the pixel size in the image (magnification). The resolution of the Helios Nanolab field-emission SEM (FESEM) is reported to be 0.8 nm at 2kV at the optimal working distance utilising the through the lens (TTL) detector [142]. As such it is a reasonable assumption to assume RMS roughnesses calculated in the region of 1 nm or below are at the limit of the SEM image resolution, and likely to be heavily influenced by image segmentation thresholds as well as image post-processing.

5.4 Discussion

In chapter 4 we have discussed the effects of dislocations on the PEC etching process, however in the case of the nanobeams shown in this chapter it is expected that the residual material shown in Fig.5.25 is not directly related to the presence of dislocations. The lack of any dislocation related contrast in STEM imaging, coupled with the large number of features observed per nanobeam support this hypothesis. In fact, Fig.5.25 shows a good correlation between the presence of the cavity holes and the unetched material on the underside of the nanobeam, a feature seen also for material on the underside of the nanobeam examined by ET as shown in Fig.5.18. The ICP process used to etch the cavity holes may in fact result in ion-implantation in the regions below the holes, resulting in the presence of non-radiative recombination centres [143] which hinder the PEC etching process resulting in unetched material located in the vicinity of the ICP-etched holes.
In terms of the ET experiments, it seems the high magnification tilt series provides a more realistic reconstructed isosurface with fewer artefacts. We have seen in Fig.5.15 that the

streak artefact observed in the low magnification series can severely disrupt the reconstruction of the cavity holes, which are features which influence the optical properties of the cavity [144]. A potential source for the artefacts seen in the reconstruction is the SEMGLU: the nanobeam was observed to bend due to inhomogeneous curing of the glue during the lift-out process,however the contrast provided by the glue in the STEM-HAADF images was observed to change during the acquisition of the tilt-series suggesting that the curing of the glue may have continued during the experiments, thus potentially disrupting the ET experiment. We observe that the FIB tomography experiment provides results which are far easier to interpret, as it requires no consideration for the projection requirement. However when comparing the FIB tomography and the ET data sets we can observe that the reconstructed morphology of the nanobeams can be heavily influenced by stack alignment errors in the FIB tomography data set relative to the ET data set. As such the FIB tomography data set may require manual alignment, a time-consuming task.
In both experiments, it is crucial to acknowledge the introduction of operator bias in the only step of the reconstruction which is not automated, which is the selection of the threshold value for segmentation. G. Divitini has shown that the selection of an appropriate threshold for segmentation is key in obtaining accurate quantitative information concerning the 3D morphology of samples studied by both ET and FIBT [74].

5.5 Summary

In this chapter we have used multiple microscopy and tomography methods to examine 1-D photonic crystal cavities in the form of suspended nanobeams fabricated using a two-step etching process which involves one dry etching step and one PEC etching step. Due to the complex geometric requirements for these cavities we have found that both electron tomography and FIB tomography provide methods to elucidate issues in the fabrication process related to the etching and lithography, albeit with several intrinsic drawbacks. We have demonstrated that conventional FIB lift-out processes are not compatible with the nanobeam cavities, as the protective layer of C or Pt tends to coat the nanobeam sample and thus hinders TEM examination. Due to these limitations we have devised a lift-out method based on SEM-cured glue which enables contamination-free lift-out of the nanobeam cavities.
We have also performed STEM-HAADF on the nanobeam samples prepared using the SEMcured glue lift-out method, which revealed incomplete etching of the cavity holes. We have also collected a STEM-HAADF tilt series using a SEM-cured glue prepared nanobeam, thus allowing us to reconstruct the 3D morphology of the nanobeam. Although the ET data

reconstructed from the tilt series provides excellent resolution for the features examined in the nanobeam, we have also seen the presence of some artefacts arising from the tilt in the nanobeam sample, as well as the bright contrast seen at the edges of the ICP etched cavity holes.
Finally, we have also performed FIB-tomography on a portion of a nanobeam. When compared to the ET experiment results, the reconstruction of the FIB-T exhibited far fewer artifacts as the reconstruction is simply an addition of all the 'slices' imaged during the experiment, rather than back-projected slices reconstructed from the data set as with ET. Nonetheless, stacking errors in the FIB-tomography data set can result in artificial corrugation being introduced into the reconstruction, as was the case with the microdisks in Chapter 4.

5.6 Future Work

We have performed ET and FIB-T on nanobeam cavities, with a view to eventually perform ET and then FIB-T on the same nanobeam in order to compare the two techniques. Currently the ET experiment on the nanobeam produces a plethora of reconstruction artifacts which may hinder quantitative analysis of the nanobeam morphology, thus the application of FIBT and ET to the same nanobeam may help in clarifying which features observed in the reconstruction can be attributed to artifacts.
Micro-PL may also be used to characterise the optical properties of the nanobeams, thus providing a benchmark against which to compare the morphology of the nanobeams obtained using tomographic techniques.
Finally, the morphology of the nanobeams obtained via ET and FIB-T may be used in FDTD simulations in order to examine the effects of various fabrication issues such as incomplete PEC etching, or RIE etching profiles on the optical properties of the nanobeams.

Chapter 6

Characterisation of III-Nitride Microrods

6.1 Background

The growth of GaN nano- and micro-rods provides an attractive solution for the mitigation of various material issues which plague hetero-epitaxially grown III-nitrides, as discussed in section **??**. Threading dislocations (TDs) in III-nitride rods have been shown to bend toward the sidewall facets in free-standing rods rather than threading through the entire rod, resulting in a defect-free region of the rod [145, 146]. Furthermore, the large surface-to-bulk-volume ratio of free-standing rods results in effective lateral strain relaxation [147], allowing for a reduction in the piezoelectric polarization fields in III-nitrides. As a result of these potential benefits, many nanorod based optoelectronic devices have been demonstrated, ranging from lasers to single photon sources, as discussed in greater detail in section **??**. This section will introduce the work done in characterising the effect of different growth conditions on the structural and optical properties of MOVPE grown III-nitride microrods.

6.1.1 Nanorod Growth

The growth of III-nitride micro- and nanorods remains an active area of research, due to the plethora of methods available and the large range of potential applications requiring rods of different sizes, densities and with varying structural and compositional properties. Top-down methods for the production of rods involving lithography-related synthesis have been widely investigated. This approach is shown schematically in Fig.6.1. Approaches such as photon [148] and electron beam lithography [149], plasma and wet etching [150] and FIB micro-machining [151] which enable the production of site-controlled, uniform rods have

been reported. However, these methods intrinsically produce surface damage in the rods and are limited by the resolution of the patterning techniques [152].

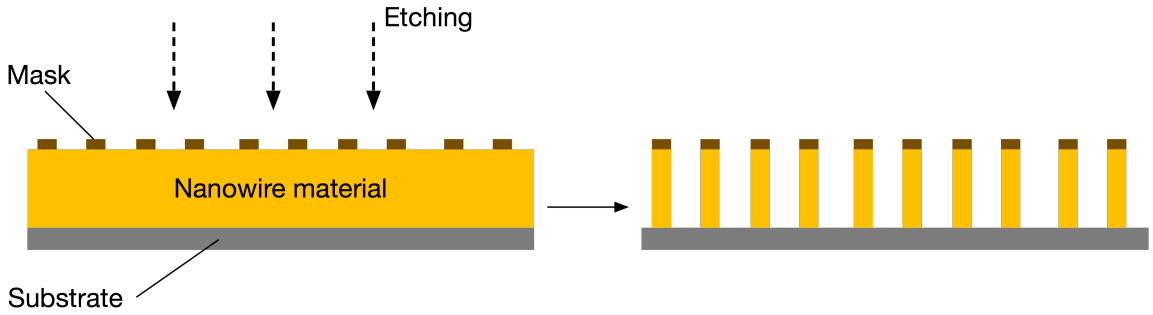

Fig. 6.1 Top-down approach to nanorod fabrication. The mask is not required if a site-specific etching method such as electron beam lithography or FIB micromachining is used. Reproduced from [152]

Bottom-up methods are thus preferred in applications where surface damage can hinder device performance. In this context we will discuss nanowire epitaxy, although processes such as oxide-assisted laser ablation of GaN may also be used for the production of nanowires where no directional or positional control is required [153]. In the case of catalyst induced epitaxy, Au [154], Fe [155], Ni [156] or La [157] catalytic particles can be used in an N-rich environment to grow nanorods epitaxially. In these cases, the growth rate of the rods is determined by the availability of group III atoms, which accumulate in the extrinsic metal particles [158]. Vapour-liquid-solid (VLS) growth is the primary mechanism for the catalyst-induced growth of rods. The VLS process can be considered as a three phase system with the supply, collector and crystal in the vapour, liquid and solid phase respectively. The three phase boundary (TPB) is the perimeter of the growth front in the nanorod [159]. During the growth process the semiconductor material is incorporated into the nanorod through the vapour-liquid interface due to the metallic particle. The further addition of semiconductor source material results in the precipitation of the material, resulting in the liquid/solid interface often known as the growth interface.This is shown schematically in Fig.6.2. Catalyst-induced growth provides excellent control of the rod dimensions as the diameter of the rods is determined by the size of the catalytic particles, however these particles remain on top of the rods after the growth is completed.

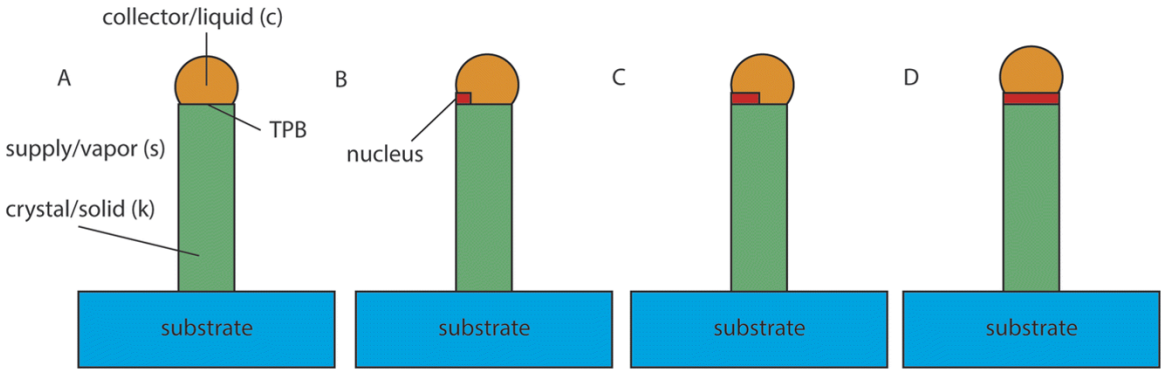

Fig. 6.2 Catalyst induced nanowire growth mechanism. Reproduced from [159].

In order to avoid issues which may arise due to the use of catalytic particles, extrinsic particle free epitaxy may be used. Such methods involve either direct epitaxy [156] or selective area epitaxy [160]. In the case of direct epitaxy, the nanowires are obtained in specific growth conditions chosen to enhance vertical growth and restrict lateral growth of III-nitride layers thus producing rods. Selective area epitaxy involves a substrate patterning step prior to growth in order to induce rod growth. It has been suggested that the growth of III-nitride rods by extrinsic particle free epitaxy MOVPE requires a V/III ratio below 200 and hydrogen carrier gas [161]. These conditions promote vertical growth in the *c*-direction with *m*-plane facets for N-polar GaN due to the passivating effect of the hydrogen on the nitrogen atoms on the surface of the crystal [162]. The vertical growth of undoped rods is however generally limited to aspect ratios below 1 [161]. Si, typically used as an *n*-type dopant, has been shown to induce vertical growth, resulting in aspect ratios exceeding 100 [146, 163].

6.2 Experimental

In this section we will describe the work done by the author in characterising microrods grown at the Cambridge Centre for Gallium Nitride by Dr. Tongtong Zhu.

6.2.1 Microrod Growth

The microrod samples were grown by MOVPE in a 6 x 2 in. Thomas Swan close-coupled showerhead reactor on 2 inch *c*-plane sapphire substrates using trimethylgallium, trimethylindium, and ammonia as precursors and silane as source of silicon. After annealing the sapphire substrate at 1050°C for 10 mins in a H_2 atmosphere, a low temperature GaN nucleation layer of thickness 5 nm was deposited at 550°C and annealed in H_2 at 1000°C for 3 mins to serve as a seed layer for the subsequent microrod growth. The GaN microrods were then grown at

995°C using H_2 as the carrier gas and a V/III ratio of 50. Two samples were grown in order to demonstrate the effect of Si on the structural and optical properties of core-shell InGaN/GaN microrods. For sample A (C6364A), the GaN microrod was grown using a reactor pressure of 300 Torr, and a constant silane flow of 0.2 µmol/min was supplied throughout for 720 s to enhance the vertical growth rate. Sample B (C6525A) was grown at a reactor pressure of 500 Torr. A similar silane flow was supplied only for 120 s to initiate the vertical growth. The silane flow was then ramped down to 0.02 µmol/min in 60 seconds and continued for another 240 s for the nanorod growth. After the GaN microrod growth, five-period core-shell InGaN/GaN multiple quantum wells were grown under identical conditions for both samples with a V/III ratio of 5000 at 300 Torr and using N_2 as the carrier gas. The InGaN QWs were grown at 730°C and the GaN barriers were grown at 885°C.

6.2.2 Microrod Emissive Properties

Microrods from sample A are shown in Fig.6.3. We can see from the panchromatic CL image shown in Fig.6.3.b that only the top 1 μm of the rods is brightly emitting.

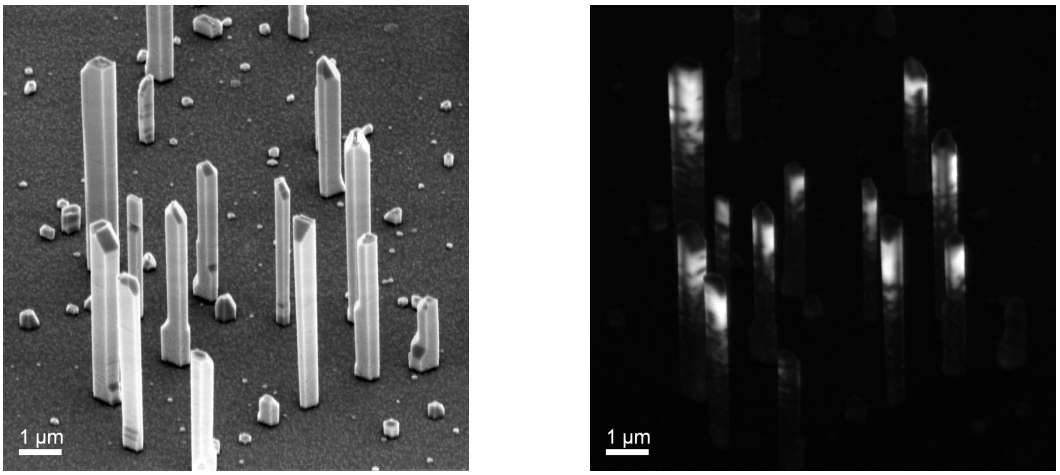

(a) (b)

Fig. 6.3 a) SEM micrograph and b) panchromatic CL image at 5 kV of microrods from sample A. Images courtesy of Dr. Tongtong Zhu.

Microrods from sample B are shown in Fig.6.4. In contrast to the rods shown in Fig.6.3, rods from the sample B show relatively uniform emission in the panchromatic CL, though some dark regions are observable at the base of some rods.

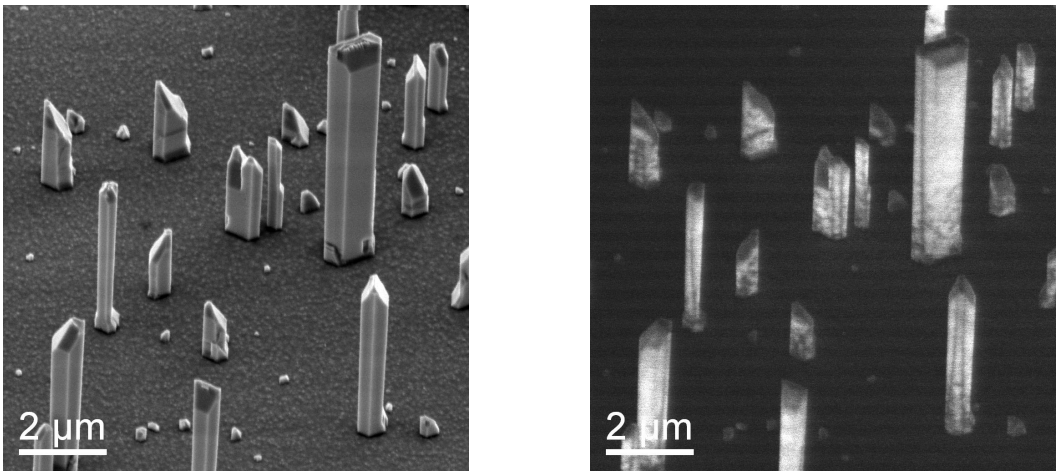

(a) (b)

Fig. 6.4 a) SEM micrograph and b) panchromatic CL image at 5kV of microrods from sample B. Images courtesy of Dr. Tongtong Zhu.

Microrods from both samples were harvested and dispersed on a silicon substrate for correlated optical and structural analysis. A representative rod harvested from sample A is shown in Fig.6.5. A CL linescan was taken through the centre of the rod and is shown in Fig.6.6. The linescan was taken over approximately 6 μm (corresponding to the length of the rod) at a step size of 10 nm with a dwell time of 0.5s per acquisition.

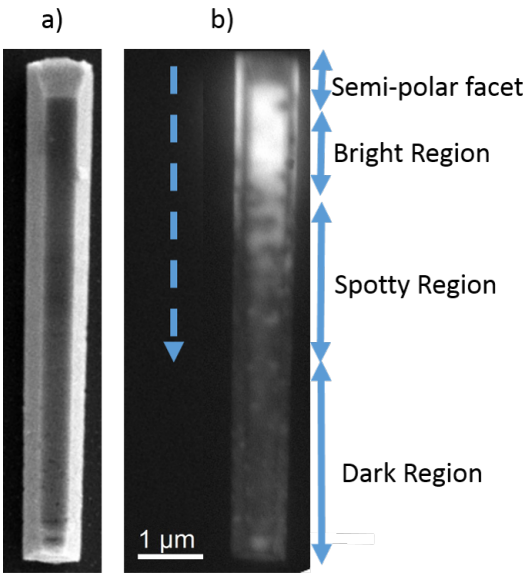

Fig. 6.5 a) SEM image and b) panchromatic CL for a rod harvested from sample A on a silicon substrate. Different regions of the rod which are apparent in the panchromatic CL are labelled.

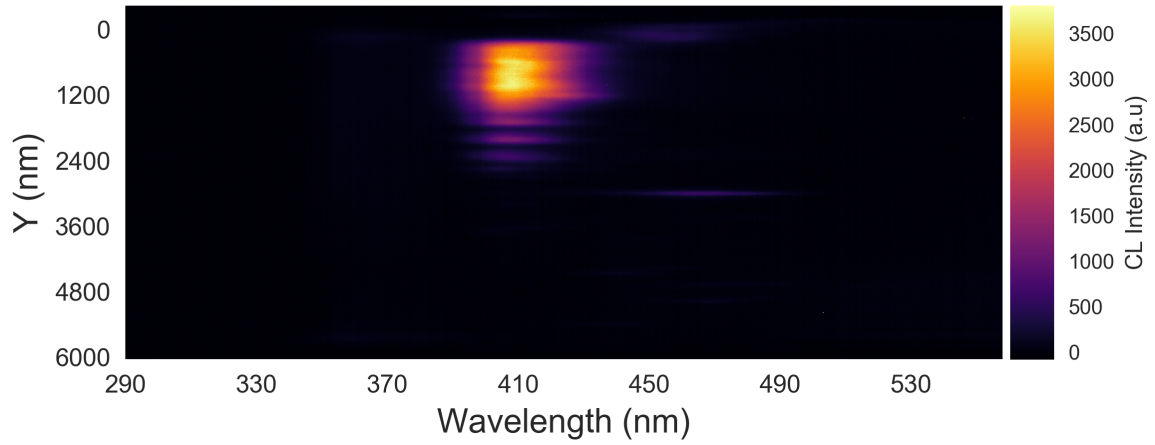

Fig. 6.6 CL linescan taken at 10 nm steps along a rod from sample A denoted by the dashed blue arrow in Fig.6.5.

Moving from the top to the bottom of the rod the trend shown by Fig.6.6 is clear: the CL emission eventually vanishes. Sample CL spectra taken from different regions of the rod are shown below in Fig.6.7, with their respective normalisation factors. It appears that emission from the darker portion of the rod with a peak at 448 nm is greatly redshifted relative to the upper regions which shows peak CL emission around 410 nm.

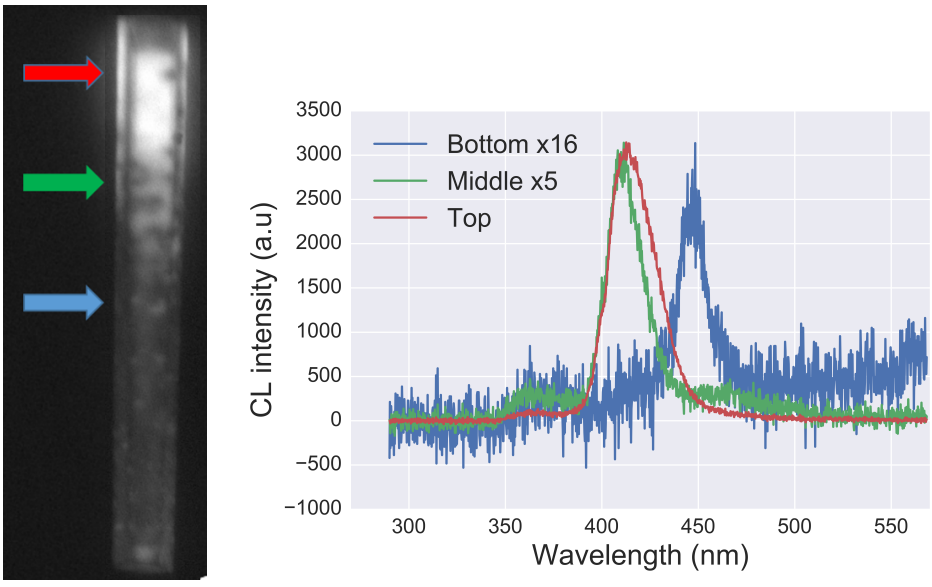

(a) (b)

Fig. 6.7 a) Panchromatic CL image showing the locations at which the CL spectra were taken b) CL spectra taken from the top, middle and bottom of the linescan with the respective normalisation factors shown in the legend.

The same experiment was repeated with rods harvested from sample B. These microrods exhibited far more homogeneous emission, as evidenced by the panchromatic CL image shown in Fig.6.8.b.

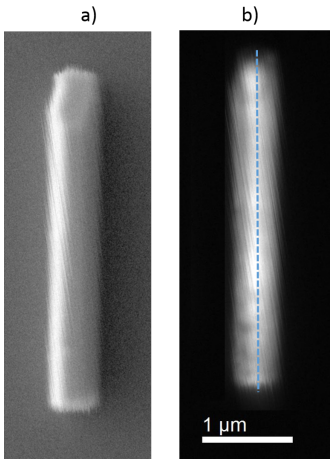

Fig. 6.8 a) SEM image and b) panchromatic CL for a rod harvested from sample B on a silicon substrate. The dashed blue line shows the location of the CL line scan.

A line scan along the entire length of the brightly emitting rod was taken with a step size of 14 nm and a dwell time of 0.5 s per acquisition, the location of the linescan is denoted by the dashed blue line in Fig.6.8.b. The linescan data is shown in Fig.6.9. We can observe that although there is a slight shfiting of the peak CL wavelength and a reduction in the CL linewidth along the length of the microrod, the peak intensity remains relatively constant from the top to the bottom when compared with the microrod harvested from sample A.

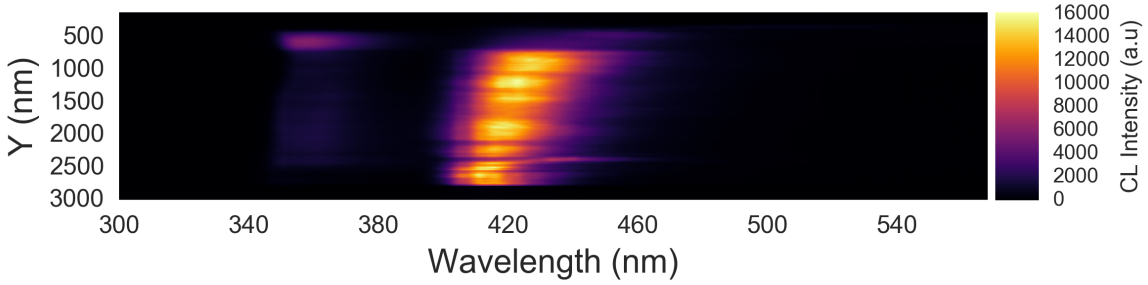

Fig. 6.9 CL line scan denoted by the dashed blue arrow in Fig.6.8.

Non-normalised Individual CL spectra taken from the top, middle and bottom regions of the rod are shown in Fig.6.10.b. We can observe that the peak CL intensities observed along the rod are generally consistent from the top to the bottom of this microrod when compared to the results from microrod A.We note the peak CL wavelength shifts from 420 nm to 408 nm moving from the top to the bottom of the rod, an effect which can also be seen in Fig.6.9.

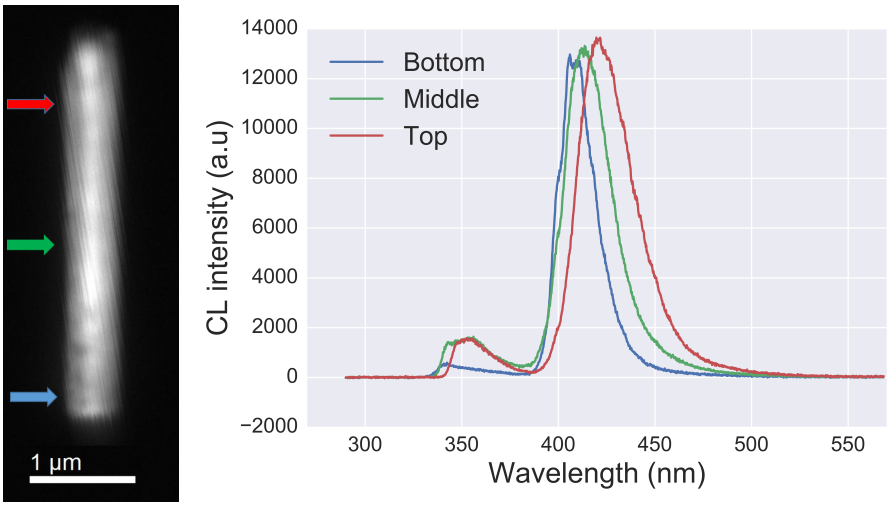

(a) (b)

Fig. 6.10 a) Panchromatic CL image showing the locations at which the CL spectra were taken b) CL spectra taken from the top, middle and bottom of the linescan.

6.2.3 Microrod Structure and Composition

6.2.3.1 STEM

In order to elucidate the structural differences between the brightly emitting and dark portions of sample A we fabricated axial cross-sections of nanorod by FIB.

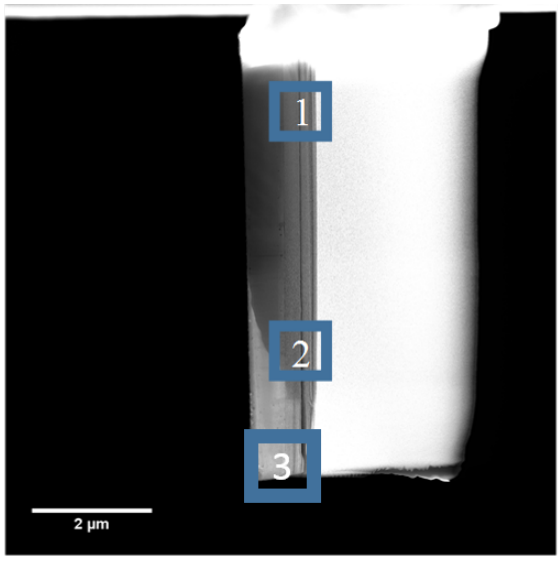

Fig. 6.11 Low magnification STEM-HAADF image of a TEM lamella of the rod shown in Fig.6.5 prepared by FIB.

A HAADF-STEM image of a sample prepared from a microrod harvested from sample A is shown in Figure 6.11, with regions of interest denoted '1' corresponding to a brightly emitting region and '2,3' to dark region in the CL, as shown in Fig.6.5.b. STEM-HAADF images from region 1 are shown below in Fig.6.12, in which we can see the morphology of the non-polar QWs. These images show few structural perturbations in the rod morphology.

This is in stark contrast to Fig.6.13, which shows STEM-HAADF images taken in region 2. In this region we can see the QW stack and surface of the microrod are non-uniform, features which can be linked to the presence of the defect outlined in Fig.6.13.b which is likely to be a void defect as evidenced by the darker contrast in HAADF-STEM and the well defined void facets which are similar in morphology to those described by Yankovich *et al.* [164].

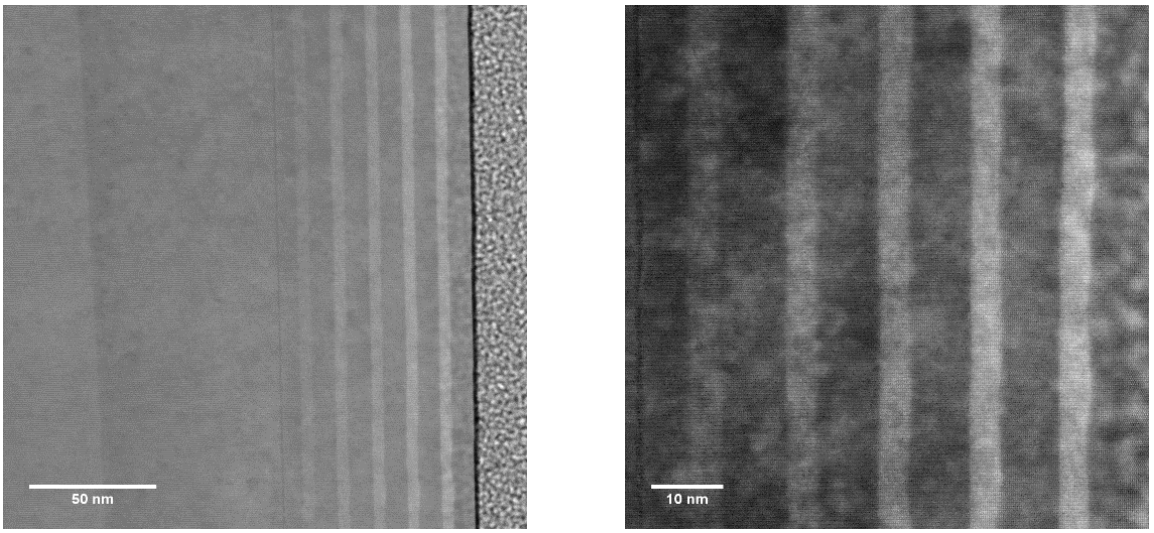

(a) (b)

Fig. 6.12 STEM-HAADF images taken from region 1 of the rod from sample A.

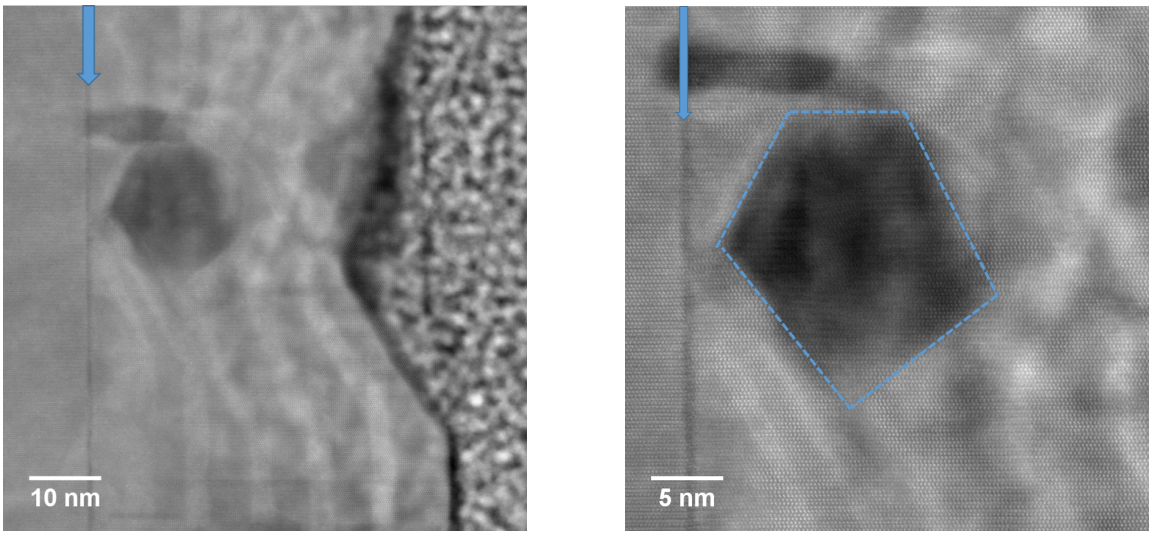

(a) (b)

Fig. 6.13 STEM-HAADF images taken from region 2 of the rod from sample A. The dark feature highlighted by the blue arrow is present in both the top and bottom regions of the rod. A large void defect is highlighted by the dashed lines.

A STEM-BF image of region 2, highlighting the presence of voids (green arrows) and features providing darker contrast which are believed to be stacking faults (blue arrows) in this region, corresponding well to the lower region of rods from sample A which exhibited little to no emission in the CL. Although stacking faults themselves have been shown to emit luminescence (though only when examined at low temperature in the CL), they are often bound by partial dislocations which themselves act as non-radiative recombination centres [30]. The presence of voids is expected to increase the local density of surface states, thus also providing an increase in non-radiative recombination centres [164]. Both types of defects are expected to quench CL emission, as seen at the bottom of microrods from sample A.

Fig.6.15 shows a STEM-BF image taken of region 3 of the microrod. Here we can observe the microrod contains a high density of defects, and the microrod surface is highly corrugated due to the sub-optimal growth conditions. The approximate regions where the QW stack should be are delineated by the dashed lines. There is a distinct lack of the QW stack in these regions when compared to the image taken from region 2 shown in Fig.6.14, indicating this region is also likely to show little to no CL emission, in good agreement with the CL data shown in Fig.6.5.b. Large voids are labelled using the red circles.

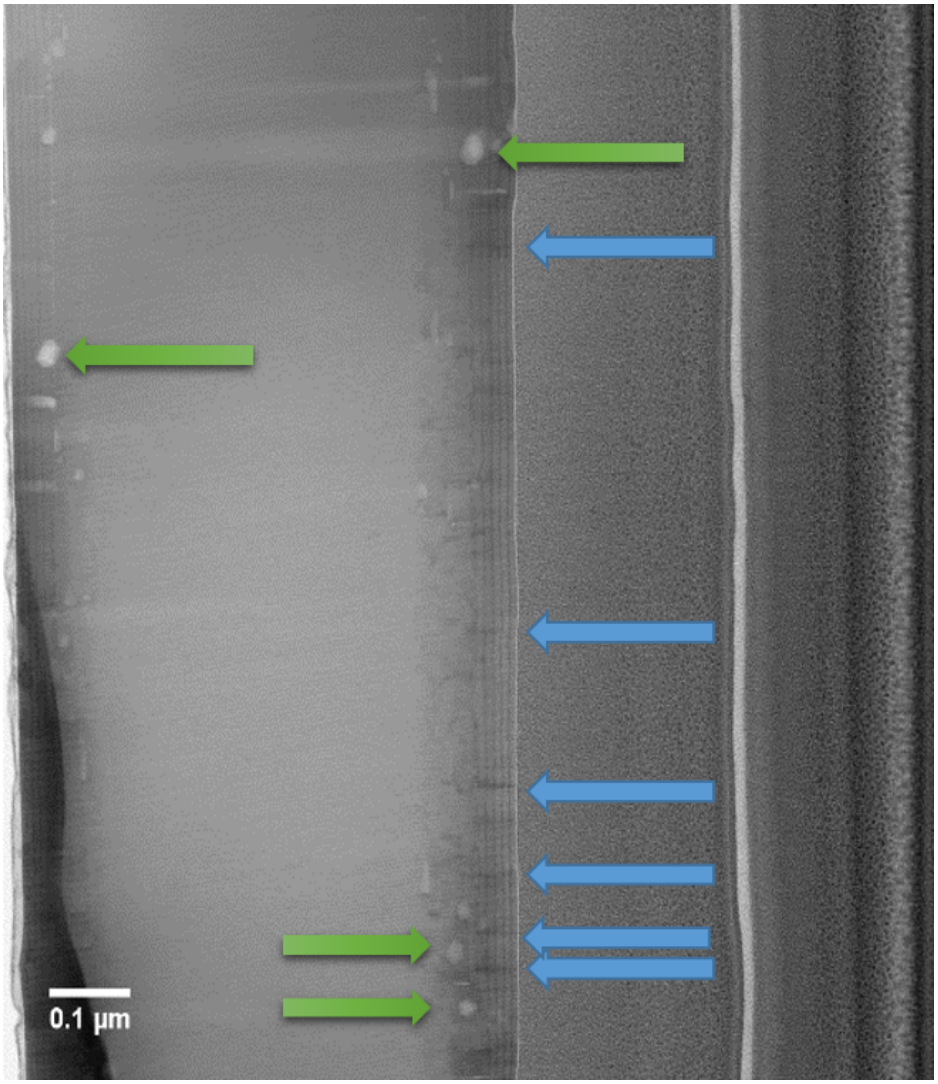

Fig. 6.14 Low magnification STEM-BF image of region 2 from sample A, chosen to highlight the presence of stacking faults, which appear darker in contrast in STEM-BF.

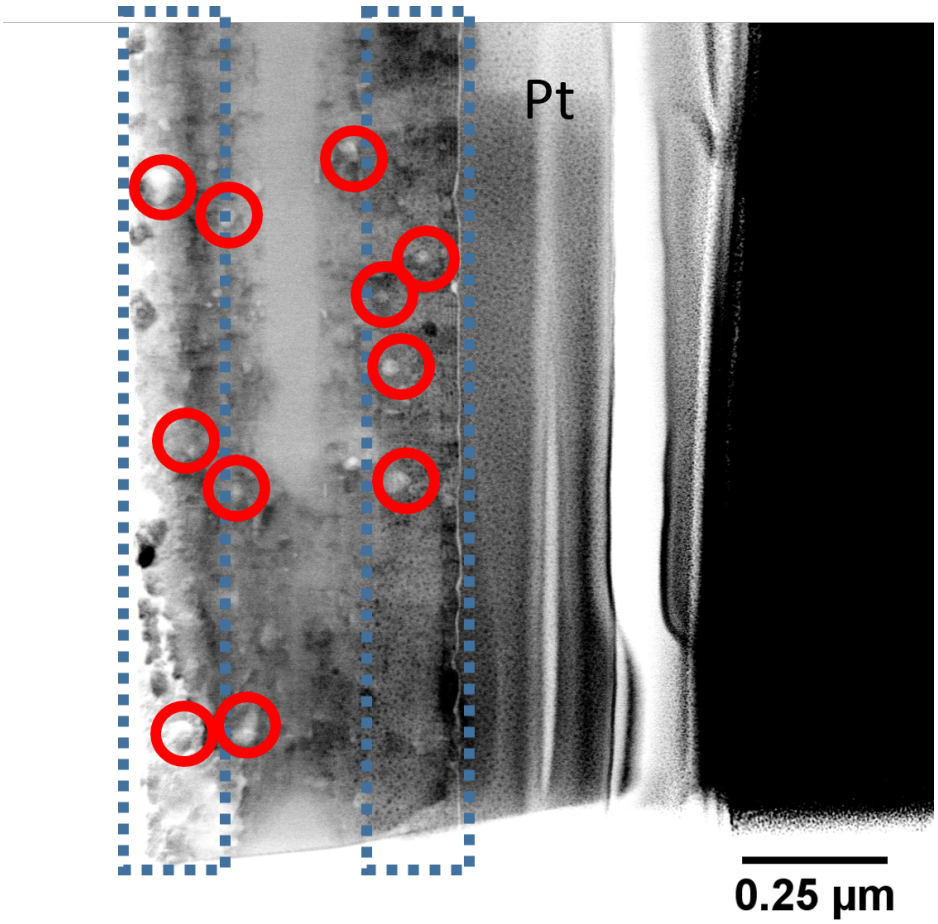

Fig. 6.15 Low magnification STEM-BF image of region 3 from sample A, chosen to highlight the presence of voids and the non-uniform morphology of the microrod in this region. Large voids are labelled using the red circles, and the regions which are expected to contain the QW stack are delineated by the dashed lines.

We repeated this analysis on a TEM lamella prepared from a rod harvested from sample B. STEM-HAADF images from the top and bottom of this rod are shown in Fig.6.16.a. and b respectively. In these images once can observe that the bottom of this rod exhibits a morphology far more consistent with that at the top of the rod. Fig.6.16.b shows a representative STEM-HAADF image of the bottom region of a microrod from sample B where the 'voids' seen at the bottom of the rod in Fig.6.13 are present in far lower densities. Some changes in morphology were still observed at the bottom of this rod, such as the bend in the QW stack shown in Fig.6.16.b, delineated by the red ellipsoid. Fig.6.17 shows further examples of non-uniformity in the QW stack in the bottom region of a microrod from sample B. In Fig.6.17.a we can see the distortion of the QW spacing in the stack Fig.6.17.b shows the disruption of the QW stack due to the presence of a void. These disruptions to the structure of the rod are however far fewer in number than those observed for the rod from sample A and shown in Fig.6.13.

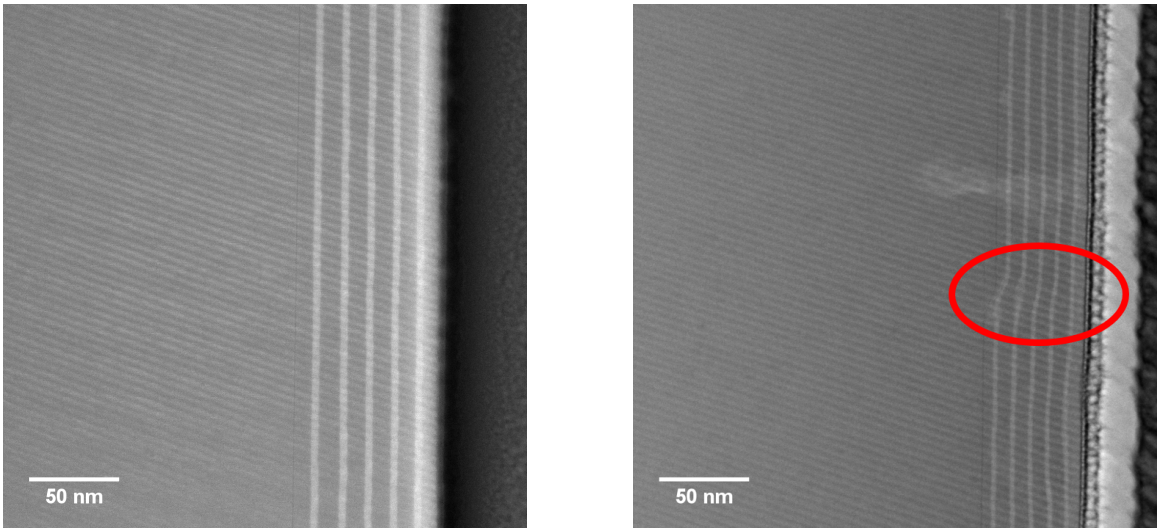

(a) (b)

Fig. 6.16 STEM-HAADF images taken from a) the top and b) the bottom of a rod harvested from sample B.

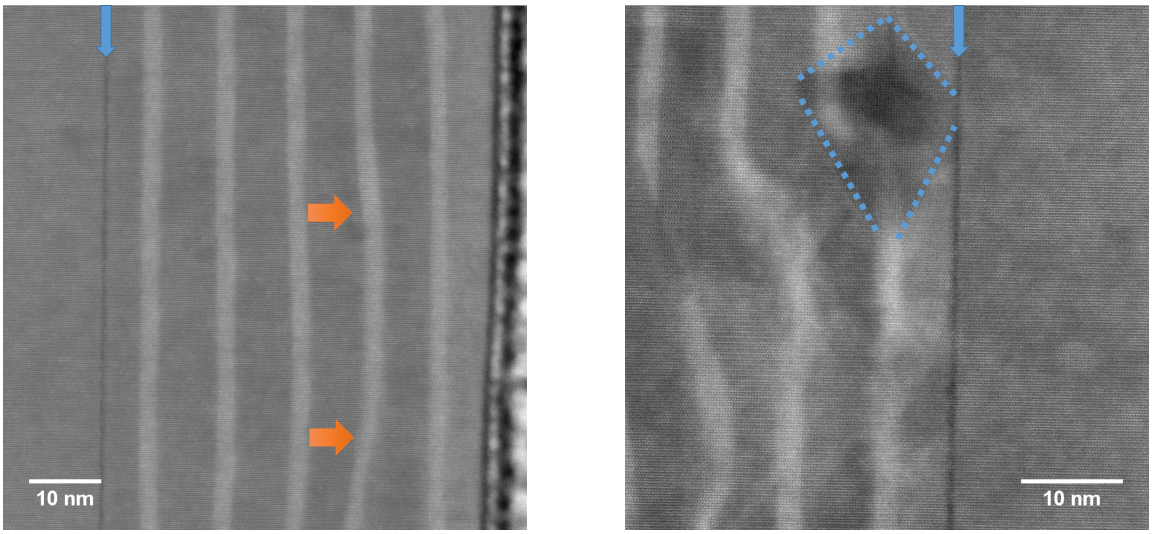

(a) (b)

Fig. 6.17 STEM-HAADF images of a) QW distortion and b) void related disruption of the QW stack in the lower region of a rod harvested from sample B.

A common feature for rods taken from both samples is the dark contrast which can be observed preceding the first QW from the rod core and is highlighted using the blue arrows in figures 6.13 and 6.17. The composition and origin of this feature will be investigated further in the rest of this work.

6.2.4 The Effect of Si on Microrod Growth

Tessarek *et al.* have reported the observation of a similar thin layer of dark contrast in STEM-HAADF images taken of microrods grown by MOVPE using a similar recipe to those described in section 6.1.1. Using STEM-EDX, the authors reported the presence of Si in this layer and attributed this to the formation of a SiN_x layer present due to the supply of post-growth supply of ammonia [161]. In this section we will confirm the presence of Si in this layer in our microrods and examine the effect of this on microrod emission and morphology.

6.2.4.1 Dual Plan-View TEM Lamella Preparation

In order to characterise the SiN_x layer seen in the previous section, as well as to lay the ground work for future correlated experiments studying changes along the length of the microrods we devised a method of producing multiple TEM lamellae from a single rod using the FIB/SEM dual-beam, thus allowing for the characterisation of multiple sections along

the growth axis. To our knowledge this is the first time this procedure has been carried out. The methodology is presented in Fig.6.18 which shows the following: the target rod is first welded onto the Omniprobe as is typical in FIB/SEM-based TEM lamella preparation methods. Following this, a stub consisting of Pt is deposited on the TEM grid, in order to ensure the final axial section is not obscured by the grid itself when examined in the TEM due to the small cross-sectional dimensions of the rod as shown in Fig.6.18.a. The rod is then attached onto the stub at the location along the rod from which we wish to produce a sample (shown in Fig.6.18.b). This rest of the rod is then released using ion-beam milling as shown in Fig.6.18.c, thus allowing for this process to be repeated as many times as the length of the rod will allow. This section of the rod is then thinned down to electron transparency using standard FIB sample preparation methods. A prepared sample is shown in Fig.6.18.d. We estimate that this method allows for sections to be cut at intervals of 400-500 nm along microrod. In this particular case we have performed the process twice, producing one axial sample from the top and one from the bottom of rods from both sample A and B.

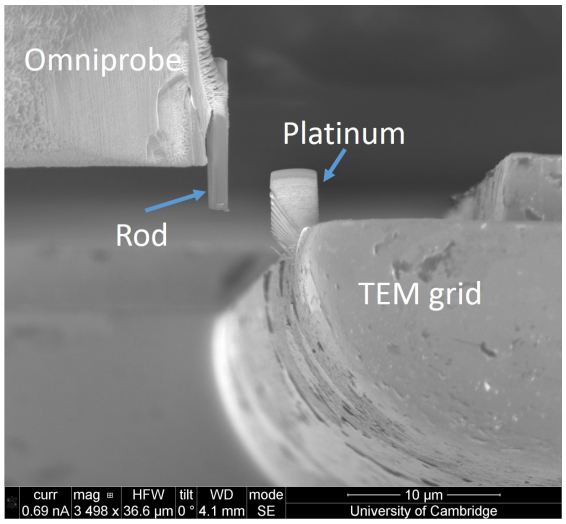

(a) Approach

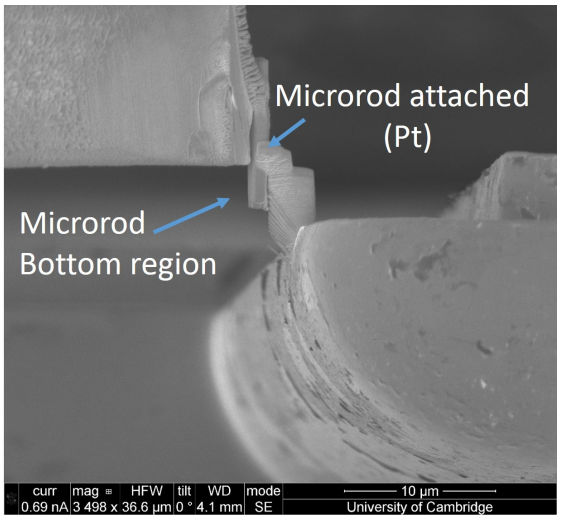

(b) Welding

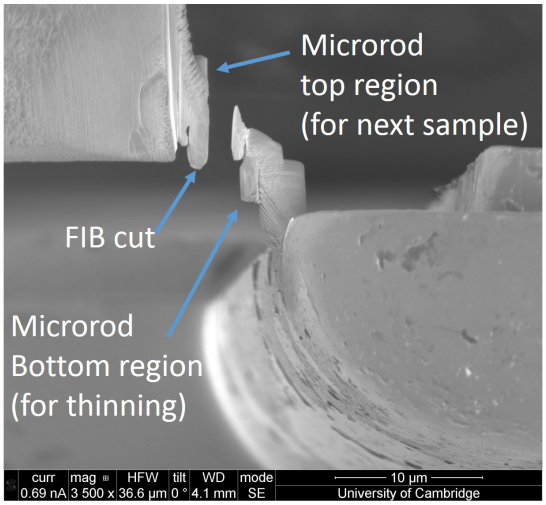

(c) Release

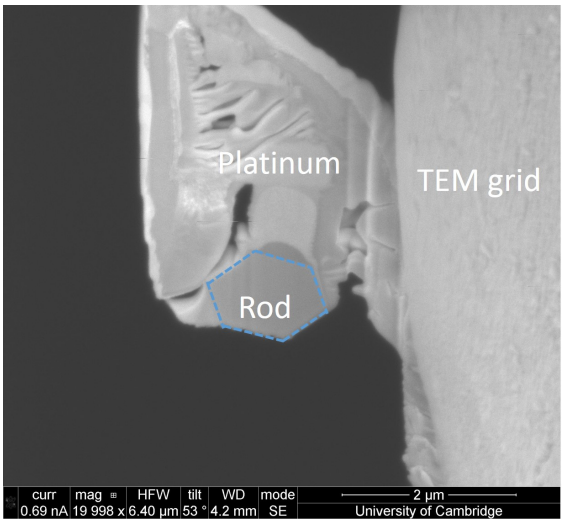

(d) Final lamella

Fig. 6.18 Axial cross-section lamella preparation. The three steps shown above (a, b and c) may be repeated as many times as the length of the rod allows, allowing for the preparation of multiple cross-sections from the same rod. d) shows a finished sample, viewed along the microrod growth axis (this image is taken at 45 degrees relative to the other three images in this set).

6.2.4.2 Si Content Quantification

As discussed in section 6.1.1, the two microrod samples were grown with different silane flows. In section 6.2.3.1 we have examined structural differences between the top and bottom of both rods, corresponding to differences to CL emission homogeneity as shown in 6.2.2. Furthermore we have shown the presence of a feature preceding the QW stack in STEM-HAADF which is believed to be a SiN_x layer resulting from the silane flow necessary to enhance vertical rod growth [161]. In this section we will use STEM-EDX in order to confirm the presence of Si in this layer, and investigate the relationship between the Si content and structural and emissive properties of the rods. For this experiment we have prepared plan-view samples from the top and bottom of rods harvested from both sample A and B. Fig.6.20.a shows a portion of a plan-view TEM sample prepared from the bottom of a rod from sample A. The radial growth of the rod beyond the dark layer (labelled using the blue arrows) seems to have been hindered, heavily disrupting the growth of QWs and resulting in a smaller rod radius, in this case the distance between the thin, dark layer and the edge of the rod is approximately 20 nm.

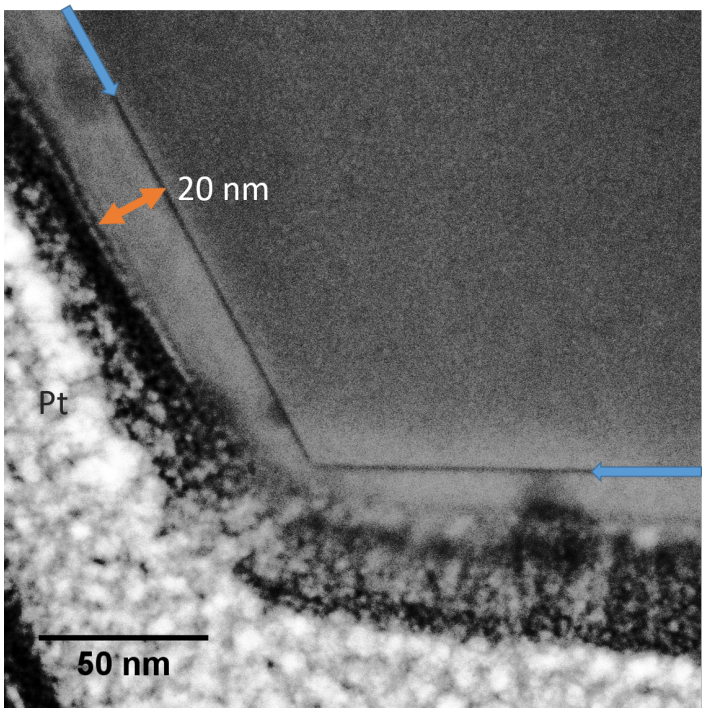

Fig. 6.19 a) STEM-HAADF image of a TEM sample prepared from the bottom of a rod from sample A. The contrast in this image has been enhanced for clarity.

Fig.6.20.b shows the presence of a low In content (2.0-3.5 %) in this region, suggesting the growth conditions at the bottom of rods from sample A can result in the formation of

a thick low In content layer rather than a QW stack. This disruption in the growth of the QW stack has been shown in Fig.6.15. As such the low CL emission observed at the bottom of rods harvested from sample A may be due not only to the presence of voids and defects disrupting the QW stack morphology and acting as non-radiative recombination centres, but simply also a lack of QW formation. Fig.6.20.c shows the Si content extracted from the EDX map, thus confirming the presence of Si in the layer generating dark contrast in the STEM-HAADF images. The Si content detected in this layer in this region is in the range 7-10%.

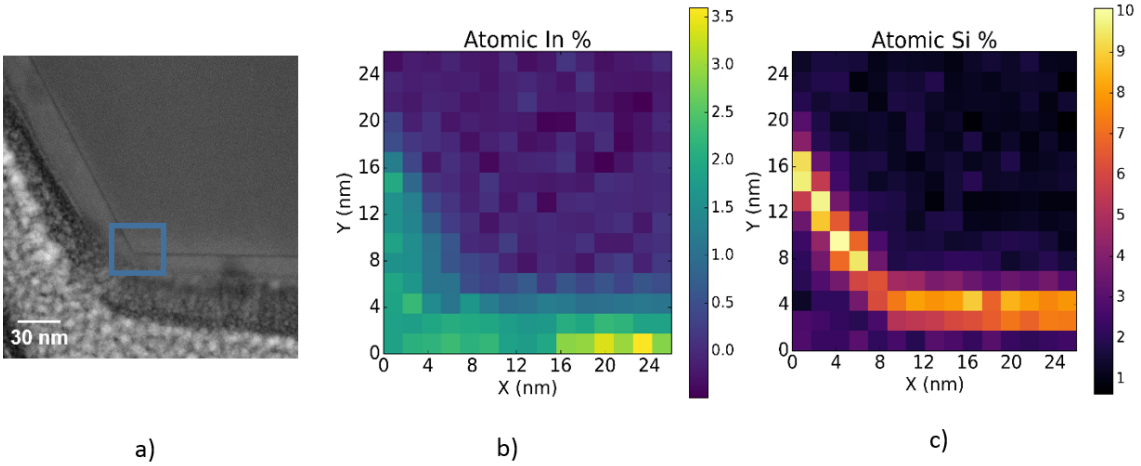

Fig. 6.20 a) STEM-HAADF image of a TEM sample prepared from the bottom of a rod from sample A b) In and c) Si content extracted from EDX maps taken from the region labelled by the blue box.

In the interpretation of these results it is important to consider the possibility this layer may be an extremely highly Si-doped GaN layer rather than a SiN_x layer. However, the results shown in Fig.6.20.b would indicate an Si doping concentration of approximately $4.5 \times 10^{21} cm^3$, an order of magnitude higher than the highest reported Si doping concentration of $2.8 \times 10^{20} cm^3$ in MBE grown nanowires [165] which was already reported to exceed the theoretically predicted Si solubility limit [166]. Furthermore, the N-rich conditions (see section 6.1.1) for the growth of these microrods is likely to result in the formation of a SiN_x [166]. As such, we attribute this dark layer seen in the STEM-HAADF images to the presence of a SiN_x layer. In light of this, it is also important to consider the quantified Si content of this layer is likely to be an underestimate: due to the fundamental limitation of electron-probe size in the microscope neighbouring layers are likely to be sampled with the SiN_x layer, resulting in an underestimate of the Si content in the layer. Markut *et al.* report the stochiometry of the SiN_x mask as a $SiGaN_3$ monolayer [167], on this basis of which

we expect the upper bound on the detected Si content to be 20 %, though it is important to note that the analysis performed by Markut *et al.* was performed on a *c*-plane structure and may differ slightly from that present on the *m*-plane facets of the microrods studied here. However, the porous morphology of the SiN_x mask [168] is crucial in interpreting the Si content detected by EDX here: as a result of this morphology we can expect the Si content to effectively be a measure of SiN_x coverage along the depth of the TEM lamella, thus providing us with a manner in which to quantitatively compare SiN_x coverage at different regions of the microrod. Fig.6.21.a. shows a STEM-HAADF image of a plan-view TEM sample prepared from the top of the same rod shown in Fig.6.20.a. Here we can see the QW stack has been formed, and the radius of the rod is larger beyond the SiN_x layer. Fig.6.21 shows the Si content of the SiN_x layer extracted from the EDX map, which in this region of the rod lies in the 2-5 % range, far lower than that detected in Fig.6.20.b at the bottom of the rod. We can thus hypothesize that the coverage of the SiN_x layer has an effect on the morphology of the QW stack and thus the optical properties of the rod.

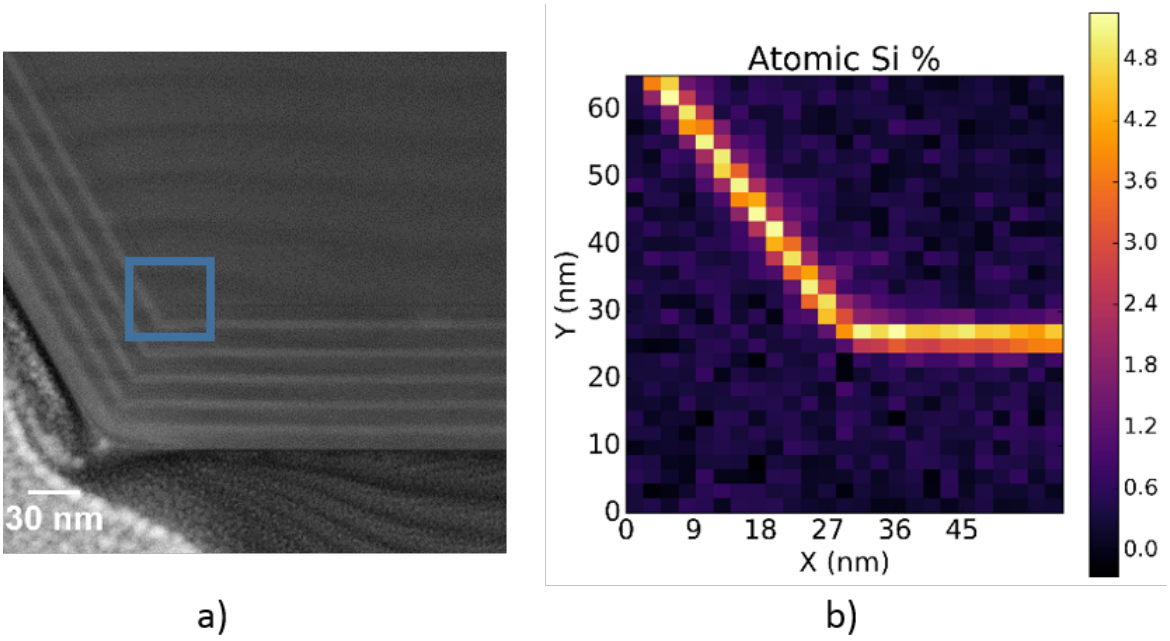

Fig. 6.21 a) STEM-HAADF image of a TEM sample prepared from the top of a rod from sample A b) Si content extracted from EDX maps take from the region labelled by the blue box.

The effects of SiN_x coverage on the structural and optical properties of the rods are supported by the figures 6.22 and 6.23 which show the same experiment performed on top and bottom regions of a microrod from sample B. As noted previously, rods from sample B exhibited CL emission over the majority of the length of the rod as opposed to only the

upper portion for rods from sample A. Fig.6.22.b shows the Si content of the SiN_x layer in the bottom portion of a rod harvested from sample B, which lies in the range 3-6.4% in the region examined. This Si content is very similar to that shown in Fig.6.23.b, which shows the value extracted in the upper region of the same rod which lies in 2.4-5.6%. As expected, this 'low' Si content corresponds to regions with good QW morphology and CL emission which are present along the majority of the rod length for sample B.

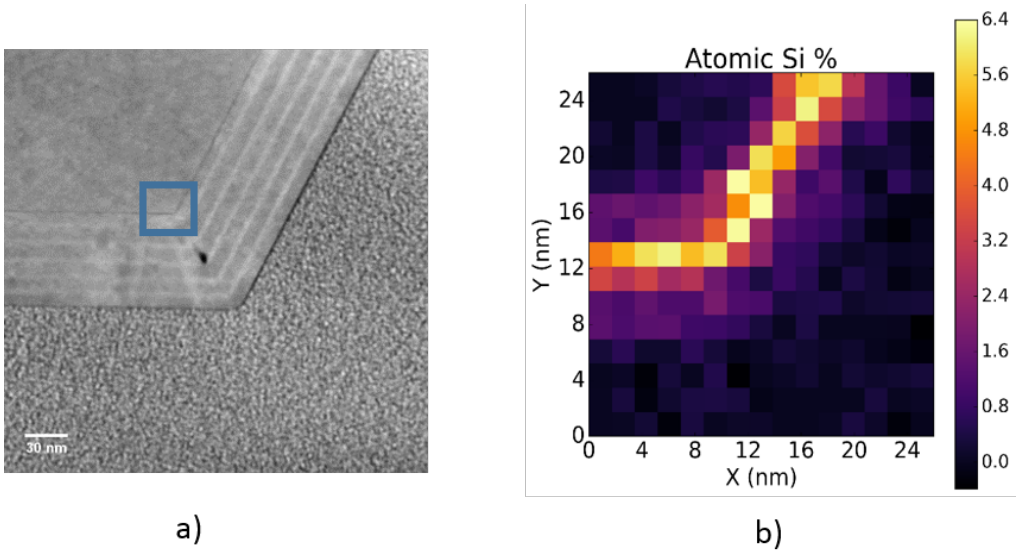

Fig. 6.22 a) STEM-HAADF image of a TEM sample prepared from the bottom of a rod from sample B b) Si content extracted from EDX maps take from the region labelled by the blue box.

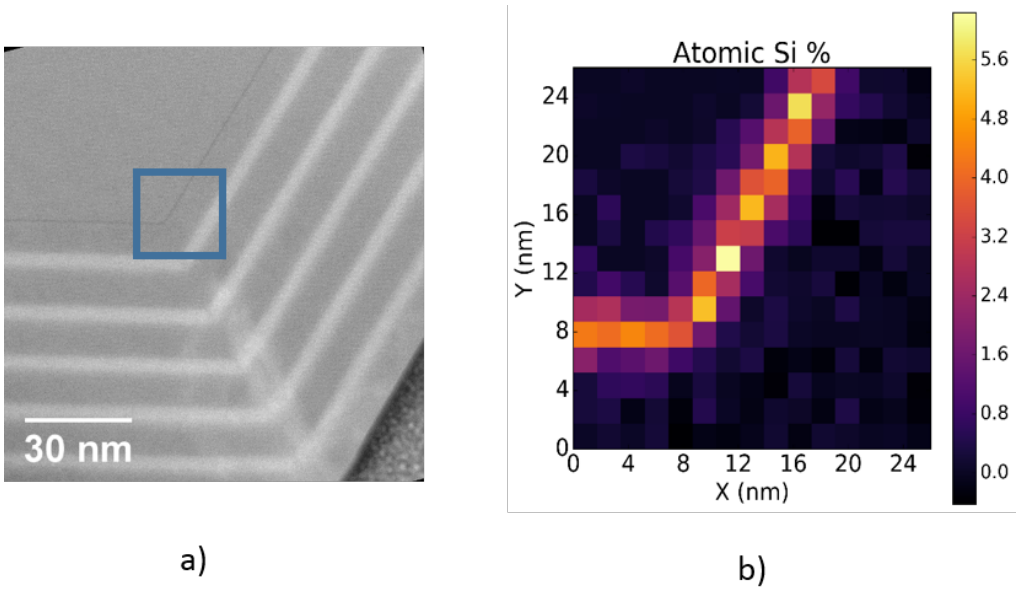

Fig. 6.23 a) STEM-HAADF image of a TEM sample prepared from the top of a rod from sample B b) Si content extracted from EDX maps take from the region labelled by the blue box.

The results from the plan-view samples are summarised in the table below. The peak fitting process performed in Hyperspy allows for the estimation of error and is within 1-2% for the measurements here.

Table 6.1 SiN_x layer Si atomic %

	Bottom	Top
Sample A	7-10 %	2-5 %
Sample B	3-6.4 %	2.4-5.6 %

6.2.4.3 Discussion

The use of silane to generate an SiN_x nanomask during epitaxial GaN growth was first reported by Vennéguès *et al.* [169]. Since then, the use of an SiN_x as an interlayer for the reduction of threading dislocation densities in III-nitride epitaxial films has been thoroughly investigated [170, 168, 171]. Tanaka *et al.* also demonstrated the use of silane as a surfactant in inducing three-dimensional growth resulting in GaN quantum dots (QDs) with dimensions of approximately 100 nm on an AlGaN surface [172]. Oliver *et al.* have also exploited this effect in inducing the growth of InGaN islands on GaN, noting an increase in InGaN island density with increasing pre-growth silane exposure time [173]. The porous SiN_x layer

resulting from the introduction of silane results in islands grown from the holes in the mask whilst the mask itself hinders the growth of the epitaxial layer, thus inducing 3D growth. This is shown in Fig.6.24.

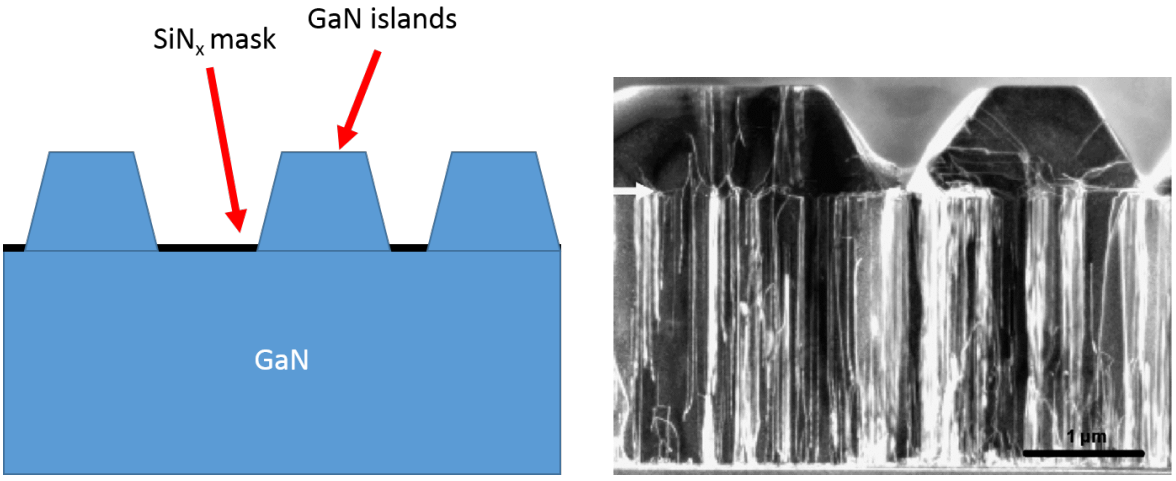

(a) (b)

Fig. 6.24 a) Schematic of SiN_x induced 3D growth and b) cross-sectional TEM image of an SiN_x interlayer (white arrow) on a GaN layer with GaN islands grown through the holes in the SiN_x layer. Adapted from [168]. Note that the SiN_x layer thickness is not to scale here, and has been expanded for the sake of clarity.

Tessarek *et al.* suggest that the formation of the SiN_x layer on the non-polar facets of microrods is due to the presence of a Ga-droplet located at the top of the GaN rods during growth [161]. The Ga-droplet transforms into GaN due to the ammonia supply during post-growth cool down, and as such is only observable if the ammonia supply is interrupted during cool down. This droplet is highly attractive for Ga atoms in the gas phase and on the sidewalls of the microrod during growth, whilst Si and N atoms experience less adsorbance in this droplet due to their low solubility in liquid Ga [174, 175] thus resulting in a higher concentration of Si and N atoms on the microrod sidewall surfaces during growth. Following the growth of the microrod core during which silane is supplied (see section 6.1.1), ammonia is supplied continuously as the growth temperature is ramped down for QW growth temperature, thus resulting in the formation of the SiN_x layer. This combination of silane and ammonia is typically used to grow SiN_x on GaN [170]. We expect the SiN_x coverage to be greater at the bottom of the rod, which experiences a longer silane exposure time during the growth process.

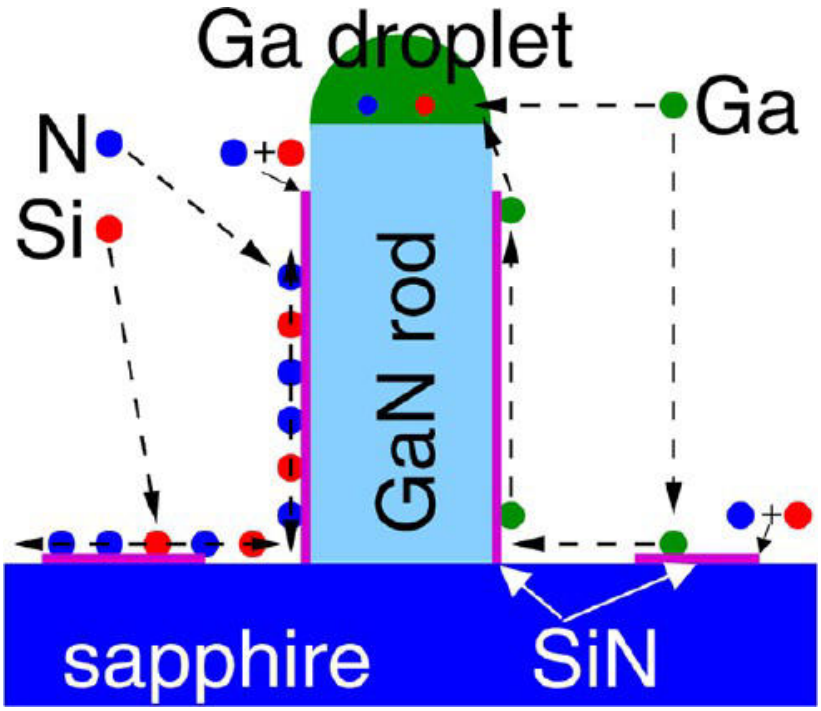

Fig. 6.25 Schematic of the SiN_x layer formation process: Si and N atoms experience low solubility in the Ga-droplet at the top of the rod and are thus present in greater concentration on the sidewall facets of the microrod. Reproduced from [161].

In the context of the rods studied in this work, it is crucial to relate the Si content detected in the STEM-EDX experiments to the SiN_x layer coverage. Reduced SiN_x coverage resulting either from a lower silane concentration or a lower exposure time [176, 177] will lead to smoother surfaces as a result of complete GaN island overgrowth and coalescence prior to the growth of the InGaN QW stack. Xie *et al.* reported incomplete coalescence of an overgrown GaN layer on a SiN_x layer for SiN_x deposition times exceeding 360 seconds [176] even following a GaN overgrowth thickness of 4.5 μm. As such, we expect the coverage of the SiN_x layer on the non-polar facets of the rods can heavily influence the subsequent growth of the InGaN QW stack and thus the optical properties of the rod. Indeed, in areas at the bottom of rods from sample A which show low emission in the CL we note the presence of voids, which are likely to result from the incomplete lateral coalescence of islands grown from the SiN_x layer such as the feature shown in Fig.6.13.b. Indeed, the presence of voids has been reported in epitaxial layer overgrowth (ELOG) of GaN, where a mask is intentionally used to induce 3D growth in order to reduce dislocation densities, as shown in Fig.6.26 [178, 179].

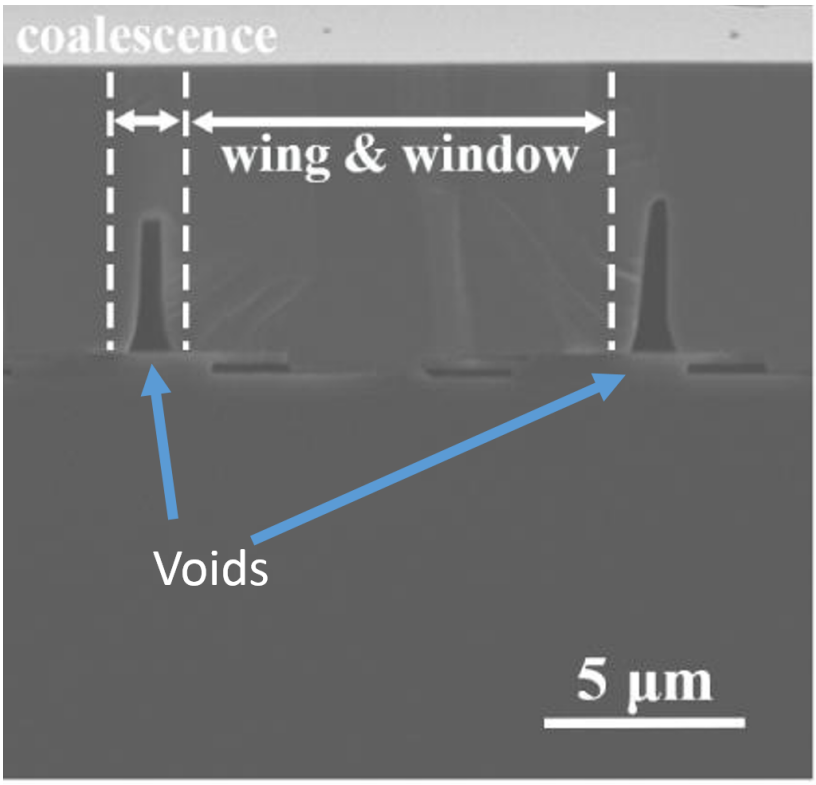

Fig. 6.26 Cross-sectional SEM image showing voids formed during ELOG of GaN. Adapted from [179]. In the context of ELOG, 'wing' and 'window' describe sections of the epilayer grown laterally over the mask and from the holes in the mask respectively.

Thus, though the use of silane is helpful in enhancing the vertical growth of the rods, the exposure time and silane concentration must be tailored carefully in order to achieve optimal coalescence conditions and thus obtain a uniform QW stack morphology and smooth microrod surface to allow for uniform emission over the length of the rod, a property desirable for applications such as LEDs and lasers. It is also important to note that the 'roughening' property of the SiN_x on the subsequent growth of III-nitride epitaxial layers is in some cases desirable, specifically in the growth of confined nanostructures such as QDs. As previously discussed, the use of nanomasks to grow III-nitride QDs [172, 180, 181] has been thoroughly investigated in *c*-plane growth. As such, for applications such as single photon sources where QDs are required, the silane flow during the growth of the microrods may be tailored to encourage roughening of the subsequent InGaN active region in an attempt to grow non-polar QDs on the sidewall facets of the microrods.

6.3 Summary

In this section we have examined the effect of Si on the morphology and optical properties of GaN/InGaN core-shell rods. Using SEM-CL we have shown the optical properties of the rods are heavily dependent on the silane concentration and exposure time during the rod growth, as reduced silane concentration and exposure time resulted in a more homogeneously emitting rod. By performing STEM-HAADF imaging on cross-sectional TEM lamellae prepared from the rods we correlated poorly emitting regions in the CL with regions containing a large amount of defects such as stacking faults and voids, as well as poor surface morphology. Following this we performed STEM-EDX on axial cross-sections prepared from the top and bottom regions of the rods, demonstrating a higher Si content detected in the SiN_x layer of the rods in regions with poor morphology, high defect densities and poor CL emission. We have also related the detected Si content of the SiN_x to the porosity of this layer, which heavily influences the subsequent overgrowth and coalescence of the GaN/InGaN active region. As such, we have determined that although the use of silane during rod growth is important to enhance growth in the vertical direction, it is also crucial to keep the silane concentration and exposure time as low as possible in order to maintain uniform microrod morphology and optical properties.

6.4 Future Work

We have used axial cross-section lift out methods to examine the effect of SiN_x coverage on microrod structure and emission. In the future, we may use correlated CL - radial cross-section TEM measurements to establish the structural cause of specific features in the emission such the blue shift of the QW emission going along the rod shown in Fig.6.9. It is also valuable to attempt to tune the silane concentration and flow to maximise the length of the rod whilst maintaining good optical and structural properties. Halting the growth of the rods early may be useful in examining the manner in which SiN_x induces 3D growth on the non-polar facets of the rod, as well as the manner in which growth parameters may affect the subsequent coalescence of the 3D islands grown from the SiN_x mask. In terms of further exploring the optical properties of the microrods, temperature dependent micro-PL experiments may be useful in determining the internal quantum efficiency of rods grown under different conditions. The presence of WGMs has been reported in III-nitride microrods [182], as such it may also be of interest to examine homogeneously emitting rods for WGM based lasing.

Chapter 7

Concluding Remarks

The work in this thesis has consisted of the use and development of various microscopy techniques in order to perform correlated measurements on III-nitride photonic devices and materials, relating their structural and optical properties.

We have utilised multiple microscopy techniques to identify the cause of inhomogeneous EL in III-nitride LEDs. Hyperspectral EL and SEM-CL mapping was performed over a set of inhomogeneities in order to determine their spectral properties. Examination of the features in the SEM-CL revealed the presence of large hexagonal defects at the centre of the inhomogeneities. A TEM lamella containing the apex of the hexagonal defect was produced using a FIB-based technique based on the deposition of marker layers. This allowed for STEM-EDX mapping of the region surrounding the defect apex, revealing the presence of Al from the AlGaN EBL in the active region. Conventional TEM techniques were used to observe a bundle of TDs associated with the hexagonal defect, establishing that the defects are likely due to sub-optimal template growth conditions. APSYS simulations demonstrated the presence of *p*-doped AlGaN can indeed enhance local EL through the injection of holes into the active region, establishing the presence of *p*-doped material within the active region due to the hexagonal defect as a likely cause for the inhomogeneities observed.

Factors hindering the fabrication of III-nitride cavity structures were studied using a combination of TEM and tomography. The presence of unetched material on the underside of microdisk cavities has been shown to deleteriously affect the cavity's optical properties. Using FIB sample preparation methods we have extracted a portion of unetched material from the underside of a microdisk cavity and identified the presence of an edge dislocation in this material. Furthermore we have show the feasibility in using FIB-tomography in studying the roughness and damage caused by improper PEC etching. Wehave also extended these FIB-based sample preparation and tomography methods to the study of 1-D photonic crystal cavities in the form of suspended nanobeams fabricated using a two-step etching process.

Due to the complex geometric requirements for these cavities relative to microdisks we have found that both electron tomography and FIB tomography provide methods to elucidate issues in the fabrication process related to the etching and lithography, albeit with several intrinsic limitations to both the ET and FIBT experiments which require consideration when interpreting the data.

The effect of Si on the morphology and optical properties of GaN/InGaN core-shell rods was studied using a correlated microscopy approach. Panchromatic CL revealed the effect of silane concentration and exposure time during the rod growth on the optical properties of the microrods. By performing STEM-HAADF imaging on cross-sectional TEM lamellae prepared from the rods we established the presence of an SiN_x layer preceding the first QW of the active region was observed, whilst also correlating poorly emitting regions in the CL with regions containing a large amount of defects such as stacking faults and voids, as well as poor surface morphology. By quantifying the Si content of the SiN_x in different regions of the rod and relating this to the coverage of the SiN_x we established that lower SiN_x coverage results in more complete coalescence of the microrod sidewalls, thus resulting in uniform QW morphology and emission along the length of the microrod.

It is important to note the crucial role the FIB/SEM dual-beam instrument has played in this research involving correlated microscopy. The versatility and accuracy of the ion-beam milling allows for the preparation of TEM samples from specific regions of samples, albeit in a destructive manner. The destructive nature of the ion-beam and the amorphisation and gallium implantation it can induce in crystalline III-nitride samples is also an important consideration: in the preparation of thin samples the induced damage can run throughout the thickness of the specimen if not controlled. Nonetheless, we have shown throughout this work that the dual-beam instrument effectively bridges the gap between site-specific luminescence spectroscopy such as CL and nanoscopic structural and compositional analysis techniques such as STEM. With regards to the use of the dual-beam instrument to perform tomography, we note the limiting factor in terms of the depth resolution which is the slice thickness. In order to further improve the depth resolution of FIBT reconstructions, future experiments may involve the use of instruments such as the ORION nano-fab which contains additional neon and helium ion-beams and enables slicing down to thicknesses of 5 nm. This type of instrument would also provide an increase in imaging resolution (approximately 0.5 nm), thus improving the overall resolution of the FIBT experiments. We also note the general improvement this type of instrument would provide for the TEM sample preparation process, as metallic contamination is eliminated when using inert gas ion beams for micromachining processes.

The incorporation of further microscopy techniques may help in providing more depth to these correlated studies. Particularly in cases where the roughness of surfaces is studied, such as the etched microcavities and the microrods, AFM may be useful in providing an accurate benchmark against which to compare roughness values evaluated by ET and FIBT. PL spectroscopy would be particularly useful in evaluating the Q-factors for the microdisks and nanobeams studied by tomography, and in conjunction with FDTD simulations may provide an excellent platform from which to optimise the fabrication of such cavities. In the study of the effect of Si on the growth of microrods, it may be useful to apply aberration-corrected HRTEM to the SiN_x combined with DFT calculations to elucidate the stochiometry and structure of the non-polar masking layer, as has been performed by Market *et al.* for the polar equivalent.

The surprising robustness of III-nitride photonic devices to defects, when compared to other III-V semiconductor materials has perhaps ironically made the study of defects a crucial part of research in III-nitride materials. This is a theme present throughout this work: we have presented the manner in which defects can distort the EL of LEDs, their disruptive nature in the PEC etching of undercut cavities and the correlation between their presence and the quenching of CL in microrods. In fact, the correlated study of the optical and structural properties of III-nitride materials may not be so fascinating without the presence of defects: it is their ability to distort their local structural and electrical properties that make this type of study relevant within this materials group.

Beyond the III-nitride group of materials, the tomography techniques studied here may be particularly useful in studying fabricated cavities in general. Q-factors of cavities are often much higher in materials outside the III-nitrides, partially due to the high chemical and thermal stability of the nitrides resulting in difficult fabrication. As such, we expect the optical properties of cavities fabricated from other material groups to be far more sensitive to variations in thickness and roughness and truly test the resolution limits of the tomography techniques presented here.

Finally, it is hoped that the work presented in this thesis has demonstrated the value in performing studies correlating the optical and structural properties of semiconductor materials, and the crucial role the FIB/SEM dual-beam instrument has played in enabling these studies.

References

[1] C. J. Humphreys, "USE Solid-State Lighting," *MRS Bulletin*, vol. 33, no. April, pp. 459–471, 2008.

[2] S. Nakamura, T. Mukai, and M. Senoh, "High-Power GaN P-N Junction Blue-Light-Emitting Diodes," *Japanese Journal of Applied Physics*, vol. 30, no. 12A, pp. 1998–2001, 1991.

[3] S. Najda, P. Perlin, L. Marona, M. Leszczy, R. Czernecki, S. Watson, A. E. Kelly, A. Malcolm, P. Blanchard, and H. White, "Novel laser diode technology for free-space communications," *SPIE*, pp. 10–12, 2015.

[4] H. Berlien, H. Breuer, G. Müller, N. Krasner, T. Okunata, and D. Sliney, *Applied Laser Medicine*. Springer Berlin Heidelberg, 2012.

[5] S. Kako, C. Santori, K. Hoshino, S. Götzinger, Y. Yamamoto, and Y. Arakawa, "A gallium nitride single-photon source operating at 200 K.," *Nature materials*, vol. 5, pp. 887–92, nov 2006.

[6] S. E. Bennett, "Dislocations and their reduction in GaN," *Materials Science and Technology*, vol. 26, no. 9, pp. 1017–1028, 2010.

[7] E. T. Yu, X. Z. Dang, P. M. Asbeck, S. S. Lau, and G. J. Sullivan, "Spontaneous and piezoelectric polarization effects in III-nitride heterostructures," *Journal of Vacuum Science & Technology B: Microelectronics and Nanometer Structures*, vol. 17, p. 1742, 1999.

[8] I. Vurgaftman and J. R. Meyer, "Band parameters for nitrogen-containing semiconductors," *Journal of Applied Physics*, vol. 94, no. 6, pp. 3675–3696, 2003.

[9] M. E. Vickers, M. J. Kappers, T. M. Smeeton, E. J. Thrush, J. S. Barnard, and C. J. Humphreys, "Determination of the indium content and layer thicknesses in InGaN/GaN quantum wells by x-ray scattering," *Journal of Applied Physics*, vol. 94, no. 3, pp. 1565–1574, 2003.

[10] F. Scholz, "Semipolar GaN grown on foreign substrates: a review," *Semiconductor Science and Technology*, vol. 27, p. 024002, feb 2012.

[11] J. Wu, W. Walukiewicz, K. M. Yu, J. W. Ager, E. E. Haller, H. Lu, and W. J. Schaff, "Small band gap bowing in $In_{1-x}Ga_xN$ alloys," *Applied Physics Letters*, vol. 80, no. 25, pp. 4741–4743, 2002.

[12] M. D. McCluskey, C. G. Van de Walle, L. T. Romano, B. S. Krusor, and N. M. Johnson, "Effect of composition on the band gap of strained $In_xGa_{1-x}N$ alloys," *Journal of Applied Physics*, vol. 93, no. 7, pp. 4340–4342, 2003.

[13] P. G. Moses and C. G. Van De Walle, "Band bowing and band alignment in InGaN alloys," *Applied Physics Letters*, vol. 96, no. 2, pp. 2–5, 2010.

[14] T. J. Puchtler, A. Woolf, T. Zhu, D. Gachet, E. L. Hu, and R. A. Oliver, "Effect of Threading Dislocations on the Quality Factor of InGaN/GaN Microdisk Cavities," *ACS Photonics*, vol. 2, pp. 137–143, 2015.

[15] C. X. Ren, "Polarisation fields in III-nitrides: effects and control," *Materials Science and Technology*, vol. 00, no. 0, p. 1743284715Y.000, 2015.

[16] O. Ambacher and J. Majewski, "Pyroelectric properties of Al (In) GaN/GaN hetero- and quantum well structures," *Journal of physics: D*, vol. 3399, 2002.

[17] M. Sumiya and S. Fuke, "Review of polarity determination and control of GaN," *MRS Internet Journal of Nitride Semiconductor Research*, vol. 9, no. 1, pp. 1–32, 2004.

[18] C. Wood and D. Jena, *Polarization Effects in Semiconductors: From Ab Initio Theory to Device Applications*. Springer, 2007.

[19] J. E. R. Miguel, C. J. Gladys, and O. L. César, "Computational calculation of the electronic and magnetic properties of 1x1-MN / GaN (M = V , Cr and Mn) multilayers," *International Journal of Physical Sciences*, vol. 9, no. 24, pp. 538–544, 2014.

[20] V. Fiorentini, F. Bernardini, F. D. Sala, A. D. Carlo, P. Lugli, and T. Vergata, "Effects of macroscopic polarization in III-V nitride multiple quantum wells," *Physical Review B*, vol. 60, no. 12, pp. 8849–8858, 1999.

[21] S. F. Chichibu, A. Uedono, T. Onuma, B. A. Haskell, A. Chakraborty, T. Koyama, P. T. Fini, S. Keller, S. P. Denbaars, J. S. Speck, U. K. Mishra, S. Nakamura, S. Yamaguchi, S. Kamiyama, H. Amano, I. Akasaki, J. Han, and T. Sota, "Origin of defect-insensitive emission probability in In-containing (Al,In,Ga)N alloy semiconductors.," *Nature materials*, vol. 5, pp. 810–6, oct 2006.

[22] J. H. Ryou, P. D. Yoder, J. Liu, Z. Lochner, H. S. Kim, S. Choi, H. J. Kim, and R. D. Dupuis, "Control of quantum-confined stark effect in InGaN-based quantum wells," *IEEE Journal on Selected Topics in Quantum Electronics*, vol. 15, no. 4, pp. 1080–1091, 2009.

[23] M. A. Reshchikov and H. Morko, "Luminescence properties of defects in GaN," *Journal of Applied Physics*, vol. 97, no. 6, 2005.

[24] H. Strite, S., Morkoç, "GaN, AlN, and InN: A review," *Journal of Vacuum Science & Technology B*, vol. 10, no. 4, pp. 1237–1266, 1992.

[25] R. People and J. C. Bean, "Calculation of critical layer thickness versus lattice mismatch for Ge_xSi_{1-x}/Si strained-layer heterostructures," *Applied Physics Letters*, vol. 47, no. 3, p. 322, 1985.

[26] X. Ning and F. Chien, "Growth defects in GaN films on sapphire: The probable origin of threading dislocations," *Journal of materials . . .* , no. 0001, 1996.

[27] M. A. Moram, C. S. Ghedia, D. V. S. Rao, J. S. Barnard, Y. Zhang, M. J. Kappers, and C. J. Humphreys, "On the origin of threading dislocations in GaN films," *Journal of Applied Physics*, vol. 106, no. 7, p. 073513, 2009.

[28] R. A. Oliver, M. J. Kappers, C. McAleese, R. Datta, J. Sumner, and C. J. Humphreys, "The origin and reduction of dislocations in Gallium Nitride," *Journal of Materials Science: Materials in Electronics*, vol. 19, pp. 208–214, mar 2008.

[29] L. Z.-Y. Liu, *Advanced Transmission Electron Microscopy of GaN-based Materials and Devices*. PhD thesis, University of Cambridge, 2011.

[30] J. Lahnemann, U. Jahn, O. Brandt, T. Flissikowski, P. Dogan, and H. T. Grahn, "Luminescence associated with stacking faults in GaN," *Journal of Physics D: Applied Physics*, vol. 47, no. 42, p. 423001, 2014.

[31] W. Rieger, R. Dimitrov, D. Brunner, E. Rohrer, O. Ambacher, and M. Stutzmann, "Defect-related optical transitions in GaN," *Physical Review B*, vol. 54, no. 24, p. 17596, 1996.

[32] Y. Rebane, Y. Shreter, and M. Albrecht, "Stacking Faults as Quantum Wells for Excitons in Wurtzite GaN," *Physica Status Solidi (a)*, vol. 164, no. 141, 1997.

[33] J. Lahnemann, O. Brandt, U. Jahn, C. Pfüller, C. Roder, P. Dogan, F. Grosse, A. Belabbes, F. Bechstedt, A. Trampert, and L. Geelhaar, "Direct experimental determination of the spontaneous polarization of GaN," *Physical Review B*, vol. 86, pp. 1–5, 2012.

[34] G. Nogues, T. Auzelle, M. Den Hertog, B. Gayral, and B. Daudin, "Cathodoluminescence of stacking fault bound excitons for local probing of the exciton diffusion length in single GaN nanowires," *Applied Physics Letters*, vol. 104, p. 102102, mar 2014.

[35] A. Hangleiter, F. Hitzel, C. Netzel, D. Fuhrmann, U. Rossow, G. Ade, and P. Hinze, "Suppression of nonradiative recombination by V-shaped pits in GaInN/GaN quantum wells produces a large increase in the light emission efficiency," *Physical Review Letters*, vol. 95, no. 12, pp. 1–4, 2005.

[36] S. H. Han, D. Y. Lee, H. W. Shim, J. Wook Lee, D. J. Kim, S. Yoon, Y. Sun Kim, and S. T. Kim, "Improvement of efficiency and electrical properties using intentionally formed V-shaped pits in InGaN/GaN multiple quantum well light-emitting diodes," *Applied Physics Letters*, vol. 102, no. 25, 2013.

[37] H.-L. Tsai, T.-Y. Wang, J.-R. Yang, C.-C. Chuo, J.-T. Hsu, Z.-C. Feng, and M. Shiojiri, "Observation of V Defects in Multiple InGaN/GaN Quantum Well Layers," *Materials Transactions*, vol. 48, no. 5, pp. 894–898, 2007.

[38] S. Christopoulos, G. B. H. von Högersthal, A. J. D. Grundy, P. G. Lagoudakis, A. V. Kavokin, J. J. Baumberg, G. Christmann, R. Butté, E. Feltin, J.-F. Carlin, and N. Grandjean, "Room-Temperature Polariton Lasing in Semiconductor Microcavities," *Physical Review Letters*, vol. 98, no. 12, p. 126405, 2007.

[39] K. J. Vahala, "Optical microcavities," *Nature*, vol. 424, no. 6950, pp. 839–846, 2003.

[40] A. F. Jarjour, R. A. Taylor, R. A. Taylor, M. J. Kappers, C. J. Humphreys, and A. Tahraoui, "Cavity-enhanced blue single-photon emission from a single InGaN/GaN quantum dot," *Applied Physics Letters*, vol. 91, no. 5, p. 052101, 2007.

[41] I. Aharonovich, A. Woolf, K. J. Russell, T. Zhu, N. Niu, M. J. Kappers, R. A. Oliver, and E. L. Hu, "Low threshold, room-temperature microdisk lasers in the blue spectral range," *Applied Physics Letters*, vol. 103, no. 2, p. 021112, 2013.

[42] G. Malpuech, A. Di Carlo, A. Kavokin, J. J. Baumberg, M. Zamfirescu, and P. Lugli, "Room-temperature polariton lasers based on GaN microcavities," *Applied Physics Letters*, vol. 81, no. 3, pp. 412–414, 2002.

[43] A. Imamoglu, D. Awschalom, G. Burkard, D. P. DiVincenzo, D. Loss, M. Sherwin, and a. Small, "Quantum information processing using quantum dot spins and cavity QED," *Physical Review Letters*, vol. 83, no. 20, pp. 4204–4207, 1999.

[44] K. Hennessy, A. Badolato, M. Winger, D. Gerace, M. Atatüre, S. Gulde, S. Fält, E. L. Hu, and A. Imamoglu, "Quantum nature of a strongly coupled single quantum dot-cavity system," *Nature*, vol. 445, no. 7130, pp. 896–899, 2007.

[45] A. C. Tamboli, E. D. Haberer, R. Sharma, K. H. Lee, S. Nakamura, and E. L. Hu, "Room-temperature continuous-wave lasing in GaN/InGaN microdisks," *Nature Photonics*, vol. 1, pp. 61–64, jan 2007.

[46] S. Chang, N. B. Rex, R. K. Chang, G. Chong, and L. J. Guido, "Stimulated emission and lasing in whispering-gallery modes of GaN microdisk cavities," *Applied Physics Letters*, vol. 75, no. 2, p. 166, 1999.

[47] E. D. Haberer, R. Sharma, C. Meier, A. R. Stonas, S. Nakamura, S. P. DenBaars, and E. L. Hu, "Free-standing, optically pumped, GaN/InGaN microdisk lasers fabricated by photoelectrochemical etching," *Applied Physics Letters*, vol. 85, no. 22, p. 5179, 2004.

[48] D. Simeonov, E. Feltin, A. Castiglia, A. Castiglia, J. F. Carlin, R. Butte, and N. Grandjean, "High quality nitride based microdisks obtained via selective wet etching of AlInN sacrificial layers," *Applied Physics Letters*, vol. 92, no. 17, pp. 2008–2010, 2008.

[49] E. Yablonovitch, "Inhibited Spontaneous Emission in Solid-State Physics and Electronics," *Physical Review Letters*, vol. 58, no. 20, pp. 2059–2062, 1987.

[50] S. John, "Strong localization of photons in certain disordered dielectric superlattices," *Physical Review Letters*, vol. 58, no. 23, pp. 2486–2489, 1987.

[51] K. Ishizaki, M. Koumura, K. Suzuki, K. Gondaira, and S. Noda, "Realization of three-dimensional guiding of photons in photonic crystals," *Nature Photonics*, vol. 7, no. 2, pp. 133–137, 2013.

[52] A. Tandaechanurat, S. Ishida, D. Guimard, M. Nomura, S. Iwamoto, and Y. Arakawa, "Lasing oscillation in a three-dimensional photonic crystal nanocavity with a complete bandgap," *Nature Photonics*, vol. 5, no. 2, pp. 91–94, 2011.

[53] Y. Gong and J. Vukovic, "Photonic crystal cavities in silicon dioxide," *Applied Physics Letters*, vol. 96, no. 3, pp. 2009–2011, 2010.

[54] P. B. Deotare, M. W. McCutcheon, I. W. Frank, M. Khan, and M. Lončar, "High quality factor photonic crystal nanobeam cavities," *Applied Physics Letters*, vol. 94, no. 12, pp. 8–11, 2009.

[55] M. Notomi, E. Kuramochi, and H. Taniyama, "Ultrahigh-Q nanocavity with 1D periodicity," *Conference Proceedings - Lasers and Electro-Optics Society Annual Meeting-LEOS*, vol. 16, no. 15, pp. 689–690, 2008.

[56] P. Lalanne and J. P. Hugonin, "Bloch-Wave Engineering for High-Q, Small-V Microcavities," *IEEE Journal of Quantum Electronics*, vol. 39, no. 11, pp. 1430–1438, 2003.

[57] N. V. Triviño, R. Butté, J.-F. Carlin, and N. Grandjean, "Continuous Wave Blue Lasing in III-Nitride Nanobeam Cavity on Silicon," *Nano Letters*, vol. 15, no. 2, pp. 1259–1263, 2015.

[58] N. Niu, A. Woolf, D. Wang, T. Zhu, Q. Quan, R. A. Oliver, and E. L. Hu, "Ultra-low threshold gallium nitride photonic crystal nanobeam laser," *Applied Physics Letters*, vol. 106, no. 23, p. 231104, 2015.

[59] M. Arita, S. Ishida, S. Kako, S. Iwamoto, and Y. Arakawa, "AlN air-bridge photonic crystal nanocavities demonstrating high quality factor," *Applied Physics Letters*, vol. 91, no. 5, p. 051106, 2007.

[60] W. H. P. Pernice, C. Xiong, C. Schuck, and H. X. Tang, "High-Q aluminum nitride photonic crystal nanobeam cavities," *Applied Physics Letters*, vol. 100, no. 9, 2012.

[61] A. Bao, "Group iii-nitride nanowires," *Materials Science and Technology*, vol. 0, no. 0, pp. 1–12, 2016.

[62] S. Arafin, X. Liu, and Z. Mi, "Review of recent progress of III-nitride nanowire lasers," *Journal of Nanophotonics*, vol. 7, no. 1, pp. 074599–074599, 2013.

[63] J. C. Johnson, H.-J. Choi, K. P. Knutsen, R. D. Schaller, P. Yang, and R. J. Saykally, "Single gallium nitride nanowire lasers.," *Nature materials*, vol. 1, no. 2, pp. 106–110, 2002.

[64] F. Qian, Y. Li, S. Gradecak, H.-G. Park, Y. Dong, Y. Ding, Z. L. Wang, and C. M. Lieber, "Multi-quantum-well nanowire heterostructures for wavelength-controlled lasers.," *Nature materials*, vol. 7, no. 9, pp. 701–706, 2008.

[65] A. Das, J. Heo, M. Jankowski, W. Guo, L. Zhang, H. Deng, and P. Bhattacharya, "Room temperature ultralow threshold GaN nanowire polariton laser," *Physical Review Letters*, vol. 107, no. 6, pp. 1–5, 2011.

[66] C.-y. Wu, C.-t. Kuo, C.-y. Wang, and C.-l. He, "Plasmonic Green Nanolaser Based on a Metal-Oxide-Semiconductor Structure," *Nano letters*, pp. 4256–4260, 2011.

[67] S. Deshpande, J. Heo, A. Das, and P. Bhattacharya, "Electrically driven polarized single-photon emission from an InGaN quantum dot in a GaN nanowire.," *Nature communications*, vol. 4, p. 1675, jan 2013.

[68] M. J. Holmes, K. Choi, S. Kako, M. Arita, and Y. Arakawa, "Room-Temperature Triggered Single Photon Emission from a III-Nitride Site-Controlled Nanowire Quantum Dot.," *Nano letters*, jan 2014.

[69] Y. Zhang, *Characterisation of GaN using Transmission Electron Microscopy*. PhD thesis, University of Cambridge, 2008.

[70] C. B. C. David B. Williams, *Transmission Electron Microscopy*. Springer US, 2009.

[71] M. A. Moram, Y. Zhang, M. J. Kappers, Z. H. Barber, and C. J. Humphreys, "Dislocation reduction in gallium nitride films using scandium nitride interlayers," *Applied Physics Letters*, vol. 91, no. 15, p. 152101, 2007.

[72] A. Howie, "Image contrast and localized signal selection techniques," *Journal of Microscopy*, 1979.

[73] "Characteristic x-rays." http://www.ammrf.org.au/myscope/analysis/eds/xraygeneration/characteristic/.

[74] G. Divitini, *Electron microscopy studies of photo-active TiO2 nanostructures*. PhD thesis, University of Cambridge, 2012.

[75] D. J. De Rosier and A. Klug, "Reconstruction of Three Dimensional Structures from Electron Micrographs," *Nature*, vol. 217, pp. 130–134, 1968.

[76] P. A. Midgley and R. E. Dunin-Borkowski, "Electron tomography and holography in materials science.," *Nature materials*, vol. 8, no. 4, pp. 271–280, 2009.

[77] G. Möbus and B. J. Inkson, "Nanoscale tomography in materials science," *Materials Today*, vol. 10, no. 12, pp. 18–25, 2007.

[78] N. Kawase, M. Kato, H. Nishioka, and H. Jinnai, "Transmission electron microtomography without the "missing wedge" for quantitative structural analysis," *Ultramicroscopy*, vol. 107, no. 1, pp. 8–15, 2007.

[79] J. J. Fernández, J. I. Agulleiro, A. Martínez, I. García, and F. J. Chichón, "Image processing in electron tomography," *Microscopy: Science, Technology, Applications and Education*, no. Figure 1, pp. 19–28, 2010.

[80] P. A. Midgley and M. Weyland, "3D electron microscopy in the physical sciences: The development of Z-contrast and EFTEM tomography," *Ultramicroscopy*, vol. 96, no. 3-4, pp. 413–431, 2003.

[81] P. Gilbert, "Iterative methods for the three-dimensional reconstruction of an object from projections," *Journal of Theoretical Biology*, vol. 36, no. 1, pp. 105–117, 1972.

[82] P. A. Penczek, "Fundamentals of Three-Dimensional Reconstruction from Projections," pp. 1–33, 2010.

[83] J. Frank, *Electron Tomography*. Springer New York, 2006.

[84] R. A. Oliver, "Advances in AFM for the electrical characterization of semiconductors," *Reports on Progress in Physics*, vol. 71, p. 076501, jul 2008.

[85] T. Zhu, *Nanoscale Electrical Characterisation of Gallium Nitride*. PhD thesis, University of Cambridge, 2010.

[86] B. Yacobi and D. Holt, *Cathodoluminescence Microscopy of Inorganic Solids*. Springer US, 1990.

[87] T. Puchtler, *Development of structures and materials for InGaN/GaN cavity quantum electro-dynamics*. PhD thesis, University of Cambridge, 2014.

[88] P. R. Edwards and R. W. Martin, "Cathodoluminescence nano-characterization of semiconductors," *Semiconductor Science and Technology*, vol. 26, p. 064005, jun 2011.

[89] R. W. Martin, P. R. Edwards, K. P. O'Donnell, M. D. Dawson, C.-W. Jeon, C. Liu, G. R. Rice, and I. M. Watson, "Cathodoluminescence spectral mapping of III-nitride structures," *Physica Status Solidi (a)*, vol. 201, pp. 665–672, mar 2004.

[90] P. Sercel, H. Zarem, J. Lebens, and L. Eng, "A novel technique for the direct determination of carrier diffusion lengths in GaAs/AlGaAs heterostructures using cathodoluminescence," *International Electron Devices Meeting*, pp. 285–288, 1989.

[91] C. L. Paul R. Edwards, Lethy Krishnan Jagadamma, Jochen Bruckbauer and R. W. M. Philip Shields, Duncan Allsopp, Tao Wang, "High-resolution cathodoluminescence hyperspectral imaging of nitride nanostructures," *Microscopy and Microanalysis*, pp. 1212–1219, 2012.

[92] N. M. Haegel, *Measurement of Minority Charge Carrier Diffusion Length in Gallium Nitride Nanowires Using Electron Beam Induced Current*. PhD thesis, Naval Postgraduate School, 2009.

[93] E. Yakimov, "Electron-beam-induced-current study of defects in GaN; experiments and simulation," *Journal of Physics: Condensed Matter*, vol. 13069, 2002.

[94] W. Jansen and M. Slaughter, "Elemental mapping of minerals by electron microprobe.," *American Mineralogist*, vol. 67, no. 5-6, pp. 521–533, 1982.

[95] M. J. Wallace, P. R. Edwards, M. J. Kappers, M. A. Hopkins, F. Oehler, S. Sivaraya, R. A. Oliver, C. J. Humphreys, D. W. E. Allsopp, and R. W. Martin, "Effect of the barrier growth mode on the luminescence and conductivity micron scale uniformity of InGaN light emitting diodes," *Journal of Applied Physics*, vol. 117, no. 11, p. 115705, 2015.

[96] T. Ishitani and T. Yaguchi, "Cross-sectional sample preparation by focused ion beam: a review of ion-sample interaction.," *Microscopy research and technique*, vol. 35, no. 4, pp. 320–333, 1996.

[97] S. Bals, W. Tirry, R. Geurts, Z. Yang, and D. Schryvers, "High-quality sample preparation by low kV FIB thinning for analytical TEM measurements.," *Microscopy and microanalysis : the official journal of Microscopy Society of America, Microbeam Analysis Society, Microscopical Society of Canada*, vol. 13, no. 2, pp. 80–86, 2007.

[98] L. Holzer, F. Indutnyi, P. Gasser, B. Münch, and M. Wegmann, "Three-dimensional analysis of porous $BaTiO_3$ ceramics using FIB nanotomography," *Journal of Microscopy*, vol. 216, no. 1, pp. 84–95, 2004.

[99] W. Rasband, "Imagej," 1997-2017.

[100] M. U. P. Thévenaz, U.E. Ruttimann, "A Pyramid Approach to Subpixel Registration Based on Intensity," *IEEE Transactions on Image Processing*, vol. 7, no. 1, pp. 27–41, 1998.

[101] W. E. Lorensen and H. E. Cline, "Marching cubes: A high resolution 3D surface construction algorithm," *Proceedings of the 14th annual conference on Computer graphics and interactive techniques - SIGGRAPH '87*, vol. 21, no. 4, pp. 163–169, 1987.

[102] N. K. V. D. Laak, R. A. Oliver, M. J. Kappers, and C. J. Humphreys, "Role of gross well-width fluctuations in bright , green-emitting single InGaN/GaN quantum well structures," *Appl. Phys. Lett.*, vol. 121911, no. 2007, pp. 1–4, 2013.

[103] R. A. Oliver, F. C.-P. Massabuau, M. J. Kappers, W. A. Phillips, E. J. Thrush, C. C. Tartan, W. E. Blenkhorn, T. J. Badcock, P. Dawson, M. A. Hopkins, D. W. E. Allsopp, and C. J. Humphreys, "The impact of gross well width fluctuations on the efficiency of GaN-based light emitting diodes," *Applied Physics Letters*, vol. 103, no. 14, p. 141114, 2013.

[104] A. Polyakov, N. Smirnov, A. Usikov, A. Govorkov, and B. Pushniy, "Studies of the origin of the yellow luminescence band, the nature of nonradiative recombination and the origin of persistent photoconductivity in n-GaN films," *Solid-State Electronics*, vol. 42, no. 11, pp. 1959–1967, 1998.

[105] S. Chichibu, A. Abare, M. Mack, M. Minsky, T. Deguchi, D. Cohen, P. Kozodoy, S. Fleischer, S. Keller, J. Speck, J. Bowers, E. Hu, U. Mishra, L. Coldren, S. DenBaars, K. Wada, T. Sota, and S. Nakamura, "Optical properties of InGaN quantum wells," *Materials Science and Engineering: B*, vol. 59, pp. 298–306, may 1999.

[106] J. L. Lyons, A. Janotti, and C. G. Van De Walle, "Carbon impurities and the yellow luminescence in GaN," *Applied Physics Letters*, vol. 97, no. 15, pp. 10–13, 2010.

[107] R. Oliver, M. Kappers, J. Sumner, R. Datta, and C. Humphreys, "Highlighting threading dislocations in MOVPE-grown GaN using an in situ treatment with SiH4 and NH3," *Journal of Crystal Growth*, vol. 289, pp. 506–514, apr 2006.

[108] K. Watanabe, J. R. Yang, S. Y. Huang, K. Inoke, J. T. Hsu, R. C. Tu, T. Yamazaki, N. Nakanishi, and M. Shiojiri, "Formation and structure of inverted hexagonal pyramid defects in multiple quantum wells InGaN/GaN," *Applied Physics Letters*, vol. 82, no. 5, pp. 718–720, 2003.

[109] M. Shiojiri, C. C. Chuo, J. T. Hsu, J. R. Yang, and H. Saijo, "Structure and formation mechanism of V defects in multiple InGaN/GaN quantum well layers," *Journal of Applied Physics*, vol. 99, no. 7, 2006.

[110] M. M. Da Silva, a. R. Vaz, S. a. Moshkalev, and J. W. Swart, "Electrical Characterization of Platinum Thin Films Deposited by Focused Ion Beam," *ECS Transactions*, vol. 9, no. 1, pp. 235–241, 2007.

[111] F. de la Peña, T. Ostasevicius, V. T. Fauske, P. Burdet, P. Jokubauskas, M. Sarahan, D. Johnstone, M. Nord, J. Taillon, J. Caron, K. E. MacArthur, E. Prestat, A. Eljarrat, S. Mazzucco, T. Furnival, M. Walls, G. Donval, B. Martineau, A. Garmannslund, L. F. Zagonel, T. Aarholt, C. Gohlke, and Iygr, "hyperspy v1.1.1,"

[112] G. Lorimer, "Quantitative X-ray microanalysis of thin specimens in the transmission electron microscope; a review," *Mineralogical Magazine*, vol. 51, no. 359, pp. 49–60, 1987.

[113] J. Piprek, *Nitride Semiconductor Devices: Principles and Simulation*. Wiley-VCH, january 20 ed., 2007.

[114] J. Pal, G. Tse, V. Haxha, M. A. Migliorato, and S. Tomić, "Second-order piezoelectricity in wurtzite III-N semiconductors," *Physical Review B - Condensed Matter and Materials Physics*, vol. 84, no. 8, pp. 1–7, 2011.

[115] J. Piprek, "Origin of InGaN/GaN light-emitting diode efficiency improvements using tunnel-junction-cascaded active regions," *Applied Physics Letters*, vol. 104, no. 5, pp. 2–6, 2014.

[116] Y. Li, F. Yun, X. Su, S. Liu, W. Ding, and X. Hou, "Deep hole injection assisted by large V-shape pits in InGaN/GaN multiple-quantum-wells blue light-emitting diodes," *Journal of Applied Physics*, vol. 116, no. 12, p. 123101, 2014.

[117] Z. Quan, L. Wang, C. Zheng, J. Liu, and F. Jiang, "Roles of V-shaped pits on the improvement of quantum efficiency in InGaN/GaN multiple quantum well light-emitting diodes," *Journal of Applied Physics*, vol. 116, no. 18, p. 183107, 2014.

[118] J. H. Son, J. U. Kim, Y. H. Song, B. J. Kim, C. J. Ryu, and J. L. Lee, "Design Rule of nanostructures in light-emitting diodes for complete elimination of total internal reflection," *Advanced Materials*, vol. 24, no. 17, pp. 2259–2262, 2012.

[119] D. I. Florescu, S. M. Ting, J. C. Ramer, D. S. Lee, V. N. Merai, A. Parkeh, D. Lu, E. A. Armour, and L. Chernyak, "Investigation of V-Defects and embedded inclusions in InGaN/GaN multiple quantum wells grown by metalorganic chemical vapor deposition on (0001) sapphire," *Applied Physics Letters*, vol. 83, no. 1, p. 33, 2003.

[120] R. Datta, M. Kappers, M. Vickers, J. Barnard, and C. Humphreys, "Growth and characterisation of GaN with reduced dislocation density," *Superlattices and Microstructures*, vol. 36, pp. 393–401, oct 2004.

[121] K. Hiramatsu, "Epitaxial lateral overgrowth techniques used in group III nitride epitaxy," *Journal of Physics: Condensed Matter*, vol. 13, pp. 6961–6975, aug 2001.

[122] B. Beaumont, V. Bousquet, P. Vennéguès, M. Vaille, A. Bouillé, P. Gibart, S. Dassonneville, A. Amokrane, and B. Sieber, "Two-step method for epitaxial lateral overgrowth of GaN," *Physica Status Solidi (A) Applied Research*, vol. 176, no. 1, pp. 567–571, 1999.

[123] H. El-Ella, F. Rol, D. Collins, M. Kappers, R. Taylor, E. Hu, and R. Oliver, "InGaN super-lattice growth for fabrication of quantum dot containing microdisks," *Journal of Crystal Growth*, vol. 321, pp. 113–119, apr 2011.

[124] P. Visconti, M. A. Reshchikov, K. M. Jones, D. F. Wang, R. Cingolani, H. Morkoc, R. J. Molnar, and D. J. Smith, "Highly selective photoelectrochemical etching of nitride materials for defect investigation and device fabrication," *Journal of Vacuum Science & Technology B: Microelectronics and Nanometer Structures*, vol. 19, no. 4, p. 1328, 2001.

[125] C. Youtsey, L. T. Romano, R. J. Molnar, and I. Adesida, "Rapid evaluation of dislocation densities in n-type GaN films using photoenhanced wet etching," *Applied Physics Letters*, vol. 74, no. May 2015, p. 3537, 1999.

[126] C. Youtsey, L. T. Romano, and I. Adesida, "Gallium nitride whiskers formed by selective photoenhanced wet etching of dislocations," *Applied Physics Letters*, vol. 73, no. 6, p. 797, 1998.

[127] M. S. Minsky, M. White, and E. L. Hu, "Room-temperature photoenhanced wet etching of GaN," *Applied Physics Letters*, vol. 68, no. 11, pp. 1531–1533, 1996.

[128] D. Cherns, "The structure and optoelectronic properties of dislocations in GaN The structure and optoelectronic properties of dislocations in," *J. Phys. Condens. Matter.*, vol. 12, p. 10205, 2000.

[129] H. A. R. El-Ella, F. Rol, M. J. Kappers, K. J. Russell, E. L. Hu, and R. A. Oliver, "Dislocation density-dependent quality factors in InGaN quantum dot containing microdisks," *Applied Physics Letters*, vol. 98, no. 13, p. 131909, 2011.

[130] S. K. Rhode, M. K. Horton, M. J. Kappers, S. Zhang, C. J. Humphreys, R. O. Dusane, S. L. Sahonta, and M. A. Moram, "Mg doping affects dislocation core structures in GaN," *Physical Review Letters*, vol. 111, no. July, pp. 1–4, 2013.

[131] M. K. Horton, S. Rhode, S.-L. Sahonta, M. J. Kappers, S. J. Haigh, T. J. Pennycook, C. J. Humphreys, R. O. Dusane, and M. A. Moram, "Segregation of In to dislocations in InGaN.," *Nano letters*, vol. 15, no. 2, pp. 923–30, 2015.

[132] Y. Xin, E. M. James, I. Arslan, S. Sivananthan, N. D. Browning, S. J. Pennycook, F. Omnes, B. Beaumont, J.-P. Faurie, and P. Gibart, "Direct experimental observation of the local electronic structure at threading dislocations in metalorganic vapor phase epitaxy grown wurtzite GaN thin films," *Applied Physics Letters*, vol. 76, no. 4, p. 466, 2000.

[133] J. Elsner, R. Jones, P. K. Sitch, V. D. Porezag, M. Elstner, T. Frauenheim, M. I. Heggie, S. Oberg, and P. R. Briddon, "Theory of Threading Edge and Screw Dislocations in GaN," *Physical Review Letters*, vol. 79, no. 19, pp. 3672–3675, 1997.

[134] O. Ambacher, W. Rieger, P. Ansmann, H. Angerer, T. D. Moustakas, and M. Stutzmann, "Sub-bandgap absorption of gallium nitride determined by photothermal deflection spectroscopy," *Solid State Communications*, vol. 97, no. 5, pp. 365–370, 1996.

[135] S. Lazar, L. Weyher, J. L abd Macht, F. D. Tichelaar, and H. W. Zandbergen, "Nanopipes in GaN: photo-etching and TEM study," *The European Physical Journal Applied Physics*, vol. 28, pp. 265–291, 2004.

[136] R. A. Oliver, G. A. D. Briggs, M. J. Kappers, C. J. Humphreys, S. Yasin, J. H. Rice, J. D. Smith, and R. A. Taylor, "InGaN quantum dots grown by metalorganic vapor phase epitaxy employing a post-growth nitrogen anneal," *Applied Physics Letters*, vol. 83, no. 4, pp. 755–757, 2003.

[137] F. C.-P. Massabuau, M. J. Davies, W. E. Blenkhorn, S. Hammersley, M. J. Kappers, C. J. Humphreys, P. Dawson, and R. A. Oliver, "Investigation of unintentional indium incorporation into GaN barriers of InGaN/GaN quantum well structures," *Physica Status Solidi (B)*, pp. n/a–n/a, 2014.

[138] N. Vartak, A. Damle-Vartak, B. Richter, O. Dirsch, U. Dahmen, S. Hammad, and J. G. Hengstler, "Cholestasis-induced adaptive remodeling of interlobular bile ducts," *Hepatology*, vol. 63, no. 3, 2016.

[139] S. van der Walt, J. L. Schönberger, J. Nunez-Iglesias, F. Boulogne, J. D. Warner, N. Yager, E. Gouillart, T. Yu, and the scikit-image contributors, "scikit-image: image processing in Python," *PeerJ*, vol. 2, p. e453, 6 2014.

[140] D. V. S. Rao, K. Muraleedharan, and C. J. Humphreys, "TEM specimen preparation techniques," *Microscopy: Science, Technology, Applications and Education*, no. 320, pp. 1232–1244, 2010.

[141] C. Tomasi and R. Manduchi, "Bilateral Filtering for Gray and Color Images," *International Conference on Computer Vision*, pp. 839–846, 1998.

[142] FEI Company, *Helios Nanolab 650 Product Data*, 2013.

[143] S. Kucheyev, J. Williams, and S. Pearton, "Ion implantation into GaN," *Materials Science and Engineering: R: Reports*, vol. 33, pp. 51 – 108, 2001.

[144] M. Grande, G. Calo, V. Petruzzelli, and A. D'Orazio, "High-Q Photonic Crystal Nanobeam Cavity Based on a Silicon Nitride Membrane Incorporating Fabrication Imperfections and a Low-Index Material Layer," *Progress In Electromagnetics Research B*, vol. 37, no. December 2011, pp. 191–204, 2012.

[145] W. Bergbauer, M. Strassburg, C. Kölper, N. Linder, C. Roder, J. Lähnemann, A. Trampert, S. Fündling, S. F. Li, H.-H. Wehmann, and A. Waag, "Continuous-flux MOVPE growth of position-controlled N-face GaN nanorods and embedded InGaN quantum wells," *Nanotechnology*, vol. 21, no. 30, p. 305201, 2010.

[146] C. Tessarek, M. Bashouti, M. Heilmann, C. Dieker, I. Knoke, E. Spiecker, and S. Christiansen, "Controlling morphology and optical properties of self-catalyzed, mask-free GaN rods and nanorods by metal-organic vapor phase epitaxy," *Journal of Applied Physics*, vol. 114, no. 14, 2013.

[147] S. Zhao, H. P. T. Nguyen, M. G. Kibria, and Z. Mi, "III-Nitride nanowire optoelectronics," *Progress in Quantum Electronics*, vol. 44, pp. 14–68, 2015.

[148] G. Liu, B. Wen, T. Xie, A. Castillo, J.-Y. Ha, N. Sullivan, R. Debnath, A. Davydov, M. Peckerar, and A. Motayed, "Top-down fabrication of horizontally-aligned gallium nitride nanowire arrays for sensor development," *Microelectronic Engineering*, vol. 142, pp. 58 – 63, 2015.

[149] C. B. Maliakkal, J. P. Mathew, N. Hatui, A. A. Rahman, M. M. Deshmukh, and A. Bhattacharya, "Fabrication and characterization of gan nanowire doubly clamped resonators," *Journal of Applied Physics*, vol. 118, no. 11, 2015.

[150] R. Debnath, J.-Y. Ha, B. Wen, D. Paramanik, A. Motayed, M. R. King, and A. V. Davydov, "Top-down fabrication of large-area gan micro- and nanopillars," *Journal of Vacuum Science & Technology B*, vol. 32, no. 2, 2014.

[151] S. Dhara, C. Y. Lu, C. T. Wu, C. W. Hsu, W. S. Tu, K. H. Chen, Y. L. Wang, L. C. Chen, and B. Raj, "Focused ion beam induced nanojunction and defect doping as a building block for nanoscale electronics in GaN nanowires," *Journal of Physical Chemistry C*, vol. 114, no. 36, pp. 15260–15265, 2010.

[152] A. Bao, "Group iii-nitride nanowires," *Materials Science and Technology*, vol. 0, no. 0, pp. 1–12, 2016.

[153] W. Shi, Y. Zheng, N. Wang, C. Lee, and S. Lee, "Microstructures of gallium nitride nanowires synthesized by oxide-assisted method," *Chemical Physics Letters*, vol. 345, no. 56, pp. 377 – 380, 2001.

[154] W. C. Hou, L. Y. Chen, W. C. Tang, and F. C. N. Hong, "Control of seed detachment in Au-assisted GaN nanowire growths," *Crystal Growth and Design*, vol. 11, no. 4, pp. 990–994, 2011.

[155] X. F. Duan and C. M. Lieber, "Laser-assisted catalytic growth of single crystal GaN nanowires," *J Am Chem Soc*, vol. 122, no. 1, pp. 188–189, 2000.

[156] C. Chèze, L. Geelhaar, A. Trampert, O. Brandt, and H. Riechert, "Collector phase transitions during vapor-solid-solid nucleation of GaN nanowires," *Nano Letters*, vol. 10, no. 9, pp. 3426–3431, 2010.

[157] J. Chen and C. Xue, "Catalytic growth of large-scale gan nanowires," *Journal of Materials Engineering and Performance*, vol. 19, no. 7, pp. 1054–1057, 2010.

[158] L. Geelhaar, C. Chèze, W. M. Weber, R. Averbeck, H. Riechert, T. Kehagias, P. Komninou, G. P. Dimitrakopulos, and T. Karakostas, "Axial and radial growth of ni-induced gan nanowires," *Applied Physics Letters*, vol. 91, no. 9, 2007.

[159] G. Chen, T. McGuckin, C. J. Hawley, E. M. Gallo, P. Prete, I. Miccoli, N. Lovergine, and J. E. Spanier, "Subsurface imaging of coupled carrier transport in GaAs/AlGaAs core-shell nanowires," *Nano Letters*, vol. 15, no. 1, pp. 75–79, 2015.

[160] S. D. Hersee, X. Sun, and X. Wang, "The controlled growth of GaN nanowires," *Nano Letters*, vol. 6, no. 8, pp. 1808–1811, 2006.

[161] C. Tessarek, M. Heilmann, E. Butzen, A. Haab, H. Hardtdegen, C. Dieker, E. Spiecker, and S. Christiansen, "The role of Si during the growth of GaN micro- and nanorods," *Crystal Growth and Design*, vol. 14, no. 3, pp. 1486–1492, 2014.

[162] S. Li, S. Fuendling, X. Wang, S. Merzch, M. A. M. Al-Suleiman, J. D. Wei, H. H. Wehmann, A. Waag, W. Bergbauer, and M. Strassburg, "Polarity and its Influence on Growth Mechanism during MOVPE Growth of GaN Nanorods," *Crystal Growth & Design*, vol. 11, pp. 1573–1577, 2011.

[163] R. Koester, J. S. Hwang, C. Durand, D. L. S. Dang, and J. Eymery, "Self-assembled growth of catalyst-free gan wires by metal-organic vapour phase epitaxy," *Nanotechnology*, vol. 21, no. 1, p. 015602, 2010.

[164] A. B. Yankovich, A. V. Kvit, X. Li, F. Zhang, V. Avrutin, H. Y. Liu, N. Izyumskaya, Ü. Özgür, H. Morkoç, and P. M. Voyles, "Hexagonal-based pyramid void defects in GaN and InGaN," *Journal of Applied Physics*, vol. 111, no. 2, 2012.

[165] Z. Fang, E. Robin, E. Rozas-Jimenez, A. Cros, F. Donatini, N. Mollard, J. Pernot, and B. Daudin, "Si Donor Incorporation in GaN Nanowires," *Nano Letters*, vol. 15, no. 10, pp. 6794–6801, 2015.

[166] J. Neugebauer, "Surfactants and antisurfactants on group-III-nitride surfaces," *Physica Status Solidi C: Conferences*, vol. 0, no. 6 SPEC. ISS., pp. 1651–1667, 2003.

[167] T. Markurt, L. Lymperakis, J. Neugebauer, P. Drechsel, P. Stauss, T. Schulz, T. Remmele, V. Grillo, E. Rotunno, and M. Albrecht, "Blocking growth by an electrically active subsurface layer: The effect of si as an antisurfactant in the growth of GaN," *Physical Review Letters*, vol. 110, no. 3, pp. 1–5, 2013.

[168] M. Kappers, M. Moram, Y. Zhang, M. Vickers, Z. Barber, and C. Humphreys, "Interlayer methods for reducing the dislocation density in gallium nitride," *Physica B: Condensed Matter*, vol. 401-402, pp. 296–301, dec 2007.

[169] Vennéguès, B. Beaumont, S. Haffouz, M. Vaille, and P. Gibart, "Influence of in situ sapphire surface preparation and carrier gas on the growth mode of gan in movpe," *Journal of Crystal Growth*, vol. 187, no. 2, pp. 167 – 177, 1998.

[170] T. Böttcher, J. Dennemarck, R. Kröger, S. Figge, and D. Hommel, "The role of the growth temperature for the SiN interlayer deposition in GaN," *Physica Status Solidi C: Conferences*, vol. 2042, no. 7, pp. 2039–2042, 2003.

[171] C. Johnston, M. Kappers, M. Moram, J. Hollander, and C. Humphreys, "Assessment of defect reduction methods for nonpolar a-plane GaN grown on r-plane sapphire," *Journal of Crystal Growth*, vol. 311, pp. 3295–3299, jun 2009.

[172] S. Tanaka, S. Iwai, and Y. Aoyagi, "Self-assembling gan quantum dots on $al_xga_{1-x}n$ surfaces using a surfactant," *Applied Physics Letters*, vol. 69, no. 26, pp. 4096–4098, 1996.

[173] R. A. Oliver, N. K. Van der Laak, M. J. Kappers, and C. J. Humphreys, "Insights into the growth mechanism of$In_xGa_{1-x}N$ epitaxial nanostructures formed using a silane predose," *Journal of Crystal Growth*, vol. 310, no. 15, pp. 3459–3465, 2008.

[174] J. Unland, B. Onderka, A. Davydov, and R. Schmid-Fetze, "Thermodynamics and phase stability in the gan system," *Journal of Crystal Growth*, vol. 256, pp. 33 – 51, 2003.

[175] V. Schmidt, J. V. Wittemann, and U. Gosele, "Growth, Thermodynamics, and Electrical Properties of Silicon Nanowires.," *Chemical Reviews*, vol. 110, no. 1, pp. 361–388, 2010.

[176] J. Xie, Y. Fu, X. Ni, H. Morko, C. K. Inoki, T. S. Kuan, J. V. Foreman, and H. O. Everitt, "Low dislocation densities and long carrier lifetimes in gan thin films grown on a sin_x nanonetwork," *Applied Physics Letters*, vol. 90, no. 4, 2007.

[177] I. Halidou, Z. Benzarti, T. Boufaden, B. El Jani, S. Juillaguet, and M. Ramonda, "Influence of silane flow on MOVPE grown GaN on sapphire substrate by an in situ SiN treatment," *Materials Science and Engineering B: Solid-State Materials for Advanced Technology*, vol. 110, no. 3, pp. 251–255, 2004.

[178] S. E. Bennett, D. Holec, M. J. Kappers, C. J. Humphreys, and R. A. Oliver, "Imaging dislocations in gallium nitride across broad areas using atomic force microscopy.," *The Review of scientific instruments*, vol. 81, p. 063701, jun 2010.

[179] Q. Ji, L. Li, W. Zhang, J. Wang, P. Liu, Y. Xie, T. Yan, W. Yang, W. Chen, and X. Hu, "Dislocation Reduction and Stress Relaxation of GaN and InGaN Multiple Quantum Wells with Improved Performance via Serpentine Channel Patterned Mask," *ACS Applied Materials and Interfaces*, vol. 8, no. 33, pp. 21480–21489, 2016.

[180] R.-C. Tu, C.-J. Tun, C.-C. Chuo, B.-C. Lee, C.-E. Tsai, T.-C. Wang, J. Chi, C.-P. Lee, and G.-C. Chi, "Ultra-high-density ingan quantum dots grown by metalorganic chemical vapor deposition," *Japanese Journal of Applied Physics*, vol. 43, no. 2B, p. L264, 2004.

[181] W. Te-Chung, K. Hao-Chung, L. Tien-Chang, T. Ching-En, T. Min-Ying, H. Jung-Tsung, and Y. Jer-Ren, "Study of InGaN multiple quantum dots by metal organic chemical vapor deposition," *Japanese Journal of Applied Physics, Part 1 (Regular Papers, Short Notes & Review Papers)*, vol. 45, no. 4B, pp. 3560–3563, 2006.

[182] C. Tessarek, R. Roder, and T. Michalsky, "Improving the Optical Properties of Self-Catalyzed GaN Microrods toward Whispering Gallery Mode Lasing," *ACS Photonics*, vol. 1, no. 10, pp. 990–997, 2014.